AIX-MARSEILLE UNIVERSITÉ
ÉCOLE DOCTORALE SCIENCES POUR L'INGÉNIEUR
LABORATOIRE IUSTI UMR CNRS 7343

Thèse présentée pour obtenir le grade universitaire de docteur

Discipline : Mécanique, Physique, Micro et Nanoélectronique
Spécialité : Mécanique et Physique des Fluides

Minh Tuan HO

Kinetic modeling of the transient flows of single gases and gaseous mixtures

Soutenue le 30/09/2015 devant le jury :

Guillaume GALLIERO	Prof. Université de Pau et des Pays de l'Adour	Rapporteur
Yonghao ZHANG	Prof. University of Strathclyde	Rapporteur
Jacques SCHNEIDER	MCF Université de Toulon	Examinateur
Hiroki YAMAGUCHI	Assoc. Prof. Nagoya University	Examinateur
Irina GRAUR	Prof. Aix-Marseille Université	Directrice de thèse
Jean-Denis PARISSE	MCF Aix-Marseille Université	Co-directeur de thèse

to my beloved family

Acknowledgments

First and foremost, I am deeply indebted to my advisor, Irina Graur. Her patience, enthusiasm, advice and willing supports have inspired my love of research. I acknowledge kindly supports during the past three years from my co-advisor, Jean-Denis Parisse. I express my special thanks to Pierre Perrier, Vincent Pavan and Gilbert Méolans for fruitful discussions on practical and theory aspects of rarefied gas dynamics.

I also express my appreciation to Lounès Tadrist who hosts my PhD training at IUSTI laboratory. In term of computational facility, my grateful thanks are due to Yann Jobic and Meso-center team for the perfect performance of the clusters. My work at IUSTI have been greatly eased by generous administrative assistance from Pascal Campion, Jeanne Pullino and Joyce Bartolini. My sincere thanks also goes to Eric Valerio who offers me teaching opportunity at HSE Department, IUT Aix-Marseille.

I thank also my lab-mates: Alice, Prashant, Laurent, Mustafa, Marcos, Kifah, Hau, Phong, Amina, Nathalie and Matthieu for their kindness making my comfortable office time. I am grateful to Pierre, Walter, Hang and Seikou for the joyful French classes and picnics. My time in France is enjoyable and memorable with anh chi Quan-Thuy, Tuong-Uyen, Lan-Van, Ba, Hanh, Vinh, Tung, Bien, Hoan and many other Vietnamese friends.

Last but not least, I express my deeply gratitude to my parents, my younger brother and to my best friend, Kim Yen. My exciting and pleasant journey abroad would not be realized without their love, supports and encouragements.

Minh Tuan HO

Marseille, July, 2015

Abstract

A gas inside the microsystems or the porous media is in its non-equilibrium state, due to the fact that the molecular mean free path is comparable to the characteristic dimension of the media. The same state of a gas, called rarefied, is found at high altitude or in the vacuum equipment working at low pressure. All these types of flow can be described by the kinetic models derived from the Boltzmann equation. This thesis presents the development of the numerical tools for the modeling and simulations of the rarefied gas flows. The two models of the full Boltzmann equation, the Shakhov model (S-model) for the single gas and the McCormack model for the gas mixture, are considered. The discrete velocity method is used to the numerical discretization in the molecular velocity space and the TVD-like scheme is implemented in the physical space. The main aspect of this work is centered around the transient properties of the gas flows and, especially, on the transient heat and mass transfer behaviors. However, for some configurations only steady-state solutions are considered and the implicit scheme is developed to reduce the computational cost. Using the proposed numerical approach several types of the transient rarefied single gas flows as well as the binary mixture of the monoatomic gases are studied.

Résumé

Un gaz à l'intérieur d'un microsystème ou d'un milieu poreux est dans un état hors équilibre, car le libre parcours moyen des molécules est comparable à la dimension caractéristique du milieu. Ce même état degaz, appelé raréfié, se retrouve en haute altitude ou dans un équipement de vide à basse pression. Ces gaz raréfiés suivent des types d'écoulements qui peuvent être décrits par des modèles cinétiques dérivés de l'équation de Boltzmann. Dans ce travail nous présentons les principaux modèles et leurs mises en oeuvre numériquepour la simulation des écoulements de gaz raréfiés. Parmi les modèles utilisés nous présentons les deux modèles complets de l'équation de Boltzmann, le modèle de Shakhov(S-model) pour un gaz monoatomique et le modèle de Mc-Cormack pour un mélange de gaz toujours monoatomiques. La méthode des vitesses discrètes est utilisée pour la discrétisation numérique dans l'espace des vitesses moléculaires et le schéma de type TVD est mis en œuvre dans l'espace physique. L'aspect original de ce travail se situe sur les régimes transitoires et, en particuliersur les comportements non-stationnaires des transferts de chaleur et de masse. Cependant, pour certaines configurations nous considérons uniquement les conditions stationnaires des écoulements et un schéma implicite est développé afin de réduire le coût de calcul. En utilisant ces approches numériques, nous présentons les résultats pour plusieurs types d'écoulements non-stationnaires, de gaz raréfiés monoatomiqueset de mélanges binaires de gaz monoatomiques.

Résumé Français

La compréhension des phénomènes de transport à l'échelle micro et nanométrique n'est pas seulement intéressante sur le plan fondamental, mais elle est aussi de plus en plus nécessaire pour la poursuite du développement de nombreux domaines. Parmi ces domaines on trouve les industries chimiques (séparation de gaz, filtration, stockage, etc...), la microélectronique (micro échangeur de la chaleur pour le refroidissement des composants et tous les systèmes de type MEMS (MicroElectroMecanical Systems)), la médecine (lab-of-chip pour l'extraction et l'analyse d'échantillons biologiques), l'espace (micro-actuateur pour le contrôle actif des écoulements, les vols en haute altitude). Un autre domaine en forte expansion qui relève de l'approche du gaz raréfié est la technologie du vide avec toutes les applications technologiques (le dépôt de couches minces, spectromètre, valves de dosage, capteurs de pression, etc. . .). Enfin cette problématique se retrouve dans le projet ITER où l'installation principale fonctionne dans des conditions de vide poussé.

La caractéristique principale des écoulements gazeux aux petites échelles ou aux basses pressions est leur raréfaction caractérisée par le rapport entre le libre parcours moyen des molécules (λ) et la dimension caractéristique du problème (L), appelé nombre de Knudsen : Ce nombre sans dimension devient important (plus grand que un) dans deux situations : soit, à l'échelle micrométrique, quand la dimension caractéristique d'un problème est petite, soit, dans le domaine de basse pression, quand le libre parcours moyenne de molécules est très grand. Dans le premier cas, à l'échelle micrométrique, la deuxième propriété de l'écoulement apparait plus clairement : le rapport surface-volume devient beaucoup plus grand que dans un écoulement classique, et donc la description réaliste des collisions gaz-surface devient très importante.

Un gaz à l'intérieur d'un microsystème ou d'un milieu poreux est dans un état hors équilibre, (i.e. éloigné de toute situation d'équilibre local) car le libre parcours moyen des molécules est alors comparable à la dimension caractéristique du milieu. Ce même état de gaz, appelé raréfié, se retrouve en haute altitude ou dans un équipement de vide à basse pression.

Suivant la suggestion de Schaaf et Chambre datant de 1961 [1], on peut schématiser le classement des différents régimes de raréfaction en fonction du nombre de Knudsen. Les

valeurs des bornes limitant chaque régime ne représentent qu'un ordre de grandeur, car la transition entre deux régimes n'est pas brutale mais progressive. On distingue donc habituellement: Le régime hydrodynamique (défini par Kn $\leq$ 10−3), où le modèle continue (traduit par les équations de Navier-Stokes) est valide, associé à des conditions limites de paroi, classiques : conditions limites d'adhérence pour la vitesse et de continuité pour la température. Le régime de glissement (10−3 $\leq$ Kn $\leq$ 10−1), où le modèle continue est encore convenable à condition d'être alors associé à des conditions limites de glissement (de vitesse) et de saut (pour la température). Le régime transitionnel (10−1 $\leq$ Kn $\leq$ 10), où le modèle continu n'est plus valide. Pour ce régime la simulation numérique est basée sur la résolution de l'équation de Boltzmann par différents approches. Le régime moléculaire libre (Kn $\geq$ 10), où l'écoulement de gaz est fortement raréfié. Dans ce régime les collisions intermoléculaires sont nettement moins nombreuses que les collisions du gaz avec la surface solide. L'écoulement est donc « piloté » par l'interaction gaz-paroi. Un écoulement de gaz peut être décrit à deux niveaux d'analyse différents: le niveau microscopique et le niveau macroscopique. Au niveau macroscopique, le gaz est considéré comme un milieu continu. Le modèle macroscopique, basé sur le système des équations de Navier-Stokes, fournit une description détaillée du comportement des paramètres macroscopiques du gaz, tels que la densité, la vitesse macroscopique, la pression et la température. Au niveau microscopique, la structure moléculaire du gaz est prise en compte et, en plus de l'espace physique et du temps, paramètres utilisés dans les modèles macroscopiques, l'espace des vitesses moléculaires est également pris en compte et on considère donc l'espace de phases à six dimensions.

Le modèle physique le plus général, mis en oeuvre à l'échelle microscopique, est basé sur l'équation de Boltzmann, qui décrit statistiquement le comportement macroscopique d'un gaz. Du point de vue mathématique l'équation de Boltzmann est une équation intégro-différentielle où la fonction de distribution moléculaire dépend, en général, de sept variables : un vecteur de position, un vecteur de vitesse moléculaire, les deux dans l'espace de phases, et un temps. Sa résolution est donc un problème très difficile. Par conséquent, il convient de définir les conditions dans lesquelles sa solution est vraiment indispensable, ce qui signifie, les conditions dans lesquelles les modèles continus perdent leur validité. En même temps, plusieurs modèles cinétiques de l'équation de Boltzmann sont proposés à partir des années soixante. Ces modèles sont moins couteux au point de vue numérique par rapport à la résolution de l'équation de Boltzmann, mais ils reflètent aussi plus ou moins bien les propriétés de cette équation. Il et donc, indispensable de tester la capacité de ces modèles à suivre les propriétés de l'équation de Boltzmann.

L'équation de Boltzmann décrit une évolution de la fonction de distribution moléculaire et elle est théoriquement valable pour toute valeur du nombre de Knudsen. Mais sa solution analytique n'est possible que pour très peu de cas particuliers et sa solution numérique est très

coûteuse en termes de ressources informatiques. Les difficultés de sa résolution proviennent du caractère intégro-différentiel de cette équation et aussi de sa forte dimensionnalité. La solution numérique de l'équation de Boltzmann a représenté un défi pendant plusieurs décennies, mais il n'est pas facile de construire un schéma numérique qui maintienne les principales propriétés de l'équation de Boltzmann: la positivité de la fonction de distribution, la conservation des moments macroscopiques, les propriétés d'entropie, etc.

Aujourd'hui, les méthodes les plus connues pour la résolution numérique de l'équation de Boltzmann sont: la simulation directe de Monte-Carlo (Directe Simulation Monte Carlo (DSMC)), la méthode des vitesses discrètes (Discrete Velocity Method (DVM)) et la méthode spectrale rapide (Fast Spectral Method (FSM)), proposé récemment. Chacune d'elles s'applique pour une gamme particulière de paramètres d'écoulement.

La méthode la plus universelle et la plus largement utilisée en pratique est la méthode de simulation directe de Monte-Carlo (DSMC). Cette méthode est très populaire en raison de son efficacité et de sa flexibilité, mais les fluctuations statistiques, présentes dans cette méthode, en ont fait une approche inexacte pour les simulations des écoulements instationnaires ou pour les écoulements à faible vitesse. Par exemple, pour un écoulement de gaz avec un nombre de Mach $0,001$ (fréquemment rencontré dans les micro-dispositifs), environ 108 échantillons indépendants sont nécessaires pour réduire l'erreur de 1% quand il y a 100 particules simulées dans une cellule [2]. Aussi, le DSMC est-elle une méthode inefficace pour le régime de glissement puisque les dimensions de cellules spatiales et les pas de temps doivent être respectivement plus petits que le libre parcours moyen et le temps collisionnel. Des progrès ont été faits pour surmonter ces difficultés: pour le cas de faibles variations de quantités macroscopiques, la méthode de préservation de l'informations (information preservation) [3] et la méthode DSMC de la faible variance (low variance) [4, 5] ont été proposées.

Bien que le principe de la méthode des vitesses discrètes ait été proposé dès l'année 1960, ce n'est qu'aujourd'hui que cette méthode commence à être appliquée pour la simulation numérique des écoulements de gaz raréfiés. Cette possible mise en œuvre récente est surtout due au développement considérable de la technique de calculs parallèles au cours des deux dernières décennies, qui a permis la réalisation de calculs, auparavant impossibles. La méthode des vitesses discrètes est une méthode déterministe et elle n'a donc pas de fluctuations statistiques, de plus elle bien adaptée pour la simulation de l'écoulement à faible vitesse et de l'écoulement instationnaire.

Récemment, la méthode spectrale rapide (FSM) a été développée pour résoudre numériquement l'équation de Boltzmann pour un gaz monoatomiques [6, 7, 8, 9]. Elle utilise une discrétisation de Fourier Galerkin dans l'espace des vitesses, et traite les collisions binaires dans l'espace des fréquences correspondant. Comme cette méthode permet les discrétisations de

vitesses non uniforme, et comme le nombre de nœuds de fréquence peut être beaucoup plus petit que le nombre de nœuds de vitesse [9], le FSM est bien adapté pour résoudre les écoulements de gaz très raréfiés, où un grand nombre de nœuds de vitesse sont utilisés pour capturer des discontinuités de la fonction distribution de vitesse moléculaires. Le FSM peut être 50 fois plus rapide que la méthode DSMC de faible variance [9].

Comme on le sait, une solution numérique de l'équation de Boltzmann complète reste encore une tâche difficile, aujourd'hui, alors même que de puissants ordinateurs sont disponibles. Pour simplifier l'intégrale de collisions, en gardant l'essentiel de ses propriétés, un certain nombre de modèles cinétiques ont été proposés. Chacun de ces modèles cinétiques possède ses propres avantages et ses inconvénients. Ainsi, le modèle cinétique de Bhatnagar–Gross–Krook (BGK modèle) [10] propose une forme approchée de l'intégrale de collision relativement simple, mais ce modèle donne un nombre de Prandtl inapproprié, ce qui provoque une erreur sur les calculs de flux de chaleur. Dans le même temps, les équations cinétique modèle BGK [10], aussi S modèle [11] et ES modèle [12] (où un nombre de Prandtl correct est obtenu) peuvent être un des outils efficaces et largement utilisées pour les calculs pratiques.

Dans la pratique les mélanges de gaz sont plus utilisés que les gaz purs et, il existe peu de modèles satisfaisants pour ces mélanges [13, 14, 15, 16, 17, 18]. La modélisation des phénomènes de transport dans les mélanges gazeux est beaucoup plus complexe que celle des gaz purs et, ceci pour plusieurs raisons. Tout d'abord, les écoulements de mélange gazeux nécessitent la détermination de plus de paramètres que les écoulements de gaz purs. Outre les paramètres de raréfaction des gaz, la pression et la température, les écoulements de mélange de gaz dépendent des compositions des espèces du mélange et de leurs affinités relatives avec la phase solide. Deuxièmement, en plus des forces classiques telles que les gradients de pression et de température, des forces additionnelles apparaissent dans les mélanges, fonctions du gradient des fractions molaires. Troisièmement, plusieurs nouveaux phénomènes transversaux apparaissent dans un mélange tel que, par exemple, la diffusion thermique. En raison de cette complexité, la difficulté de modélisation des écoulements de mélanges gazeux augmente considérablement par rapport à celle d'un gaz pur.

L'objectif principal de ce travail de thèse est le développement d'approches efficaces pour les simulations numériques de cas pratiques d'écoulements de gaz raréfiés purs et de mélanges de gaz sur la base des équations cinétiques modèles et de la mise en oeuvre de la méthode des vitesses discrètes (DVM).

La méthode des vitesses discrètes est utilisée pour la discrétisation numérique dans l'espace des vitesses moléculaires et le schéma de type TVD est mis en œuvre dans l'espace physique. L'aspect original de ce travail se situe sur les régimes transitoires et, en particulier pour les comportements non-stationnaires des transferts de chaleur et de masse. Cepen-

dant, pour certaines configurations nous considérons uniquement les conditions stationnaires des écoulements et nous développons un schéma implicite afin de réduire le coût de calcul. Dans le cadre de ces approches numériques, nous présentons les résultats pour plusieurs types d'écoulements non-stationnaires, de gaz raréfiés monoatomiques et de mélanges binaires de gaz monoatomiques.

Nous avons présenté la comparaison détaillée des résultats de la simulation numérique de plusieurs types d'écoulements de gaz raréfié, obtenus à l'aide des équations cinétiques modèle linéarisées et non linéaires, avec les résultats correspondants obtenus à partir de l'équation de Boltzmann : tant ceux de l'équation Boltzmann complète (résolue par la méthode DSMC) que ceux de l'équation de Boltzmann linéarisée. Nous avons ainsi montré que ces équations modèles fournissent des résultats fiables pour de modestes efforts de calcul et qu'elles peuvent donc être très efficaces pour les applications pratiques.

Chapter 2

Le transfert de chaleur à travers un gaz raréfié a été étudié depuis l'étude fondamentale de Maxwell [19]. Le cas particulier du transfert de chaleur à travers un gaz raréfié placé entre deux sphères concentriques a été étudié théoriquement Réf. [20]. Les solutions analytiques ont été obtenues en résolvant l'équation cinétique et en prenant en compte l'accommodation thermique incomplète à la surface de la sphère interne [21]. Une expression du flux de chaleur en régime transitoire a été proposée dans la Réf. [22] en modifiant l'expression correspondante, obtenue pour la géométrie d'écoulements entre deux plaques parallèles. Le problème du transfert de chaleur d'une sphère à son environnement, comme un cas limite du transfert entre deux sphères, a également été étudié dans les Refs. [23, 24], respectivement pour les gaz monoatomiques et poly-atomiques.

Au cours des dernières années, l'intérêt pour le problème du transfert de chaleur a surgi une fois de plus en liaison avec le développement rapide des MEMS et NEMS. En raison de la petite taille caractéristique de ces dispositifs le gaz à l'intérieur est raréfié et leur gestion thermique devient importante et particulière. La configuration des deux sphères concentriques peut également être utilisée comme une configuration simple pour les mesures du coefficient d'accommodation thermique [25]. Dans ce Chapitre, le transfert de chaleur entre deux sphères concentriques est considéré pour une large variation du degré de raréfaction du gaz, du rapport de températures des surfaces des sphères et du rapport des rayons de ces surfaces. Les expressions analytiques des températures et flux de chaleur radiaux, dans les régimes de glissement et moléculaire libre, sont proposés pour un coefficient d'accommodation arbitraire entre le gaz et les deux surfaces sphériques. Dans le régime d'écoulement transitionnel, le modèle cinétique (S-modèle) a été résolu numériquement à l'aide de la méthode des vitesses discrètes. L'approximation « upwind » est utilisée pour les dérivées spatiales. L'algorithme implicite,

développé dans ce travail nous permet de réduire considérablement le temps de calcul lorsque la solution stationnaire est nécessaire.

Les comportements des paramètres macroscopiques (de flux de chaleur, de température, de pression et de densité numérique) sont examinés en détail pour divers rapports de températures des surfaces sphériques et pour différents rapports des rayons de ces surfaces. Un comportement non monotone du flux de chaleur en fonction du paramètre de raréfaction est obtenu dans le cas du fort rapport de température des surfaces des sphères. Pour les petites et moyennes valeurs du paramètre de raréfaction on trouve une variation de pression importante dans le sens radial.

Des expressions analytiques pour la température et le flux de chaleur dans le régime de glissement ont été obtenues pour des rapports arbitraires de températures et de rayons des sphères et un très bon accord a été trouvé entre ces expressions analytiques et la solution numérique de l'équation cinétique S-modèle.

Une expression approchée du flux de chaleur, valable pour tous les régimes d'écoulement et pour des rapports arbitraires de températures et de rayons des sphères, est proposée dans l'hypothèse d'une réflexion spéculaire-diffuse sur la surface de la sphère interne et d'une réflexion totalement diffuse sur la sphère externe.

Chapitre 3

Le problème du transfert de chaleur entre deux cylindres coaxiaux a été largement étudié au cours des dernières décennies à la fois expérimentalement et théoriquement. Cette configuration a été considérée pour l'étude des "grands nombres de Knudsen" i.e. lorsque le libre parcours moyen des molécules de gaz est nettement plus grand que le rayon du cylindre interne. Il a été montré que pour le régime moléculaire libre, le coefficient d'accommodation thermique peut être facilement exprimé à l'aide de la différence de température entre les surfaces des deux cylindres et de la pression qui règne entre eux. Ces résultats constituent la base de l'utilisation de la "méthode de basse pression», qui est l'une des techniques de mesure classique du coefficient d'accommodation thermiques réalisés dans [26].

Le transfert de chaleur à travers un gaz raréfié entre deux cylindres concentriques a été étudié par de nombreuses auteurs [27, 28, 29, 30, 31, 32, 33]. Dans la plupart des cas, l'analyse a été effectuée en utilisant les modèles cinétiques linéarisées, ce qui est tout à fait justifié lorsque la différence de température entre les cylindres est faible [27, 28, 31] ou le rapport des rayons des cylindres est grande [32]. Pour la grande différence de température entre les cylindres l'approche non linéaire a également été mis en œuvre [29, 30, 34, 33]. Cependant, toutes ces études portent sur des conditions d'écoulement en état stationnaire. Néanmoins, les

informations sur le transfert de chaleur transitoire (instationnaire) sont très importantes du point de vue scientifique et pratique. Dans les phases de conception et de développement des jauges de Pirani [35], l'évaluation de la pression dans le temps est une information vitale pour un ajustement des caractéristiques du capteur. Il faut noter que la géométrie de ce type de jauges reproduit la géométrie de deux cylindres coaxiaux. Les jauges de Pirani sont souvent utilisées dans des chambres de transfert dans l'industrie des semi-conducteurs ou dans des chambres de ventilation avec des cycles rapides. Dans les applications de ventilation rapide les capteurs de Pirani indiquent temporairement une pression qui est supérieure ou inférieure à la pression réelle. Cet effet est dépendant de la géométrie du capteur et de la façon dont la compensation de température est mise en oeuvre. Il serait utile dans la phase de conception de modéliser ces comportements instationnaires de pression et de flux de chaleur afin d'optimiser la conception des jauges de Pirani. En outre, les jauges de Pirani de l'impulsion dépendent à la fois de la conductivité thermique du gaz et de la capacité calorifique du fil et du gaz. Une meilleure compréhension de la physique sous-jacente et l'amélioration correspondante de la modélisation peuvent être utilisées ici pour optimiser les différents modes de fonctionnement.

Quelques articles consacrés aux simulations des propriétés transitoires d'un gaz raréfié doivent être cités [36, 37, 38]. Le sujet, plus proche de la présente étude, est considérée dans la Réf. [36], où les auteurs étudient le transfert de chaleur transitoire entre deux plaques parallèles en raison du chauffage ou du refroidissement rapide de l'une de ces deux plaques. Les simulations sont réalisées dans le régime d'écoulement de glissement mettant en application à la fois les approches continue et cinétique (basée sur la méthode DSMC).

Le but du présent travail est d'étudier l'évolution transitoire du transfert de chaleur à travers un gaz raréfié confiné entre deux cylindres coaxiaux pour une large gamme du degré de raréfaction du gaz. Le modèle cinétique (S-modèle) instationnaire est résolu numériquement pour simuler l'évolution temporelle des paramètres de gaz. Le temps nécessaire pour atteindre les conditions de régime permanent pour les différents paramètres du gaz est évalué pour différents niveaux de raréfaction et pour divers gaz. Dans le régime d'écoulement de glissement le flux de chaleur est calculé à partir du bilan énergétique et il est comparé au flux obtenu à partir de l'équation modèle cinétique.

Les simulations ont été effectuées à partir de l'écoulement moléculaire libre jusqu'au régime hydrodynamique pour différents rapports de rayons des deux cylindres et différents ratios de températures des surfaces. On constate que, pour le plus petit ratio de température $T = 1,3$ le temps pour atteindre l'état d'équilibre, pour le flux de chaleur moyen, varie d'environ $2,5$ à 44 fois le temps caractéristique lorsque l'on passe du régime d'écoulement moléculaire libre au régime l'hydrodynamique. Un minimum a été observé au début du régime transitionnel d'écoulement. En comparant le comportement des gaz monoatomiques dans la géométrie

réelle d'une jauge de pression on obtient que, pour une même pression, pour le Xénon le temps nécessaire pour atteindre l'état d'équilibre est 6 fois plus long que pour l'Hélium. Lorsque le rapport de la température augmente jusqu'à $T = 2$ le temps pour atteindre l'état d'équilibre diminue d'environ 5%. Dans le régime d'écoulement de glissement le temps pour atteindre l'état d'équilibre peut également être trouvé à partir de la solution de l'équation de l'énergie complétée par les conditions aux limites de saut de température.

Chapitre 4

L'écoulement de gaz à travers d'un orifice est un problème d'un grand intérêt pratique pour la conception de l'équipement du vide, les applications spatiales ou de la microfluidique. Les jets sous-détendus à travers les orifices sont principalement utilisés dans les systèmes d'analyse de particules pour séparer et isoler des molécules ou des ions pour déterminer leurs propriétés physiques et chimiques. Les caractéristiques temporelles de ces jets sont importantes pour la recherche du temps de réponse des jauges à vide, qui se développent pour les mesures des variations rapides de pression [39].

Les écoulements stationnaires à travers des orifices, des fentes et des tubes courts ont été étudiés avec succès en appliquant la méthode DSMC et les équations cinétiques [40, 41, 42, 43, 44, 45, 46, 47]. Toutefois, seulement quelques résultats sur les écoulements raréfiés instationnaires à travers d'un orifice [48], d'un tube court [38], d'un long tube [49] ou d'une fente [50] peuvent être trouvés dans la littérature. Les conditions d'écoulement dans la Réf. [48] sont limités à nombre de Mach élevé ou modéré à cause du bruit statique significatif propre à la méthode de DSMC. Les auteurs de la Réf. [39] ont également étudié expérimentalement et numériquement l'écoulement transitoire de gaz, mais entre deux réservoirs de volumes fixes. Lorsque l'on utilise des pressions de grande amplitude variant rapidement dans le temps, on trouve que des temps caractéristiques pour atteindre l'état d'équilibre de ce système sont de l'ordre de quelques secondes.

L'écoulement transitoire de gaz raréfié à travers un orifice est étudié sur la base de S-modèle non-linéaire de l'équation cinétique. Cette équation cinétique non-linéaire instationnaire est résolue numériquement par la méthode de vitesses discrètes (DVM) pour obtenir la variation du débit massique et des paramètres macroscopiques en fonction du temps. Les simulations sont réalisées pour tous les régimes de l'écoulement : du régime moléculaire libre au régime hydrodynamique, pour quatre valeurs de rapport de pression entre les deux réservoirs. L'évolution du débit massique dans le temps est analysée et il se trouve que le temps nécessaire pour atteindre la valeur de débit massique stationnaire dépend essentiellement du rapport de pression entre les deux réservoirs et du régime d'écoulement de gaz dans le réservoir de sortie. Ce temps pour atteindre les conditions de l'état d'équilibre pour le débit de masse est estimé. Il faut de $2,35$ à $30,37$ fois la durée du temps caractéristique pour obtenir le débit de masse à l'état

d'équilibre. Le temps maximal pour atteindre l'état d'équilibre est trouvé dans le régime de glissement pour un rapport de pression de $0,9$ entre les réservoirs. Une méthode d'interpolation simple est réalisée pour calculer le débit massique dans le régime d'écoulement transitionnel. Une expression empirique simple est proposée pour l'évaluation de débit massique en fonction du temps. On montre numériquement que l'écoulement à travers l'orifice dans les conditions considérées ne devient jamais vraiment « choked ».

La technique développée a été utilisée pour la simulation de l'écoulement de vapeur de rubidium dans le domaine de très basse pression dans le cadre du projet AWAKE du CERN.

Chapitre 5

L'écoulement de gaz à travers un canal long de section rectangulaire est un problème pratique fréquemment rencontré dans les MEMS et les applications de la technologie du vide. Ce type de l'écoulement a été largement étudié sur la base de la théorie cinétique et la revue détaillée de ces études peut être trouvée dans la Réf. [51]. Une grande quantité d'expériences sur les microconduits avec des sections transversales diverses, mais uniformes, ont été réalisées dans les dernières décennies [52, 53, 54, 55, 56, 57, 58]. Cependant, dans de nombreuses applications pratiques la section transversale varie le long du canal. Comme exemple de ce genre d'écoulement on peut citer la fuite du gaz à travers une soupape de compresseur [59] et l'écoulement dans un micro palier [60, 61]. Quelques résultats des simulations numériques de l'écoulement à travers de canaux de sections coniques variables [62] et de sections rectangulaire et coniques [63] peuvent être trouvés dans la littérature.

Une méthode simple, proposée précédemment par d'autres auteurs, est appliquée ici pour calculer le débit massique de gaz à travers un canal de section rectangulaire variable. Les calculs sont basés sur les résultats de la solution numérique du S-modèle de l'équation cinétique linéarisée, obtenus par d'autres auteurs, et complétés ici en utilisant la même approche. La technique proposée permet de calculer le débit massique à travers un long canal de section rectangulaire variable pour des rapports de pressions et de températures arbitraires et pour une large gamme de raréfaction du gaz. Des expressions analytiques explicites sont proposées dans le cas du régime hydrodynamique et du régime moléculaire libre. Une méthode d'interpolation simple est réalisée pour calculer le débit massique dans le régime d'écoulement transitionnel.

Chapitre 6

Certains auteurs [64, 65, 58] ont trouvé expérimentalement que la perméabilité d'un canal d'une section variable est plus élevée lorsque ce canal est perfusé dans la direction convergente. Dans un sens plus général, un comportement non-symétrique de l'écoulement suivant la direction (effet de diode) a d'abord été trouvé et étudié dans les écoulements de liquide, notam-

ment par les auteurs des Réfs. [66, 67]. Plus récemment, dans le cas des écoulements gazeux, on a trouvé que cet effet de diode augmente avec la raréfaction dans le régime de glissement et disparaît dans le régime hydrodynamique [58]. Lorsque les deux extrémités d'un canal des sections variables sont dans le régime moléculaire libre, cet effet théoriquement ne devrait pas exister [32, 68].

Des mesures du débit massique à travers un canal d'une section rectangulaire variable ont été effectuées par des collègues de l'université de Bremen. Différents gaz, CO2, N2, Ar ont été utilisés pour les une large gamme de pressions dans les entré et sortie du canal. L'effet de diode donnant un débit plus grand dans la direction convergente (jusqu'au 15%) a été observé expérimentalement.

Basé sur ces observations expérimentales précédentes nous présentons ici un modèle analytique de l'écoulement isotherme dans un conduit de section transversale variable. Nous appliquons l'approche basée sur la solution de l'équation de Stokes avec les conditions limites de glissement de vitesse. Cette équation a été résolue analytiquement et des expressions de débit massique qui différent pour les deux sens de perfusions du canal ont été trouvées. En même temps l'approche numérique, décrite dans la Chapitre 5, a été utilisée pour la simulation numérique de l'écoulement dans le canal de section variable, dans les deux sens de l'écoulement et pour la gamme de pression considérée expérimentalement. Les résultats des trois approches expérimentale, analytique et numérique, sont en bon accord et ils nous permettent de confirmer, décrire et comprendre le phénomène de la diodicité de l'écoulement de gaz. Par le biais des deux approches analytique et numérique nous pourrions prédire le débit massique à travers un long canal de section rectangulaire variable pour des gradients de pression arbitraires.

L'effet de diode analysé ici est essentiellement un phénomène physique et soulève donc la question académique de l'explication du phénomène. Toutefois, il pourrait être applicable, par exemple dans les futures MEMS si l'effet diode peut être poussé jusqu'à des valeurs significatives. Des applications probables sont à prévoir dans les dispositifs de dosage et de pompage des écoulements de gaz où des « diodes réelles » ne permettent la circulation que dans un seul sens.

Chapter 7

Dans de nombreuses applications pratiques comme la technologie du vide, les milieux poreux et l'industrie chimique, les informations sur le transfert de chaleur et de masse des mélanges de gaz raréfiés sont indispensables. Dans ce contexte, les cas-test de référence sont d'une grande importance car ils peuvent nous aider à valider de nouveaux modèles numériques, développés pour la description des écoulements de mélanges gazeux ou de tester la validité des

approches existantes dans les diverses conditions physiques. Ici, les écoulements de Couette et de Fourier entre deux plaques parallèles sont choisis comme les cas-tests de référence car ils constituent des problèmes classiques de la mécanique des fluides. Bien que des solutions pour un gaz pur puissent être trouvées dans la littérature [69] et [70], seulement quelques articles sont consacrés à des mélanges gazeux.

L'écoulement de Couette pour des mélanges gazeux binaires est d'abord étudié dans les Refs. [71, 72, 73, 74, 75] sur la base des modèles cinétiques de l'équation de Boltzmann, tels que le modèle de Hamel [13] pour les molécules maxwelliennes et le modèle McCormack pour un potentiel intermoléculaire arbitraire [14]. Notamment, en utilisant le modèle de McCormack, nous étudions l'influence des interactions intermoléculaires sur la vitesse et la contrainte de cisaillement pour les trois mélanges (Ne-Ar, He-Ar et He-Xe) [74] ainsi que l'influence de l'interaction gaz-surface sur les propriétés de l'écoulement du mélange He-Ar entre les plaques de molybdène et de tantale [75]. Plus tard, l'équation de Boltzmann linéarisée (LBE) pour le modèle de l'interaction moléculaires de sphère dures (HS) a été résolue à l'aide d'une version analytique de la méthode des ordonnées discrètes (ADO méthode) [76], et la précision de la méthode de McCormack a été évaluée pour un mélange de He-Ar: le modèle McCormack est capable de prédire la contrainte de cisaillement de chaque composant et la vitesse de l'espèce plus lourde avec la précision suffisante (1- 3 chiffres de précision) [75, 76], cependant, la vitesse de l'espèce la plus légère et, plus encore le flux de chaleur deviennent très différents des résultats donnés par la solution de l'équation Boltzmann linéarisé (différence bien au-dessus de 100% pour certains cas).

Très peu d'articles sont consacrés au transfert de chaleur à travers un mélange de gaz. L'écoulement de Fourier est d'abord simulé en résolvant l'équation de Boltzmann non linéaire à l'aide d'une technique de différences finies itérative [77]. Ensuite, le transfert de chaleur entre deux plaques planes avec une petite différence de température est étudié en utilisant le modèle McCormack [78] et une équation de Boltzmann linéarisée [79]. On trouve un premier résultat surprenant à priori : le flux de chaleur normalisée pour les mélanges Ne-Ar et He-Xe, obtenue à partir des équations linéarisées, sont trouvés en accord avec les résultats de l'équation de Boltzmann complète non-linéaire avec un écart relatif maximal d'environ 4%. Par contre, entre le modèle McCormack et l'équation de Boltzmann linéarisée, on trouve de grandes différences dans les profils de densité et de température: pour la densité, on observe jusqu'à 15% pour le mélange Ne-Ar et 51% pour le mélange He-Xe, alors que pour la température les différences maximales observées sont 12% et 20% pour les mélanges Ne-Ar et He-Xe, respectivement. L'influence des potentiels intermoléculaires sur le flux de chaleur entre deux plaques parallèles est étudié pour trois mélanges binaires de nobles gaz (Ne-Ar, He-Ar, He-Xe) sur la base du modèle de McCormack [80]: le flux de chaleur est sensible au potentiel intermoléculaire, et la différence entre le modèle des sphères dures et le Potentiel Réalistique [81] peuvent atteindre

15% en régime hydrodynamique.

Pour résumer, on trouve seulement deux articles consacrés à la comparaison entre le modèle McCormack et l'équation Boltzmann linéarisée pour les mélanges de Ne-Ar et He-Xe [79] et He-Ar [76]. Par conséquent, de nouvelles comparaisons systématiques entre le modèle McCormack et l'équation Boltzmann linéarisée seront utiles pour la poursuite du développement des outils mathématiques et numériques pour la simulation des écoulements de mélange gazeux.

Les écoulements de Couette et de Fourier entre les deux plaques parallèles sont simulés à l'aide du modèle cinétique de McCormack, de l'équation de Boltzmann linéarisée et de l'équation de Boltzmann non-linéaire. Deux types de mélange de gaz sont considérés: l'un avec des masses moléculaires similaires (Ne-Ar) et une autre avec des masses moléculaires très différentes (He-Xe). Trois valeurs de concentrations sont considérées et les simulations sont réalisées pour divers régimes : régime moléculaire libre, transitionnel et de glissement. Pour les écoulements de Couette et de Fourier de mélange gazeux, le modèle McCormack donne des solutions fiables, qui sont en bon accord avec les solutions de l'équation de Boltzmann linéarisée.

Chapitre 8

L'écoulement de Couette stationnaire a été largement étudié pour une large gamme de la raréfaction du gaz en utilisant l'équation de Boltzmann stationnaire ou les modèles cinétiques [82, 83, 84, 85, 86]. Les écoulements de Couette oscillatoires, plus complexes, ont été également simulés à l'aide de la méthode de Monte Carlo [87, 88], en résolvant les équations cinétique modèle [89, 90, 91, 92] ou par l'application de la méthode Lattice Boltzmann [93]. Dans le régime d'écoulement hydrodynamique le problème peut être facilement résolu sur la base de l'équation de Navier-Stokes [94]. Plusieurs solutions ont été proposées pour le régime de glissement, en utilisant les conditions aux limites du première [87, 90, 92] et du second ordre [88]. Dans certains articles, [95, 96], les oscillations transversales de l'une des deux plaques parallèles ont été considérées. Cependant, toutes ces simulations ont été réalisées pour un gaz pur. Un seul article a été trouvé dans la littérature, [97], où l'écoulement oscillatoire transversal du mélange de gaz a été simulé en utilisant le modèle linéarisé de type BGK pour le mélange gazeux. A la connaissance de l'auteur, le modèle McCormack n'a pas été appliqué à l'écoulement oscillatoire d'un mélange de gaz. Or ce modèle permet de capturer l'évolution de paramètres de l'écoulement dans le temps, naturellement sans aucune hypothèse supplémentaire sur la forme de la fonction de distribution.

Malgré l'absence des simulations des écoulements de mélange gazeux oscillants, le spectre de leurs applications pratiques apparait large, y compris dans divers dispositifs MEMS, comme les micro accéléromètres, et aussi les capteurs inertiels (inertial sensing), la transduction

acoustique (acoustic transduction), la manipulation de signaux optiques (optical signal manipulation), les filtres résonants (resonant filters) et les composantes de fréquence radio (the radio frequency components). Des appareils comme les résonateurs à l'échelle nanométrique, les commutateurs (switches) ou les vannes (valves) ont des applications dans des tâches aussi diverses que le traitement de l'information, la manipulation moléculaire, et la détection [98, 99, 100, 101].

Le but de ce travail est d'élargir l'approche, développée dans [102, 103] pour la simulation d'écoulement de gaz transitoire, dans le cas de l'écoulement oscillatoire d'un mélange de gaz. Dans ce Chapitre, on donne tout d'abord une brève description du modèle de McCormack pour un mélange de gaz, avec des commentaires sur l'approche numérique pour le problème oscillatoire mis en œuvre. L'approche développée a d'abord été testée pour deux problèmes classiques: l'écoulement de Couette stationnaire d'un mélange de gaz et l'écoulement de Couette oscillatoire d'un gaz pur. Les résultats de ces cas-tests sont comparés avec les résultats obtenus, au préalable, par les autres auteurs. On trouve un très bon accord, avec ces résultats obtenus précédemment. Puis, les deux mélanges, Ne-Ar et He-Xe, sont simulés en utilisant l'approche numérique proposée et le comportement dynamique de l'écoulement de Couette oscillatoire pour les mélanges est étudié. Pour le mélange Ne-Ar on constate que les caractéristiques du mélange, comme les amplitudes de contrainte de cisaillement du mélange et les vitesses de mélange, sont très proches de celles trouvées pour l'écoulement oscillant d'un gaz pur et, donc, les résultats pour un gaz pur peuvent être utilisées pour les estimations de paramètres des mélanges dans le cas, où les masses moléculaires des composants sont relativement proches l'un de l'autre. Toutefois, dans le cas du mélange He-Xe les résultats sont très différents (jusqu'à 30%) par rapport aux résultats pour un gaz pur. On a ainsi trouvé dans ce cas que, l'amplitude de la contrainte de cisaillement du mélange est inférieure à celle du gaz pur. On a également constaté que, même pour une valeur relativement importante du rapport entre fréquence de collision et fréquence de l'oscillation de la plaque paramètre de vitesse d'oscillation, qui correspond à des oscillations lentes, les résultats pour le mélange Ne-Ar sont très différentes de celles pour le cas de l'écoulement stationnaire correspondant.

En conclusion, comme perspectives de ce travail de thèse, nous pouvons citer les points suivants :

Développement d'un solveur de l'équation cinétique dans un logiciel open source tels que OpenFOAM.

Développement d'une approche numérique hybride qui couple l'équation cinétique avec les équations de Navier-Stokes pour simuler l'écoulement de gaz-liquide à deux phases.

Développement d'un outil numérique sur la base de l'équation cinétique pour simuler l'écoulement de gaz raréfié en milieu poreux qui peut avoir de nombreuses applications dans

l'ingénierie du pétrole et dans l'ingénierie membranaire.

Contents

List of Figures

List of Tables

List of Appendices

Nomenclature

Roman symbols

$\dot{M}$	mass flow rate
$\mathbf{q}$	heat flux vector
$\mathbf{u}$	macroscopic/bulk velocity vector
$\mathbf{V}$	perculiar velocity vector
$\mathbf{v}$	molecular velocity vector
c	dimensionless molecular velocity vector
D	diodicity
f	velocity distribution function
G	reduced mass flow rate
h	height of the channel
K	constant
k	Boltzmann constant
Kn	Knudsen number
L	length of the channel
m	molecular mass
Ma	Mach number
N	total number of grid points
n	number density

p	pressure
Pr	Prandtl number
R	radius
r	radial coordinate
T	temperature
t	time
W	dimensionless mass flow rate
w	with of the channel

Subscripts

0	reference quantity
C	cold
g	gas
H	hot
i, j, k, l, m, n	index variables
w	wall

Superscripts

$'$	dimensional quantity
dif	diffusor direction
Hyd	hydrodynamic flow regime
noz	nozzle direction

Acronyms

BE	Boltzmann Equation
BGK	Bhatnagar-Gross-Krook
CFL	Courant-Federichs-Lewis
$DSMC$	Direct Simulation Monte Carlo
DVM	Discreate Velocity Method

FDM	Finite Difference Method
LBE	Linearised Boltzmann Equation
$MEMS$, $NEMS$	Micro/Nano-ElectroMechanical Systems
S	Shakhov
TVD	Total Variation Diminishing
VHS	Variable Hard Sphere

Greeks symbols

α	accomodation coefficient
Δ	finite different quantity
δ	rarefaction parameter
κ	thermal conductivity
μ	viscosity
ν	molecular collision frequency
ω	viscosity index
ϕ, Φ, θ, Θ	angular coordinate
σ	slip coefficient
υ_0	most probable molecular velocity
ξ	temperature jump coefficient

Other symbols

ℓ	equivalent mean free path
$\mathcal{R}$	radius ratio of the exteral and internal surfaces
$\mathcal{T}$	temperature ratio of the hot and cold surfaces

Chapter 1

Introduction

A gas flow may be described in two levels: microscopic and macroscopic levels. At the macroscopic level, a gas is considered as a continuous medium. The system of the Navier-Stokes equations, the macroscopic model, provides the detailed description of the behavior of the gas macroscopic parameters such as density, bulk velocity, pressure and temperature. However this macroscopic approach does not work anymore, when the gas rarefaction increases, *i.e.*, the ratio between the mean free path λ of the molecules and the characteristic dimension ℓ of the problem, the Knudsen number,

$$Kn = \lambda / L \tag{1.1}$$

becomes important. Contrarily to the macroscopic approach, at the microscopic level, the interactions of the gas molecules are taken into account and, in addition to the physical space and time, parameters used in the macroscopic models, the molecular velocity space is also considered.

What approach is better to use for the gas flow simulations? The answer can be done considering the value of the Knudsen number ranges.

Conventionally four different flow regimes can be distinguished:

- Hydrodynamic flow regime, where the continuum approach is valid; $Kn < 0.001$;
- Slip flow regime, where the continuum approach still keep applicable, but has to be completed by the velocity slip and temperature jump boundary conditions; $0.001 < Kn < 0.1$
- Transitional flow regime, where the continuum approach is not valid anymore and the

approaches based on the kinetic simulations have to be applied; $0.1 < Kn < 10$

- Free molecular flow regime, where only the kinetic approach is valid; $Kn > 10$.

Taking into account this classification of the flow regimes the high Knudsen number flows take place in two physical conditions: either the molecular mean free path is large which is the case of the low pressure flow (vacuum and space applications), or the characteristic dimensions of the flow is small. This case corresponds to the flows at the microscale (microelectromechanical systems (MEMS) and porous media). Due to the micrometer or nanometer characteristic dimension of the MEMS or NEMS devices or pore sizes a gas flow inside is often in the slip, transitional or even in the free molecular regime, even at the atmospheric pressure. In addition, at this small scale, the surface-to-volume ratio is much larger than that of the conventional case, therefore the gas-surface interaction starts to play an essential role.

From the presented classification of the gas flow regimes it is clear that when the Knudsen number of a gas flow becomes larger than 0.1 the kinetic approach starts to be indispensable to be used for the correct description of the single gas and the gas mixture flows. The main equation allowing the description the gas flow at the microscopic level and to provide in the same time the macroscopic flow parameters is the Boltzmann kinetic equation. This equation can be written down for a single gas and also for a gas mixture. The mathematical modeling of transport phenomena in gaseous mixtures is far more complicated than in a single gas for several reasons. First, gaseous mixture flows are determined by more parameters than single gas flows. Besides the parameters for gas rarefaction, pressure, and temperature, a mixture flow depends upon the species composing a mixture and their relative affinities to the solid phase. Second, in addition to the typical driving forces like pressure and temperature gradients, additional forces arise in mixtures from mole fraction gradient. Third, several new cross phenomena appear in a non-equilibrium mixture such as thermo-diffusion, diffusion thermoeffect, etc. As a result of this complexity, the computational effort to model gaseous mixture drastically increases in comparison to that of a pure gas.

1.1 Kinetic theory of gases and Boltzmann equation

The kinetic theory of gases is dedicated to the analysis of the macroscopic properties of gases taking into account the properties at the microscopic (molecular) level. Daniel Bernoulli, who published the expression $p = \rho u^2/3$ relating the gas pressure to the mean square velocity of gas molecules in 1738, was a pioneer in the applications of the mathematical methods to the kinetic theory of gases [108]. More than a century later, a fundamental concept of mean free path λ of gas molecules was introduced by Rudolf Clausius in 1858. In 1860, James Clerk Maxwell, who

is regarded as the founder of the modern kinetic theory of gases, proposed the concept of the molecular velocity distribution function (VDF) f_0^M for an equilibrium gas [109]

$$f_0^M(\mathbf{v}) = n_0 \left(\frac{m}{2\pi k T_0}\right)^{3/2} \exp\left[-\frac{m(\mathbf{v}-\mathbf{u_0})^2}{2kT_0}\right], \tag{1.2}$$

where k is Boltzmann constant; m, $\mathbf{v}$ are the mass and velocity of a gas molecule, respectively; while n_0, $\mathbf{u_0}$, T_0 are the equilibrium number density, bulk velocity and temperature of the gas. For the non-equilibrium gas, the VDF $f(\boldsymbol{r}, \mathbf{v}, t)$ is defined in such a way that $f(\boldsymbol{r}, \mathbf{v}, t)\, d\mathbf{r}d\mathbf{v}$ is the number of molecules in a phase space volume $d\mathbf{r}d\mathbf{v}$ which have the velocities between $d\mathbf{v}$ and $\mathbf{v} + d\mathbf{v}$ during a time interval dt. The macroscopic quantities of a gas, *e.g.*, number density n, bulk velocity $\mathbf{u}$, temperature T, stress tensor $\mathbf{P}$ and heat flux $\mathbf{q}$ are calculated from the moments of the VDF as following

$$\begin{aligned}
n(\mathbf{r}, t) &= \int_{R^3} f(\mathbf{r}, \mathbf{v}, t)\, d\mathbf{v}, \\
\mathbf{u}(\mathbf{r}, t) &= \frac{1}{n}\int_{R^3} \mathbf{v} f(\mathbf{r}, \mathbf{v}, t)\, d\mathbf{v}, \\
T(\mathbf{r}, t) &= \frac{m}{3nk}\int_{R^3} V^2 f(\mathbf{r}, \mathbf{v}, t)\, d\mathbf{v}, \\
P_{ij}(\mathbf{r}, t) &= m\int_{R^3} V_i V_j f(\mathbf{r}, \mathbf{v}, t)\, d\mathbf{v}, \\
\mathbf{q}(\mathbf{r}, t) &= m\int_{R^3} \mathbf{V} V^2 f(\mathbf{r}, \mathbf{v}, t)\, d\mathbf{v},
\end{aligned} \tag{1.3}$$

where $\mathbf{V} = \mathbf{v} - \mathbf{u}$ is the peculiar velocity.

In the same year, Maxwell also published the formulae for the transport coefficients of a gas: the viscosity μ, thermal conductivity κ and D diffusion coefficient, derived from his own concept of the VDF and Clausius' mean free path [110]. Maxwell's works highly influenced Ludwig Boltzmann to conduct the research on the non-equilibrium gas behaviors. In 1872, Boltzmann derived the equation of the molecular transport [111], which can be considered as a key component of the kinetic theory of gases

$$\frac{\partial f}{\partial t} + \mathbf{v}\cdot\frac{\partial f}{\partial \mathbf{r}} + \mathbf{F}\cdot\frac{\partial f}{\partial \mathbf{v}} = I(f, f_*). \tag{1.4}$$

The Boltzmann equation (BE) (1.4) describes the temporal (t) and spatial ($\mathbf{r}$) evolution of the molecular VDF $f(\boldsymbol{r}, \mathbf{v}, t)$. Here $\boldsymbol{F}$ represents an external force exerted on the molecules per mass unit. The first three terms in the BE (1.4) the unsteady, convective and external force terms, respectively, are analogous to those of the Navier-Stokes equations. However, the collision term $I(f, f_*)$ on the right hand side of eq. (1.4) [112, 70], representing the rate at

which the distribution functions f, f_* vary due to the collisions, is the most challenge one

$$I(f, f_*) = \int_{R^3} \int_{S^2} \left(f' f'_* - f f_* \right) \mathbf{g} b db d\epsilon d\mathbf{v}_*. \tag{1.5}$$

In Eq. (1.5), the functions f, f_*, f', f'_* are the velocity distribution functions corresponding to the pre-collision $(\mathbf{v}, \mathbf{v}_*)$ and post collision $\left(\mathbf{v}', \mathbf{v}'_*\right)$ molecular velocities, $\mathbf{g} = \mathbf{v} - \mathbf{v}_*$ is the relative molecular velocity of a pair of molecules before the collision, b and ϵ are the impact parameters, the distance of the closest approach, usually bounded by a certain value b_m, and the azimuth angle, respectively.

The collision integral (1.5) can be decomposed into the gain I^+ and lost I^- terms as $I(f, f_*) = I^+ - I^-$, which represent the molecule balance in the velocity space.

$$I^+ = \int_{R^3} \int_{S^2} f' f'_* \mathbf{g} b db d\epsilon d\mathbf{v}_*, \tag{1.6}$$

while the lost term I^- represents the rate at which molecules lost (change) their velocity $\mathbf{v}$ after collision

$$I^- = \nu(\mathbf{v}) f. \tag{1.7}$$

Here the collision frequency $\nu(\mathbf{v})$ is determined by

$$\nu(\mathbf{v}) = \int_{R^3} \int_{S^2} f_* \mathbf{g} b db d\epsilon d\mathbf{v}_*. \tag{1.8}$$

In the same article of Boltzmann [111], the H-theorem was introduced

$$\frac{dH}{dt} \leq 0, \tag{1.9}$$

where the H-function is defined as

$$H = \int_{R^3} f \ln f d\mathbf{v}. \tag{1.10}$$

The H-theorem (1.9) implies that a gas system alway tends to evolute to an equilibrium state, where the equality in expression (1.9) is obtained and the absolute Maxwellian distribution function (1.2) becomes the unique solution [113].

In more general case the BE has seven dimensions: three in spatial space, three in molecular velocity space and one in time. Moreover, the exceedingly complicated structure of the fivefold collision integral in the right hand side of the integro-differential BE equation (1.4) makes it extremely hard to be solved. Nearly a half century after the BE was derived, the first attemp to solve it was published by Sydney Chapman [114, 115] and David Enskog [116]. They obtained independently the solution of the BE by approximating the VDF in the form of an infinite series. The zero, first and second orders of Chapman-Enskog expansion applied to the BE yields to the Euler, Navier-Stokes and Burnett equations, respectively [112]. Another method to solve the BE was developed by Harold Grad in 1949 [117]. First, the VDF is approximated by expanding into the series of Hermitian polynomials around an equilibrium distribution function. All coefficients in those polynomials depend only on the set of moments, determining a gas state ($n, \mathbf{u}, T, \mathbf{P}, \mathbf{q}$ in Grad 13 moment method). The closed system of moment equations is then obtained from the approximated VDF. More a gas is rarefied higher number of moments is required to obtain a solution.

The continuum model, *i.g.*, the system of the Navier-Stokes equations, can also be obtained from the BE by multiplying Eq. (1.4) by the quantities $\left\{m, m\mathbf{v}, \frac{1}{2}m\|\mathbf{v}\|^2\right\}$ and then integrating over the molecular velocity space. It is to note that the corresponding moments of the collision integral in eq. (1.5) vanish $\int_{R^3} \phi(\mathbf{v}) I(f, f_*) d\mathbf{v} = 0$ for the collision invariants $\phi(\mathbf{v}) = \{1, \mathbf{v}, \|\mathbf{v}\|^2\}$. By this way one obtains the macroscopic conservation equations of mass, momentum and energy. Nevertheless, these conservation equations are not closed due to lacking of the expressions for the stress tensor and heat flux (and diffusion flux in the case of a gas mixture) via the macroscopic parameters. The so-called transport coefficients can be obtained to close the macroscopic conservation equation system for a given intermolecular potential.

The analytical approaches for the Boltzmann equation are absolutely restricted to very simple situations, hence, numerical simulations are commonly employed to deal with a wide range of issues. Furthermore, advances in computer technology paved the way for the development of the new numerical methods for the solution of the BE. These numerical approaches can be classified into the statistical and deterministical methods. The DSMC method [118, 107, 119] is a statistic method, in which the simulated molecules represent the larger number of real molecules and the collisions are calculated in probabilistic manner. The DSMC method works well for the strong non-equilibrium flows and it is widely used in practice, nevertheless it suffers from statistical fluctuations, when the gas flow is not far from equilibrium (low Knudsen number regimes and slow flows). In addition, the DSMC method becomes exceedingly expensive for the non-stationary flows. In the other hand, the BE can be deterministically approximated by the Discrete Velocity Method (DVM) [120, 121]. When using this method the infinite molecular velocity space are limited to a finite set of the molecular velocities. The DVM approach simplifies the collision integral to a series of quadratic terms, and consequently the

BE is reduced to a system of simultaneous discrete nonlinear first-order differential equations. Though the DVM offers accurate fluctuation-free solutions, it requires expensive computational efforts in order to keep (project) the post-collision velocities into the nodes, already existing for the pre-collision velocities. Other deterministic method, the Fourier spectral method based on a Fourier-Galerkin approximation of the BE is proposed recently [122]. This method offers a very accurate discretization in velocity space with reasonable computational efforts [123]. This method is further generalized to the Fast Spectral Method to reduce the computational cost [6]. This method allows also taking into account easily the various intermolecular potential in the collision kernel [8].

1.2 Kinetic model equations

Because of the exceedingly complicated structure of the fifth order collision integral in the right hand side of the integro-differential BE (1.4), only few exact solutions have been obtained so far under very particular conditions. The direct numerical solutions of the Boltzmann equation, by a statistical or a deterministically methods are also very time consuming. Hence, many attempts were undertaken to construct the kinetic models [10, 12, 11, 124, 125], where the collision integral (1.5) is simplified by a following relaxation form:

$$I^{mod}(f) = \nu^{mod}\left(f^{mod} - f\right) \tag{1.11}$$

The model collision term $I^{mod}(f)$ of the collision integral $I(f, f_*)$ is proportional to the difference between the molecular VDF f and the local equilibrium distribution function f^{mod}. The coefficient of proportionality is determined to be the relaxation rate ν^{mod} of the collision frequency $\nu(\mathbf{v})$. Only for the pseudo Maxwell molecules, molecules with inverse power-five potential, the collision frequency $\nu(\mathbf{v})$ does not depend on the molecular velocity $\mathbf{v}$ and it is completely defined by the temperature and density of a gas. The model collision term $I^{mod}(f)$ retains the qualitative and average properties of the collision integral $I(f, f_*)$ [126]: (i) conservation of mass, momentum and energy, (ii) fulfilling H-theorem, (iii) the local equilibrium distribution function is held in equilibrium state, (iv) reproducing the correct transport coefficients in the continuum limit. The kinetic equation (1.4), where the collision term (1.5) is replaced by a collision model (1.11), is then called a model kinetic equation. This thesis aims to implement the kinetic models, in which the relaxation rate ν^{mod} is independent of the molecular velocity, as they are commonly used in rarefied-gas-dynamics research community. Further details on the kinetic models with velocity-dependent relaxation rate can be found in Refs. [127, 128, 129, 130].

Recently, the Fokker-Planck based kinetic models are proposed to approximated the BE [131, 132, 133]. The Fokker-Planck model has the collision term described by a diffusion-type process in velocity space instead of jump-type process, eq. (1.11), in the traditional kinetic models of the BE. This model allows coarser grid in time and physical space; consequently, it is computationaly efficient, especially in the slip and transitional flow regimes.

1.2.1 BGK model

In 1954, the first kinetic model equation, called BGK (Bhatnagar-Gross-Krook) or BKW (Boltzmann-Krook-Welander) equation, was suggested independently in Refs. [10] and [134]. In this model, the local equilibrium distribution function f^{BGK} is simply the local Maxwellian distribution function

$$f^{M} = n\left(r\right)\left(\frac{m}{2\pi kT\left(r\right)}\right)^{3/2}\exp\left[-\frac{m\mathbf{V}^{2}}{2kT\left(r\right)}\right]. \tag{1.12}$$

The relaxation rate ν^{BGK} is a free parameter determined by different reasoning. For isothermal flow problems, it can be chosen in such a way that the viscosity coefficient μ, obtained by applying the Chapman-Enskog expansion to the BGK model, has the same expression as that derived from the BE by the same procedure

$$\nu^{BGK} = \frac{p}{\mu}. \tag{1.13}$$

For pure heat transfer problem, the relaxation rate can be selected to retrieve the thermal conductivity κ coefficient instead of the viscosity μ coefficient. In case of a monoatomic gas it leads to

$$\nu^{BGK} = \frac{2}{3}\frac{p}{\mu}. \tag{1.14}$$

The two previous examples of the relaxation rate choices reveal that the correct viscosity and thermal conductivity coefficients cannot be recovered simultaneously, when the BGK model is used. Consequently, the main drawback of the BGK model is that it yields the wrong Prandlt number ($Pr = 1$) instead of 2/3 for the monoatomic gases. Nonetheless, the BGK model has been widely used due to its simplicity, modest computational cost and satisfactory results for the momentum and thermal-dominated flow problems.

1.2.2 S-model

Various kinetic models have been proposed to provide a correct Prandlt number [12, 11, 124]. In 1968, Shakhov proposed a generalization of the BGK model, so-called S-model [11]. In this model the collision term has the same form as in eq. (1.12), but the equilibrium distribution function is defined

$$f^S = f^M \left[1 + \frac{2m\mathbf{Vq}}{15n(kT)^2}\left(\frac{m\mathbf{V}^2}{2kT} - \frac{5}{2}\right)\right]. \tag{1.15}$$

This model is constructed with the requirement that some number of the first moment equations, obtained from the approximate equation (1.11), coincide with the exact Boltzmann equations. Since the differential parts of the full Boltzmann equation and the model kinetic equation coincide, the differential parts of the moment equations will also coincide. Consequently, the necessary condition for coincidence of the moment equations amounts to equality of the corresponding moments of the exact and approximate collision operators.

The new local equilibrium distribution function f^S is expanded by Hermitian series around the local Maxwellian distribution function f^M. This Hermitian series is then restricted to the third-order polynomial to restore up to third-order moments. The coefficients of the Hermitian polynomial are then determined by equalizing several first moments of the model collision operator with the corresponding moments of the full collision operator calculated by the third-order, thirteen-moment approximation to the VDF.

The relaxation rate ν^S for the S-model kinetic equation is determined as in eq. (1.13). The technique proposed by Shakhov can be applied to an arbitrary N-oder moment approximation providing that the N-oder moments of the full collision integral are available. The BGK model is recovered from the second-order moment approximation.

It should be noted that the H-theorem for this model has been proved only for its linearized form. In addition, the Shakhov local equilibrium distribution function f^S (1.15) may become negative, due to the terms proportional to the third order of the molecular velocity. Nevertheless, the S-model has been frequently and successfully used for simulation of rarefied gas flows in various geometrical configurations.

1.2.3 McCormack model

In 1973, McCormack presented a linearized kinetic model for s-component monatomic mixture [14]

$$\frac{\partial h_\alpha}{\partial t} + \mathbf{v}_\alpha \cdot \frac{\partial h_\alpha}{\partial \mathbf{r}} = \sum_{\beta=1}^{s} L_{\alpha\beta}^{(N)}, \tag{1.16}$$

where α, β are the gas specie indexes; h_α is the perturbation distribution function of specie α around its absolute Maxwellian. The N-order model collisional term $L_{\alpha\beta}^{(N)}$ composes of lost term, $-\gamma_{\alpha\beta} h_\alpha$, and gain term, which is expressed in a series of orthonormal polynomials. The coefficients of these polynomials are determined by equalizing the moments of the model collision operator with corresponding moments of the full linearized collision operator calculated by the Grad moment approximation to the VDF. The third-order collision term of the McCormack model $L_{\alpha\beta} = L_{\alpha\beta}^{(3)}$ is given by expression (7.11).

McCormack model reproduces correctly all the transport coefficients in a gas mixture, *i.e.* viscosity, heat conductivity, diffusion and thermal diffusion coefficients. Moreover, various intermolecular interaction laws (Hard Sphere, Lennard-Jones [70] and Realistic potential [81]) can be specified via the omega integrals $\Omega_{\alpha\beta}^{(ij)}$ (see eq. (A.3). The McCormack model satisfies H-theorem and indifferentiability principle, *i.e.* when the all species are identical, the model reduces to model of single gas (S-model in the case of McCormack model). Recently, this model is extended to the non-linear collision operator [17]. Other kinetic models describing rarefied gaseous mixtures can be found in [135, 13, 15, 16, 18].

1.3 Thesis objective and outline

This thesis aims to develop various numerical tools for simulation of rarefied gas flows based on the kinetic model equations and discrete velocity method. Two model kinetic equations (S-model, McCormack model), in which the collisional term of the full Boltzmann equation is replaced by the more simple relaxation term, are chosen for the simulation of the single gas flows and the flows of the gas mixtures. The both steady state and transient flows are considered. For the steady state flows the implicit numerical scheme are developed, which allows to obtain the steady state solution rapidly. To simulate the transient flows the explicit scheme is used, allowing to follow the time evolution of the macroscopic flow parameters. The proposed approaches are tested for various geometrical configurations. The obtained numerical results are compared with the data, found in the open literature, and with the available analytical solutions. For several geometrical configurations the comparison with the experimental data are carried out.

This thesis is organized into 9 Chapters:

- **Chapter 1** gives a description of the physical conditions, where a gas is considered to be

rarefied and therefore the traditional continuum description breaks down and so the other approaches, based on the kinetic theory, have to be applied. Then, a brief introduction to the Boltzmann equation and its kinetic models is provided. Thesis objectives and structure are also listed in this Chapter.

- **Chapter 2** reports the complete study of the steady heat transfer through a rarefied gas confined between two concentric spheres. In the slip and free molecular flow regimes the analytical expressions are provided for the arbitrary temperature and radius ratios. The limits of the analytical expressions applicability are established by confronting the numerical and analytical solutions. These results will be then used for the experimental extraction of the energy accommodation coefficient. The experimental two concentric spheres configuration, contrarily to the most frequently used two coaxial cylinders configuration, allows to analyze the non-metal surfaces, which are very difficult to test in the two cylinders geometry.

- In **Chapter 3**, we study the transient behavior of the heat flux between two coaxial cylinders. The steady state time, as a time of steady state flow establishment, is investigated for a large range of the gas rarefaction. The transient heat flux evolution, derived from the energy balance allows to estimate the time of steady state flow establishment in the slip flow regime. The analytical solution is derived also in the slip flow regime. This study allows the estimation of the time needed to the Pirani pressure sensors to have the stable pressure measurements. This work was done in collaboration with the INFICON company (http://www.inficon.com/), the world leader in the Pirani sensor fabrication. This approach allows us also to develop the new two dimensional numerical model of a loaded used nuclear fuel canister filled with helium gas to predict the cladding temperature during vacuum drying conditions. This last work was carried out in collaboration with University of Reno, Nevada, US.

- In **Chapter 4**, we focus on the transient flow of rarefied gas through an orifice caused by various pressure ratios between the reservoirs in a wide range of the gas rarefaction. The time of steady flow establishment and the steady state distribution of the flow parameters are compared with previously reported data obtained by the DSMC method. The numerical code, developed in this chapter was also used for the numerical simulation of the rubidium vapor expansion in the very low pressure domain in the frame of the AWAKE project in CERN.

- **Chapter 5** studies the mass flow rate of rarefied gas driven by pressure and/or temperature gradients through a long rectangular channel of variable cross-section aspect ratio. Some examples of the isothermal and non-isothermal flows through the channels with variable rectangular cross sections are given. The analytical expressions in the case of

the hydrodynamic and free molecular flow regimes are proposed. These results are used in the next chapter to simulate the experimentally found "diode effect". In **Chapter 6**, we apply the numerical method developed in the previous Chapter to calculate the mass flow rate in diverging and converging flow directions for arbitrary pressure gradients. The numerical results are compared with analytical solutions and measurement data, provided by the Center for Environmental Research and Sustainable Technology (UFT) of the Bremen University, Germany. The gas flow "diode effect": the mass flow rate is significantly higher when the duct is perfused in converging direction, firstly found experimentally, was then confirmed by the numerical simulations.

- **Chapter 7** deals with binary mixture of monoatomic gas. The numerical approach, based on the McCormack model, is developed for the simulations of the two simple, one dimensional in the physical space, configurations: Couette flow and Fourier flow. The detailed comparison is carried out between the obtained here numerical results and the solution of the linearized Boltzmann equation for the binary gas mixture of the monoatomic gases. The influence on the gas-surface interaction is also studied. The obtained here results are also compared with the solution of the non-linear Boltzmann equation for the gas mixture in order to establish the limit of the applicability of the linearized approach.

- The oscillatory gas flow of the gas mixture is simulated in **Chapter 8**. The transient and oscillation gas mixture flow behaviors are analyzed and the analogy between the single gas flows are found under several flow conditions. The limits of the applicability of the steady state and transient solutions are established.

- The general conclusions and the outlook on future work are given in **Chapter 9**.

Chapter 2

Heat transfer between two concentric spheres

The heat transfer through rarefied gases was investigated since the fundamental study of Maxwell [19]. The particular case of the heat transfer between two concentric spheres at arbitrary rarefied condition was first studied theoretically in Ref. [20]. The analytical solutions were obtained by solving kinetic equation in the four-moment approximation. Then, these analytical solutions were extended in Ref. [21] to taken into account the incomplete thermal accommodation at the internal sphere. The expression of heat flux in transitional regime was proposed in Ref. [22] by modifying the analogous expression for two parallel plate geometry. The problem of heat transfer from a sphere to surrounding environment, as a limiting case of two spheres problem, was also investigated in Refs. [23, 24] for monoatomic and polyatomic gases, respectively. However, all these studies were restricted to the small temperature difference between the spheres. The results for an arbitrary temperature difference was obtained in Ref. [104] for free molecular regime using the revised theory of thermal transpiration. The authors of Ref. [136] used the four moment technique similar to that used in Ref. [20], expanding the unknown parameters in terms of the temperature difference between two spheres. The authors retained the additional terms in these expansions, up to the second order terms, in order to predict the heat flux in the case of larger temperature difference between two spheres.

During the last few years interest in the heat transfer problem has arisen once again and it is related to the fast development of the MEMS and NEMS. Due to the small characteristic size of these devices the gas inside is rarefied and their thermal management becomes important. The two concentric sphere configuration can also be used as a simple set-up for the measurement of the thermal accommodation coefficient [25].

In the present paper the heat transfer between two concentric spheres is considered for a broad range of the gas rarefaction, of the temperature and radius ratios between the spherical surfaces.

The analytical expressions for the radial temperature and heat flux distributions in the slip and free molecular flow regimes are provided for the arbitrary accommodation between the gas and the spherical surfaces. In the transitional flow regime the S-model kinetic equation is solved numerically.

2.1 Problem statement

Two concentric spheres with the radii R'_H and R'_C ($R'_H < R'_C$) containing a monoatomic gas at rest between them are considered. The internal and external spheres are kept at the temperatures T'_H and T'_C, respectively. The heat transfer through rarefied gas in these configurations is governed by following dimensionless parameters: the temperature $\mathcal{T}$ and radius $\mathcal{R}$ ratios of the two surfaces

$$\mathcal{T} = \frac{T'_H}{T'_C}, \qquad \mathcal{R} = \frac{R'_C}{R'_H}, \tag{2.1}$$

and the rarefaction parameter δ_0 defined as following

$$\delta_0 = \frac{R_0}{\ell}, \qquad \ell = \frac{\mu_0 \upsilon_0}{p_0}, \qquad \upsilon_0 = \sqrt{2kT_0/m}. \tag{2.2}$$

Here R_0 is the reference length of the problem, ℓ is the equivalent mean free path, p_0 is the reference pressure, μ_0 and υ_0 are the gas viscosity and the most probable molecular velocity at the reference temperature T_0, respectively; k is the Boltzmann constant and m is the molecular mass of the gas. For convenience, the reference values in Eq. (2.2) are taken as follows

$$T_0 = T'_C, \qquad R_0 = R'_C - R'_H. \tag{2.3}$$

It is to note that the gas rarefaction parameter δ_0 in Eq. (2.2) is inversely proportional to the Knudsen number. The cases of $\delta_0 = 0$ and $\delta_0 \to \infty$ correspond to the free molecular and hydrodynamic flow regimes, respectively.

We assume that the heat transfer problem, considered here, is spatially symmetric and therefore the macroscopic parameters depend on the r' coordinate only.

The heat transfer between two parallel plates or between two coaxial cylinders is analogous to that between two concentric spheres in term of one-dimensional in physical space. In the following Sections, the general expressions for the three geometries (plates, cylinders and spheres) will be provided when they are available. In those expressions, the geometry index

$a = 0, 1, 2$ corresponds to the plate, cylinder, sphere geometries, respectively.

2.2 Continuum approach

In the hydrodynamic and slip flow regimes the temperature variation between two surfaces may be obtained from the energy balance

$$\frac{\partial}{\partial r'}\left(r'^{a}\kappa'\frac{\partial T'}{\partial r'}\right) = 0, \tag{2.4}$$

where r' is the radial coordinate of physical region between the spheres, κ' is the gas thermal conductivity. It is to note that here the hypothesis of zero macroscopic gas velocity is used and only the conduction heat transfer is considered. The Fourier law can be applied to calculate the heat flux

$$q'_r = -\kappa'\frac{dT'}{dr'}, \tag{2.5}$$

where q'_r is the radial component of the heat flux vector. For the monoatomic gases the gas thermal conductivity is related to the gas viscosity as follows

$$\kappa' = \frac{15}{4}\frac{k}{m}\mu'. \tag{2.6}$$

In order to define the dependence of the viscosity on the temperature the molecular interaction potential must be specified. In the following we will use the inverse power law potential [107]. This model leads to a power law temperature dependence for the viscosity coefficient

$$\mu' = \mu_0\left(\frac{T'}{T_0}\right)^{\omega}, \tag{2.7}$$

where ω is the viscosity index, which is equal to 0.5 for the Hard Sphere model and 1 for the Maxwell model.

In the hydrodynamic flow regime the temperature continuity may be assumed on the spheres' walls. However, in the slip flow regime the temperature jump conditions [69] must be used as the boundary conditions for Eq. (2.4)

$$T'_g = T'_w + \xi\ell\left.\frac{dT'}{dr'}\right|_w, \tag{2.8}$$

where T'_g is the gas temperature near the wall, T'_w is the wall temperature, ξ is the temperature jump coefficient [137]. This coefficient depends on the gas nature and the surface state through the accommodation coefficient. The values of the temperature jump coefficient ξ were obtained from the solution of the kinetic equations (BGK and Boltzmann equations) by several authors [134, 138, 139, 140, 141, 142]. These values, derived under assumption of the complete accommodation of the molecules at the surface, vary in the narrow range $1.931 - 1.954$ [143]. The expressions, allowing the calculation of the temperature jump coefficient for the non complete accommodation in the frame of the Maxwell diffuse-specular scattering, are provided in [134, 138, 139].

It is convenient to introduce the dimensionless variables as follows

$$r = \frac{r'}{R_0}, \qquad n = \frac{n'}{n_0}, \qquad T = \frac{T'}{T_0}, \qquad p = \frac{p'}{p_0}, \qquad q_r = \frac{q'_r}{p_0 \upsilon_0}, \qquad \mu = \frac{\mu'}{\mu_0}. \tag{2.9}$$

The reference number density n_0 is taken as the average over the physical space value of the number density n'_{av}

$$n_0 = n'_{av} = \frac{a+1}{R'^{a+1}_C - R'^{a+1}_H} \int_{R'_C}^{R'_H} n' r'^a dr'. \tag{2.10}$$

The average density number is used as the reference value instead of number density on the cold surface for the following reasons. First, the average value of number density can be easier related to the measurements of the pressure between the two surfaces. Second, in the numerical simulation, the average number density is kept as constant, while the number density on the cold surface, generally, varies at every time step. The reference pressure p_0 is defined by the equation of state.

Using the dimensionless variables (2.9) and expression for the heat flux (2.6) we obtain the dimensionless form of the energy conservation equation, Eq. (2.5), as following

$$\frac{\partial (r^a q_r)}{\partial r} = 0, \qquad \text{where} \qquad q_r(r) = -\frac{15}{8\delta_0} \mu \frac{dT}{dr}. \tag{2.11}$$

Below the analytical solutions of Eq. (2.11) are provided in the slip and hydrodynamic flow regimes derived for the arbitrary temperature and radius ratios.

2.2.1 Slip flow regime

In the slip flow regime Eq. (2.11) subjected to the temperature jump boundary conditions can be solved analytically. The dimensionless form of the temperature jump boundary conditions on the walls, Eq. (2.8), becomes

$$T = \begin{cases} T_H + \frac{\xi_H}{\delta_0} T^{\omega+1/2} \frac{dT}{dr}, & r = R_H, \\ T_C - \frac{\xi_C}{\delta_0} T^{\omega+1/2} \frac{dT}{dr}, & r = R_C. \end{cases} \tag{2.12}$$

Here ξ_H and ξ_C are the temperature jump coefficients on the hot and cold surfaces, respectively. The assumption of the constant value of the pressure between the spheres is used to obtain the previous expressions. It is to note that the dimensionless value of the bottom plate or the external cylinder/sphere temperature is equal to 1, see Eqs. (2.3,2.9), but in the following the notation T_C is retained for the convenience of presentation.

To write the completely explicit expression of the temperature distribution between the spheres a linearization of the temperature is carried out and the terms of the order of ε^2 are neglected, where $\varepsilon = \frac{T_w - T_g}{T_w}$, Eq. (2.8). The temperature profile between the surfaces with the accuracy ε^2 reads

$$T(r) = \left\{ \frac{1}{2} \left[T_{gH}^{\omega+1} + T_{gC}^{\omega+1} + \mathcal{A} K_{R1} \right] \right\}^{\frac{1}{\omega+1}}, \tag{2.13}$$

where

$$\mathcal{A} = \frac{T_H^{\omega+1} - T_C^{\omega+1}}{K_{R2} + \frac{1}{\delta_0} \left(\frac{\xi_H}{R_H^a} T_H^{\omega+1/2} + \frac{\xi_C}{R_C^a} T_C^{\omega+1/2} \right)}, \tag{2.14}$$

$$T_{gH}^{\omega+1} = T_H^{\omega+1} \left[1 - \mathcal{B}_H \right], \qquad T_{gC}^{\omega+1} = T_C^{\omega+1} \left[1 - \mathcal{B}_C \right], \tag{2.15}$$

$$\mathcal{B}_H = \frac{\xi_H}{\delta_0} \frac{\mathcal{A}}{R_H^a \sqrt{T_H}}, \qquad \mathcal{B}_C = -\frac{\xi_C}{\delta_0} \frac{\mathcal{A}}{R_C^a \sqrt{T_C}}, \tag{2.16}$$

$$K_{R1} = \begin{cases} 2r - R_H - R_C, & a = 0 \\ 2\ln r - \ln R_H - \ln R_C, & a = 1 \\ \frac{2}{r} - \frac{1}{R_H} - \frac{1}{R_C}, & a = 2 \end{cases}$$
$$K_{R2} = \begin{cases} R_C - R_H, & a = 0 \\ \ln R_C - \ln R_H, & a = 1 \\ \frac{1}{R_H} - \frac{1}{R_C}, & a = 2. \end{cases} \tag{2.17}$$

When the parameters $\mathcal{A}$, $\mathcal{B}_H$, $\mathcal{B}_C$, T_{g_H} and T_{g_C} are calculated via Eqs. (2.14 - 2.17) the temperature distribution may be found using Eq. (2.13). It is to note that the temperature distribution (2.13) is obtained here for the arbitrary temperature and radius ratios.

The heat flux between the surfaces now can be found from Eqs. (2.11) and (2.13):

$$q_r(r) = \frac{15}{8\delta_0}\frac{1}{\omega+1}\frac{\mathcal{A}}{r^a}. \tag{2.18}$$

2.2.2 Hydrodynamic regime

In the hydrodynamic flow regime the gas temperature near a wall is equal to the wall temperature, so equation (2.11) may be solved analytically and the temperature profile yields:

$$T(r) = \left\{\frac{1}{2}\left[T_H^{\omega+1} + T_C^{\omega+1} + \mathcal{A}K_{R1}\right]\right\}^{\frac{1}{\omega+1}}, \tag{2.19}$$

where

$$\mathcal{A} = \frac{T_H^{\omega+1} - T_C^{\omega+1}}{K_{R2}}, \tag{2.20}$$

The heat flux distribution may be found from Eqs. (2.11) and (2.19):

$$q_r(r) = \frac{15}{8\delta_0}\frac{1}{\omega+1}\frac{\mathcal{A}}{r^a}. \tag{2.21}$$

2.3 Kinetic model equation

In the transitional and free molecular flow regimes, the S-model kinetic equation [11] is solved. The S kinetic model was recently successfully used for simulation of flow of rarefied gases in various geometrical configurations [144, 145, 146, 33, 147, 42, 50]. However, it should be noted that the H-theorem for this model has been proved only for its linearized form. Considering the symmetry of the problem relatively to the center point, the time-dependent S-model kinetic equation for sphere geometry reads

$$\frac{\partial f'}{\partial t'} + \upsilon_p \cos\theta \frac{\partial f'}{\partial r'} - \frac{\upsilon_p \sin\theta}{r'} \frac{\partial f'}{\partial \theta} = \nu'(f^{S'} - f'). \tag{2.22}$$

Here, the physical space of sphere geometry is described by the spherical coordinate systems (r, Θ, ϕ). In the other hand, the molecular velocity space is described by the spherical coordinate systems $(\upsilon_p, \theta, \varphi)$. In Eq. (2.22), $f'(t', r', \mathbf{v})$ is the molecular velocity distribution function; ν' is the molecular collision frequency; t' is the time. The molecular velocity vector $\mathbf{v}$ has three components projected on the physical coordinate system as $\mathbf{v} = (\upsilon_p \cos\theta, \upsilon_p \sin\theta \cos\varphi, \upsilon_p \sin\theta \sin\varphi)$. The Shakhov equilibrium distribution function $f^{S'}$ in Eq. (2.22) has the form

$$\begin{aligned} f^{S'}(n', T', \mathbf{V}, \mathbf{q}') &= f^{M'} \left[1 + \frac{2m\mathbf{V}\mathbf{q}'}{15n'(kT')^2} \left(\frac{m\mathbf{V}^2}{2kT'} - \frac{5}{2} \right) \right], \\ f^{M'}(n', T', \mathbf{V}) &= n' \left(\frac{m}{2\pi k T'} \right)^{3/2} \exp\left(-\frac{m\mathbf{V}^2}{2kT'} \right), \end{aligned} \tag{2.23}$$

where $\mathbf{V} = \mathbf{v} - \mathbf{u}'$ is the peculiar velocity vector; $\mathbf{u}' = (u'_r, 0, 0)$ is the bulk velocity vector; $\mathbf{q}' = (q'_r, 0, 0)$ is the heat flux vector; $f^{M'}$ is the local Maxwellian distribution function

$$f^{M'} = n'(r) \left(\frac{m}{2\pi k T'(r)} \right)^{3/2} \exp\left[-\frac{m\mathbf{V}^2}{2kT'(r)} \right]. \tag{2.24}$$

In this model, the molecular collision frequency is assumed to be independent of the molecular velocity and can be evaluated [11] by

$$\nu' = \frac{p'}{\mu'}. \tag{2.25}$$

The bulk and molecular velocities are normalized by the most probable molecular velocity υ_0, Eq. (2.2)

$$\mathbf{u} = \frac{\mathbf{u}'}{\upsilon_0}, \qquad \mathbf{c} = \frac{\mathbf{v}}{\upsilon_0}, \tag{2.26}$$

where $\mathbf{c}$ is the dimensionless molecular velocity vector. The dimensionless distribution function and time are defined as follows

$$f = \frac{f'\upsilon_0^3}{n_0}, \qquad t = \frac{t'}{t_0}, \qquad t_0 = \frac{R_0}{\upsilon_0}. \tag{2.27}$$

Incorporating the dimensionless quantities (2.9), (2.26), (2.27) into S-model kinetic equation (2.22), the dimensionless form of the governing equation is obtained

$$\frac{\partial f}{\partial t} + c_p \cos\theta \frac{\partial f}{\partial r} - \frac{c_p \sin\theta}{r} \frac{\partial f}{\partial \theta} = \delta_0 n T^{1-\omega}(f^S - f). \tag{2.28}$$

On the hot and cold surfaces, the Maxwell-type diffuse-specular condition is employed as

$$\begin{aligned} f\left(t, R_H, c_p, \theta\right) &= \left(1-\alpha_H\right) f\left(t, R_H, c_p, \pi-\theta\right) + \alpha_H f^M\left(t, n_{w_H}, T_H, c_p\right), \quad 0 < \theta < \frac{\pi}{2}, \\ f\left(t, R_C, c_p, \theta\right) &= \left(1-\alpha_C\right) f\left(t, R_C, c_p, \pi-\theta\right) + \alpha_C f^M\left(t, n_{w_C}, T_C, c_p\right), \quad \frac{\pi}{2} < \theta < \pi, \end{aligned} \tag{2.29}$$

where α_C and α_H are the accommodation coefficients at the external and internal surfaces, respectively. The number densities for the part of diffuse reflected molecules, Eq. (2.29), at the surfaces are calculated from the non-penetration conditions

$$\begin{aligned} n_{w_C} &= \frac{\int_0^{2\pi}\int_0^{\pi/2}\int_0^{\infty} c_p \cos\theta f\left(t, R_C, c_p, \theta\right) d\mathbf{c}}{\left(\pi T_C\right)^{-3/2} \int_0^{2\pi}\int_{\pi/2}^{\pi}\int_0^{\infty} c_p \cos\varphi \exp\left(-c_p^2/T_C\right) d\mathbf{c}}, \\ n_{w_H} &= \frac{\int_0^{2\pi}\int_{\pi/2}^{\pi}\int_0^{\infty} c_p \cos\theta f\left(t, R_H, c_p, \theta\right) d\mathbf{c}}{\left(\pi T_H\right)^{-3/2} \int_0^{2\pi}\int_0^{\pi/2}\int_0^{\infty} c_p \cos\varphi \exp\left(-c_p^2/T_H\right) d\mathbf{c}}, \end{aligned} \tag{2.30}$$

here $d\mathbf{c} = c_p^2 \sin\theta dc_p d\theta d\phi$ is the the volume element in the molecular velocity space.

The macroscopic flow parameters are defined in terms of the distribution function as

$$
\begin{aligned}
n\left(t,r\right) &= \int_0^{2\pi}\int_0^{\pi}\int_0^{\infty} f\left(t,r,c_p,\theta\right) d\mathbf{c},\\
u_r\left(t,r\right) &= \frac{1}{n}\int_{-\infty}^{\infty}\int_0^{2\pi}\int_0^{\pi}\int_0^{\infty} c_p\cos\theta f\left(t,r,c_p,\theta\right) d\mathbf{c},\\
T\left(t,r\right) &= \frac{2}{3n}\int_0^{2\pi}\int_0^{\pi}\int_0^{\infty}\left[\left(c_p\cos\theta-u_r\right)^2+\left(c_p\sin\theta\right)^2\right] f\left(t,r,c_p,\theta\right) d\mathbf{c},\\
q_r\left(t,r\right) &= \int_0^{2\pi}\int_0^{\pi}\int_0^{\infty} c_p\cos\theta\left[\left(c_p\cos\theta-u_r\right)^2+\left(c_p\sin\theta\right)^2\right] f\left(t,r,c_p,\theta\right) d\mathbf{c}.
\end{aligned}
\tag{2.31}
$$

2.3.1 Free molecular flow regime

In the free molecular regime the kinetic equation (2.28) can be solved analytically for arbitrary temperature and radius ratio. We assume here the diffuse-specular reflection, Eqs. (2.29), with the accommodation coefficient α_H, α_C on the hot and cold surfaces, respectively. The number density, temperature and heat flux profiles between the two surfaces read

$$
n(r) = \frac{1-K_{\alpha 1}K_{T1}K_{R1}^{(a)}}{1-K_{\alpha 1}K_{T1}K_{R2}^{(a)}}, \tag{2.32}
$$

$$
T(r) = \frac{1-K_{\alpha 1}K_{T2}K_{R1}^{(a)}}{1-K_{\alpha 1}K_{T1}K_{R1}^{(a)}}, \tag{2.33}
$$

$$
q_r(r) = \frac{1}{\sqrt{\pi}}K_{\alpha 2}K_{T3}K_{R3}^{(a)}\frac{1}{1-K_{\alpha 1}K_{T1}K_{R2}^{(a)}}. \tag{2.34}
$$

Here K_α, K_T are the coefficients determined by accommodation coefficients and by temperature of the two surfaces, respectively

$$
\begin{aligned}
K_{\alpha 1} &= \frac{\alpha_H\,(2-\alpha_C)}{\alpha_H+\alpha_C-\alpha_H\alpha_C},\\
K_{\alpha 2} &= \frac{\alpha_H\alpha_C}{\alpha_H+\alpha_C-\alpha_H\alpha_C},\\
K_{T1} &= 1-\sqrt{\mathcal{T}^{-1}},\\
K_{T2} &= 1-\sqrt{\mathcal{T}},\\
K_{T3} &= \mathcal{T}-1.
\end{aligned}
\tag{2.35}
$$

The coefficients $K_R^{(a)}$ are determined by the geometry of the problem, in which the index $a=0,1,2$ correspondes to the plate, cylinder, sphere geometries, respectively

$$
\begin{aligned}
K_{R1}^{(0)} &= \frac{1}{2},\\
K_{R1}^{(1)} &= \frac{1}{2}\frac{\arcsin\left(R_C/r\right)}{\pi/2},\\
K_{R1}^{(2)} &= \frac{1}{2}\left[1-\sqrt{1-\left(R_C/r\right)^2}\right],\\
K_{R2}^{(0)} &= \frac{1}{2},\\
K_{R2}^{(1)} &= \frac{1}{2}\left\{1-\frac{1}{\pi/2}\left[\frac{\arccos\left(\mathcal{R}^{-1}\right)}{1-\mathcal{R}^{-2}}-\frac{1}{\sqrt{\mathcal{R}^2-1}}\right]\right\},\\
K_{R2}^{(2)} &= \frac{1}{2}\left[1-\frac{(\mathcal{R}+1)\sqrt{\mathcal{R}^2-1}}{\mathcal{R}^2+\mathcal{R}+1}\right],\\
K_{R3}^{(a)} &= \left(\frac{R_C}{r}\right)^a.
\end{aligned}
\tag{2.36}
$$

In the free molecular flow regimes, the analytical expressions for number density, temperature and heat flux were obtained previously using the revised theory of thermal transpiration [148, 104, 149]

$$
n(r) = \frac{1-K_{T1}K_{R1}^{(a)}}{1-K_{T1}K_{R2}^{(a)}},
\tag{2.37}
$$

$$
T(r) = \frac{1-K_{T2}K_{R1}^{(a)}}{1-K_{T1}K_{R1}^{(a)}},
\tag{2.38}
$$

$$
q_r(r) = \frac{1}{\sqrt{\pi}}K_{\alpha R}^{(a)}K_{T3}K_{R3}^{(a)}\frac{1}{1-K_{T1}K_{R2}^{(a)}}.
\tag{2.39}
$$

In contrast to Eqs. (2.32-2.34), here in the Eqs. (2.37-2.39), the influence of accommodation coefficients K_α is taken into account implicitly in the coefficient K_T by means of replacing

surface temperature (T_H, T_C) with gas temperature vicinity to the walls (T_{gH}, T_{gC})

$$\begin{aligned} K_{T1} &= 1 - \sqrt{\frac{T_{gC}^{(a)}}{T_{gH}^{(a)}}}, \\ K_{T2} &= 1 - \sqrt{\frac{T_{gH}^{(a)}}{T_{gC}^{(a)}}}, \\ K_{T3} &= (\mathcal{T} - 1)\sqrt{T_{gC}}, \end{aligned} \tag{2.40}$$

where

$$\begin{aligned} T_{gH}^{(a)} &= \frac{\alpha_H \left[\alpha_C \left(1 - \mathcal{R}^{-a}\right) + \mathcal{R}^{-a}\right] \mathcal{T} + (1 - \alpha_H)\alpha_C}{\alpha_C + \alpha_H \left(1 - \alpha_C\right) \mathcal{R}^{-a}}, \\ T_{gC}^{(a)} &= \frac{\alpha_H \left(1 - \alpha_C\right) \mathcal{R}^{-a} \mathcal{T} + \alpha_C}{\alpha_C + \alpha_H \left(1 - \alpha_C\right) \mathcal{R}^{-a}}. \end{aligned} \tag{2.41}$$

In addition, in the formulation of heat flux (2.39) the coefficient $K_{\alpha R}$ is defined by

$$K_{\alpha R}^{(a)} = \frac{\alpha_H \alpha_C}{\alpha_C + \alpha_H \left(1 - \alpha_C\right) \mathcal{R}^{-a}} \tag{2.42}$$

The profiles (2.37-2.39) are derived under the same conditions as in the present study (2.32-2.34): the steady state condition of a simple gas at rest in a closed system under no external forces; the surface temperature distribution is assumed to be arbitrary but independent of time. However the author of Ref. [148, 104, 149] used different Maxwell type model for the gas-surface interaction with two accommodation coefficients. The reflection of the molecules from the surface was assumed to be completely diffuse, so the accommodation coefficient of the tangential momentum is equal to one and it was also assumed to have arbitrary thermal accommodation. In the frame of this model the molecules reflect from the surface according to the Maxwellian distribution function, however the temperature of the reflected molecules is equal to the surface temperature only when the thermal accommodation coefficient is equal to 1. This approach with two accommodation coefficients in the frame of the Maxwellian scattering kernel was used in several papers [20, 148, 104, 136, 149, 23, 24, 22]. It is evident that our approach with fully diffusive reflection boundary condition and Wu's approach with perfect thermal accommodation yield the identical expressions for the profile of the macroscopic parameters. However, in general case of non-complete accommodation the both approaches yield different profiles for the macroscopic quantities, which will be illustrated in Section 2.5.

The obtained number density, temperature and heat flux profiles are compared in Section 2.5 with the numerical solution of Eq. (2.28) subjected to the Maxwellian specular-

diffuse boundary conditions on the internal sphere and to the diffuse boundary condition ($\alpha_C = 1$) on the external sphere.

2.3.2 Approximate relation for all flow regime

The number density, temperature and heat flux profiles, valid in the full range of rarefaction parameter δ_0, but only for the small temperature ratio ($\mathcal{T} \to 1$) were obtained in Ref. [20] by the moment method, where complete thermal accommodation was assumed. The generalization of these results for the case of non-complete accommodation on the internal cylinder/sphere surface was developed by Springer and Wan [21], where the heat flux expression is found in the following form:

$$q_r(r) = \frac{q_r^{Hyd}(r)}{1 + \frac{1}{\alpha}\frac{15}{8}\frac{\sqrt{\pi}}{\delta_H}K_R^{(a)}}, \tag{2.43}$$

where δ_H is the rarefaction parameter calculated according to expression (2.2), where the reference parameters with the subscript 0 are taken on the hot plate/cylinder/sphere, *i.e.* $R_0 = R_H$, $T_0 = T_H$ and $p_0 = p_H$. The coefficient $K_R^{(a)}$corresponding to cylinder and sphere geometries are $K_R^{(1)} = 1/\ln\mathcal{R}, K_R^{(2)} = R_C$, respectively. The heat flux in the hydrodynamic regime q_r^{Hyd} can be taken from Eq.(2.21).

In several papers [150, 151, 152] it was proposed to invert expression (2.43) by writing it in the form

$$\frac{1}{q_r(r)} = \frac{1}{q_r^{Hyd}(r)} + \frac{1}{q_r^{FM}(r)}, \tag{2.44}$$

where q_r^{FM} is the heat flux in free molecular regimes.

The advantage of the heat flux presentation in form (2.21) is that we can calculate separately analytical expressions in the hydrodynamic and free molecular flow regimes for the arbitrary temperature ratio. Here we propose to use Sherman's expression (2.44) with q_r^{Hyd} and q_r^{FM} defined by Eqs. (2.21), (2.34), respectively, to cover all range of the possible temperature ratio.

The both relations (2.43) and (2.44) will be compared with the numerical solution of the S-model kinetic equations (2.28) in Section 2.5.3.

2.4 Numerical scheme for kinetic equation

In this Section, only the numerical technique used to solve S-model kinetic equation (2.28) for cylinder geometry is described in detail due to analogy with that for plate and sphere geometries. First, the discrete velocity method (DVM) is applied to split the continuum molecular velocity space c_p in the governing equation (2.28) into discrete velocity set c_{p_l}, $l = 1, 2, .., N_{c_P}$. These velocities c_{p_l} are taken to be the roots of the Hermite polynomial of order N_{c_P} accordingly mapped from $(-\infty, \infty)$ to $[0, \infty)$. Then the set of N_{c_P} kinetic equations, corresponding to N_{c_P} values of discrete velocity c_{p_l}, is discretized in time and space by finite difference method (FDM). The orientation angle θ of the molecular velocity ($0 \leq \theta \leq \pi$) is divided into N_θ uniform segments defined by $\theta_m, m = 0, 1, .., N_\theta$. The gap between the cylinders is separated into N_r equal intervals characterized by $r_i, i = 0, 1, .., N_r$. Let us denote the numerical solution of Eq. (2.28) at the time level s as $f^s_{i,l,m} = f\left(t^s, r_i, c_{p_l}, \varphi_m\right)$ and define $\Delta t^s = t^{s+1} - t^s$, $\Delta r_i = r_{i+1} - r_i$, $\Delta\theta_m = \theta_{m+1} - \theta_m$, $\Delta f^s = f^{s+1}_{i,l,m} - f^s_{i,l,m}$.

In this study we are interested only in the steady-state situation, therefore the fully time-implicit Godunov-type scheme is applied [153, 154]

$$\begin{aligned} &\left(\frac{1}{\Delta t^s} + n\delta_0 T^{1-\omega} + c_p\cos\theta\frac{\partial}{\partial r} - \frac{c_p\sin\theta}{r}\frac{\partial}{\partial\theta}\right)\Delta f^s = RHS^s, \\ &RHS^s = n\delta_0 T^{1-\omega}\left(f^{Ss} - f^s\right) - c_p\cos\theta\frac{\partial f^s}{\partial r} + \frac{c_p\sin\theta}{r}\frac{\partial f^s}{\partial\theta}. \end{aligned} \tag{2.45}$$

The left hand side of Eq. (2.45) is the implicit part, where the spacial derivatives are approximated by the first order upwind scheme. The advantage of this discretization is that the solution Δf^s can be obtained directly, *i.e.*, without calculation of the inverse matrix, just by marching in appropriate direction. The right hand side of Eq. (2.45) (RHS^s) is the explicit part, where the spacial derivatives are approximated by the second order accurate TVD upwind scheme. As an example for the case of $\cos\theta_m > 0$ and $\sin\theta_m > 0$, Eq. (2.45) is approximated by

$$\begin{aligned} &\frac{\Delta f^s_{i,l,m}}{\Delta t^s} + n_i\delta_0 T_i^{1-\omega} + c_{p_l}\cos\theta_m\frac{\Delta f^s_{i,l,m} - \Delta f^s_{i-1,l,m}}{\Delta r_{i-1}} - \frac{c_{p_l}\sin\theta_m}{r_i}\frac{\Delta f^s_{i,l,m+1} - \Delta f^s_{i,l,m}}{\Delta\varphi_l} \\ &= n_i\delta_0 T_i^{1-\omega}\left(f^{Ss}_{i,l,m} - f^s_{i,l,m}\right) - c_{p_l}\cos\theta_m\frac{F^s_{i+1/2,l,m} - F^s_{i-1/2,l,m}}{0.5\left(r_{i+1} - r_{i-1}\right)} + \frac{c_{p_l}\sin\theta_m}{r_i}\frac{F^s_{i,l,m+1/2} - F^s_{i,l,m-1/2}}{0.5\left(\theta_{m+1} - \theta_{m-1}\right)}, \end{aligned} \tag{2.46}$$

where

$$F^s_{i+1/2,l,m} = \begin{cases} f^s_{i,l,m} + 0.5\Delta r_i minmod\left(D^s_{i+1/2,l,m}, D^s_{i-1/2,l,m}\right), & \cos\theta_m > 0 \\ f^s_{i+1,l,m} - 0.5\Delta r_i minmod\left(D^s_{i+3/2,l,m}, D^s_{i+1/2,l,m}\right), & \cos\theta_m < 0 \end{cases}$$
$$F^s_{i,l,m+1/2} = \begin{cases} f^s_{i,l,m} + 0.5\Delta \varphi_m minmod\left(D^s_{i,l,m+1/2}, D^s_{i,l,m-1/2}\right), & \sin\theta_m > 0 \\ f^s_{i,l+1,m} - 0.5\Delta \varphi_m minmod\left(D^s_{i,l,m+3/2}, D^s_{i,l,m+1/2}\right), & \sin\theta_m < 0 \end{cases} \tag{2.47}$$

$$D^s_{i+1/2,l,m} = \frac{f^s_{i+1,l,m} - f^s_{i,l,m}}{\Delta r_i},$$
$$D^s_{i,l,m+1/2} = \frac{f^s_{i,l,m+1} - f^s_{i,l,m}}{\Delta \theta_m}. \tag{2.48}$$

Here the nonlinear limiter *minmod* introduced in [155, 156] is given by

$$minmod\,(a,b) = 0.5\,[sign\,(a) + sign\,(b)]\,\min\left(|\ a\ |, |\ b\ |\right). \tag{2.49}$$

Once obtaining values of the distribution function, the integrals in Eqs. (2.31) are evaluated by applying Gauss-Hermite quadrature for $\int dc_p$ and Simpson 3/8 rule for $\int d\varphi$.

The developed numerical method allows to have the second order accuracy for the derivation in the physical space by using the TVD approximation. By keeping the time derivation we can simulate the time-dependent phenomena. However, in the case of steady-state problem the implementation of the implicit scheme allows to reduce considerably the computational time.

2.5 Results and discussion

In this Section first the numerical parameters used in the simulation will be provided together with the range of the three dimensionless governing parameters of the heat transfer problem, Eqs. (2.1, 2.2). Then, the influence of these dimensionless parameters on the distribution of the macroscopic parameters is considered. Next, in Section 2.5.3 the limits of the provided solutions in the slip and free molecular flow regimes are discussed. Finally, in Section 2.5.4 the influence of the gas-surface interaction is studied in the frame of the Maxwell diffuse-specular scattering.

Table 2.1: Numerical grid parameters.

$N_r \times N_\theta$		$N_r \times N_{cp}$	
$\delta_0 < 10$	$\delta_0 \geq 10$	$\mathcal{T} = 1.1,\ 1.5$	$\mathcal{T} = 5$
3200×1602	6400×798	8	24

2.5.1 Numerical parameters

The numerical simulations are conducted for three values of temperature ratio $\mathcal{T} = 1.1, 1.5, 5$, three values of radius ratio $\mathcal{R} = 1.1, 2, 10$ and for a wide range of rarefaction parameter δ_0 varying from 0.01 to 100. After the various numerical tests the optimal dimensions of the numerical grid are found (shown in Table 2.1), which guarantees the accuracy for energy conservation law ($r^2 q_r = constant$) of the order of 0.1%.

It is to note that the similar total number of numerical grid points ($N_r \times N_\theta$) are needed for the case of small ($\delta_0 < 10$) and large ($\delta_0 \geq 10$) values of the rarefaction parameter. However, for the small δ_0 values more important grid in the molecular velocity space (for the angle θ) is required while for the large δ_0 values larger number of points in the physical space is needed. In the case of large temperature ratio between two surfaces the number of the grid points for the magnitude of the molecular velocity N_{c_p} is essentially larger than for the case of the small and moderate temperature ratios. This fact is related to an error, which appears when one replaces the infinite integration interval, in Eqs. (2.31), by the finite one. Usually the integration interval is chosen as $[0, a\sqrt{T_{max}}]$, where $a \approx 4$. Therefore, for the larger temperature ratio the larger number of points is required to ensure the same integration accuracy.

One comment can be added concerning also the number of points in physical (N_r) and molecular velocity ($N_{c_p} \times N_\theta$) spaces: these numbers are more important in comparison to the similar case of the flow between two coaxial cylinders [102]. It is related to the form of the conservation law: for the two concentric spheres the quantity $r^2 q_r$ has to be conserved instead of $r q_r$ for two coaxial cylinders that requires much more computational points to achieve the same accuracy.

2.5.2 Bulk quantities

In this subsection the influence of the three dimensionless governing parameters of the problem, namely rarefaction parameter, temperature ratio and radius ratio, Eq. (2.1), on the behavior of the bulk quantities is studied. The Hard Sphere model is used, so the viscosity index ω in Eq. (2.7) is equal to 0.5. The complete accommodation at the both surfaces of the spheres is assumed here, $\alpha_C = \alpha_H = 1$.

Table 2.2: Dimensionless heat flux at the internal sphere $q_r(R_H)$ for the temperature ratio $\mathcal{T} = 1.1, 1.5, 5$ and radius ratio $\mathcal{R} = 1.1, 2, 10$ and complete accommodation. The heat flux values for the rarefaction parameter equal to 0 are calculated using the analytical expression (2.34).

$\mathcal{R}$	δ_0	$q_r(R_H)$		
		$\mathcal{T} = 1.1$	1.5	5
1.1	0.	5.737×10^{-2}	3.017×10^{-1}	2.807
	0.01	5.701×10^{-2}	3.004×10^{-1}	2.816
	0.1	5.555×10^{-2}	2.945×10^{-1}	2.851
	1.	4.393×10^{-2}	2.355×10^{-1}	2.440
	10.	1.514×10^{-2}	8.185×10^{-2}	9.413×10^{-1}
	100.	2.032×10^{-3}	1.106×10^{-2}	1.336×10^{-1}
2	0.	5.676×10^{-2}	2.889×10^{-1}	2.430
	0.01	5.652×10^{-2}	2.880×10^{-1}	2.432
	0.1	5.612×10^{-2}	2.866×10^{-1}	2.450
	1.	5.159×10^{-2}	2.661×10^{-1}	2.409
	10.	2.473×10^{-2}	1.294×10^{-1}	1.287
	100.	3.653×10^{-3}	1.974×10^{-2}	2.309×10^{-1}
10	0.	5.644×10^{-2}	2.825×10^{-1}	2.266
	0.01	5.624×10^{-2}	2.816×10^{-1}	2.265
	0.1	5.618×10^{-2}	2.814×10^{-1}	2.268
	1.	5.553×10^{-2}	2.786×10^{-1}	2.275
	10.	4.751×10^{-2}	2.373×10^{-1}	1.927
	100.	1.550×10^{-2}	8.020×10^{-2}	7.325×10^{-1}

The numerical solution of the kinetic equation (2.28) is obtained for three values of temperature ratio $\mathcal{T} = 1.1, 1.5, 5$, three values of radius ratio $\mathcal{R} = 1.1, 2, 10$ and for a wide range of rarefaction parameter δ_0 varying from 0.01 to 100.

Table 2.2 provides the values of the heat flux at the internal sphere $q_r(R_H)$ for a wide range of rarefaction parameter δ_0 and for three values of the temperature ratio and three values of the radius ratio. Using the heat flux conservation equation (2.11) and the data from Table 2.2 the values of the heat flux may be found in any point between the spheres.

From dimensionless heat flux q_r provided in Table 2.2, one can calculate easily the corresponding dimensional heat flux q'_r by using Eq. (2.9). For example, considering He confined between two concentric spheres that have radii $R'_H = 5mm$, $R'_C = 50mm$ and temperatures $T'_H = 330K$, $T'_C = 300K$, the most probable molecular velocity and viscosity coefficient are $v_0 = 1116.05m/s$ and $\mu_0 = 1.985 \cdot 10^{-5} Nsm^{-2}$ [107], respectively. If one considers reference pressure $p_0 = 0.4923Pa$, then the gas is in transitional regime ($\delta_0 = 1.$ calculated from Eqs. (2.2), (2.3)). The dimensionless heat flux at the internal sphere (case $\mathcal{T} = 1.1$, $\mathcal{R} = 10$ in Table 2.2) is equal to $5.553 \cdot 10^{-2}$ and the corresponding dimensional heat flux is $30.51 W/m^2$.

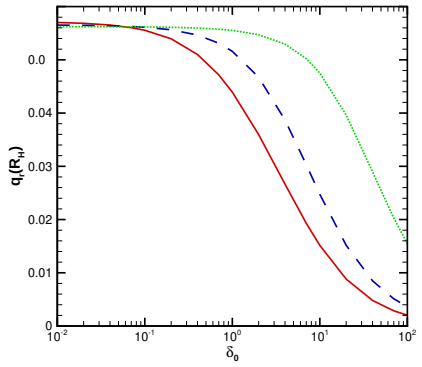

(a) $\mathcal{T} = 1.1$

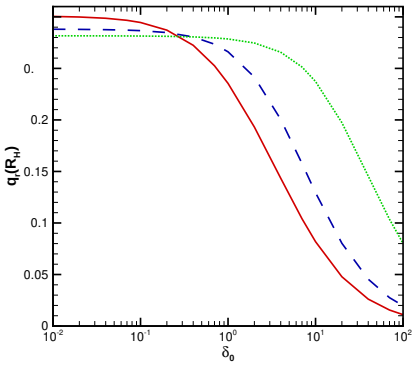

(b) $\mathcal{T} = 1.5$

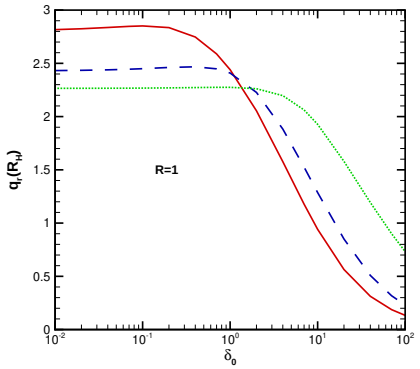

(c) $\mathcal{T} = 5$

Figure 2.1: Heat flux at the internal sphere $q_r(R_H)$ as a function of rarefaction parameter δ_0 for three sphere' radius ratios $\mathcal{R} = 1.1$, 2 and 10. Three temperature ratios are plotted: (a) $\mathcal{T} = 1.1$, (b) 1.5 and (c) 5.

The behavior of the heat flux at the internal sphere $q_r(R_H)$ as a function of rarefaction parameter δ_0 is presented in Fig. 2.1 for temperature ratio $\mathcal{T} = 1.1, 1.5, 5$ and radius ratio $\mathcal{R} = 1.1, 2, 10$. It is seen that in most cases the dimensionless heat flux decreases monotonically with δ_0 increased. In particular, the heat flux is decreased very slowly for $\delta_0 < 1$, while its decreasing becomes much faster for $\delta_0 > 1$. However, it is seen that in the case of large temperature ratio $\mathcal{T} = 5$ the behavior of the heat flux is non monotonic, see Fig. 2.1c, with a maximum which location depends on the sphere radius ratio $\mathcal{R}$. It is to note that the similar behavior of the heat flux was found in Ref. [33] in the case of the two coaxial cylinders with the large temperature ratio.

However, in the range of the rarefaction parameter $0 \leq \delta_0 \leq 0.1$, the behavior of the heat flux between two spheres is different from that between two cylinders. The later is found in Ref. [33] to be independent from the radius ratio for both small and large temperature ratios. But it is not the case for two concentric spheres, see Fig. 2.1 and relation (2.34), where the influence of the radius ratio on the heat flux can be seen explicitly. This result can be explained by the difference in choice of the reference number density n_0 used in normalization

of the heat flux. If we chose $n_0 = n'_{wC}$ (number density on the external sphere calculated from the non-penetration boundary conditions (2.30)) instead of $n_0 = n'_{av}$, Eq. (2.10), we obtain the following equation

$$\frac{q'_r(r)}{n'_{wC} k T_0 \upsilon_0} = \frac{\alpha}{\sqrt{\pi}} (\mathcal{T} - 1) \left(\frac{R_H}{r}\right)^2 \tag{2.50}$$

instead of Eq. (2.34) for dimensionless heat flux with an arbitrary radius ratio $\mathcal{R}$. This expression is analogous to Eq. (B.7) in Ref. [33] and we cannot see the influence of the sphere radius on the heat flux as it was reported in Ref. [33]. Therefore it is worth to underline that the choice of the reference parameter is very important and the choice of the average number density allows us to have the more precise description of the heat transfer properties.

The temperature profiles $T(r)$ between two spheres are shown in Fig. 8.1. First, the influence of the temperature ratio $\mathcal{T}$ is analyzed for small radius ratio $\mathcal{R} = 1.1$. The temperature distributions are plotted for four values of the rarefaction parameter $\delta_0 = 0.1$, 1, 10 and 100, see Fig. 8.1 (a), (c) and (e), left column. The temperature distributions have quasi linear shape, which changes only slightly when the temperature ratio increases. The shape of the temperature profiles changes considerably when the radius ratio changes. On Fig. 8.1 (b), (d) and (f), right column, the temperature profiles are presented for the large radius ratio $\mathcal{R} = 10$ and all three temperature ratios. For the all considered rarefaction parameters, except $\delta_0 = 100$, the temperature decreases rapidly with r increases and it differs only in less than 5% from the cold sphere temperature for $r > 0.5$. The temperature jump is clearly seen for all three parameters determining the heat transfer problem, Eqs. (2.1, 2.2). The temperature jump is larger near to the internal sphere surface and it increases with increasing of the temperature ratio and decreasing of the rarefaction parameter.

The pressure profiles $p(r)$ are shown in Fig. 2.2. The pressure decreases monotonically from the internal to the external sphere. The ratio of the pressure near to the hot and cold spheres (p_H/p_C) increases with the decrease in δ_0. For the small radius ratio $\mathcal{R} = 1.1$, see Fig. 2.2 (a), (c) and (e), left column, this pressure ratio varies maximum from $\sim 1\%$ for $\mathcal{T} = 1.1$ to $\sim 17\%$ for $\mathcal{T} = 5$. In the case of the large radius ratio $\mathcal{R} = 10$, see Fig. 2.2 (b), (d) and (f), right column, this pressure ratio varies maximum from $\sim 2.5\%$ for $\mathcal{T} = 1.1$ to $\sim 64\%$ for $\mathcal{T} = 5$. The pressure is constant in the region far enough from the internal sphere; however, it increases drastically near to the internal sphere, especially in the rarefaction parameter range $0 \leq \delta_0 \leq 10$.

The density number profiles $n(r)$ are shown in Fig. 2.3. We found anew, as for the temperature and pressure profiles, two different types of behavior: for the small and for the large radius ratios, shown in Fig. 2.3, left and right column, respectively.

It should be noted that the behaviors of the macroscopic parameters shown in Figs. 8.1-2.3 have been also observed in the two surfaces geometries as the two parallel plates and two coaxial cylinders, see for example Refs. [146], [33].

2.5.3 Range of validity of the analytical approaches and approximate expressions

The analytical expressions for the heat flux, obtained in previous Sections for the slip and free molecular flow regimes, are compared with the numerical solution of the S-model kinetic equation (2.28) for the case of the complete accommodation of the molecules with the both internal and external surfaces ($\alpha_C = \alpha_H = 1$), see boundary conditions (2.29). The corresponding curves for the heat flux on the internal sphere surface are plotted on Figure 2.4. The expressions derived for the all rarefaction parameter range in Refs. [150, 151, 20, 152, 149], Eqs. (2.43, 2.44), are also plotted on Figure 2.4 for the rarefaction parameter δ_0 ranging from 0.01 to 100. Various pairs of the temperature and radius ratio are considered.

In the free molecular regime the good agreement is found between the obtained here analytical solution, Eq. (2.34), and the numerical solution of the S-model equation for all considered pairs of the temperature and radius ratios. The analytical free molecular solution is very close to the numerical solution. In the case of the large radius ratio $\mathcal{R} = 10$ the both solutions practically coincide up to $\delta_0 \sim 0.3$.

In the slip flow regime very good agreement between analytical and numerical solutions is observed for $\mathcal{T} = 1.1$ and 1.5 and $\mathcal{R} = 1.1$ up to $\delta_0 \sim 2$, see Fig. 2.4 (a),(c). It is to note that for the calculation of the analytical solution the both temperature jump coefficients in Eqs. (2.14 - 2.16) are equal to 1.95. However, when the radius ratio increases up to $\mathcal{R} = 10$ the both solutions start to deviate for the rarefaction parameter larger than $\delta_0 \sim 70$, see Fig. 2.4 (b),(d). This fact can be explained by the behavior of the pressure distribution between the spheres, which is not constant for the rarefaction parameter less than 100, see Fig. 2.2(b).

When considering the large temperature ratio $\mathcal{T} = 5$, Fig. 2.4 (e),(f), even for the small radius ratio $\mathcal{R} = 1.1$ the both solutions start to deviate from $\delta_0 \sim 70$. The pressure behavior between the spheres is more or less constant, see Fig. 2.2(e), and the deviation of both solutions cannot be explained, as previously, by the fails of the hypothesis of the pressure constancy, which was used to derive the analytical solution. In this case of the large temperature ratio, $\mathcal{T} = 5$, the definition of the rarefaction parameter δ_0, which is based on the external sphere temperature, cannot characterize correctly the problem and the definition based on the mean temperature between two surfaces has to be used in order to apply correctly the analytical solution for the heat flux prediction. The both points, evoked above, lead to the disagreement between the numerical and analytical solutions for the case of $\mathcal{T} = 5$ and $\mathcal{R} = 10$: the pressure

constancy hypothesis is not valid from $\delta_0 \sim 100$ and the rarefaction parameter has to be defined using the mean temperature in order to taken into account the large variation of temperature between the spheres' surfaces.

On Fig. 2.4 the expressions derived for the all rarefaction parameter range in Refs. [150, 151, 20, 152, 149], are also plotted. The good agreement is found between the numerical solution of the S-model kinetic equation and Eq. (2.43), which was derived for the small temperature differences between the spheres, for $\mathcal{T} = 1.1$ and even for $\mathcal{T} = 1.5$. To predict the heat flux values for the all rarefaction range and an arbitrary temperature and pressure radius ratio we propose here to use Eq. (2.44), derived previously, with the here obtained expressions in the hydrodynamic and free molecular regimes, Eqs. (2.21), (2.34), respectively. Surprisingly good agreement is found for all considered here temperature and radius ratios when Eq. (2.44) is used. The similar good agreement with relation (2.44) was found by the authors of Ref. [157] in the two cylinders geometry case.

The analytical temperature and heat flux profiles between two spheres in slip flow regime obtained here, Eqs. (2.13, 2.18), are shown in Fig. 2.5 together with the numerical results for various values of the rarefaction parameters ($\delta_0 = 7,\ 20,\ 70$) and $\mathcal{T} = 1.5$, $\mathcal{R} = 2$. Very good agreement between analytical and numerical profiles is observed on Figure 2.5 for $\delta_0 = 20$ and 70. However, when δ_0 decreases up to 7 the analytical temperature profile starts to deviate from the numerical one near the both hot and cold surfaces. However, the analytical and numerical heat flux profiles still keep close shape also for this relatively low value of the rarefaction parameter.

2.5.4 Influence of gas-surface interaction

The influence of gas-surface interaction on the macroscopic quantities of a gas between two spherical surfaces is investigated by varying of the accommodation coefficient on the internal sphere from 0.6 to 1.0. The complete accommodation is assumed on the external sphere surface.

In Fig. 2.6 the dimensionless heat flux at internal sphere as a function of rarefaction parameter is plotted for three values of the accommodation coefficient at the internal sphere surface ($\alpha_H = \alpha = 0.6,\ 0.8$ and 1.), Eq. (2.29), and complete accommodation at the external sphere ($\alpha_C = 1.$). The numerical solution of the S-model kinetic equation is compared with the derived here analytical solution in free molecular regime, Eq. (2.34), which takes into account the non-complete accommodation of the molecules on the internal sphere surface. The case of $\mathcal{R} = 2$ is chosen, because the other radius ratios ($\mathcal{R} = 1.1, 10$) are already shown on Fig. 2.4, but only for $\alpha = 1$. It is clear from Fig. 2.6 that accommodation coefficient has significant

influence on heat flux in the free molecular and transitional flow regimes. This influence is reduced in slip regime and vanished completely in hydrodynamic regime. As it was shown on Fig. 2.4 for the complete accommodation of the molecules on the internal and external spheres surfaces the good agreement is also found between the numerical solution of the S-model kinetic equation and the approximate expression Eq. (2.44) with Eqs. (2.21), 2.34), which allow taking into account the various accommodation on the internal sphere surface.

Fig. 2.7 shows the profile of density number, temperature and heat flux between the two spheres in the near free molecular regime ($\delta_0 = 0.01$) for two values of the accommodation coefficient at the internal sphere ($\alpha_H = \alpha = 0.6$ and 1.0) and complete accommodation at the external sphere. Here the numerical solution of S-model kinetic equation with the Maxwell type, Eqs. (2.29), boundary conditions are compared with the two analytical solutions for free molecular regime: the Eqs. (2.37-2.39) obtained previously in Ref. [104] and here derived expressions Eqs. (2.32-2.34). It is to note that the author of Ref. [104] used a Maxwell type model of the boundary conditions, which is different from that used here, Eqs. (2.29). The accommodation process is separated in two stages with two corresponding accommodation coefficients: first the accommodation of tangential momentum, coefficient α in Eqs. (2.29), is assumed to be complete, however the accommodation of energy is taken into account by assuming the temperature of the reflected molecules to be different from that of the surface and related with the later through the thermal accommodation coefficient. It is evident that for the complete accommodation the both approaches give the same results, however they are different for the non-complete accommodation.

In the case of small temperature difference ($\mathcal{T} = 1.1$), see Fig. 2.7, all the profiles are very close to each other. For the large temperature difference ($\mathcal{T} = 5.$) and $\alpha = 0.6$, the profiles given by the S-model kinetic solution and present analytical expression are still very close to each other. However, the number density and temperature profiles from Ref. [104] deviate form the two other results, especially in the region near to the internal sphere. It is interesting to note that, although the density number and temperature profiles, given by author of [104], are different the heat flux profiles are identical to the results, obtained here.

Fig. 2.8 illustrates the value of the number density, temperature and heat flux of the internal, middle and external points as a function of accommodation coefficient. The two analytical solutions in free molecular regime are compared: the approach proposed in Ref. [104] and the here derived expressions Eqs.(2.32-2.34). It is shown anew that the results for the heat flux are very close for the two approaches. In contrast, the density number and temperature distributions between two spherical surfaces given by the two approaches are only identical for the two limit values of the accommodation coefficient ($\alpha = 0.$ and 1.0) and the deviation has a maximum for $\alpha \approx 0.4$. The difference between two solution is evidently maximal on the internal

sphere surface. From the comparison, presented in this Section, it is difficult to conclude what boundary conditions are preferable. Up to now only heat flux values are available from the measurements, but the both Maxwell-type boundary conditions give similar results for the heat flux. Therefore the more detailed experimental investigations are needed to establish the correct simulation of the non-complete accommodation of the molecules with the wall.

2.6 Conclusions

The heat flux between two concentric spheres is simulated using the nonlinear form of the S-model kinetic equation for the large range of the rarefaction parameter. Small, moderate and large temperature and radius ratios are considered. The classical Maxwell diffuse-specular boundary conditions are used at the internal sphere surface and the complete accommodation is assumed on the external sphere. The time-dependent governing equations are discretized based on the discrete velocity method. The upwind approximation is used for the spatial derivatives. The implicit algorithm allows us to reduce considerably the computational time when only steady state solution is needed.

The behaviors of the macroscopic parameters (heat flux, temperature, pressure and number density) are examined in details for various temperature ratio between the sphere surfaces and for different sphere radius ratio. Non monotonic behavior of the heat flux as a function of the rarefaction parameter δ_0 is found in the case of the strong temperature ratio between the spheres' surfaces. The essential pressure variation in the radial direction is found for the small and moderate values of the rarefaction parameter.

The analytical relations for the temperature and the heat flux in the slip flow regime is obtained for the arbitrary temperature and radius ratio and very good agreement has been found between these analytical expressions and the numerical solution of the S-model equation.

The approximate expression for the heat flux valid for all flow regimes and arbitrary temperature and radius ratio and under an assumption of the diffuse-specular reflection on the internal sphere and diffuse reflection on the external sphere is proposed.

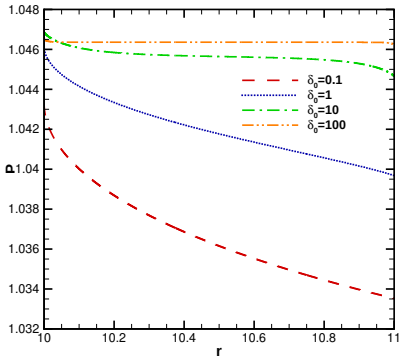

(a) $\mathcal{T} = 1.1$, $\mathcal{R} = 1.1$

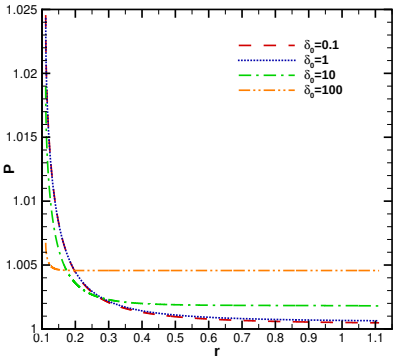

(b) $\mathcal{T} = 1.1$, $\mathcal{R} = 10.$

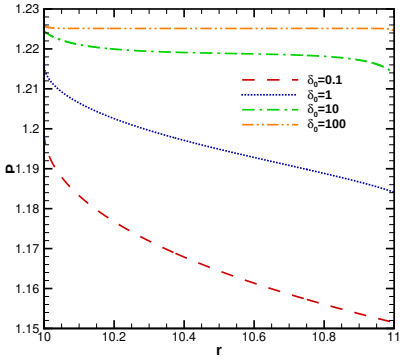

(c) $\mathcal{T} = 1.5$, $\mathcal{R} = 1.1$

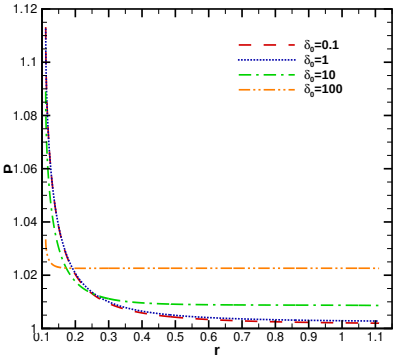

(d) $\mathcal{T} = 1.5$, $\mathcal{R} = 10.$

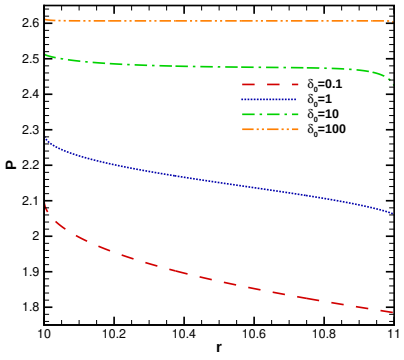

(e) $\mathcal{T} = 5.$, $\mathcal{R} = 1.1$

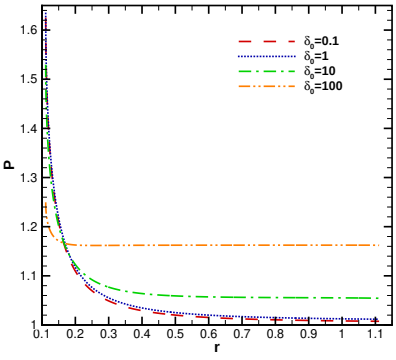

(f) $\mathcal{T} = 5.$, $\mathcal{R} = 10.$

Figure 2.2: Pressure profiles $p(r)$ as a function of the distance r between the spheres for three sphere' radius ratios $\mathcal{R} = 1.1$, 2 and 10 and three temperature ratios $\mathcal{T} = 1.1$, 1.5 and 5.

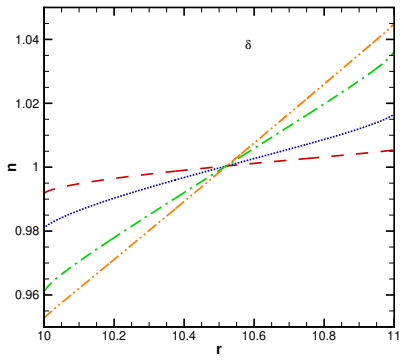

(a) $\mathcal{T} = 1.1$, $\mathcal{R} = 1.1$

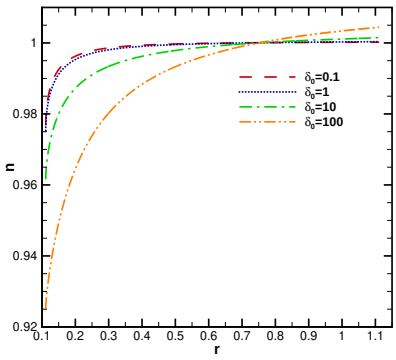

(b) $\mathcal{T} = 1.1$, $\mathcal{R} = 10$.

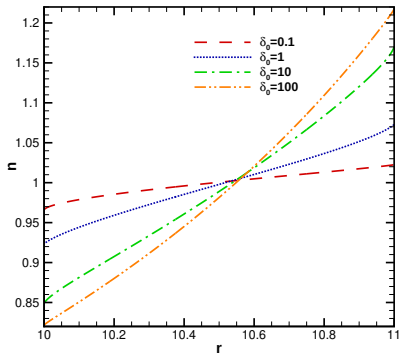

(c) $\mathcal{T} = 1.5$, $\mathcal{R} = 1.1$

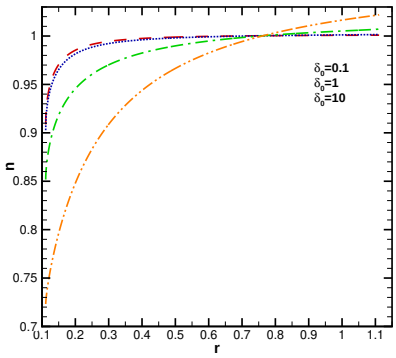

(d) $\mathcal{T} = 1.5$, $\mathcal{R} = 10$.

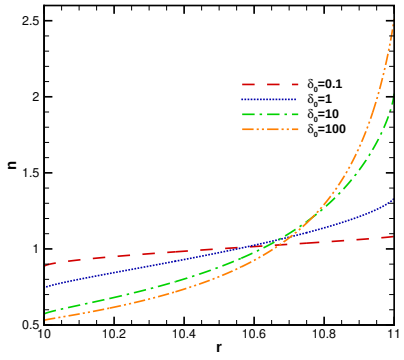

(e) $\mathcal{T} = 5.$, $\mathcal{R} = 1.1$

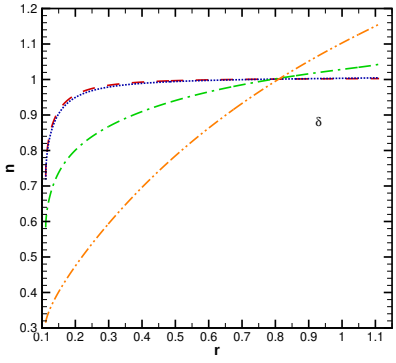

(f) $\mathcal{T} = 5.$, $\mathcal{R} = 10$.

Figure 2.3: Density number profiles $n(r)$ as a function of the distance r between the spheres for three sphere' radius ratios $\mathcal{R} = 1.1$, 2 and 10 and three temperature ratios $\mathcal{T} = 1.1$, 1.5 and 5.

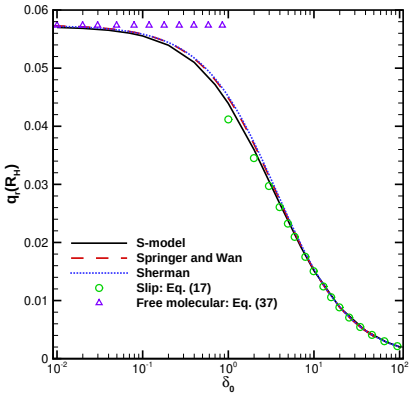

(a) $\mathcal{T} = 1.1$, $\mathcal{R} = 1.1$

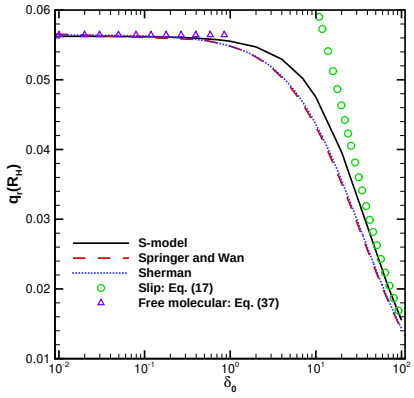

(b) $\mathcal{T} = 1.1$, $\mathcal{R} = 10.$

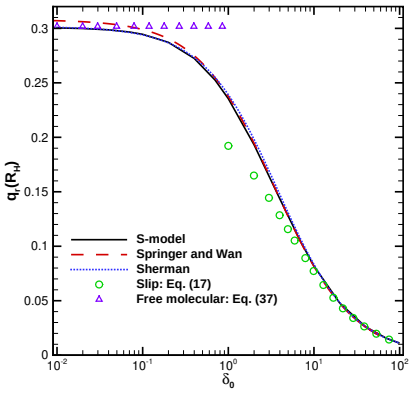

(c) $\mathcal{T} = 1.5$, $\mathcal{R} = 1.1$

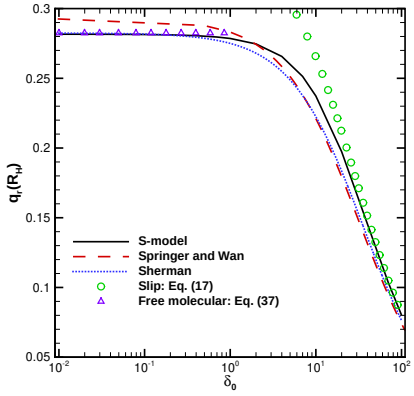

(d) $\mathcal{T} = 1.5$, $\mathcal{R} = 10.$

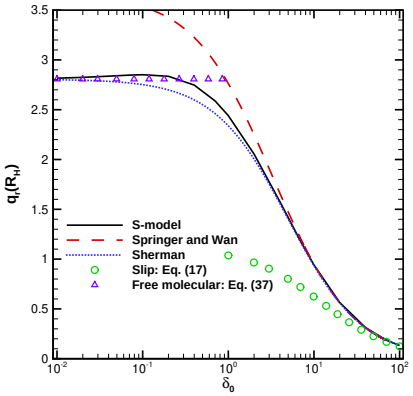

(e) $\mathcal{T} = 5.$, $\mathcal{R} = 1.1$

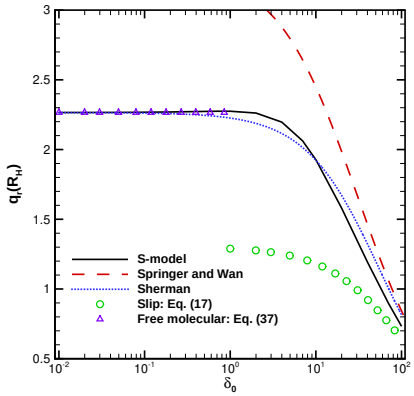

(f) $\mathcal{T} = 5.$, $\mathcal{R} = 10.$

Figure 2.4: S-model solutions in all flow regimes are compared with analytical expression (2.43), valid in all flow regimes, provided by Springer and Wan [21] in the case of small temperature difference $\mathcal{T} \to 1$; Sherman's expression (2.44), valid also in all flow regimes, with the expressions (2.21, 2.34), proposed here for general case of the temperature and radius ratios; the free molecular regime solution, derived in the present study (2.34) and the obtained here analytical solution in the slip regime (2.18) valid for all temperature and radius ratios.

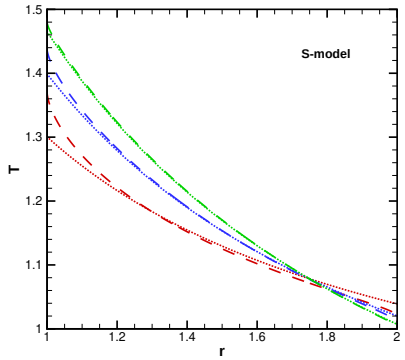

(a) Dimensionless temperature$T\,(r)$

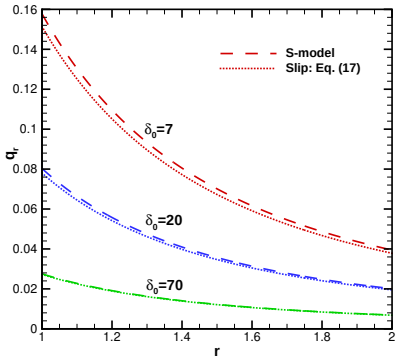

(b) Dimensionless heat flux$q_r\,(r)$

Figure 2.5: (a) The temperature and (b) heat flux profiles, obtained from the numerical solution of the S-model kinetic equation for the case $\mathcal{T} = 1.5$ and $\mathcal{R} = 2$, are compared with the proposed here analytical expression for slip regime, Eqs. (2.13, 2.18).

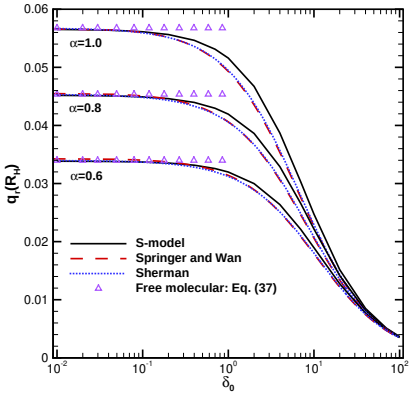

(a) $\mathcal{T} = 1.1$, $\mathcal{R} = 2$.

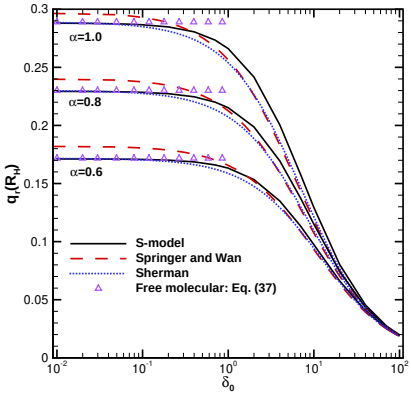

(b) $\mathcal{T} = 1.5$, $\mathcal{R} = 2$.

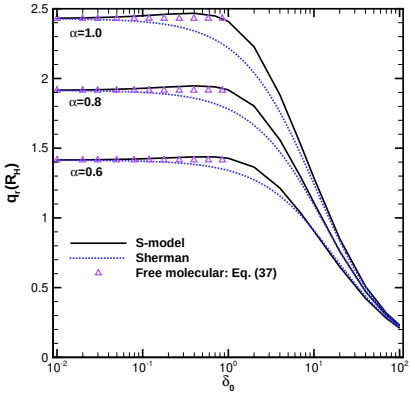

(c) $\mathcal{T} = 5.$, $\mathcal{R} = 2$.

Figure 2.6: The dimensionless heat flux at the internal sphere surface. The complete accommodation on the external sphere surface is assumed and the Maxwell diffuse-specular reflection is assumed on the internal sphere surface with the accommodation coefficient equal to 0.6, 0.8 and 1.0.

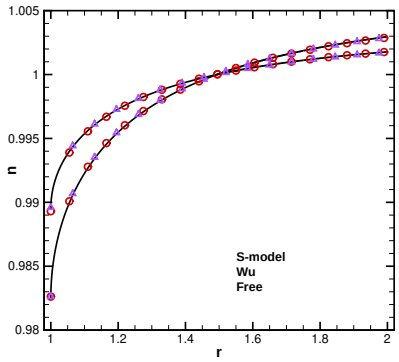

(a) Density number$\mathcal{T} = 1.1$, $\mathcal{R} = 2$.

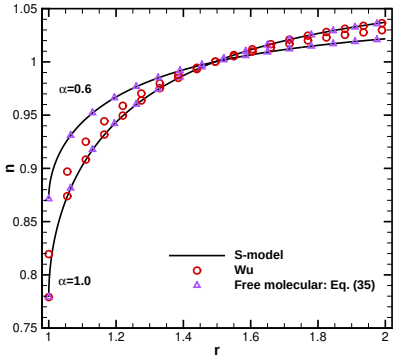

(b) Density number $\mathcal{T} = 5.$, $\mathcal{R} = 2$.

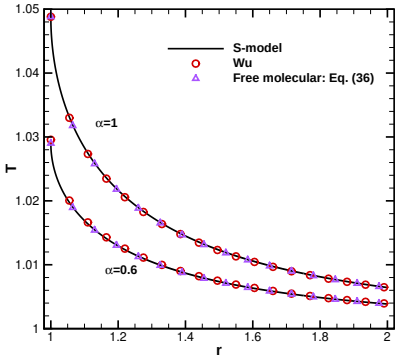

(c) Temperature $\mathcal{T} = 1.1$, $\mathcal{R} = 2$.

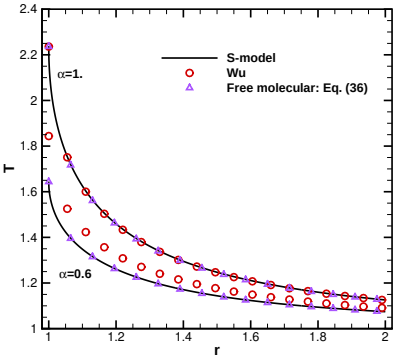

(d) Temperature $\mathcal{T} = 5.$, $\mathcal{R} = 2$.

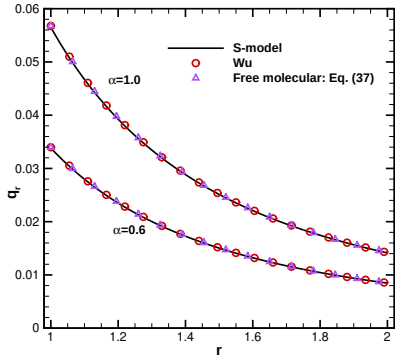

(e) Heat flux $\mathcal{T} = 1.1$, $\mathcal{R} = 2$.

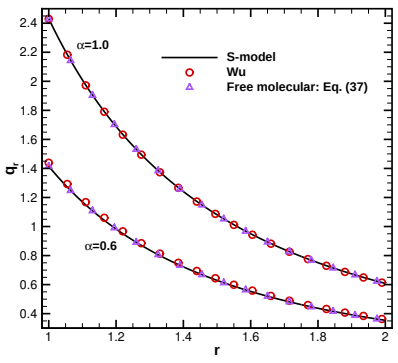

(f) Temperature $\mathcal{T} = 5.$, $\mathcal{R} = 2$.

Figure 2.7: The profiles of the number density, temperature and heat flux between the two concentric spheres in free molecular regime for the case of the complete accommodation on the external sphere surface and for the accommodation equal to 0.6 and 1.0 on the internal sphere surface. Two solutions are compared: Eqs. (2.37-2.39) obtained by Wu [104] and the here derived expressions Eqs. (2.32-2.34). The two approached are compared with the numerical solution of the S-model kinetic equation.

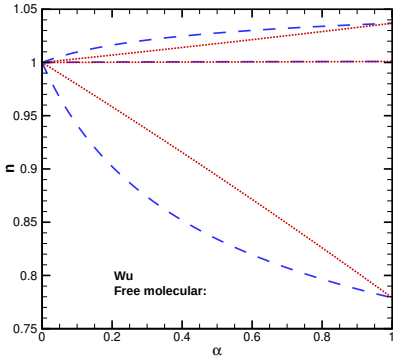

(a) Density number

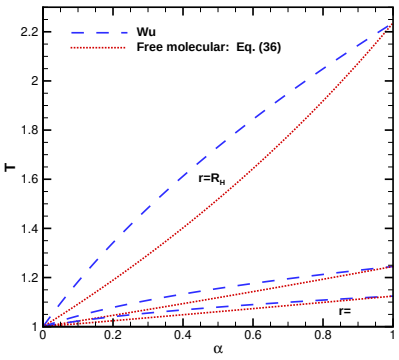

(b) Temperature

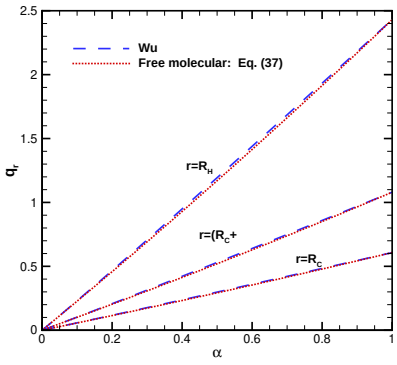

(c) Heat flux

Figure 2.8: The number density, temperature and heat flux at the internal, middle and external points as a function of the accommodation coefficient on the internal sphere surface for the case $\mathcal{T} = 5.$ and $\mathcal{R} = 2.$

Chapter 3

Unsteady heat transfer between two coaxial cylinders

The heat conduction through a rarefied gas between two concentric cylinders has been investigated by many researches[27, 28, 29, 30, 31, 32, 33]. In the most cases, the analysis has been carried out using the linearized kinetic models, which is completely justified when the temperature difference between the cylinders is small [27, 28, 31] or the cylinders' radius ratio is large [32]. For the large temperature difference between the cylinders the nonlinear approach has also been implemented [29, 30, 34, 33]. However, all these studies concern the steady state flow conditions. Nevertheless, the information about the transient heat transfer is very important from the scientific and practical point of view. In the design and development stages of the Pirani gauges [35], the pressure evaluation in time is vital information for an adjustment of the sensor characteristics. Pirani sensors are often used in transfer chamber in the semiconductor industry or in chambers with rapid venting cycles. In rapid venting applications Pirani sensors show temporarily a pressure that is higher or lower than the true pressure. This effect is dependent on the sensor's geometry and the way temperature compensation is implemented. It would be helpful in the design phase to be able to model these pressure and heat pulses in order to optimize the design of Pirani gauges. In addition, for pulsed Pirani gauges the signal depends on both the thermal conductivity of the gas and the heat capacity of wire and gas. A better understanding of the underlying physics and the corresponding modeling can be used to optimize different operating modes.

A few papers devoted to the simulations of the transient properties of a rarefied gas have to be cited [36, 37, 38]. The topic, the more close to the present study, is considered in Ref. [36], where the authors investigate the transient heat transfer between two parallel plates due to the rapid heating or cooling of one of these two plates. The simulations are carried out in the slip flow regime applying both the continuum and kinetic (based on the DSMC method) approaches.

The aim of the present study is to investigate the transient evolution of the heat transfer

through the rarefied gases confined between two coaxial cylinders over a broad range of the gas rarefaction. The unsteady S-model kinetic equation is solved numerically to simulate the time evolution of gas parameters. The time to reach the steady state conditions for the averaged over the distance between two cylinders gas characteristics is evaluated for different rarefaction level and for various gases. In the slip flow regime the transient heat flux evolution is calculated from the energy balance and it is compared to that obtained from the model kinetic equation.

3.1 Problem statement

Two coaxial cylinders containing a gas at rest are considered, with the radii R'_H and R'_C for the internal and the external cylinder, respectively, $R'_H < R'_C$. These cylinders are supposed to be of an infinite length and kept initially at the same temperature T'_C, then instantaneously the temperature of the internal cylinder increases up to T'_H ($T'_H > T'_C$) and this new temperature difference is maintained over time. We are interested in the evolution of the gas parameters between these two coaxial cylinders as a function of time.

The governing parameters and continuum approach are analogous to heat transfer problem between two concentric spheres, which is studied in Chapter 2. The unsteady version of dimensionless energy conservation Eq. (2.11) written for two coaxial cylinder geometry

$$\frac{\partial T}{\partial t} = \frac{5}{4\delta_0} T \frac{1}{r} \frac{\partial}{\partial r} \left(\mu r \frac{\partial T}{\partial r} \right). \tag{3.1}$$

3.2 Kinetic model equation

For the simulation of the transient heat transfer in the transitional and near free molecular flow regimes the S-model kinetic equation [11] is used. Considering the axial symmetry of the problem the S-model kinetic equation in the completely conservative form may be written as [158, 145]

$$\frac{\partial}{\partial t'} \left(r' f' \right) + \frac{\partial}{\partial r'} \left(r' f' \upsilon_p \cos\varphi \right) - \frac{\partial}{\partial \varphi} \left(f' \upsilon_p \sin\varphi \right) = r' \nu' \left(f^{S'} - f' \right). \tag{3.2}$$

Here, the physical space is described by the cylindrical coordinate systems (r, ϕ, z). In the other hand, the molecular velocity space are described by the cylindrical coordinate systems $(\upsilon_p, \varphi, \upsilon_z)$. The molecular velocity vector $\mathbf{v}$ has three components projected on the physical

coordinate system as $\mathbf{v} = (v_p \cos\varphi, v_p \sin\varphi, v_z)$. The similar procedure to Eqs. (2.23-2.27) is applied in order to obtain the dimensionless form of the governing equation

$$\frac{\partial}{\partial t}(rf) + \frac{\partial}{\partial r}(rfc_p \cos\varphi) - \frac{\partial}{\partial \varphi}(fc_p \sin\varphi) = r\nu\delta_0 n T^{1-\omega}\left(f^S - f'\right). \tag{3.3}$$

In order to reduce the computational effort, the dependence of distribution function f on c_z component of the molecular velocity vector may be eliminated by introducing two reduced distribution functions

$$\Phi = \int_{-\infty}^{\infty} f dc_z, \ \Psi = \int_{-\infty}^{\infty} f c_z^2 dc_z. \tag{3.4}$$

More detail on the projection procedure can be found in [146] for plate geometry and in [159] for cylinder geometry.

The numerical method used to solve Eq. (3.3) is similar to that presented in Section 2.4. Here we choose numerical grid $N_r \times N_{cp} \times N\varphi = 1600 \times 12 \times 100$ for most of the simulation cases. However, when the $\delta_0 < 0.5$, a finer mesh in molecular velocity space is essential, therefore $N_{cp} = 25$ is implemented.

3.3 Results and discussion

The following conditions are chosen for the numerical simulations of the transient heat transfer. At time moment $t = 0$ the temperature of both cylinders is supposed to be equal to T_C, then the temperature of the internal cylinder increases instantaneously and becomes $T_H = \mathcal{T} T_C$, where $\mathcal{T} = 1.3$ and 2. The cylinders radius ratio is chosen to be equal to $R_C/R_H = 50$. The gas rarefaction varies from the near free molecular ($\delta_0 = 0.01$) to the hydrodynamic ($\delta_0 = 100$) flow regime. The calculations stop when the convergence criterion, defined as follows,

$$||q_r||_{L_2} = \sqrt{\sum_{i=0}^{Nr} (q_{r_i}^{l+1} - q_{r_i}^{l})^2} \Big/ \sqrt{\sum_{i=0}^{Nr} (q_{r_i}^{l+1})^2} \tag{3.5}$$

and calculated using the L_2 norm, becomes smaller than ε, a positive number (taken here 10^{-8}). The number of time steps needed to reach the steady state is given in the next Section for various values of the rarefaction parameter.

The heat flux $Q_a(t)$, pressure $P_a(t)$ and velocity $U_a(t)$, averaged over the space coordi-

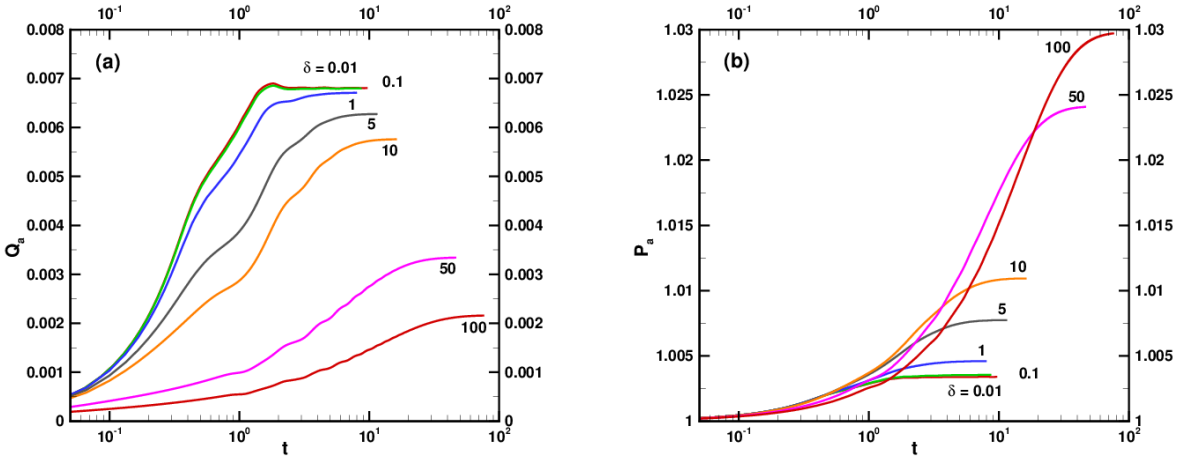

Figure 3.1: Averaged dimensionless heat flux $Q_a(t)$ (a) and pressure $P_a(t)$ (b) between the cylinders as functions of time, $\mathcal{T} = 1.3$. The rarefaction parameter δ_0 varies from 0.01 to 100.

Table 3.1: The dimensionless time to reach the steady state value t_s for the averaged heat flux between the cylinders as a function of the gas rarefaction.

δ_0	0.01	0.05	0.1	0.5	1	5	10	50	100
t_s	2.50	2.49	2.47	2.88	3.45	5.94	8.92	29.50	44.33

nate r, are calculated as follows:

$$G_a(t) = \frac{2}{R_C^2 - R_H^2} \int_{R_H}^{R_C} g(t, r) r dr, \tag{3.6}$$

where $G_a = Q_a$, P_a, U_a and $g = q_r$, p, or u_r. The time dependent behavior of the averaged heat flux $Q_a(t)$, pressure $P_a(t)$ and velocity $U_a(t)$ for various values of the rarefaction parameter are shown on Figs. 3.1 and 3.2. The time evolution of the averaged heat flux changes slightly from the near free molecular ($\delta_0 = 0.01$) to the transitional flow regime ($\delta_0 = 1$). For the small values of the rarefaction parameter $\delta_0 = 0.01$, 0.05 and 0.1 the averaged heat flux reach its steady state after small oscillations (see Fig. 3.1a). For the δ_0 values ranging from 1 to 100 the monotone increase of the averaged heat flux is observed.

In Table 3.1 the time to reach the steady state flow t_s is defined as the moment, when the averaged flow characteristic (heat flux) differs from its steady state value for less than 1%. Analyzing Table 3.1 one may conclude that this time t_s preserves its almost constant value from the free molecular to the transitional flow regime. Then, this time starts to increase passing by a minimum value for the rarefaction parameter δ_0 varying between 0.1 and 0.5. When one approaches the hydrodynamic regime this time t_s is approximately 18 times higher than its minimum value. It is to underline that the dimensionless value of the time to reach the steady

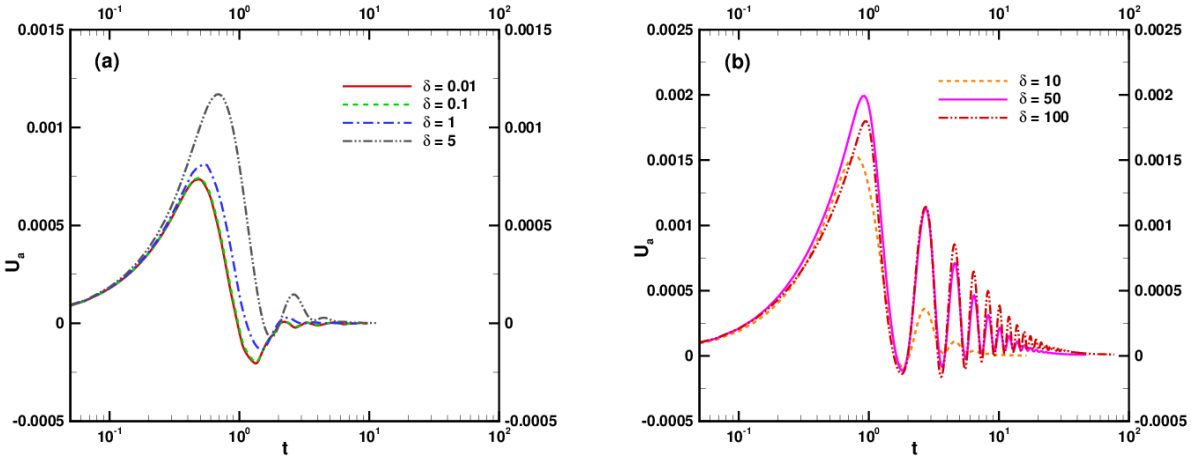

Figure 3.2: Averaged dimensionless velocity $U_a(t)$ between the cylinders as function of time, $\mathcal{T} = 1.3$. The rarefaction parameter δ_0 varies: (a) from 0.01 to 5, (b) from 10 to 100.

Table 3.2: The dimensionless time to reach the criterion (3.5) and the corresponding number of the time steps.

δ_0	0.01	0.05	0.1	0.5	1	5	10	50	100
Time to reach criterion (3.5)	10.78	8.35	8.28	7.04	7.75	11.24	15.77	44.23	72.11
Number of time steps ($\times 10^3$)	225	223	202	163	245	351	495	1412	2316

state flow t_s is reported in Table 3.1 and this time is proportional to the characteristic time $t_0 = R_0/v_0$ of the problem, introduced by Eq. (2.27). When the time to reach the steady state t_s is equal, for example, to 2.47, it means that the heat flux needs 2.47 times of the characteristic time to reach its steady state value.

In Table 3.2 the information about the total dimensionless time required by the numerical calculations to satisfy convergence criterion (3.5), together with the total number of the computational steps is given. It is clear from Table 3.2 that the minimum of this time is reached for $\delta_0 = 0.5$.

The evolution of the averaged pressure $P_a(t)$ between the cylinders as a function of time is presented on Fig. 3.1b). The averaged pressure increases monotonically with time and reaches the higher values for the larger value of the rarefaction parameter δ_0. Since the total pressure variations in time are relatively small and do not exceed 1% of their steady state values for the rarefaction parameter varying from 0.01 to 5, then it is difficult to apply the same criteria as it was used for the averaged heat flux (1% of its steady state value) in order to calculate t_s. However, from the visual comparison of the averaged heat flux and pressure evolutions we can conclude that the time to reach the steady state values for both quantities

is comparable.

The time evolution of the averaged velocity $U_a(t)$ is shown on Fig. 3.2: for the values of the rarefaction parameter δ_0 varying from 0.01 to 5 on Fig. 3.2a) and from 10 to 100 on Fig. 3.2b). It is evident that the sudden temperature change of the internal cylinder wall induces macroscopic gas motion in the gap between the cylinders. The amplitude of this oscillation increases with the rarefaction parameter increasing. The velocity disturbances go down after a few oscillations.

The simulations are also carried out for the temperature ratio between the cylinders' walls $\mathcal{T} = 2$ and the similar qualitative behaviors of the averaged parameters' evolution are found. However the values the averaged parameter increase with increasing the temperature ratio. The time to reach the steady state keeps the same tendency with δ_0 varying, as for the temperature ratio $\mathcal{T} = 1.3$, but this time t_s decreases by approximately 5% with the temperature ratio increasing up to $T_H/T_C = 2$.

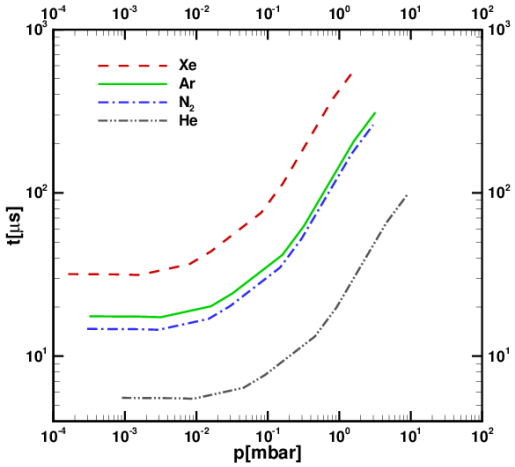

Figure 3.3: The time to reach the steady state conditions t_s (in μs) for different gases: Xenon (dashed line), Argon (solid line), Nitrogen (dash-dot line), Helium (dash-dot-dot line) is plotted as a function of the pressure (in $mbar$).

In order to have an idea about the real physical time to reach the steady state for the averaged heat flux this time is calculated for the following data. The internal and the external cylinders' radii and their temperatures are equal to $50\mu m$ and $2.5mm$, and $110°C$ and $20°C$, respectively. The time to reach the steady state value for four gases (Helium, Argon, Nitrogen and Xenon) is plotted on Fig. 3.3 as a function of pressure. The minimum value of this time t'_s varies from $6.2\mu s$ for Helium to $36\mu s$ for Xenon. The time t'_s characterizes the response time of the system, when the external condition (temperature in our case) changes. It is to note that the time to reach the steady state t_s is obtained from the numerical simulations in dimensionless form, therefore in order to obtain the real time in seconds this time is multiplied

by the characteristic time t_0 (Eq. (2.27)): $t'_s = t_s t_0$, which is inversely proportional to the most probable molecular velocity (and through it to the molecular mass).

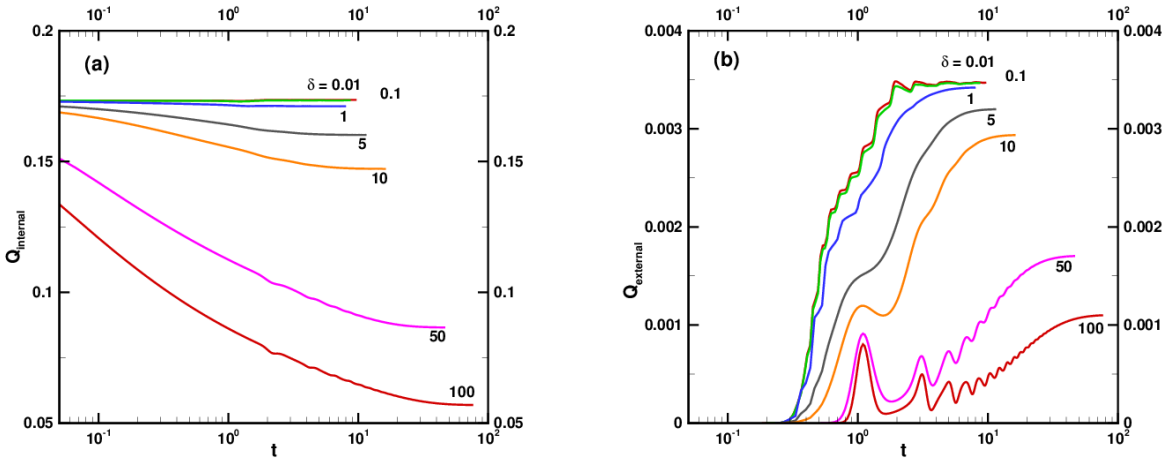

Figure 3.4: The time evolution of the dimensionless heat flux on the internal (a) and external (b) cylinders. The rarefaction parameter δ_0 varies from 0.01 to 100, $\mathcal{T} = 1.3$.

The time evolutions of the heat flux on internal and external cylinders are shown in Fig. 3.4a) and Fig. 3.4b), correspondingly. It is to note that the heat flux on the internal cylinder decreases monotonically in time for all considered values of the rarefaction parameter, contrarily to the external cylinder, where the heat flux reaches its steady state after several oscillations, see Fig. 3.4b).

In the slip flow regime the unsteady energy equation (3.1) subjected to the jump boundary conditions (2.12) is solved. The temperature jump coefficients ξ_H and ξ_C on the internal and external cylinders, respectively, are equal to 1.95 [137, 143]. As it was pointed out in Section 2.2.1, in order to obtain the temperature profile from eq. (3.1), the pressure between the cylinders is supposed to be constant. The results of the averaged heat flux evolution in time $Q_a(t)$ are plotted on Fig. 3.5 together with the corresponding results obtained from the solution of the S-model kinetic equation for three values of the rarefaction parameter $\delta_0 = 10$, 50 and 100. As can be seen in Figure 3.5a) the qualitative behavior of the averaged heat flux evolution, given by both approaches, is very similar: the averaged heat flux increases monotonically to reach its steady state value. However the absolute values of the averaged heat flux are different. If we scale the solution of eq. (3.1) to the steady state solution of the kinetic equation we can observe on Fig. 3.5b) that the time to reach the steady state value t_s, given by two approaches, is practically the same (for example, $t_s = 29.5$, for $\delta_0 = 50$, see Table 3.1). Therefore this continuum approach may be successfully used for the estimation of the time t_s in the slip flow regime.

The comparison of the steady state distribution of the temperature obtained by the

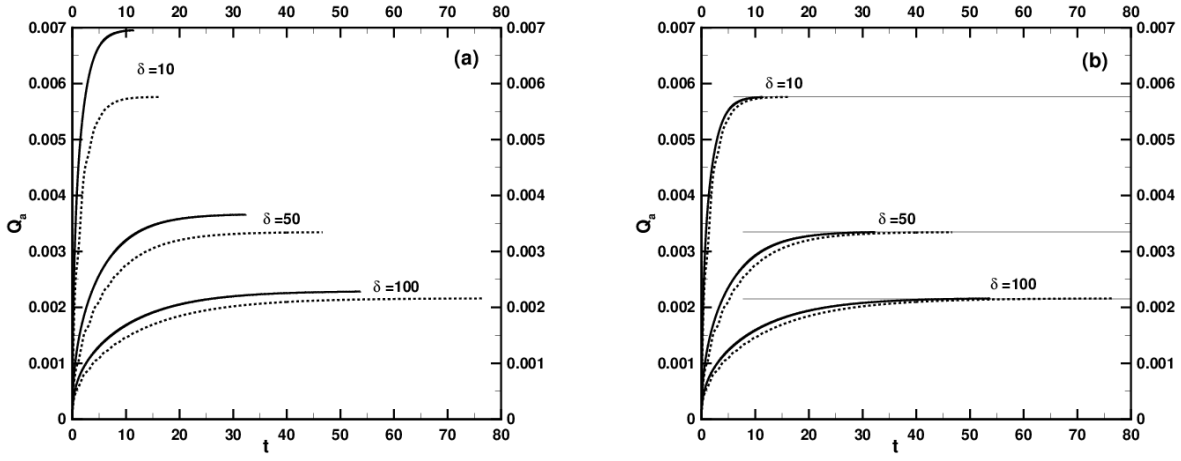

Figure 3.5: Averaged dimensionless heat flux as a function of time for $\delta_0 = 10$, 50, 100 and $\mathcal{T} = 1.3$; the solution of Eq. (3.1) with the jump boundary conditions (2.12) (solid line), the solution of the S-model kinetic equation (dotted line). (b) The steady state solution of the kinetic equation is plotted as the solid horizontal line; the solution of Eq. (3.1) is scaled to the steady state value obtained from the S-model kinetic equation.

continuum and kinetic approaches together with the analytical solution (2.13) is presented in Fig. 3.6 for $T_H/T_C = 1.3$ and the rarefaction parameter equal to $\delta_0 = 5$ (a) and $\delta_0 = 50$ (b). It is clear that for $\delta_0 = 50$ the three results are in very good agreement. However, when delta decreases ($\delta_0 = 5$) the kinetic solution starts to be different from the continuum solutions, especially in the Knudsen layer. If the steady state pressure distribution between the cylinders is analyzed (Fig. 3.7) it is clear that for $\delta_0 = 5$ the assumption of the constant pressure between the cylinders is not valid anymore. Therefore, the analytical temperature distribution between the cylinders (2.13) can be used in the slip flow regime to predict the temperature distribution until the values of $\delta_0 \geq 50$ with an error smaller than 3% near the wall of the internal cylinder. However, when the temperature ratio between the cylinders increases up to $\mathcal{T} = 2$ the difference between the continuum solution and the solution of the S-model kinetic equation increases and the error of the gas temperature prediction on the internal cylinder's wall increases up to 10% for $\delta_0 = 50$ and up to 24% for $\delta_0 = 5$, see Fig. 3.8.

3.4 Conclusions

The transient behavior of the heat flux between two coaxial cylinders due to the sudden change of the internal cylinder temperature is studied on the basis of the S-model kinetic equation. The simulations have been carried out from the near free molecular to the hydrodynamic flow regimes for one cylinders radius ratio and two cylinders' walls temperature ratios. It is found

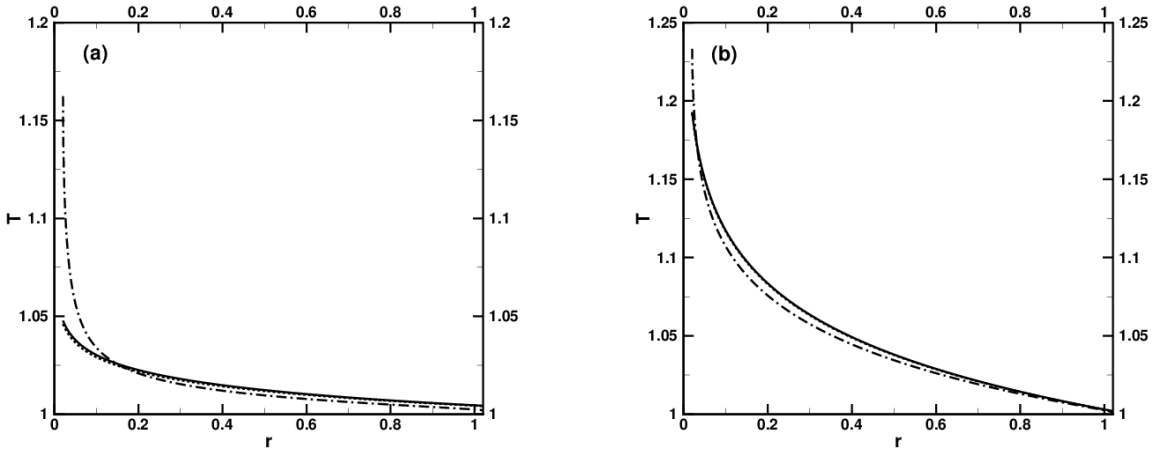

Figure 3.6: The steady state dimensionless temperature distribution between two cylinders, $\mathcal{T} = 1.3$. The solution of the S-model kinetic equation (dash-dotted line), the solution of Eq. (3.1) (dashed line), the analytical expression (2.13) (solid line). All the curves are plotted for $\delta_0 = 5$ (a) and for $\delta_0 = 50$ (b).

that for the smallest temperature ratio $\mathcal{T} = 1.3$ the time to reach the steady state value for the averaged heat flux varies approximately from 2.5 to 44 of the characteristic times between the near free molecular and the hydrodynamic flow regimes and it has a minimum in the beginning of the transitional flow regime. Comparing the monoatomic gases behavior in a real geometry it is obtained that at the same working pressure the time needed for Xenon to reach its steady state is 6 times longer than that for Helium. When the temperature ratio increases up to $\mathcal{T} = 2$ the steady state time decreases approximately by 5%. In the slip flow regime the time t_s can also be found from the solution of the energy equation subjected to the temperature jump boundary conditions.

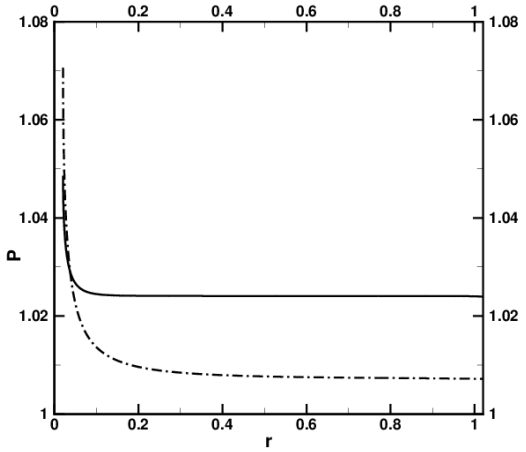

Figure 3.7: The steady state dimensionless pressure distribution between two cylinders, $\mathcal{T} = 1.3$, $\delta_0 = 5$ (dash-dotted line) and $\delta_0 = 50$ (solid line).

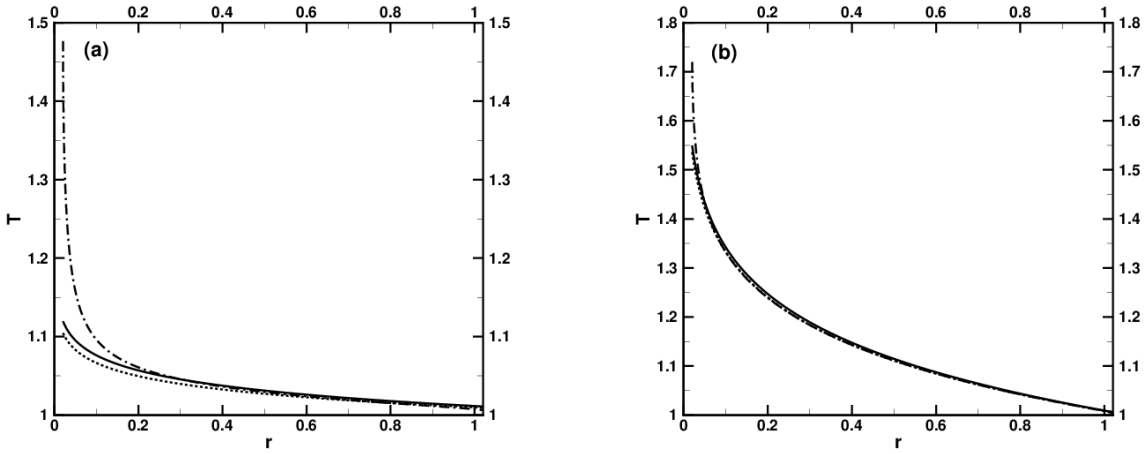

Figure 3.8: The steady state dimensionless temperature distribution between two cylinders, $\mathcal{T} = 2.$. The solution of the S-model kinetic equation (dash-dotted line), the solution of Eq. (3.1) (dashed line), the analytical expression (2.13}) (solid line). All the curves are plotted for $\delta_0 = 5$ (a) and for $\delta_0 = 50$ (b).

Chapter 4

Unsteady gas flow through a thin orifice

The nonequilibrium flows of gases appear in different technological domains like the vacuum equipment, high altitude aerodynamics and in a relatively new field as the microelectromechanical systems (MEMS). The deviation of a gas from its local equilibrium state can be characterized by the Knudsen number, which present the ratio between the molecular mean free path and the characteristic length of the problem. For the relatively large values of the Knudsen number the classical continuum approach fails to describe the gas behavior and the kinetic equations, like the Boltzmann equation or model kinetic equations, must be solved to simulate the gas flows.

The gas flow through a thin orifice is a problem of a large practical interest for the design of the vacuum equipment, space or the microfluidic applications. The under-expanded jets through the orifices are predominately used by particle analyzer systems to separate and isolate molecules, ions of substances for analyzing their physical and chemical properties. The time dependent characteristics of these jets are important for the investigation of the response time of the vacuum gauges developed for the measurements of the rapid pressure changes [39].

The steady state flows through the orifice, slit and short tube have been successfully studied applying the DSMC method and the kinetic equations [40, 41, 42, 43, 44, 45, 46, 47]. However, only a few results on the transient rarefied flows through an orifice [48], a short tube [38], a long tube [49] or a slit [50] may be found in open literature. The flow conditions in [48] are limited to high and moderate Mach number owing to significant statical noise of DSMC method at low Mach number. The authors of [39] also studied experimentally and numerically the transient gas flow, but between two tanks of the fixed volumes. The rapid high amplitude pressure changings in time are examined and their characteristic time was found to be of the order of few seconds.

The aim of this work is to analyze the transient properties of gas flow through an

orifice induced by various values of the pressure ratio over a broad range of gas rarefaction. The unsteady nonlinear S-model kinetic equation is solved numerically by Discrete Velocity Method (DVM) to obtain the mass flow rate and macroscopic parameters as a function of time. The time to reach the steady state conditions for the mass flow rate is also estimated. An empirical expression for evaluation of time-dependent mass flow rate is proposed.

4.1 Problem formulation

Consider an orifice of radius R_0 contained in an infinitesimally thin wall, which isolates two infinite reservoirs. Both the upstream and downstream reservoirs are filled with a monatomic gas but maintained at different pressures p_0 and p_1, respectively, with $p_0 > p_1$. The temperatures of the wall and of the gas in the reservoirs are equal to T_0. At time $t = 0$, the orifice is opened instantly and the gas starts to flow from the upstream reservoir to the downstream one.

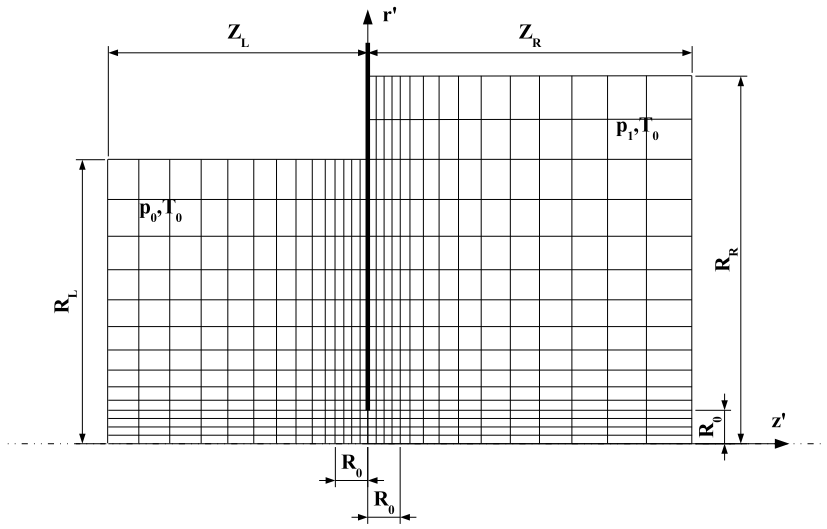

Figure 4.1: Lateral section and computational domain of the flow configuration

Let us introduce a cylindrical coordinate system $\mathbf{r}' = (r', \phi, z')$ for the physical space with the origin positioned at the center of the orifice and the Oz' axis directed along the axis of the reservoirs (see the lateral section shown in Fig. 4.1). We assume that the flow is cylindrically symmetric and does not depend on the angle ϕ and therefore the problem may be considered as two dimensional in the physical space with the position vector $\boldsymbol{s}' = (r', z')$.

The gas-surface interaction has a very small impact on an orifice flow [105]; consequently, this flow is governed by two principal parameters: the pressure ratio p_1/p_0 and gas rarefaction δ_0 determined as

$$\delta_0 = \frac{R_0 p_0}{\mu_0 \upsilon_0}, \qquad \upsilon_0 = \sqrt{\frac{2kT_0}{m}}, \tag{4.1}$$

where μ_0 is the viscosity coefficient at the temperature T_0, υ_0 is the most probable molecular speed at the same temperature; m is the molecular mass of the gas; k is the Boltzmann constant. It is to note that the gas rarefaction parameter is inversely proportional to the Knudsen number; *i.e.*, when δ_0 varies from 0 to ∞, the flow regime changes from the free molecular to the hydrodynamic regime.

It is convenient to define the characteristic time t_0 of the flow as follows

$$t_0 = \frac{R_0}{\upsilon_0}. \tag{4.2}$$

The unsteady S-model kinetic equation [11] is used to simulate the transient rarefied gas flow through the orifice. The conservative formulation of this equation [158], [102] is implemented

$$\frac{\partial}{\partial t'}\left(r' f'\right) + \frac{\partial}{\partial r'}\left(r' f' \upsilon_p \cos\varphi\right) - \frac{\partial}{\partial \varphi}\left(f' \upsilon_p \sin\varphi\right) + \frac{\partial}{\partial z'}\left(r' f' \upsilon_z\right) = r'\nu'\left(f^{S'} - f'\right). \tag{4.3}$$

The main unknown is the molecular velocity distribution function $f'(t', \mathbf{s}', \mathbf{v})$. Here, the physical space is described by the cylindrical coordinate systems (r, ϕ, z). In the other hand, the molecular velocity space are described by the cylindrical coordinate systems $(\upsilon_p, \varphi, \upsilon_z)$. The molecular velocity vector $\mathbf{v}$ has three components projected on the physical coordinate system as $\mathbf{v} = (\upsilon_p \cos\varphi, \upsilon_p \sin\varphi, \upsilon_z)$. The molecular collision frequency ν' is supposed to be independent on the molecular velocity and can be evaluated [11] by Eq. (2.25).

The equilibrium distribution function $f^{S'}$ [11] in Eq. (4.3) is defined in Eq. (2.23). In additional to two coaxial cylinder problem, here the component in $z-direction$ of (vector) macroscopic parameters is included, *i.e*, bulk velocity vector $\mathbf{u}' = (u'_r, 0, u'_z)$, the heat flux vector $\mathbf{q}' = (q'_r, 0, q'_z)$. It is useful to define the dimensionless variables as follows

$$\begin{gathered} t = \frac{t'}{t_0},\ \boldsymbol{s} = \frac{\boldsymbol{s'}}{R_0}, \quad \boldsymbol{c} = \frac{\mathbf{v}}{\upsilon_0},\ \boldsymbol{u} = \frac{\boldsymbol{u'}}{\upsilon_0}, \quad n = \frac{n'}{n_0}, \\ T = \frac{T'}{T_0},\ p = \frac{p'}{p_0}, \quad \boldsymbol{q} = \frac{\boldsymbol{q'}}{p_0 \upsilon_0},\ \mu = \frac{\mu'}{\mu_0},\ f = \frac{f' \upsilon_0^3}{n_0}, \end{gathered} \tag{4.4}$$

with the help of the state equation $p_0 = n_0 k T_0$. In relations (4.4), the dimensionless molecular

velocity vector $\boldsymbol{c}$ is equal to $(c_p \cos\varphi, c_p \sin\varphi, c_z)$.

In this study, the inverse power law potential is employed as the molecular interaction potential; therefore, viscosity can be calculated by power law temperature dependence as

$$\mu = T^{\omega}, \tag{4.5}$$

where ω is the viscosity index, which is equal to 0.5 for Hard Sphere model and 1 for the Maxwell model [107].

Incorporating dimensionless quantities (4.4) into S-model kinetic equation (4.3), the dimensionless conservative form of governing equation is obtained

$$\frac{\partial}{\partial t}(rf) + \frac{\partial}{\partial r}(rfc_p\cos\varphi) - \frac{\partial}{\partial\varphi}(fc_p\sin\varphi) + \frac{\partial}{\partial z}(rfc_z) = r\delta nT^{1-\omega}\left(f^S - f\right). \tag{4.6}$$

The above equation is subjected to the following boundary conditions. The distribution function of outgoing from the axis molecules f^+ is calculated from the distribution function of incoming to the axis molecules f^- taking into account the axisymmetric condition as

$$f^+_{r=0}(t, z, r, \varphi, c_p, c_z) = f^-_{r=0}(t, z, r, \pi - \varphi, c_p, c_z), \tag{4.7}$$

where the superscripts $+$ and $-$ refer to the outgoing and incoming molecules, respectively. It is supposed that the computational domain is large enough for obtaining the equilibrium far-field. Hence, we assume that the molecules entering the computational domain are distributed according to the Maxwellian law with the parameters determined by the zero-flow at the pressure and temperature corresponding to each reservoir as follows

$$\begin{aligned} f^-_{r=R_L}(t, z, r, \varphi, c_p, c_z) = f^-_{z=-Z_L}(t, z, r, \varphi, c_p, c_z) &= \frac{1}{\pi^{3/2}}\exp\left(-c_p^2 - c_z^2\right), \\ f^-_{r=R_R}(t, z, r, \varphi, c_p, c_z) = f^-_{z=Z_R}(t, z, r, \varphi, c_p, c_z) &= \frac{p_1}{\pi^{3/2}}\exp\left(-c_p^2 - c_z^2\right), \end{aligned} \tag{4.8}$$

here R_L, R_R and Z_R, Z_L are the radial and axial dimensions of the left and right reservoirs, respectively.

Since the influence of the gas-wall interaction on the flow is weak (see Ref. [105]) , the fully diffuse scattering is implemented for the molecules reflected from both sides of the wall,

which separates the two reservoirs, *i.e.*

$$f^{+}_{z=0^{\mp},r>1}\left(t,z,r,\varphi,c_p,c_z\right)=\frac{n_w^{\mp}}{\pi^{3/2}}\exp\left(-c_p^2-c_z^2\right), \tag{4.9}$$

where the superscripts $\mp$ refers the left $(-)$ and the right $(+)$ sides of the wall. The unknown values of the number density at the wall surfaces $n_w^{\mp}$ are found from the impermeability conditions

$$n^{\mp}_{w,z=0^{\mp},r>1}\left(t,z,r\right)=\pm 4\sqrt{\pi}\int\limits_0^{\infty}\int\limits_0^{\pi}\int\limits_0^{\infty}c_z f^{\mp}_{z=0^{\mp}}\left(t,z,r,\varphi,c_p,c_z\right)d\mathbf{c}, \tag{4.10}$$

where $d\mathbf{c}=c_p dc_p d\varphi dc_z$.

The dimensionless macroscopic flow parameters are defined through the distribution function as follows

$$\begin{aligned}
n\left(t,z,r\right)&=2\int\limits_{-\infty}^{\infty}\int\limits_0^{\pi}\int\limits_0^{\infty}f d\mathbf{c}, & T\left(t,z,r\right)&=\frac{4}{3n}\int\limits_{-\infty}^{\infty}\int\limits_0^{\pi}\int\limits_0^{\infty}C f d\mathbf{c},\\
u_r\left(t,z,r\right)&=\frac{2}{n}\int\limits_{-\infty}^{\infty}\int\limits_0^{\pi}\int\limits_0^{\infty}c_p\cos\varphi f d\mathbf{c}, & u_z\left(t,z,r\right)&=\frac{2}{n}\int\limits_{-\infty}^{\infty}\int\limits_0^{\pi}\int\limits_0^{\infty}c_z f d\mathbf{c},\\
q_r\left(t,z,r\right)&=2\int\limits_{-\infty}^{\infty}\int\limits_0^{\pi}\int\limits_0^{\infty}c_p\cos\varphi C f d\mathbf{c}, & q_z\left(t,z,r\right)&=2\int\limits_{-\infty}^{\infty}\int\limits_0^{\pi}\int\limits_0^{\infty}c_z C f d\mathbf{c},
\end{aligned} \tag{4.11}$$

where $C=\left(c_p\cos\varphi-u_r\right)^2+\left(c_p\sin\varphi\right)^2+\left(c_z-u_z\right)^2$.

The mass flow rate is practically the most significant quantity of an orifice flow and can be calculated as

$$\dot{M}\left(t'\right)=2\pi m\int\limits_0^{R_0}n'\left(t',0,r'\right)u_z'\left(t',0,r'\right)r'dr'. \tag{4.12}$$

The steady state mass flow rate into vacuum $p_1/p_0=0$ under the free molecular flow conditions $(\delta_0=0)$ was obtained analytically in Refs. [160, 161, 107] as

$$\dot{M}_{fm}=\frac{R_0^2\sqrt{\pi}}{\upsilon_0}p_0, \tag{4.13}$$

and this quantity is used as reference value for the reduced mass flow rate

$$W\left(t'\right)=\frac{\dot{M}\left(t'\right)}{\dot{M}_{fm}}. \tag{4.14}$$

The dimensionless mass flow rate is obtained by substituting Eqs. (4.4,4.12,4.16) into Eq. (4.14)

$$W\left(t\right)=4\sqrt{\pi}\int_{0}^{1}n\left(t,0,r\right)u_{z}\left(t,0,r\right)rdr. \tag{4.15}$$

Initially the upstream and downstream reservoirs, separated by a diaphragm, are maintained at the pressures p_0 and p_1, respectively, and at the same temperature T_0. At time $t = 0$, just after the diaphragm opening, the mass flow rate is equal to $W = 1 - p_1/p_0$.

In the next sections we present the numerical approach for the solution of the kinetic equation (4.6).

4.2 Method of solution

Firstly, the discrete velocity method (DVM) is used to separate the continuum molecular magnitude velocity spaces $c_p = (0, \infty)$, $c_z = (-\infty, \infty)$ in the kinetic equation (4.6) into discrete velocity sets c_{p_m}, c_{z_n}, which are taken to be the roots of Hermite polynomial. The polar angle velocity space $\varphi = [0, \pi]$ is equally discretized into set of φ_l. Next, the set of independent kinetic equations corresponding to discrete velocity sets c_{p_m}, c_{z_n} is discretized in time and space by Finite difference method (FDM).

For each reservoir its radial and axial dimensions are taken here to be equal ($R_L = Z_L$ and $R_R = Z_R$), and equal to D_L and D_R, respectively. The influence of the dimensions D_L and D_R on the macroscopic parameters distribution is discussed in Section 4.3.6. In the physical space, the uniform grid ($2N_O * N_O$) with square cells is constructed near the orifice ($z = (-1, 1)$,$r = (0, 1)$), where N_O is the number of the grid points through the orifice. At the remaining computational domain ($z = (-Z_L, -1) \cup (1, Z_R)$,$r = (1, R_{L/R})$), the non-uniform discretization using increasing power-law of 1.05 is implemented for both radial and axial directions, as it is illustrated in Fig. 4.1.

The spacial derivatives are approximated by one of two upwind schemes: the first-order accurate scheme or second-order accurate TVD type scheme. The time derivative is

approximated by the time-explicit Euler method. The combination of a second-order spatial discretization with forward Euler time-marching is unstable, according to a linear stability analysis [156]. However the presence of the non-linear limiter keeps it stable [156, 162]. The details of the implemented approximations are discussed in Section 4.3.1.

As an example the second-order accurate TVD upwind scheme with the time-explicit Euler approximation is given for the case of $\cos\varphi_l > 0$, $\sin\varphi_l > 0$ and $c_{z_n} > 0$, when the kinetic equation (4.6) is replaced by the set of independent discretized equations

$$\begin{aligned}
&\frac{r_j f^{k+1}_{i,j,l,m,n} - r_j f^{k}_{i,j,l,m,n}}{\Delta t^k} + c_{p_m}\cos\varphi_l \frac{F^k_{i,j+1/2,l,m,n} - F^k_{i,j-1/2,l,m,n}}{0.5\,(r_{j+1} - r_{j-1})} \\
&- c_{p_m}\frac{f^k_{i,j,l+1,m,n}\sin\varphi_{l+1/2} - f^k_{i,j,l,m,n}\sin\varphi_{l-1/2}}{2\sin(\Delta\varphi_l/2)} + c_{z_n}\frac{F^k_{i+1/2,j,l,m,n} - F^k_{i-1/2,j,l,m,n}}{0.5\,(z_{i+1} - z_{i-1})} \\
&= r_j \delta n^k_{i,j}\left(T^k_{i,j}\right)^{1-\omega}\left(\left(f^S_{i,j,l,m,n}\right)^k - f^k_{i,j,l,m,n}\right),
\end{aligned} \tag{4.16}$$

where $f^k_{i,j,l,m,n} = f\left(t^k, z_i, r_j, \varphi_l, c_{p_m}, c_{z_n}\right)$, $\Delta t^k = t^{k+1} - t^k$, $\Delta z_i = z_i - z_{i-1}$, $\Delta r_j = r_j - r_{j-1}$, $\Delta\varphi_l = \varphi_l - \varphi_{l-1}$. In Eq. (4.16), the approximation of derivative of axisymmetric transport term (with respect to φ) is implemented with trigonometric correction [163], which helps to reduce considerably the total number of grid points N_φ in the polar angle velocity space φ.

The second-order edge fluxes in the point of physical space i, j are computed as

$$F^k_{i\pm1/2,j,l,m,n} = f^k_{i\pm1/2,j,l,m,n} r_j, \quad F^k_{i,j\pm1/2,l,m,n} = f^k_{i,j\pm1/2,l,m,n} r_{j\pm1/2}, \tag{4.17}$$

$$\begin{aligned}
f^k_{i+1/2,j,l,m,n} &= \begin{cases} f^k_{i,j,l,m,n} + 0.5\Delta z_{i+1}\mathrm{minmod}(D_{i+1/2,j,l,m,n}, D_{i-1/2,j,l,m,n}) & \text{if } c_{z_n} \geq 0, \\ f^k_{i+1,j,l,m,n} - 0.5\Delta z_{i+1}\mathrm{minmod}(D_{i+3/2,j,l,m,n}, D_{i+1/2,j,l,m,n}) & \text{if } c_{z_n} < 0, \end{cases} \\
f^k_{i,j+1/2,l,m,n} &= \begin{cases} f^k_{i,j,l,m,n} + 0.5\Delta r_{j+1}\mathrm{minmod}(D_{i,j+1/2,l,m,n}, D_{i,j-1/2,l,m,n}) & \text{if } \cos\varphi_l \geq 0, \\ f^k_{i,j+1,l,m,n} - 0.5\Delta r_{j+1}\mathrm{minmod}(D_{i,j+3/2,l,m,n}, D_{i,j+1/2,l,m,n}) & \text{if } \cos\varphi_l < 0. \end{cases}
\end{aligned} \tag{4.18}$$

where $r_{j+1/2} = 0.5\,(r_j + r_{j+1})$ and

$$D_{i+1/2,j,l,m,n} = \frac{f^k_{i+1,j,l,m,n} - f^k_{i,j,l,m,n}}{\Delta z_{i+1}}, \quad D_{i,j+1/2,l,m,n} = \frac{f^k_{i,j+1,l,m,n} - f^k_{i,j,l,m,n}}{\Delta r_{j+1}}. \tag{4.19}$$

Table 4.1: Numerical grid parameters

Phase space	Reservoir	Total number of grid points
Physical space z, r	Left	$N_O = 40$ $N_{zl} \times N_{rl} = 96 \times 96$
	Right	$N_{zr} \times N_{rr} = 101 \times 101$
Molecular velocity space φ, c_p, c_z	Left & Right	$N_\varphi \times N_{cp} \times N_{cz} = 40 \times 16 \times 16$

The slope limiter *minmod* introduced in [155, 156] is given by

$$\text{minmod}(a, b) = 0.5(\text{sign}(a) + \text{sign}(b)) \min(|a|, |b|). \tag{4.20}$$

The details of computational grid parameters are given in Table 4.1.

Concerning the temporal discretization, the time step should satisfy the classical Courant-Friedrichs-Lewy (CFL) condition [164] and must also be smaller than the mean collision time, or relaxation time, which is inverse of the collision frequency ν. Consequently, the time step must satisfy the following criterion

$$\Delta t \leq CFL / \max_{i,j,l,m,n} \left(\frac{c_{p_m}}{\Delta r_j} + \frac{c_{p_m}}{r_1 \Delta \varphi_l} + \frac{c_{z_n}}{\Delta z_i}, \nu_{i,j} \right). \tag{4.21}$$

As the mass flow rate is the most important characteristic of the flow through an orifice the convergence criterion is defined for this quantity as follows

$$\frac{\left| W\left(t^{k+1}\right) - W\left(t^k\right) \right|}{W\left(t^k\right) \Delta t^k} \leq \varepsilon, \tag{4.22}$$

where ε is a positive number and it is taken equal to 10^{-6}. It is to note that this convergence criterion differs from that used in Ref. [50], where the transient flow through a slit is simulated. Here we introduce the time step in the expression of the convergence criterion. It allows us to have the same convergence criterion when the size of the numerical grid in the physical space and consequently the time step according to the CFL condition (4.21) change. The expression of the convergence criterion (4.22) may be considered as the criterion on the velocity of the mass flow rate changes. The time moment, when the criterion (4.22) is achieved, is notified as t_ε and the corresponding mass flow rate as $W = W(t_\varepsilon)$. It is to underline that the mass flow rate was chosen here as the convergence parameter, as it is the most important and useful characteristic of the flow. However the calculation were conducted in the most cases, except $p_1/p_0 = 0.9$ and $\delta = 10$, until time equal to 40, when the criterion (4.22) was already satisfied, in order to observe the steady state flow establishment in the flow field far from the orifice. The comments on the whole steady state flow field establishment are given in Section 4.3.3.

The numerical method is implemented as follows. First, the distribution function $f_{i,j,l,m,n}^{k+1}$ in the internal grid points at the new time step $k+1$ is calculated explicitly by Eq. (4.16) from the data of the current time step k. At the boundaries, the distribution function is calculated using the boundary conditions (4.7-4.9). Once the distribution function is known, the values of the macroscopic parameters for the new time step are obtained by evaluating the integrals in Eqs. (4.11). To do that, the Gauss-Hermite quadrature formulas are applied to calculate the integrals over c_p, c_z spaces, while the trapezoidal rule is used for the approximation of the integrals over φ space. After that, the mass flow rate for the new time step is evaluated by applying the trapezoidal rule for the integral in Eq. (4.15). The macroscopic parameters and the mass flow rate are recorded as a function of time. This procedure is iterated until the convergence criterion (4.22) is met; *i.e.*, steady flow conditions for the mass flow rate are reached.

It is to be noticed that the problem is six-dimensional in the phase space: two variables in the physical space, three variables in the molecular velocity space and the time. In order to obtain the reasonable computational time the numerical code in parallelized by using the OpenMP technology. From the resolution of system (4.16) the velocity distribution function f can be calculated at the new time level separately for each value of the molecular velocity, so these calculations are distributed among the separated processors units. The final results on the macroscopic parameters are obtained by the summation of the corresponding quantities over all processors.

The parallelization gives the opportunity to run the program code on multi-core processor. To have an estimation about computational effort and speedup, the wall-clock times for executing the numerical code are recorded. The second-oder accurate TVD scheme requires 434 seconds for the first 100 time steps with 8 cores of processors AMD 8435 $2600MHz$ and $4Gb$ of memory for each core, whereas the first-order accurate scheme takes 242 seconds for the same task. These wall-clock times are 2585 and 1518 seconds for second-oder accurate TVD scheme and first-order accurate scheme, respectively, when only 1 core is used.

4.3 Results and discussion

The numerical simulations are conducted for four values of the pressure ratio $p_1/p_0 = 0, 0.1, 0.5, 0.9$ which correspond to flow into vacuum, flow of strong, medium and weak non-equilibrium. For each value of pressure ratio p_1/p_0 the calculations are carried out with four values of rarefaction parameter $\delta_0 = 0.1, 1, 10, 100$; *i.e.*, from the near free molecular to hydrodynamic flow regimes.

Table 4.2: Dimensionless flow rate W (4.15) vs rarefaction parameter δ_0 and pressure ratio p_1/p_0. Present results $W = W(t_\varepsilon)$, the results from Ref. [43] (W^a), where the steady BGK-model kinetic equation was solved using the fixed point method, the results obtained in Ref. [105] (W^b) by the DSMC technique.

δ_0	$p_1/p_0 = 0.$			0.1		0.5			0.9		
	W	W^a	W^b	W	W^b	W	W^a	W^b	W	W^a	W^b
0.1	1.020	1.020	1.014	0.919	0.910	0.515	0.515	0.509	0.1039	0.105	0.1025
1.	1.150	1.152	1.129	1.054	1.032	0.636	0.635	0.613	0.1356	0.140	0.1297
10.	1.453	1.472	1.462	1.427	1.435	1.188	1.216	1.188	0.4009	0.432	0.4015
100.	1.527	1.508	1.534	1.519	1.524	1.339	1.325	1.344	0.6725	0.669	0.6741

4.3.1 Different approximations of the spatial derivatives

Two numerical schemes are implemented for the approximation of the spatial derivatives: the first-order accurate scheme and the TVD scheme with *minmod* slope limiter. The CFL number for both schemes was equal to 0.95. The computational time per time step by using the same computational grid is in 70% longer for TVD scheme than for the first-order accurate scheme. However, in order to reach the same uncertainty of the mass flow rate the four times larger number of grid points in each dimension of physical space is needed for the first-order accurate scheme, $N_O = 160$, instead of 40 for the TVD scheme. Therefore all simulations are carried out by using the TVD scheme.

After the various numerical tests the optimal dimensions of the numerical grid are found (shown in Table 4.1), which guarantee the numerical uncertainty for the mass flow rate of the order of 1%. The time step, determined by Eq. (4.21), depends crucially on the classical CFL condition subjected to the additional restriction for the time step to be smaller than the mean collision time. However, for the chosen numerical grid in the physical space, see Table 4.1, the latter restriction is satisfied automatically. Therefore a unique time step $\Delta t = 0.1543 \times 10^{-4}$ is used for all the presented here cases.

4.3.2 Mass flow rate

The steady-state values of the mass flow rate $W = W(t_\varepsilon)$ are presented in Table 4.2. These values are in good agreement with the results of Refs. [43, 105] obtained from the solution of the stationary BGK-model kinetic equation by the fixed point method [43] and by applying the DSMC approach [105]. The discrepancy is less than 5% for all considered cases.

The values of mass flow rate $W(t)$ at several time moments, from $t = 0.$ to 40., are given in Table 4.3. The column (t_ε) corresponds to the time needed to reach the convergence

criterion (4.22).

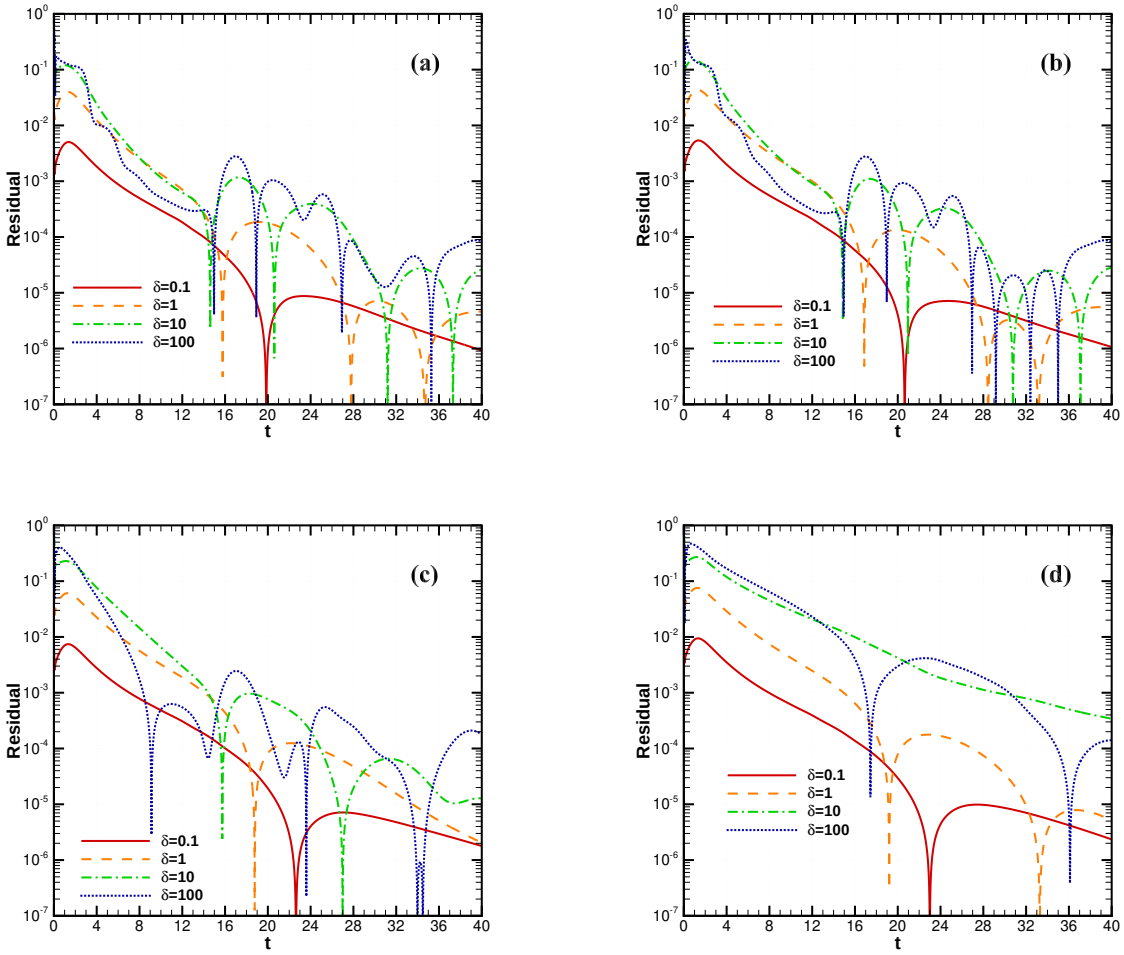

Figure 4.2: The time evolution of residual for $p_1/p_0 = 0$. (a), $p_1/p_0 = 0.1$ (b), $p_1/p_0 = 0.5$ (c), $p_1/p_0 = 0.9$ (d)

To have an estimation of the computational efforts required to achieve the convergence criterion (4.22) the corresponding dimensionless time t_ε and the number of the time steps are presented in Tables 4.3 and 4.4, respectively. The time evolution of the residual, defined according to Eq. (4.22), is shown on Fig. 4.2 for different pressure ratios to illustrate the convergence velocity of the numerical technique. The slowest convergence rate for $p_1/p_0 = 0.$ and 0.1 is corresponding to hydrodynamic regime, whilst that for $p_1/p_0 = 0.5$ and 0.9 is in slip regime. Nevertheless, the fastest convergence rate is observed at transitional regime for all pressure ratios.

The evolution of the mass flow rate $W(t)$ to its steady state value (given in Table 4.3) is also demonstrated in Fig. 4.3 for different pressure ratios. The time interval shown in Fig. 4.3 is restricted to the time equal to 40 even if the flow does not completely establish for this time moment in the case of pressure ratio equal to 0.9. The common behavior is observed for

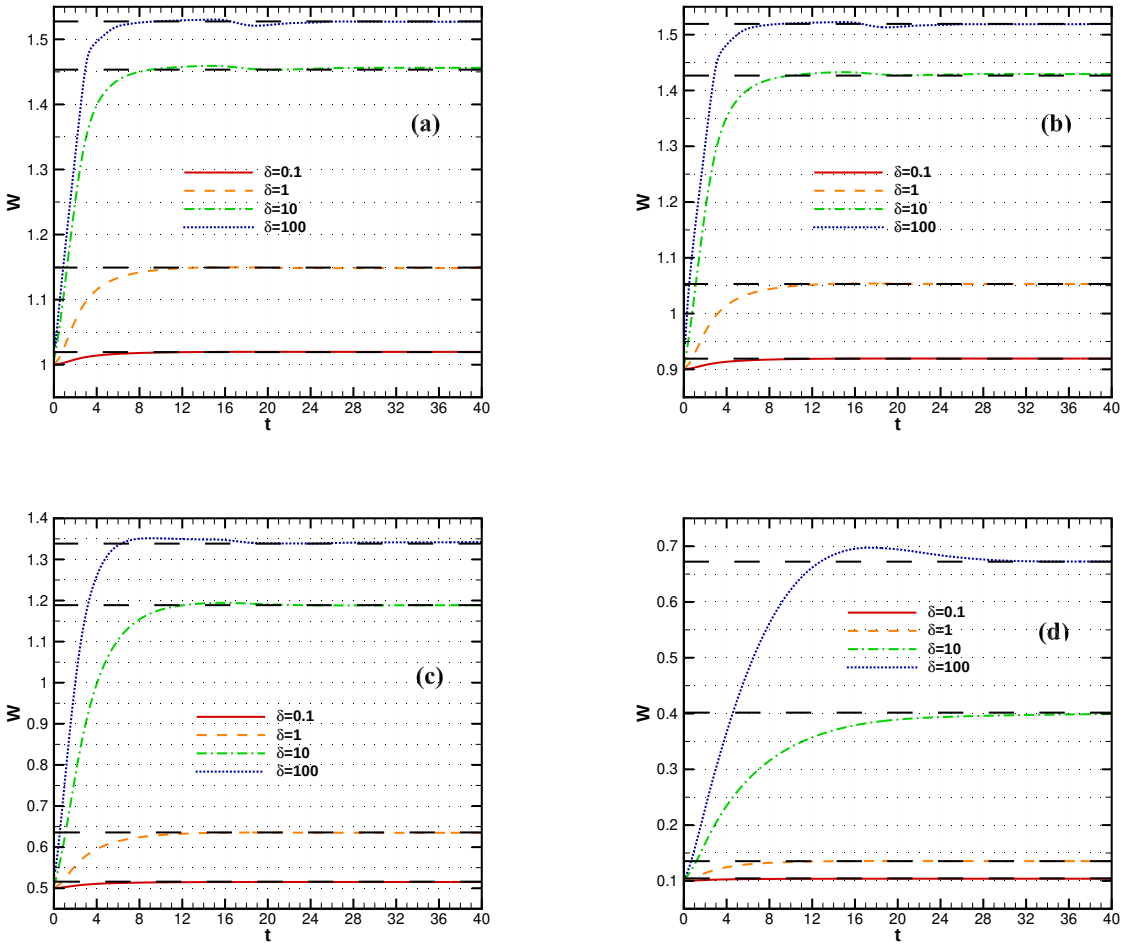

Figure 4.3: The time evolution of mass flow rate W curve and steady state solution (horizontal dashed line) for $p_1/p_0 = 0.$ (a), $p_1/p_0 = 0.1$ (b), $p_1/p_0 = 0.5$ (c), $p_1/p_0 = 0.9$ (d)

the pressure ratios 0. and 0.1 with relatively rapid mass flow rate establishment. It is to note that, in the hydrodynamic regime, the slope of the mass flow rate evolution reduces sharply for both pressure ratios near the time equal to 3 whilst this slope reduction is smooth for other pressure ratios. We can observe anew the longer time of the steady state flow establishment for $p_1/p_0 = 0.9$ in whole range of the rarefaction parameter, see Fig. 4.3d).

In the hydrodynamic flow regime the mass flow rate has a maximum, than it decreases to reach after its steady state value from above. This tendency is visible in the hydrodynamic regime, but the same trend appears in all other regimes, though there it is less apparent because the amplitude of the mass flow rate changes is smaller. The non-monotonic behavior of the residual, see Fig. 4.2, confirms the oscillatory character of the mass flow rate conducting in time. This behavior is related to the propagation of the initial perturbations created by the orifice opening toward the boundary of the computational domain. It is to note that the similar behavior of the mass flow rate was observed also in [48].

To characterize the mass flow rate evolution in time we introduce also the time t_s as the last time moment when the mass flow rate differs by 1% from its steady state value $W(t_\varepsilon)$. The values of t_s for various pressure ratios and the rarefaction parameters are provided in Table 4.3. The two main trends for time t_s, column (t_s) in Table 4.3, are found: for the pressure ratios 0, 0.1 and 0.5 the longest time to reach the steady state is needed under the transitional flow regime ($\delta_0 = 1.$), whilst for the pressure ratio 0.9 this maximum of time t_s appears in the slip flow regime ($\delta_0 = 10.$). For the all considered pressure ratios the minimum of t_s corresponds to the near free molecular flow regime ($\delta_0 = 0.1$). It is to note that the exceptionally long time to steady state flow establishment is found in the case $p_1/p_0 = 0.9$ and $\delta_0 = 10.$.

The time to steady state mass flow rate establishment, t_s, is compared to the corresponding quantity t_s^*, obtained by DSMC method in Ref. [48], see the last column of Table 4.3. The values of t_s^* provided in Ref. [48] are slightly smaller than those obtained in the present simulations. The largest difference between two values in more than 2 times, corresponds to the pressure ratio equal to 0.5 in the near hydrodynamic regime ($\delta_0 = 100$), see Table 4.3. It is noteworthy that due to the statistical scattering of the DSMC technique the estimation of the time to establish the steady flow is more difficult from the DSMC results than by applying the DVM method.

From dimensionless time t_s provided in Table 4.3, one can calculate easily the dimensional time t_s' needed to obtain the steady-state mass flow rate by using Eqs. (4.1,4.2,4.4). For example, He at room temperature $T_0 = 300K$ has the most probable molecular speed $\upsilon_0 = 1116.05m/s$ and viscosity coefficient $\mu_0 = 1.985 \times 10^{-5} Nsm^{-2}$ (provided in [107]) . If one consider an orifice of the radius $R_0 = 0.5mm$ and pressure in the upstream reservoir $p_0 = 44.31Pa$, the gas flow is in transitional regime ($\delta_0 = 1.$). The dimensionless time of the expansion into vacuum (case $p_1/p_0 = 0$ in Table 4.3) is equal to 6.95 and the corresponding dimensional time is $3.11\mu s$.

The mass flow rate as a function of time was fitted using the following model

$$W(t) = W_{t=0} + (W_{t=t_\varepsilon} - W_{t=0})\,(1 - \exp(-t/\tau))\,, \tag{4.23}$$

where the value at the time moment $t = 0$ is calculated as $W_{t=0} = 1 - p_1/p_0$ and $W_{t=t_\varepsilon}$ is the value of the mass flow rate corresponding to the time moment $t = t_\varepsilon$ where the convergence criterion (4.22) is achieved. Both the values are given in Tables 4.2 and 4.3. The fitting parameter (characteristic time) τ for various pressure ratios and rarefaction parameters are provided in Table 4.5 with the corresponding uncertainty. It is to note that very similar values of τ are found for the pressure ratios 0 and 0.1 for all rarefaction range. For the pressure ratios 0.5 and 0.9 and for the high level of gas rarefaction also the similar values of the fitting

Table 4.3: Mass flow rate W for different time moments. The time t_s of the steady state flow establishment as a function of the rarefaction parameter δ_0 and the pressure ratio p_1/p_0; t_s^* corresponds to the data from Ref. [48]. Time t_s is here the dimensionless value, obtained using Eqs. (4.2) and (4.4).

p_1/p_0	δ_0	W						t_ε	t_s	t_s^*
		$t = 0.$	1.	5.	10.	20.	40.			
0.	0.1	1.	1.003	1.016	1.019	1.020	1.020	19.71	2.35	
	1.	1.	1.028	1.126	1.146	1.149	1.148	15.77	6.95	
	10.	1.	1.120	1.423	1.455	1.453	1.456	20.60	6.15	
	100.	1.	1.171	1.511	1.528	1.522	1.527	35.26	5.07	
0.1	0.1	0.9	0.903	0.915	0.918	0.919	0.919	20.48	2.61	
	1.	0.9	0.928	1.027	1.049	1.054	1.053	16.87	7.84	6.4
	10.	0.9	1.035	1.383	1.427	1.427	1.429	20.94	7.05	7.3
	100.	0.9	1.145	1.500	1.520	1.514	1.519	26.94	5.24	4.4
0.5	0.1	0.5	0.503	0.512	0.514	0.515	0.515	22.39	3.64	
	1.	0.5	0.523	0.607	0.629	0.635	0.635	18.76	9.91	8.7
	10.	0.5	0.623	1.060	1.177	1.191	1.189	26.94	9.84	9.1
	100.	0.5	0.756	1.309	1.351	1.339	1.342	23.59	5.54	14.0
0.9	0.1	0.1	0.1007	0.1030	0.1036	0.1039	0.1039	22.82	4.44	
	1.	0.1	0.1059	0.1275	0.1338	0.1356	0.1354	19.20	10.83	
	10.	0.1	0.1292	0.2602	0.3396	0.3893	0.3991	152.6	30.37	
	100.	0.1	0.1571	0.4248	0.6222	0.6943	0.6727	36.10	26.02	

Table 4.4: Number of time steps to satisfy convergence criterion (4.22)

δ_0	Total number of time steps N ($\times 100$)			
	$p_1/p_0 = 0.$	0.1	0.5	0.9
0.1	1277	1327	1451	1479
1.	1022	1093	1216	1244
10.	1335	1357	1746	9889
100.	2285	1746	1529	1339

parameter τ are found. However in the slip and hydrodynamic flow regimes these values become larger, see Table 4.5.

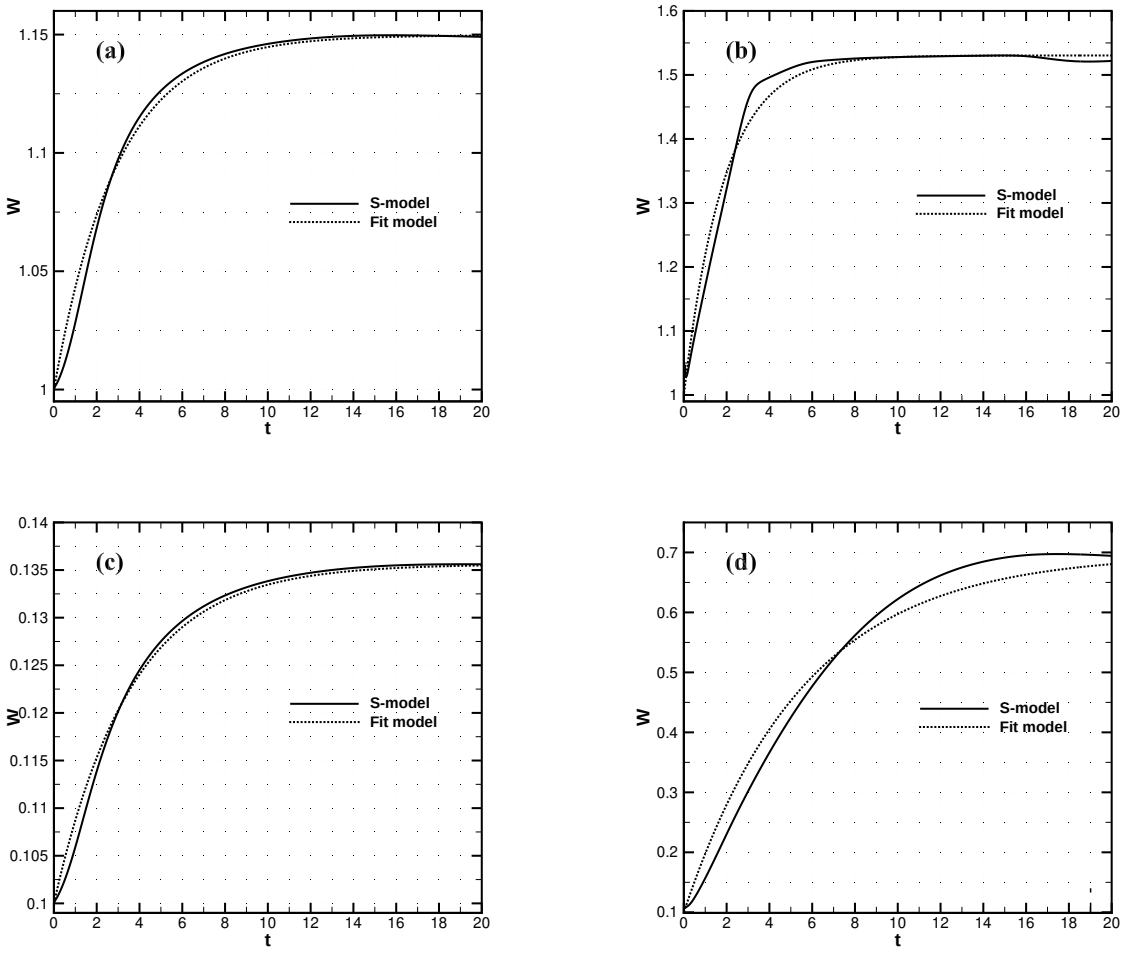

Figure 4.4: The time evolution of mass flow rate W obtained from S-model (solid line) and fit model Eq. (4.23) (dashed line) for $p_1/p_0 = 0., \delta_0 = 1.$ (a), $p_1/p_0 = 0., \delta_0 = 100.$ (b), $p_1/p_0 = 0.9, \delta_0 = 1.$ (c), $p_1/p_0 = 0.9, \delta_0 = 100.$ (d)

Figure 4.4 demonstrates that the exponential representation in form of Eq. (4.23) gives the good estimation for the time evolution of the mass flow rate. The coefficient of determination R^2 of the fitting curve is equal, for example, to 0.990 for the case $p_1/p_0 = 0.9$ and $\delta_0 = 1$ and decreases to 0.973 for $p_1/p_0 = 0.9$ and$\delta_0 = 100$. The maximal difference between the values of the mass flow rate, given by the fitting curve and by the numerical solution of the S-model kinetic equation, is less than 5% for the case $p_1/p_0 = 0.9$ and $\delta_0 = 100$ and it is of the order of 0.3% for the same pressure ratio and $\delta_0 = 1.$.

Table 4.5: Characteristic time τ with 99% confidence interval obtained from fit model Eq. (4.23)

δ_0	Characteristic time τ			
	$p_1/p_0 = 0.$	0.1	0.5	0.9
0.1	3.415±0.029	3.484±0.028	3.546±0.024	3.561±0.023
1.	2.940±0.034	3.112±0.031	3.429±0.028	3.551±0.028
10.	2.286±0.032	2.393±0.030	3.269±0.039	6.459±0.013
100.	1.879±0.032	1.731±0.019	2.072±0.037	5.597±0.083

4.3.3 Flow field

After the diaphragm opening the gas starts to flow toward the downstream reservoir. However, even in the upstream reservoir the flow field becomes perturbed from its initial state. From the near free molecular ($\delta_0 = 0$) to the slip flow regime ($\delta_0 = 10$) for all considered pressure ratios $p_1/p_0 = 0 - 0.9$ the time behavior of the macroscopic parameters are very similar. The two typical examples of the macroscopic parameters variation in time are presented in Fig. 4.5 for the cases $p_1/p_0 = 0.1$ and 0.5 and $\delta_0 = 1$. The number density n smoothly changes from its value in the upstream reservoir to its downstream value. The temperature drops through the orifice due to the flow acceleration and increases up to its initial value far from the orifice in the downstream reservoir. The temperature drop is larger for the smaller values of the pressure ratio: the temperature decreasing just after the orifice is of the order of 25% for $p_1/p_0 = 0.1$ and $\delta_0 = 1$ and it becomes very small (less than 1%) when the pressure ratio increases up to 0.9. The macroscopic flow velocity increases through the orifice and its rise depends also on the pressure ratio: for the smaller value of the pressure ratio the flow acceleration is higher. Far from the orifice in the upstream and downstream reservoirs the flow velocity goes down to zero. It is to note that for the larger pressure ratio $p_1/p_0 = 0.9$ even in the case of the near hydrodynamic flow regimes, $\delta_0 = 100$, the time dependent behaviors of the macroscopic parameters are similar to the previously described.

The results obtained in Ref. [48] by using the DSMC technique are also shown in Fig. 4.5. The provided here DSMC data correspond to the steady state solution. Its is clear that both techniques give very similar results. Only the temperature behaviors for $p_1/p_0 = 0.5$ are slightly different which can be related to the influence of the boundary conditions in the downstream reservoir.

4.3.4 Near hydrodynamic regime

Completely different behavior is observed for the all considered pressure ratios, except the case of $p_1/p_0 = 0.9$, in the near hydrodynamic flow regime ($\delta_0 = 100$). For the pressure ratio

$p_1/p_0 = 0.5$, see Fig. 4.6, the shock wave appears in the right reservoir and it moves toward the downstream boundary.

For the pressure ratio ($p_1/p_0 = 0.1$) the particular flow behavior is observed: the spatial cell structure of axisymmetric mildly under-expanded jet appears, formed by the system of incident and reflected shock and compression waves, see Fig. 4.7. The distribution of the macroscopic flow parameters for this case is shown on Fig. 4.8. In contrast with the previous case, the first cell shock structure does not move and the second shock wave forms after the first one with time. The shock wave position may be determined by the maximum of the number density gradient which is located at $z_M/R_0 = 4.31$. This position can be estimated also from the empirical relation [53]

$$z_M/R_0 = 1.34\sqrt{p_0/p_1}, \tag{4.24}$$

which predicts the Mach disk location at $z_M/R_0 = 4.24$ from the orifice, so very good agreement is found between the numerical result and empirical relation (4.24).

The streamlines for the case $p_1/p_0 = 0.1$ are provided in Fig. 4.9. It can be seen that the flow field is non symmetric and that the streamlines are not parallel to the axis of symmetry.

In the case of the gas expansion into vacuum ($p_1/p_0 = 0$) the shock wave does not appear any more. Expression (4.24) predicts also that the shock wave position tends to infinity ($z_M/R_0 \to \infty$). In this case the flow velocity reach its maximal value, which depends only on the gas temperature in the inlet reservoir. Under the hypothesis of the adiabatic expansion and the energy conservation the following expression for the macroscopic velocity was obtained in Ref. [165]:

$$u_{z_{max}} = \sqrt{\frac{5kT_0}{m}}. \tag{4.25}$$

The numerical value of the maximal macroscopic velocity is equal to 1.588 which is very close to that predicted by Eq. (4.25).

4.3.5 Choked conditions

It is well known that a choked flow is a limiting condition which occurs when the mass flow rate will not increase with a further decrease in the downstream pressure environment while upstream pressure is fixed [166]. Under the conditions $p_1/p_0 < (p_1/p_0)_*$, where $(p_1/p_0)_*$ is the

critical pressure ratio, the further decrease in the downstream pressure reservoir does not lead to the increase of the mass flow rate and the flow becomes "choked". However, for the case of the flow through a thin orifice the flow never becomes "choked". For the first time it was discovered in Ref. [167] in the case of the flow through a thin, square-edged orifice. Finally the physical point at which the choking occurs for adiabatic conditions is that the exit plane velocity is at sonic conditions. But in the case of the thin orifice flow the "sonic surface" has a convex shape and located in the downstream reservoir, see Fig. 4.10, where two cases of the pressure ratio $p_1/p_0 = 0$ and 0.1 are shown. Therefore the flow is not sonic through the orifice and it does not becomes really choked: the mass flow rate continue to increases when pressure ratio decreases, see Table 4.3 and Fig. 4.11, especially for the low values of the rarefaction parameter. The evaluation in time of the temperature and Mach number profiles in the orifice section are shown on Fig. 4.12, where one can see that the flow remains subsonic through the orifice with the maximum velocity near the orifice wall.

4.3.6 Influence of the computational domain dimensions

The study of an influence of the computational domain dimensions on the numerical results is carried out and the optimal dimensions of the left and right reservoirs are found as $D_L = 8$ and $D_R = 10$, respectively.

Fig. 4.13 shows the comparison of the macroscopic profiles evolution in time along the symmetrical axis for $p_1/p_0 = 0.1$ and $\delta_0 = 100$ obtained for two sizes of the downstream reservoir $D_R = 10$ and 20. It is clear from these results that the both solutions coincide until distance $z/R_0 \sim 8$ from the orifice and that the mass flow rate evolution is not affected at all by the dimension of the right computational domain. It is interesting to note that in the case of the flow through a slit much more larger computational domain must be chosen to obtain the numerical solution independent from the size of the computational domain.

4.4 Conclusions

Transient flow of rarefied gas through an orifice is studied on the basis of nonlinear S-model kinetic equation. The simulations are conducted from the free molecular to hydrodynamic regimes for four values of pressure ratio between reservoirs. The mass flow rate evolution in time is analyzed and it is found that the time to reach the steady state mass flow rate depends essentially on the pressure ratio between the reservoirs and on the gas flow regime in the left reservoir. It needs from 2.35 to 30.37 characteristic times to obtain the steady state mass flow rate, the maximal time to reach the steady state is found in the slip regime for the largest

pressure ratio 0.9. The simple fitting formula for the time dependence of the mass flow rate is proposed. It is shown numerically that the flow through the thin orifice never becomes really choked.

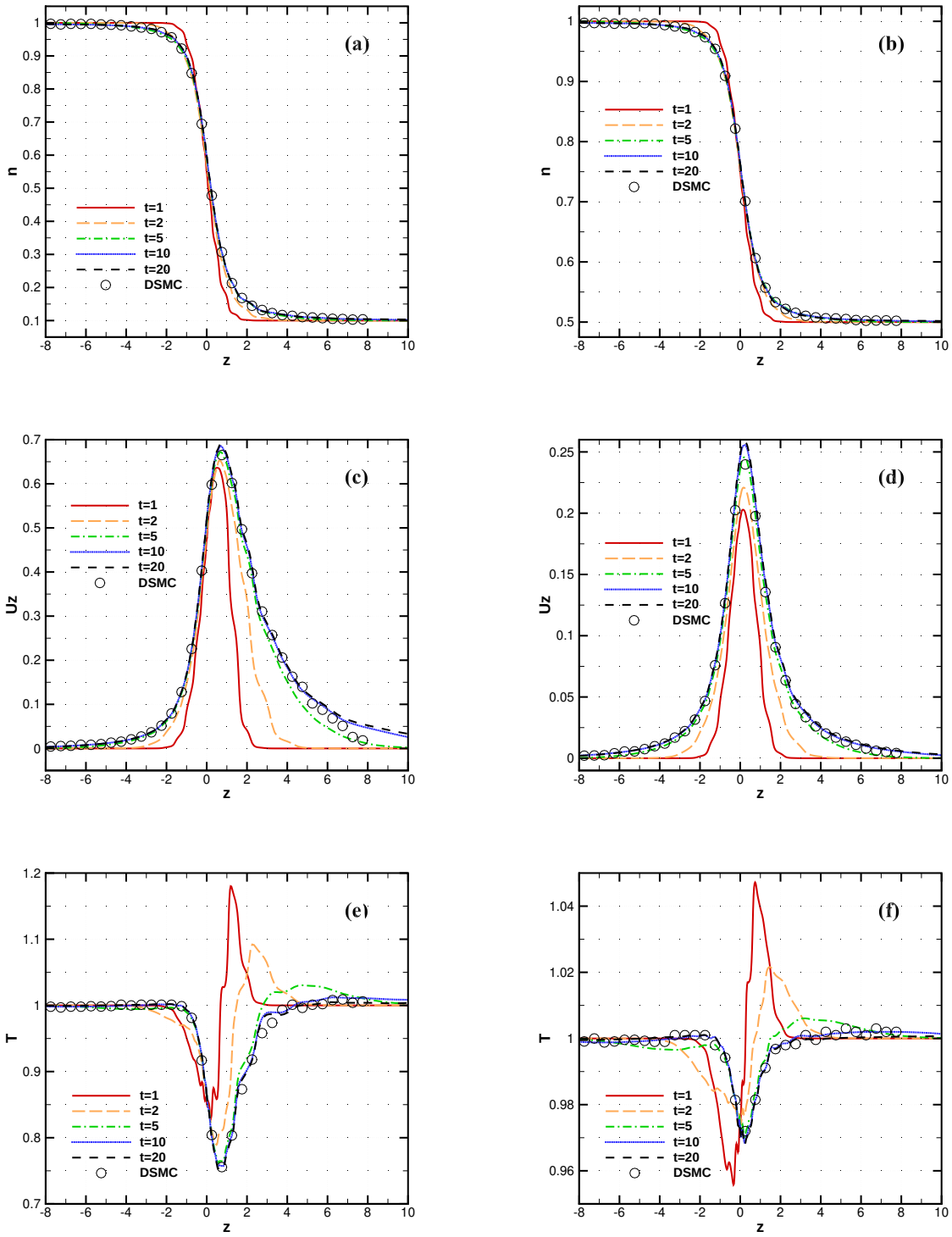

Figure 4.5: Distribution of density number (a,b), axial velocity (c,d), temperature (e,f) along the axis at several time moments for $p_1/p_0 = 0.1, \delta_0 = 1.$ (a,c,e) and $p_1/p_0 = 0.5, \delta_0 = 1.$ (b,d,f). The hollow circles correspond to the results obtained in [48] by DSMC method.

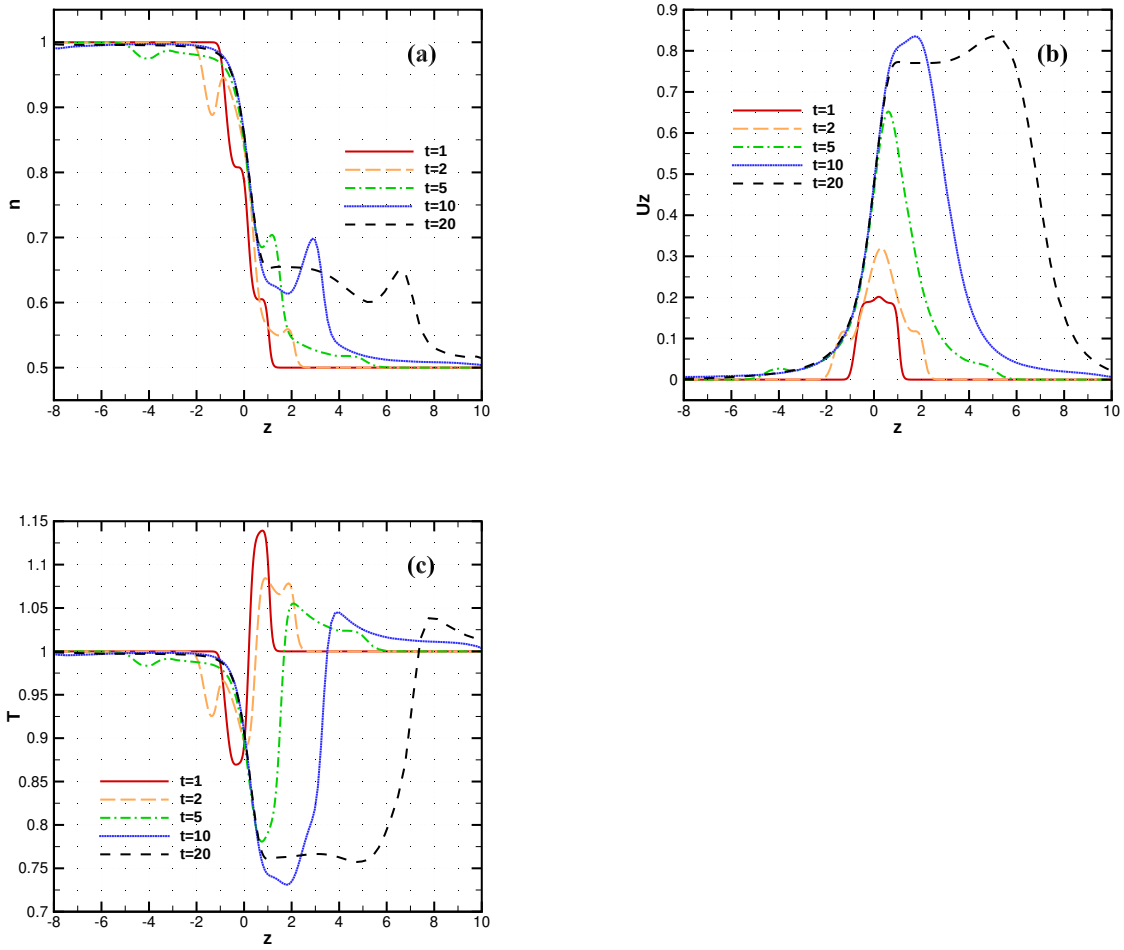

Figure 4.6: Distribution of density number (a), axial velocity (b), temperature (c) along the axis at several time moments for $p_1/p_0 = 0.5, \delta_0 = 100$.

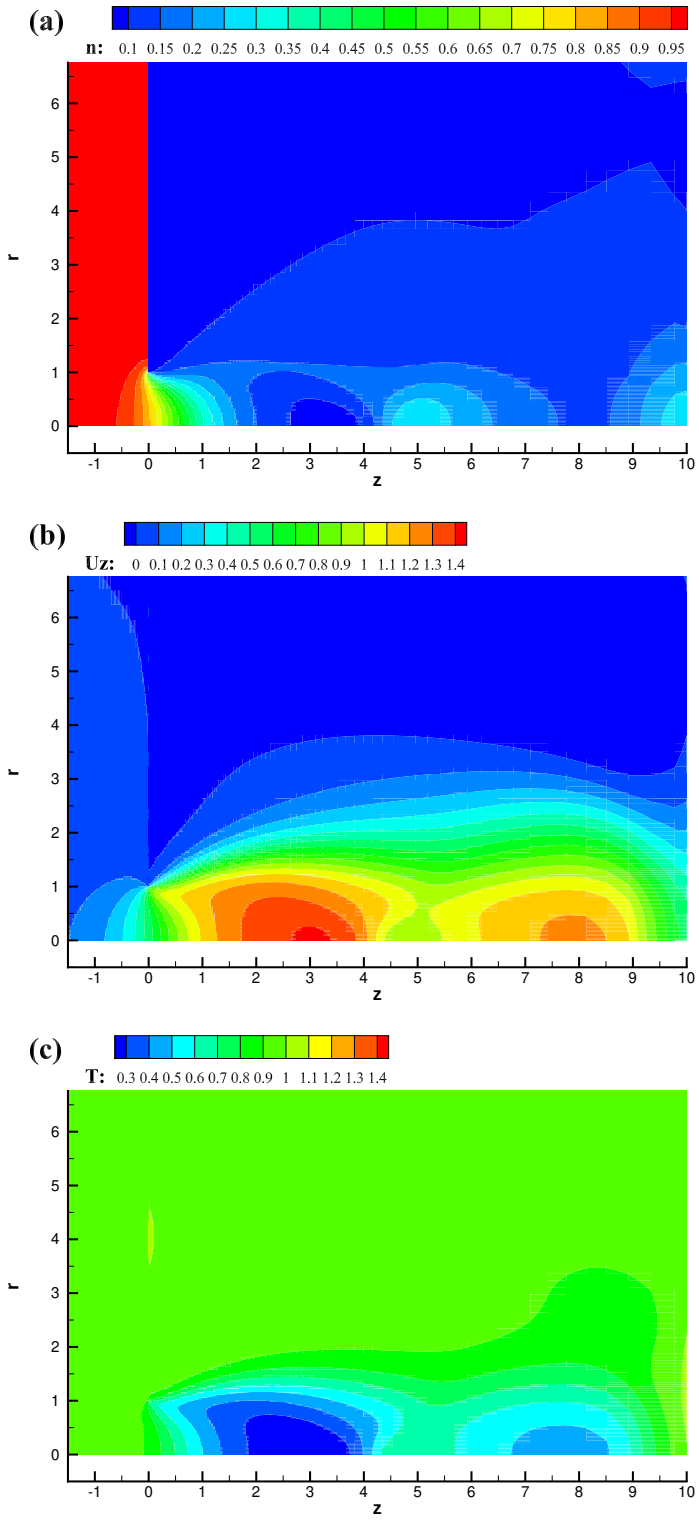

Figure 4.7: Flow field of density number (a), axial velocity (b), temperature (c) at time moment $t = 20$ for $p_1/p_0 = 0.1, \delta_0 = 100$.

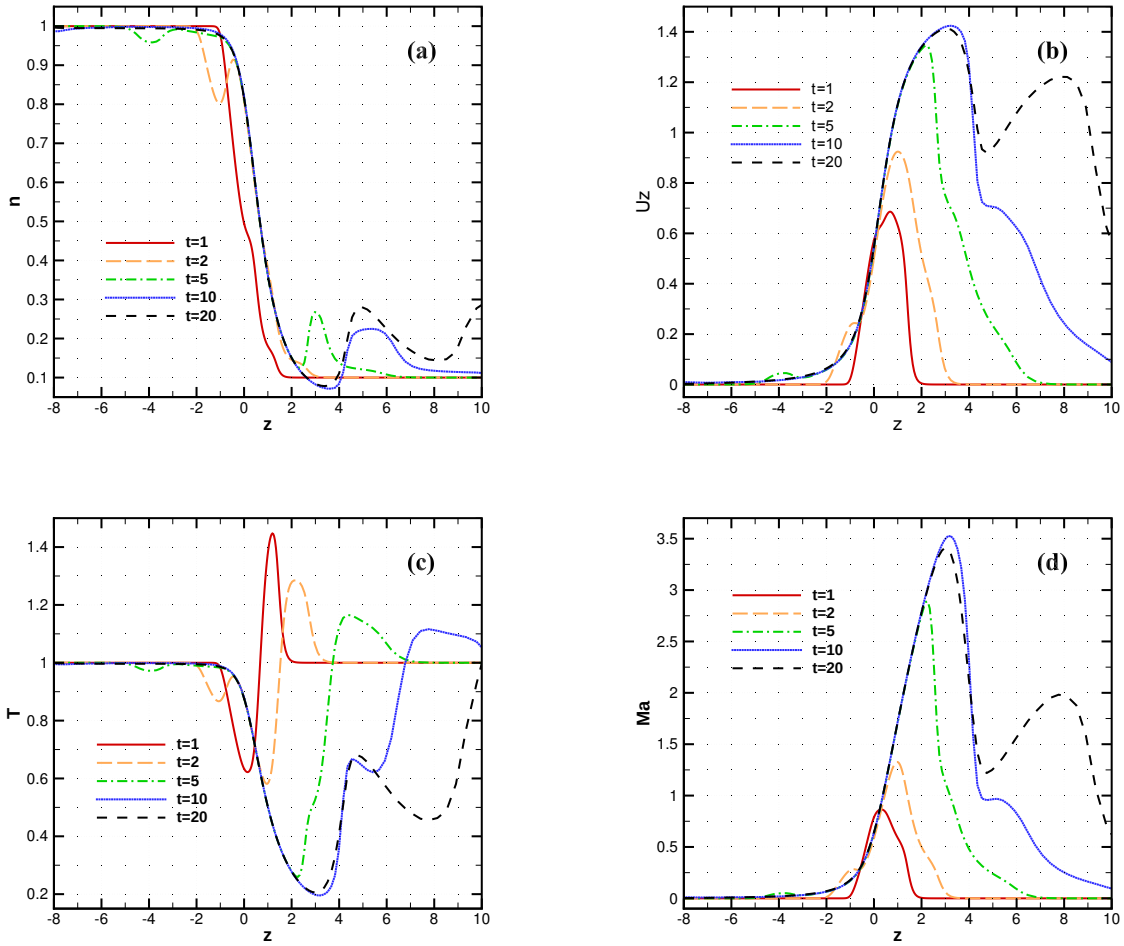

Figure 4.8: Distribution of density number (a), axial velocity (b), temperature (c), Mach number (d) along the axis at several time moments for $p_1/p_0 = 0.1, \delta_0 = 100$.

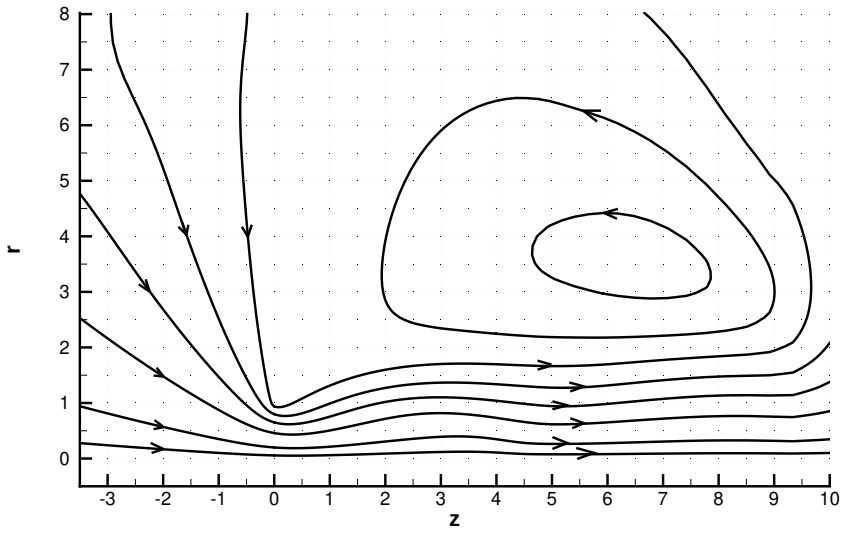

Figure 4.9: Stream lines at time moment $t = 20$ for $p_1/p_0 = 0.1, \delta_0 = 100$.

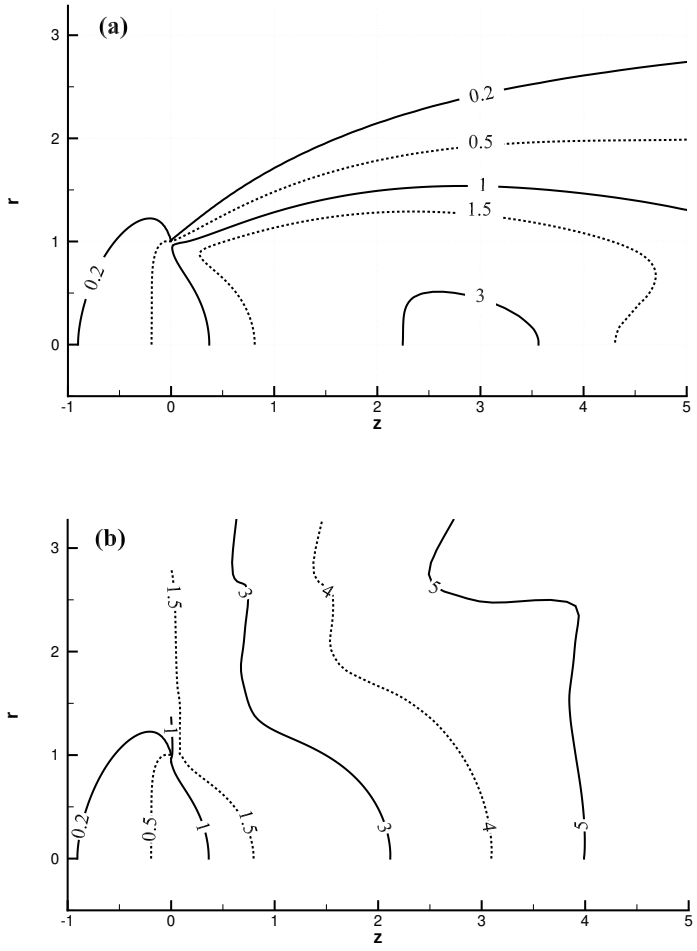

Figure 4.10: Mach number iso-lines at time moment $t = 20$ for $p_1/p_0 = 0.1, \delta_0 = 100$. (a), $p_1/p_0 = 0., \delta_0 = 100$. (b)

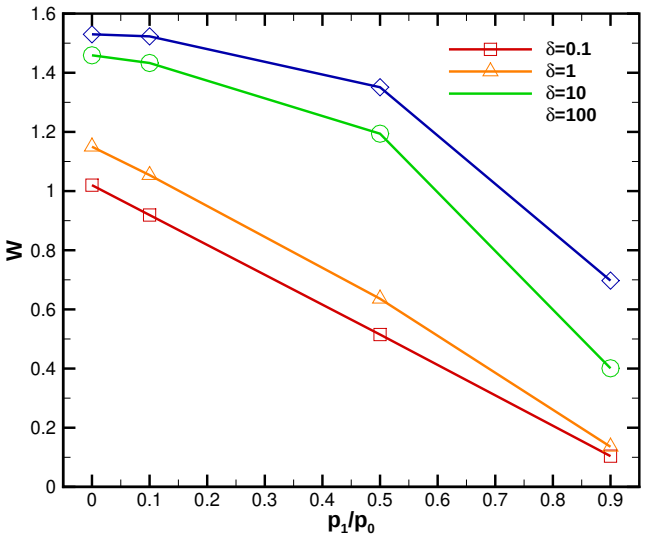

Figure 4.11: Dimensionless mass flow rate as a function of pressure ratio p_1/p_0 at different rarefaction parameters δ_0

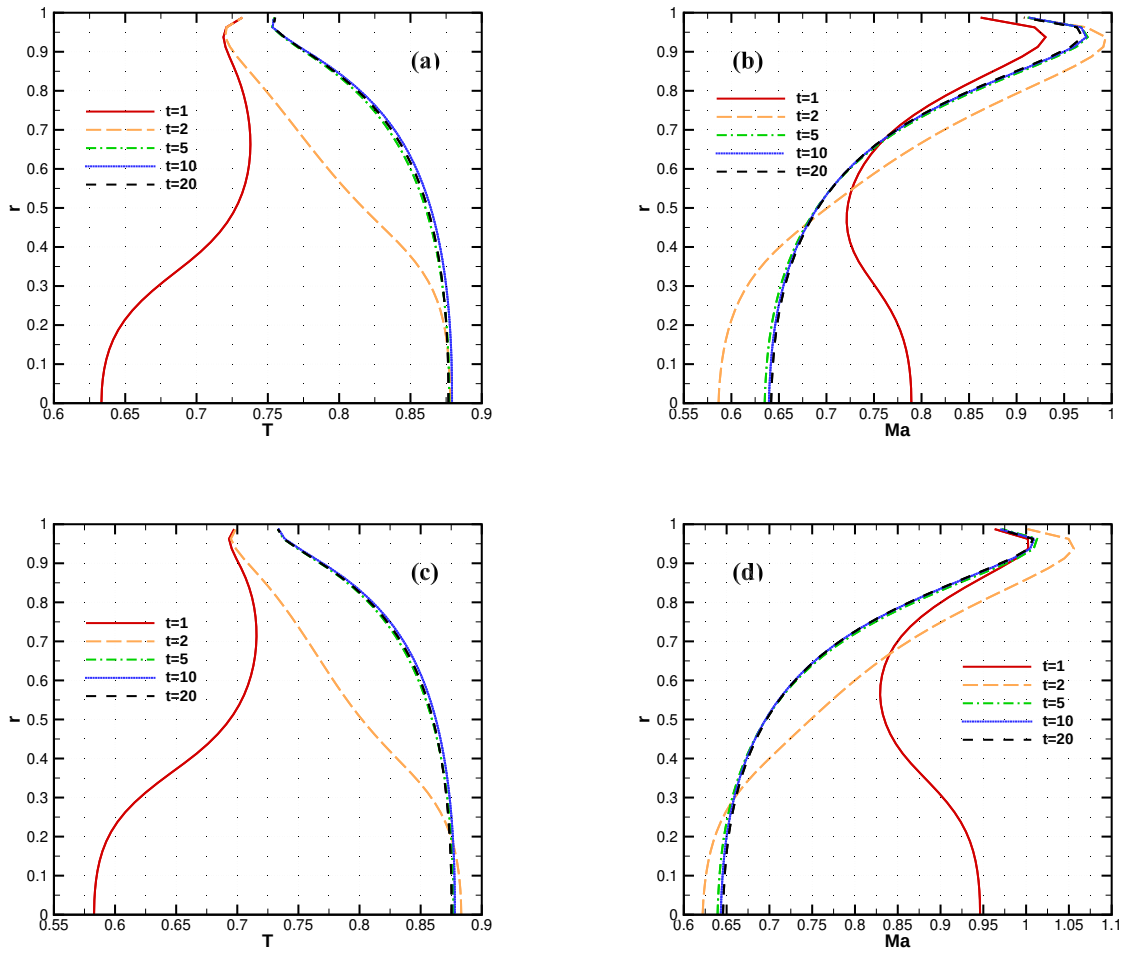

Figure 4.12: Distribution of temperature (a,c), Mach number (b,d) along the orifice at several time moments for $p_1/p_0 = 0.1, \delta = 100.$ (a,b), $p_1/p_0 = 0., \delta_0 = 100.$ (c,d)

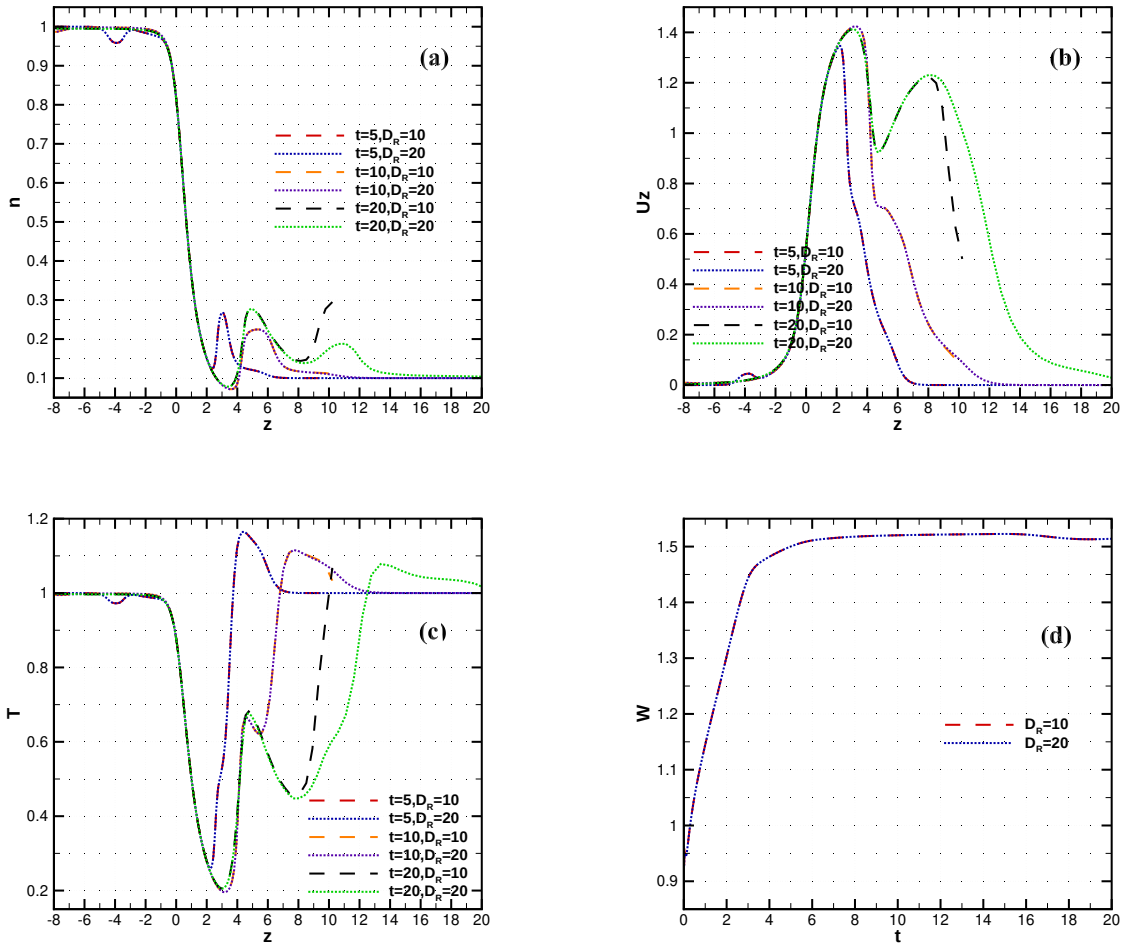

Figure 4.13: Distribution of density number (a), axial velocity (b), temperature (c) along the axis at time moments $t = 5, 10, 20$ for $p_1/p_0 = 0.1, \delta_0 = 100.$ with different computational domain sizes $D_R = 10, 20.$ The time evolution of mass flow rate W with different computational domain sizes $D_R = 10, 20$ (d)

Chapter 5

Gas flow through a channel of varying rectangular cross-section

The gas flow through a long channel of a rectangular cross section is a practical problem in the MEMS and vacuum technology applications. This kind of flow was largely studied on the basis of the kinetic theory and the detailed review may be found in Ref. [51]. However in several applications a cross section varies along the channel. As examples of such kind of flow the leakage through compressor valves [59] and the flow in the micro bearing [60, 61] may be given. A few results of the numerical simulations of the flow through variable conical cross section [62] and rectangular and conical sections [63] were found in the literature.

In this work we apply the approach, proposed in Ref. [62] and implemented to the flow through the tube of a variable radius, to the channel of a variable rectangular cross section. The proposed technique allows to calculate the mass flow rate through a long channel with variable rectangular cross section for arbitrary pressure and temperature ratios in large range of gas rarefaction.

5.1 Problem statement

Consider two reservoirs containing the same gas and connected by a long rectangular channel of variable cross-section aspect ratio. The channel width w is supposed to be the same, but the channel height h varies continuously along the channel. Its value is equal to h_1 in the first reservoir and h_2 in the second reservoir. We assume that the relation $\max(h) \leq w$ keeps along the channel. The first reservoir is maintained at the pressure p_1 and temperature T_1, while the pressure and temperature in the second reservoir are p_2 and T_2, respectively. We will calculate the mass flow rate through this channel in the whole range of the gas rarefaction. The results will be given in terms of reduced mass flow rate defined as follows

$$G = \frac{L}{h_1^2 w p_1}\sqrt{\frac{2kT_1}{m}}\dot{M}, \tag{5.1}$$

here L is the channel length, m is the molecular mass of the gas, k is the Boltzmann constant, $\dot{M}$ is the mass flow rate through the channel.

We assume the channel to be long enough ($\max(h) \ll L$) that the end effects can be neglected. According to Refs. [168, 169], the end influence in the hydrodynamic regime has the order of $\max(h)/L$, while in the free-molecular regime [170] its order is $(\max(h)/L)\ln(L/\max(h))$. These estimations are confirmed by the numerical results for a tube flow [46].

The second assumption is that the pressure and temperature gradients can be considered small in any cross section of the channel

$$\xi_P = \frac{h}{p}\frac{dp}{dx}, \qquad |\xi_P| \ll 1, \qquad \xi_T = \frac{h}{T}\frac{dT}{dx}, \qquad |\xi_T| \ll 1, \tag{5.2}$$

where x is the longitudinal coordinate in the flow direction with the origin in the first reservoir, $h = h(x)$ is a local channel's height, $p = p(x)$ and $T = T(x)$ are a local pressure and temperature, respectively. Under such a condition the mass flow rate in a cross section is calculated as [106]

$$\dot{M} = hwp\sqrt{\frac{m}{2kT}}(-G_P\xi_p + G_T\xi_T), \tag{5.3}$$

where the coefficients G_P and G_T depend on the local gas rarefaction parameter δ, defined as

$$\delta = \frac{hp}{\mu(T)}\sqrt{\frac{m}{2kT}}, \tag{5.4}$$

μ is the gas viscosity, which depends on the local temperature $T(x)$.

The values of the coefficients $G_P = G_P(\delta)$ and $G_T = G_T(\delta)$ in the case of the gas flow through a rectangular cross section channel for different flow regimes were obtained by different authors from the solution of the linearized BGK and S-model kinetic equations, or from the linearized Boltzmann equation for the diffuse or diffuse-specular boundary conditions [171, 172, 84, 173]. The detailed review on these numerical results may be found in Ref. [51]. The results used in this work will be given in the next section.

Following Ref. [62], from Eqs. (5.1-5.4) the differential equation is obtained

$$G = \frac{L}{p_1}\left(\frac{h}{h_1}\right)^2 \sqrt{\frac{T_1}{T}}\left(-G_P(\delta)\frac{dp}{dx} + G_T(\delta)\frac{p}{T}\frac{dT}{dx}\right). \tag{5.5}$$

If we assume that the temperature distribution along the channel is known we can obtain the corresponding pressure distribution and the reduced total mass flow rate G through the channel. Equation (5.5) is solved numerically using the following finite difference scheme [62]:

$$p_{i+1} = p_i + \frac{\Delta x}{G_P(\delta_i)}\left(G_T(\delta_i)\frac{p_i}{T_i}\frac{T_{i+1}-T_i}{\Delta x} - \frac{p_1 G}{L}\left(\frac{h_1}{h_i}\right)^2 \sqrt{\frac{T_i}{T_1}}\right). \tag{5.6}$$

In the previous equation $\Delta x = L/N$ is the grid step in the x direction, $0 \le i \le N$, p_i, T_i, h_i are the pressure, temperature and channel height in i grid point, respectively. The rarefaction parameter δ_i is calculated as

$$\delta_i = \delta_1 \frac{p_i h_i \mu(T_1)}{p_1 h_1 \mu(T_i)}\sqrt{\frac{T_1}{T_i}}, \qquad \delta_1 = \frac{p_1 h_1}{\mu(T_1)}\sqrt{\frac{m}{2kT_1}}. \tag{5.7}$$

Equation (5.6) is solved numerically by the shooting method (Ref. [174], Section 7.3) with the boundary condition $p(x=0) = p_1$. G is a parameter of Eq. (5.6) which is found satisfying the second boundary condition $p(x=L) = p_2$.

5.2 Determination of coefficients G_P and G_T

5.2.1 Free molecular regime

In the free molecular regime ($\delta = 0$) the coefficient G_P was found analytically in Ref. [175]

$$G_P = \frac{1}{\sqrt{\pi}}\left[\frac{w}{h}\ln\left(\frac{h}{w} + \sqrt{1+\frac{h^2}{w^2}}\right) + \ln\left(\frac{w}{h} + \sqrt{1+\frac{w^2}{h^2}}\right) - \frac{1}{3}\left(\frac{w}{w+\sqrt{w^2+h^2}} + \frac{w}{h+\sqrt{w^2+h^2}}\right)\right] \tag{5.8}$$

The coefficient G_T for the case of $\delta = 0$ is equal to

$$G_T = G_P/2. \tag{5.9}$$

In the case $h/w \to 0$ the two coefficients become [106]

$$G_P = \frac{1}{\sqrt{\pi}}\left(\ln\frac{2w}{h} + \frac{1}{2}\right), \qquad G_T = G_P/2. \tag{5.10}$$

5.2.2 Hydrodynamic regime

In the hydrodynamic flow regime ($\delta \to \infty$) the reduced mass flow rate is equal to [176]

$$G_{P_h} = \frac{\delta}{6}\left(1 - \frac{192}{\pi^5}\frac{h}{w}\sum_{n=0}^{\infty}\frac{\tanh(0.5\pi(2n+1)w/h)}{(2n+1)^5}\right). \tag{5.11}$$

In the slip flow regime the slip correction must be added, which was found in Refs. [177, 175, 178]

$$G_{P_{slip}} = \sigma_p\left[\frac{4}{3} - \frac{256}{\pi^5}\frac{h}{w}\sum_{n=0}^{\infty}\frac{\tanh(0.5\pi(2n+1)w/h)}{(1+2n)^5} - \frac{32}{\pi^4}(1-\frac{h}{w})\sum_{n=0}^{\infty}\frac{\tanh(0.5\pi(2n+1)w/h)}{(1+2n)^4}\right]. \tag{5.12}$$

Therefore the coefficient G_P for the hydrodynamic and slip regimes ($\delta > 40$) becomes

$$G_P = G_{P_h} + G_{P_{slip}}. \tag{5.13}$$

The thermal creep coefficient in these flow regimes is equal to [106]

$$G_T = \frac{\sigma_T}{\delta}. \tag{5.14}$$

The coefficients σ_p and σ_T in Eqs. (5.12), (5.14) are the velocity slip and the thermal slip coefficients, equal to 1.016 [179] and 1.175 [180], respectively. It is to be noticed that expressions (5.12) and (5.14) are valid for any slip coefficients, *e.g.*, for non-diffuse scattering or gaseous mixtures [143].

5.2.3 Transitional flow regime

In order to solve numerically Eq. (5.6) we need to known the values of the rarefaction parameter at arbitrary couple of two values: the rarefaction parameter and the channel cross-section aspect ratio $(\delta, h/w)$. The two-dimensional grid of values $G_P(\delta, h/w)$ and $G_T(\delta, h/w)$ is formed from the numerical data of Ref. [106], where the quantities $G_P(\delta)$ and $G_T(\delta)$ are calculated for

Table 5.1: Coefficient G_P obtained in Ref. [106] and in present work* from the numerical solution of the linearized S-model kinetic equation.

δ	h/w							
	0.[106]	0.0367*	0.05[106]	0.1[106]	0.25*	0.5*	0.75*	1[106]
0.001	4.273	2.510	2.344	1.978	1.496	1.150	0.962	0.837
0.01	3.050	2.345	2.218	1.910	1.465	1.134	0.951	0.831
0.02	2.713	2.238	2.132	1.860	1.442	1.122	0.942	0.826
0.04	2.400	2.101	2.018	1.790	1.412	1.105	0.930	0.816
0.05	2.306	2.051	1.975	1.763	1.400	1.099	0.925	0.812
0.08	2.120	1.940	1.879	1.702	1.373	1.084	0.915	0.801
0.1	2.038	1.886	1.832	1.671	1.359	1.076	0.909	0.796
0.2	1.823	1.724	1.688	1.573	1.315	1.053	0.892	0.779
0.4	1.651	1.591	1.567	1.486	1.279	1.037	0.880	0.768
0.5	1.613	1.560	1.537	1.465	1.271	1.036	0.879	0.766
0.8	1.561	1.517	1.498	1.438	1.270	1.043	0.885	0.769
1.	1.549	1.511	1.493	1.437	1.277	1.054	0.892	0.774
1.5	1.565	1.530	1.513	1.462	1.312	1.088	0.920	0.793
2.	1.606	1.573	1.556	1.505	1.359	1.131	0.953	0.818
4.	1.855	1.820	1.801	1.746	1.584	1.324	1.114	0.933
5.	2.000	1.961	1.941	1.882	1.709	1.429	1.210	0.995
8.	2.456	2.411	2.384	2.313	2.105	1.758	1.491	1.189
10.	2.772	2.722	2.690	2.609	2.378	1.987	1.692	1.323
15.	3.577	3.513	3.470	3.364	3.071	2.563	2.174	1.662
20.	4.393	4.316	4.262	4.129	3.771	3.146	2.660	2.006
30.	6.040	5.916	5.847	5.639	5.171	4.301	3.602	2.698
40.	7.695	7.533	7.451	7.214	6.501	5.336	4.269	3.395

large range of the gas rarefaction parameter and for four different h/w aspect ratios $h/w = 0, 0.5, 0.1, 1$, where $h/w = 0$ corresponds to the case of the flow between two parallel plates.

To complete the data of Ref. [106] the same approach is applied to obtain a solution of the linearized S-model kinetic equation [11]. The additional values of the channel cross-section aspect ratios $h/w = 0.0367, 0.25, 0.5, 0.75$ and for the rarefaction parameter varies from 0.001 to 40 are calculated. The 1000×1000 grid in the physical space is implemented, the polar coordinates are used in the molecular velocity space with 200 points for the velocity directions and 25 points in the velocity magnitude distributed according to the Gaussian rule. The values of the G_P and G_T coefficients obtained in the present work are presented in Tables 5.1, 5.2.

The method of two-dimensional interpolation is employed to calculate the values G_P and G_T in an arbitrary point $(\delta_*, (h/w)_*)$ from two-dimensional grid of $G_P(\delta, h/w)$ and $G_T(\delta, h/w)$ values. Below we explain the interpolation steps realized to calculate the value of $G_P(\delta_*, (h/w)_*)$ in a point $(\delta_*, (h/w)_*)$, which does not coincide with any values of δ and h/w reported in two-dimensional Table 5.1. The interpolation is accomplished by the following steps.

Table 5.2: Coefficient G_T obtained in Ref. [106] and in present work* from the numerical solution of the linearized S-model kinetic equation.

δ	h/w							
	0.[106]	0.0367*	0.05[106]	0.1[106]	0.25*	0.5*	0.75*	1[106]
0.001	1.8550	1.2390	1.1620	0.9839	0.7451	0.5736	0.4800	0.4181
0.01	1.2460	1.0860	1.0440	0.9165	0.7120	0.5558	0.4678	0.4110
0.02	1.0780	0.9975	0.9662	0.8658	0.6874	0.5416	0.4576	0.4037
0.04	0.9200	0.8854	0.8656	0.7960	0.6524	0.5210	0.4425	0.3912
0.05	0.8719	0.8462	0.8291	0.7695	0.6385	0.5128	0.4364	0.3857
0.08	0.7754	0.7615	0.7483	0.7078	0.6051	0.4925	0.4214	0.3716
0.1	0.7320	0.7212	0.7089	0.6763	0.5871	0.4815	0.4132	0.3637
0.2	0.6105	0.6006	0.5968	0.5814	0.5231	0.4408	0.3825	0.3390
0.4	0.4955	0.4911	0.4881	0.4806	0.4492	0.3910	0.3441	0.3071
0.5	0.4620	0.4583	0.4453	0.4490	0.4239	0.3731	0.3301	0.2953
0.8	0.3953	0.3923	0.3894	0.3848	0.3692	0.3327	0.2982	0.2684
1.	0.3633	0.3621	0.3593	0.3553	0.3428	0.3122	0.2818	0.2545
1.5	0.3092	0.3086	0.3060	0.3029	0.2946	0.2732	0.2499	0.2275
2.	0.2719	0.2718	0.2693	0.2667	0.2606	0.2443	0.2258	0.2070
4.	0.1870	0.1876	0.1856	0.1842	0.1818	0.1738	0.1644	0.1539
5.	0.1621	0.1628	0.1609	0.1598	0.1582	0.1521	0.1443	0.1366
8.	0.1154	0.1161	0.1148	0.1141	0.1131	0.1097	0.1049	0.1017
10.	0.0966	0.0972	0.0961	0.0956	0.0947	0.0921	0.0881	0.0868
15.	0.0682	0.0688	0.0680	0.0677	0.0671	0.0654	0.0628	0.0632
20.	0.0526	0.0530	0.0524	0.0522	0.0517	0.0505	0.0486	0.0495
30.	0.0358	0.0367	0.0357	0.0354	0.0354	0.0347	0.0336	0.0344
40.	0.0270	0.0279	0.0270	0.0269	0.0276	0.0274	0.0272	0.0263

Table 5.3: Coefficients G_P, G_T obtained from the numerical solution of the S-model kinetic equation for case $h/w = 0.0367$ and from 2^{nd} order interpolation in h/w-direction.

δ	G_P		G_T	
	S-model	Interpolation	S-model	Interpolation
0.001	2.510	2.706	1.2390	1.2965
0.01	2.345	2.389	1.0860	1.0906
0.02	2.238	2.257	0.9975	0.9949
0.04	2.101	2.105	0.8854	0.8816
0.05	2.051	2.052	0.8462	0.8422
0.08	1.940	1.937	0.7615	0.7568
0.1	1.886	1.883	0.7212	0.7160
0.2	1.724	1.722	0.6006	0.6006
0.4	1.591	1.589	0.4911	0.4901
0.5	1.560	1.557	0.4583	0.4478
0.8	1.517	1.515	0.3923	0.3908
1.	1.511	1.508	0.3621	0.3604
1.5	1.530	1.527	0.3086	0.3068
2.	1.573	1.569	0.2718	0.2700
4.	1.820	1.815	0.1876	0.1860
5.	1.961	1.957	0.1628	0.1612
8.	2.411	2.403	0.1161	0.1150
10.	2.722	2.712	0.0972	0.0962
15.	3.513	3.498	0.0688	0.0681
20.	4.316	4.297	0.0530	0.0525
30.	5.916	5.900	0.0367	0.0357
40.	7.533	7.515	0.0279	0.0270

Table 5.4: Coefficients G_P, G_T obtained from the numerical solution of the S-model kinetic equation for case $h/w = 0.0367$ and from 2^{nd} order interpolation in δ-direction.

δ	G_P		G_T	
	S-model	Interpolation	S-model	Interpolation
0.03	2.1614	2.1567	0.9340	0.9306
3.	1.6876	1.6815	0.2215	0.2171
25.	5.1115	5.0543	0.0435	0.0416

- A block of the reduced mass flow rate $G_P(\delta_i, (h/w)_j)_{i=1..m+1, j=1..n+1}$ values containing a point $(\delta_*, (h/w)_*)$ is searched and extracted using the bisection method (Chapter 3 of Ref. [181]) from the ordered tabular data, see Table 5.1, which contains the numerical values of G_P obtained on the basis of kinetic equation [106]. Here, i and j are the indexes for the row δ and the column h/w, respectively. The values m and n are the orders of interpolation in δ-direction and in h/w-direction, respectively.

- Using $n+1$ values of G_P in h/w direction, the n^{th} order interpolation with Neville's algorithm (given in Chapter 3 of Ref. [181]) is carried out for each of $m+1$ extracted values in δ direction and a set of values $G_P(\delta_i, (h/w)_*)_{i=1..m+1}$ is obtained.

- Then m^{th} order interpolation in the δ-direction is performed in order to obtain the value of $G_P(\delta_*, (h/w)_*)$.

The value of G_T at an arbitrary point $(\delta_*, (h/w)_*)$ is calculated by the interpolation in the same fashion as for the value of G_P.

The accuracy of the interpolation in the h/w direction is evaluated by comparing the results of the numerical solution of the linearized S-model kinetic equation for the $h/w = 0.0367$ and the interpolation results for the same values of h/w ratio, see Table 5.3. Analyzing the results of Table 5.3 one can see that the accuracy of the interpolation is of the order of 2%. The similar verification was carried out for the interpolation in the δ direction. The same type of the comparison were carried out by comparing the solution of the linearized kinetic equation and the interpolation results. When analyzing the results given in Table 5.4 one can see that the difference between the corresponding values does not also exceed 2%. However, when $\delta \to 0$ (for the small values of h/w) or $\delta \to \infty$ the coefficients G_P and G_T change steeply and the use of the sparse grid rises up the interpolation error.

In the following Sections the results of the isothermal and non isothermal flows simulations are given.

5.3 Isothermal flow

The most simple case is the isothermal flow, when the gas temperature anywhere in a system is equal to the temperature in the first reservoir: $T(x) = T_1$.

In the case, when the both inlet and outlet channel's cross sections are in the hydrodynamic flow regime ($\delta_1 \to \infty$ and$\delta_2 \to \infty$) and the outlet section is large enough ($h_2/w \to 0$, two parallel plates), the analytical solution may be found and the reduced mass flow rate becomes

Table 5.5: Reduced mass flow rate G for the isothermal case and for the $h_2/w = 0$ channel, the channel's height aspect ratio is $h_2/h_1 = 10$.

δ_1	p_2/p_1				
	0.	0.01	0.1	0.5	0.9
0.001	93.34	92.41	38.46	20.72	4.024
0.01	33.47	32.18	27.45	13.95	2.674
0.05	24.51	23.87	20.75	10.62	2.035
0.1	21.63	21.10	18.34	9.448	1.824
0.5	16.80	16.44	14.52	7.897	1.591
1.	15.83	15.54	13.94	7.951	1.656
5.	19.06	18.93	18.00	11.88	2.725
10.	25.82	25.74	24.95	17.40	4.140
50.	85.35	85.30	84.15	62.58	15.61
100.	161.1	161.0	159.2	119.4	30.02

$$G = \frac{\delta_1}{6}\left\{\frac{1}{2}\left[1-\left(\frac{p_2}{p_1}\right)^2\right]\right\}\left[\frac{1}{L}\int_0^L\left(\frac{h_1}{h(x)}\right)^3 dx\right]^{-1}. \tag{5.15}$$

To obtain the previous expression we used Eq. (5.11) which gives $G_P = \delta/6$ when $h/w \to 0$.

If we assume the linear variation of the channel height

$$h(x) = h_1 + \frac{x}{L}(h_2 - h_1), \tag{5.16}$$

from the integration of Eq. (5.15) one obtains

$$G = \frac{\delta_1}{6}\left(1-\left(\frac{p_2}{p_1}\right)^2\right)\frac{(h_2/h_1)^2}{(h_2/h_1)+1}. \tag{5.17}$$

The same results (5.17) may be obtained from the solution of the Stokes equation subjected to the non-slip boundary conditions, see Ref. [60].

In the case of the free molecular flow regime ($\delta \to 0$) and always for the case of the flow between two parallel plates ($h_2/w \to 0$) the integration of Eq. (5.5) can be done analytically. In the case of $h/w \to 0$ the coefficient G_P may be found using Eq. (5.10) and the reduced mass flow rate becomes:

$$G = \frac{1}{\sqrt{\pi}}\left(1-\frac{p_2}{p_1}\right)\left(\frac{1}{L}\int_0^L \frac{h_1^2 dx}{h(x)^2(\ln(2w/h(x)) + 0.5)}\right)^{-1}. \tag{5.18}$$

The last integral in previous expression may be evaluated numerically.

Table 5.6: Reduced mass flow rate G for the isothermal case and for the $h_2/w = 1$ channel, the channel's height aspect ratio is $h_2/h_1 = 10$.

δ_1	p_2/p_1				
	0.	0.01	0.1	0.5	0.9
0.001	15.36	15.21	13.83	7.670	1.532
0.01	15.02	14.86	13.47	7.418	1.474
0.05	14.14	13.98	12.62	6.897	1.368
0.1	13.67	13.52	12.20	6.681	1.327
0.5	12.68	12.54	11.36	6.393	1.306
1.	12.60	12.47	11.41	6.657	1.401
5.	16.35	16.27	15.54	10.35	2.381
10.	22.53	22.47	21.82	15.26	3.631
50.	74.86	74.82	73.76	54.88	13.70
100.	141.3	141.3	139.6	104.8	26.34

In order to obtain the values of the reduced mass flow rate in the transitional flow regime Eq. (5.5) must be solved numerically. In Table 5.5 the results on the reduced mass flow rate G are given for the case of the flow in very large channel ($h_2/w \to 0$, two parallel plates) and when the channel height increases in the flow direction by 10 times ($h_2/h_1 = 10$).

In Table 5.6 the results on the reduced mass flow rate G are given for the case of the flow through the channel of the square outlet cross section ($h_2/w = 1$) and when the channel height increases in the flow direction by 10 times ($h_2/h_1 = 10$).

5.4 Non-isothermal case

The non-isothermal flow is considered: the temperature in the second reservoir is supposed to be higher and equal to $T_2 = 1.5T_1$. The temperature gradient along the channel is supposed to be linear.

In Table 5.7 the results on the reduced mass flow rate are given for the case of the flow through the square ($h_2/w = 1$) outlet cross-section channel and when the channel height increases in the flow direction in 10 times ($h_2/h_1 = 10$), as for the second isothermal case, see previous section. If comparing the results of Tables 5.6 and 5.7, obtained under isothermal and non-isothermal conditions, we can observed very small influence of the temperature gradient on the reduced mass flow rate for small values of the gas rarefaction and the small values of the pressure ratio between the reservoirs. However, for the larger values of the rarefaction parameter the difference in the reduced mass flow rate becomes significant even for the gas expansion into vacuum. The influence of the temperature gradient along the channel is also large for the pressure ratio close to 1 and small values of the rarefaction parameter. In this case

Table 5.7: Reduced mass flow rate G for the non-isothermal case and for the $h_2/w = 1$ channel, the channel's height aspect ratio is $h_2/h_1 = 10$, $T_2/T_1 = 1.5$.

δ_1	p_2/p_1				
	0.	0.01	0.1	0.5	0.9
0.001	15.35	15.23	14.11	9.073	4.046
0.01	15.01	14.88	13.74	8.739	3.797
0.05	14.12	13.98	12.84	8.020	3.314
0.1	13.61	13.49	12.38	7.668	3.038
0.5	12.51	12.39	11.36	6.907	2.295
1.	12.35	12.23	11.27	6.894	2.047
5.	15.56	15.48	14.73	9.818	2.418
10.	21.17	21.10	20.43	14.27	3.472
50.	69.44	69.39	68.29	50.75	12.68
100.	130.8	130.7	129.1	96.86	24.36

the mass flow rate due to the thermal creep phenomenon (due to the temperature gradient) is directed from the cold reservoir to the hot one, that means in the same direction as the pressure-driven Poiseuille flow.

5.5 Conclusions

The simple method, proposed previously by other authors, is applied here to calculate the gas mass flow rate through the channel of the variable rectangular cross section. The calculations are based on the results of the numerical solution of the linearized S-model kinetic equation obtained by other authors and completed using the same approach in the present paper. The explicit analytical expressions are proposed in the case of the hydrodynamic and free molecular flow regimes. The simple interpolation method is realized to calculate the mass flow rate in the transitional flow regime.

Chapter 6

The gas flow diode effect in microchannel

The flow of rarefied gases through a long channel with rectangular cross section is a practical problem in the field of micro electromechanical systems (MEMS) and in vacuum technology applications. This kind of flow was widely studied on the basis of the kinetic theory and a detailed review is given in Ref. [51]. Also a vast amount of experiments on microducts with various but *uniform* cross section were performed in the last decades [52, 54, 55, 56, 57, 58].

In several applications, however, the cross section varies alongside the channel. As examples of such kind of flow the leakage through compressor valves [59] and the flow in the micro bearing [60, 61] may be given. Only few numerical simulations are carried out on the flow through ducts with variable conical and tapered rectangular cross sections [64, 32, 63, 68]. It was found that the permeability is higher when the duct is perfused in converging direction [64, 65, 58]. In a more general sense the non-symmetric behavior of the flow following the direction (diode effect) was firstly investigated in the liquid flows, notably by the authors of [66, 67]. More recently, in case of gaseous flows, this *gas flow diode effect* was found to increase with rarefaction in the slip flow regime and to disappear in the continuum regime [58]. When the both ends of a channel are in the free molecular regime, this effect theoretically should not exist, too [32, 68].

Based on these considerations and previous experimental observations [65, 58] we present an analytical model for the isothermal pressure driven flow in ducts with alongside varying cross section. In this work we apply the approach based on the solution of the Stokes equation subjected to the velocity slip boundary condition. We solve this model for the predictive calculation of the flow through a long channel with variable rectangular cross section.

In addition, and for further validation, the numerical approach developed in Ref. [68] is used. This approach allows to calculate the mass flow rate through a long channel with variable rectangular cross section for arbitrary pressure and temperature drops over a wide

range of gaseous rarefaction.

Both, analytical and numerical solutions are compared with one another and with experimental data for the CO_2, N_2, and Ar gas flow through a micro-milled channel of varying rectangular cross section.

6.1 Model development

6.1.1 Problem statement

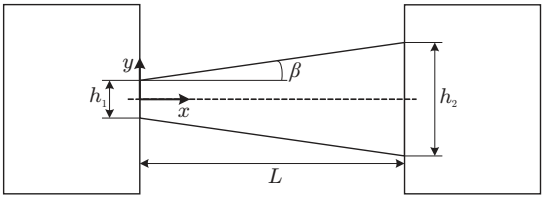

Figure 6.1: Lateral cross section of the tapered channel. The width w is supposed to remain constant and is large compared to $h(x)$. In positive x-direction the channel is referred to as a *diffusor* whereas in negative x-direction it is termed *nozzle*.

A long channel of variable cross section connects two reservoirs containing the same gas. The channel width w is supposed to remain constant alongside the channel, while the channel height h varies from h_1 in the first reservoir to h_2 ($h_2 \geq h_1$) in the second reservoir, with $\max(h) \leq w$ (Fig. 6.1). One reservoir is maintained at the pressure p_1, while the pressure in the other reservoir is p_2, respectively. We further assume isothermal conditions in the complete system and the channel to be long enough ($\max(h) \ll L$) so that the end effects can be neglected.

6.1.2 Analytical solution for the slip flow regime

In this section we derive the analytical model for the previously stated flow configuration. Here we assume that $\max(h) \ll w$ to treat the flow as two-dimensional.

In the hydrodynamic flow regime ($Kn \to 0$) the flow velocity u in the x direction through a channel cross section is obtained from the solution of the Stokes equation

$$\frac{\partial^2 u}{\partial y^2} = \frac{1}{\mu}\frac{dp}{dx}, \tag{6.1}$$

where $p = p(x)$ is the local pressure, subjected to the symmetry condition on the axis of symmetry and the non-slip condition on the upper wall:

$$\left.\frac{\partial u}{\partial y}\right|_{y=0} = 0, \qquad u(x,y)|_{y=0.5h(x)} = 0. \tag{6.2}$$

In Eq. (6.1) μ is the gaseous viscosity. By integrating twice Eq. (6.1) with the boundary conditions according to Eqs. (6.2) one obtains the streamwise velocity as

$$u(x,y) = -\frac{1}{2\mu}\frac{dp}{dx}\left(\left(\frac{h}{2}\right)^2 - y^2\right). \tag{6.3}$$

The mass flow rate is obtained by integrating the velocity profile over the channel cross section

$$\dot{M} = 2w\int_0^{0.5h(x)} \rho u(x,y)dy, \tag{6.4}$$

whereby ρ is the density of the gas. Taking account of the state equation of an ideal gas $\rho = p/(RT)$, with R the specific gas constant, the previous equation yields

$$\dot{M} = -\frac{2}{3}w\frac{p}{\mu RT}\frac{dp}{dx}\left(\frac{h}{2}\right)^3. \tag{6.5}$$

Using the property of the mass conservation in any channel cross section and integrating expression (6.5) from 0 to L we obtain

$$\dot{M}^{Hyd} = \frac{p_1^2 - p_2^2}{12\mu RTL}w\frac{h_1^2 h_2^2}{h_1 + h_2}, \tag{6.6}$$

giving us an analytical expression for the mass flow rate through the channel in the hydrodynamic regime. To obtain the previous expression we assumed here that the local channel height $h = h(x)$ varies constantly along the channel

$$h(x) = h_1 + \frac{x}{L}(h_2 - h_1). \tag{6.7}$$

This assumption is made for the further comparison with experimental data. The developed approach, however, can be applied for the case of the other dependencies (non-linear) of the local channel height from the longitudinal coordinate.

Let us consider now the slip flow regime. In this case the second of the two boundary conditions (6.2) for the Stokes equation (6.1) must be changed in slip boundary condition in

the form

$$u(x,y)\Big|_{y=0.5h(x)} = -\sigma_p \frac{\mu}{p}\sqrt{2RT}\cos\beta \left(\frac{\partial u}{\partial y}\right)\Big|_{y=0.5h(x)}, \beta = \arctan(0.5(h_2-h_1)/L). \tag{6.8}$$

This boundary condition takes account of the different inlet and outlet cross sectional areas by means of the angle β (see Fig. 6.1). In case of $h_2 = h_1$ Eq. (6.8) yields the well-known slip boundary condition for uniform ducts.

In the previous equation σ_p is the velocity slip coefficient. In the case of the diffuse reflection of the molecules from the surface its value was obtained from the solution of the BGK [179], S-model [180], and the Boltzmann [182] kinetic equations. So obtained values of the σ_p coefficient lie in the narrow range $0.968 \leq \sigma_p \leq 1.03$.

By integrating the Stokes equation with the symmetry boundary condition (first expression in Eq. (6.2)) and velocity slip boundary condition according to Eq. (6.8), the streamwise velocity is obtained as

$$u(x,y) = -\frac{1}{2\mu}\frac{dp}{dx}\left(\left(\frac{h}{2}\right)^2 - y^2 + 2\sigma_p\frac{\mu}{p}\sqrt{2RT}\cos\beta\left(\frac{h}{2}\right)\right). \tag{6.9}$$

The mass flow rate through a cross section is found by replacing in Eq. (6.4) the velocity expression according to Eq. (6.9):

$$\dot{M} = -\frac{pw}{\mu RT}\frac{dp}{dx}\left(\frac{2}{3}\left(\frac{h}{2}\right)^3 + 2\sigma_p\frac{\mu}{p}\sqrt{2RT}\cos\beta\left(\frac{h}{2}\right)^2\right). \tag{6.10}$$

In order to deduce mass flow rate values from the reservoir pressures it is necessary to integrate Eq. (6.10) along the channel from 0 to L, as it was done for Eq. (6.5). But here the calculation is not so easy as that of Eq. (6.5). To obtain an explicit expression for the mass flow rate in the slip flow regime let us first introduce the Knudsen number

$$Kn = \lambda/h_1, \qquad \text{where} \qquad \lambda = k_\lambda\frac{\mu}{p}\sqrt{2RT}. \tag{6.11}$$

Here λ is the molecular mean free path, k_λ is the coefficient which depends on the molecular interaction model. Then, the dimensionless variables are defined as following

$$X = \frac{x}{L}, \quad H = \frac{h}{h_1}, \quad P = \frac{p}{p_0}, \quad Q = \dot{M}\frac{\mu(T)RTL}{p_0^2(0.5h_1)^3 w}, \tag{6.12}$$

where the average pressure $p_0 = 0.5(p_1 + p_2)$. Using these dimensionless variables the mass flow rate in the hydrodynamic regime, Eq. (6.6), is transformed into the following non-dimensional form:

$$Q^{Hyd} = \frac{2}{3}(P_1^2 - P_2^2)\frac{H_2^2}{H_2 + 1}, \tag{6.13}$$

where $H_2 = h_2/h_1$.

To obtain the mass flow rate in the slip flow regime Eq. (6.10) is transformed into a non-dimensional form using relations (6.12)

$$Q = -\frac{2}{3}H(X)^2\left(P\frac{dP}{dX}H(X) + bKn\frac{dP}{dX}\right), \tag{6.14}$$

where the Knudsen number is defined according to Eq. (6.11). Finally the coefficient b yields

$$b = 6\frac{\sigma_p \cos\beta}{k_\lambda}. \tag{6.15}$$

Then we eliminate the X variable, using the $H(X)$ profile as stated in Eq. (6.7), *i.e.*, $dH = (H_2 - 1)dX$. In the transformed equation we introduce a double variable change: first using $Z = 1/H$, and so transforming Eq. (6.14) into a classical homogeneous first order differential equation following $P(Z)$. Then to solve this new $P(Z)$ equation, the classical way is the use of a new function change: $\Pi(Z) = P/Z$. Thus the equation is finally integrated along the X axis, from 0 to 1.

We omit here the relatively long calculations with rather cumbersome expressions and we will give only the results. As it was mentioned above we can distinguish two directions: the *diffusor* and the *nozzle* directions as noted in the caption of Fig. 6.1.

6.1.3 Diffusor configuration

In the case of the diffusor configuration, after the previously described double variable changes and after integration from 0 to 1, Eq. (6.14) reads:

$$K\ln(H_2) = \gamma_2 \ln\left(\frac{\Pi_2 - \gamma_1}{\Pi_1 - \gamma_1}\right) - \gamma_1 \ln\left(\frac{\Pi_2 - \gamma_2}{\Pi_1 - \gamma_2}\right), \tag{6.16}$$

where

$$K^2 = (bKn_0)^2 + 6Q/(H_2 - 1), \gamma_1 = -0.5bKn_0 + 0.5K, \qquad \gamma_2 = -0.5Kn_0 - 0.5K. \tag{6.17}$$

Here Π_1 and Π_2 are the values of function Π calculated for the inlet and outlet cross sections, Kn_0 is the Knudsen number according to Eq. (6.11), calculated with $p = p_0$. Theoretically Q may be obtain directly from (6.16) through expression of K (see Eq. (6.17)), but K is implicitly included in different terms of Eq. (6.16) and therefore it is difficult to obtain it analytically. Therefore we linearize Eq. (6.16) according to the Knudsen number. Indeed the present analytical method is only pertinent in the slip flow regime and the boundary condition (6.8) is a first order in Knudsen number condition: thus, in anyway only a first order Knudsen number precision is implicitly guaranteed on the parameter extracted from Eq. (6.16). Thus, changing in fact the unknown function we put

$$Q^{dif} = Q^H(1 + \mathcal{A}^{dif} Kn_0), \tag{6.18}$$

then K, and thus γ_1 and γ_2 are so linearized and $\mathcal{A}^{dif}$ is finally obtained from an algebraic equation of first power following $\mathcal{A}^{dif} Kn_0$.

After long but trivial calculations we obtain:

$$\mathcal{A}^{dif} = b\left[\frac{(P_2^2H_2^2 - B^2)(P_1^2 - B^2)}{2B(P_1 - P_2H_2)} \ln\frac{(P_1 + B)(P_2H_2 - B)}{(P_1 - B)(P_2H_2 + B)} + P_1P_2H_2 + B^2\right]/(P_1 + P_2H_2)/B^2, \tag{6.19}$$

where

$$B^2 = \frac{3}{2}\frac{Q^{Hyd}}{H_2 - 1}. \tag{6.20}$$

6.1.4 Nozzle configuration

In the case of the nozzle configuration the variable changes performed for Eq. (6.14) lead finally to a complete equation, different from Eq. (6.16), but of the same complexity: the difference

is due to the different sign of dH/dX. We effectuate then the same linearization process as described above, *i.e.*:

$$Q^{noz} = Q^{Hyd}(1 + \mathcal{A}^{noz} Kn_0). \tag{6.21}$$

In a same way as in the diffusor direction case, we obtain

$$\mathcal{A}^{noz} = b\left[\frac{((P_1H_2)^2 + B^2)(P_2^2 + B^2)}{B(P_1H_2 - P_2)}\left(\arctan\left(\frac{P_1H_2}{B}\right) - \arctan\left(\frac{P_2}{B}\right)\right) - (P_1P_2H_2 + B^2)\right] /(P_1H_2+P_2)/ \tag{6.22}$$

Of course, as expected from our previous comments the $\mathcal{A}$ first order coefficients are different depending on the flow direction.

6.1.5 Diodicity

In order to define an explicit value for the disparity in both flow directions we introduce the diodicity D as the ratio of the mass flow rates $\dot{M}$ to the difference of the squaring of the inlet and outlet pressures:

$$D = \frac{\dot{M}^{noz}/\left((p_1^{noz})^2 - (p_2^{noz})^2\right)}{\dot{M}^{dif}/\left(\left(p_1^{dif}\right)^2 - \left(p_2^{dif}\right)^2\right)}, \tag{6.23}$$

where p_1^{dif}, p_2^{dif}, p_1^{noz}, p_2^{noz} are the inlet and outlet pressure for the diffusor and nozzle directions respectively. Using expressions (6.12), (6.13), (6.18), (6.21) and assuming that the inlet and outlet pressures are the same for the diffusor and nozzle cases the diodicity of a moderately rarefied gas flow becomes

$$D = \frac{1 + \mathcal{A}^{noz} Kn_0}{1 + \mathcal{A}^{dif} Kn_0}. \tag{6.24}$$

Hence we obtain a predictive expression for D being a function only of the Knudsen number and the $\mathcal{A}$ first order coefficients according to Eqs. (6.19) and (6.22). From Eq. (6.24) it can be seen that D approaches unity with decreasing rarefaction ($Kn \to 0$: hydrodynamic flow regime). This result is in agreement with that obtained in the hydrodynamic regime: from Eqs. (6.12) and (6.13) it is clear that the mass flow rate does not depend on the direction of perfusion.

In Section 6.4 the solutions obtained by means of the analytical approach are compared to a numerical approach addressed in the following section and in detail presented in Ref. [68]. Both approaches are used to calculate the mass flow rate through a tapered channel and these numerical results are compared with experimental data.

6.2 Numerical approach

The numerical approach [68] is based on the implementation of the solution of the linearized S-model kinetic equation, obtained in [106, 68]. One additional assumption is needed when applying the linearized kinetic equation: the reduced pressure gradient has to be small in any cross section of the channel

$$\frac{h}{p}\frac{dp}{dx} \ll 1, \tag{6.25}$$

where x is the longitudinal coordinate in the flow direction with the origin in the first reservoir, see Fig. 6.1. It is to note that condition (6.25) is always satisfied for the microchannels:

$$\frac{h}{p}\frac{dp}{dx} \sim \frac{h}{p}\frac{|p_1 - p_2|}{L} = \frac{h}{L}\frac{|p_1 - p_2|}{p} \ll 1. \tag{6.26}$$

The last expression in Eq. (6.26) is always satisfied because for the micro channel $h \ll L$ and therefore condition (6.25) is satisfied for any pressure gradient.

Then using the data [106, 68] on the dimensionless coefficient $G(\delta)$ for various h/w ratios and the simple interpolation method [68] the mass flow rate is obtained from the differential equation

$$\dot{M} = -\frac{h^2 w}{\sqrt{2RT}} G_P(\delta, h/w)\frac{dp}{dx}, \tag{6.27}$$

that is solved by means of the shooting method. In Eq. (6.27) the dimensionless coefficient G_P depends on the channel height to width ratio h/w, local channel height h and the gas rarefaction parameter (local pressure), which is calculated according to

$$\delta = \frac{hp}{\mu\sqrt{2RT}}. \tag{6.28}$$

It is to note that this rarefaction parameter is inversely proportional to the Knudsen number $\delta \sim 1/Kn$, see Eq. (6.11). The detailed description of this approach may be found in Ref. [68].

It is to underline that contrarily to the analytical approach, presented in Section 6.1.2, this numerical method allows to obtain the mass flow rate for any values of the Knudsen numbers laying from the hydrodynamic to the free molecular flow regime.

In order to compare both approaches, the resulting mass flow rates of carbon dioxide, nitrogen, and argon for several values of the inlet and outlet pressures are given in Tables 6.2 - 6.7 for the diffusor and nozzle flows, respectively. Also, the deviation of the numerical simulation from the experiment is provided in Tables 6.2 - 6.7, too. The experiment is described in the following section.

6.3 Experiment

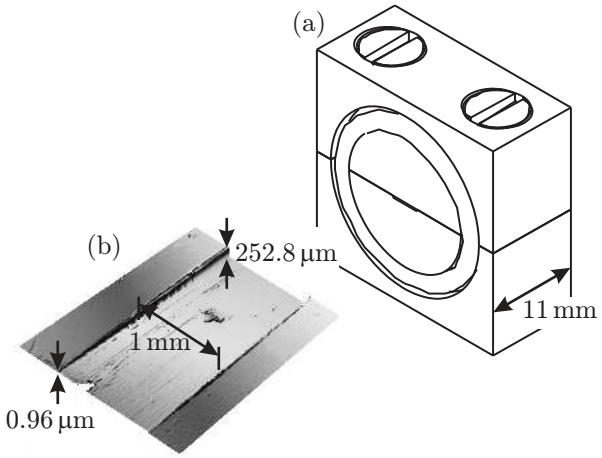

Figure 6.2: Tapered channel used in experiment. The test channel accrues by assembling one aluminum block with a micromilled notch with a plain block (a). The channel length corresponds to the block thickness. High quality optical surfaces act as sealing. The channel with alongside varying height is visualized by optical profilometry (b). This figure is adapted from Ref. [58]

The tapered channel with alongside varying height was manufactured by milling a long notch into a piece of aluminum ($AlMg_3$) using raster fly-cutting. As schematically shown in Fig. 6.2a, the notch was capped with another plain piece of aluminum with high quality optical surface. Both parts were screwed together and sealed by means of the perfectly plain surfaces. All parts were manufactured by the LFM (Laboratory for Precision Machining, University of Bremen) using a Nanotech 350FG (Moore Nanotechnolgy Systems, Keene, NH, USA). The micromilled notch with a significant inclination was visualized by optical profilometry Fig. 6.2b.

The notch of the channel has a length of $L = 11.05 \pm 0.1$,mm which corresponds to

the thickness of the aluminum block. The height is changing from $h_1 = 0.96 \pm 0.18\,\mu m$ to $h_2 = 252.80 \pm 0.16\,\mu m$ while the width of $w = 1007.50 \pm 3.13\,\mu m$ is constant, see also Fig. 6.1. Notch width and depth were measured 200 times using optical profilometry (PL μ2300, Sensofar) and arithmetic mean and uncertainty were calculated. The length was measured by means of direct light microscopy (20 times for calculation of arithmetic mean and uncertainty).

The measurements were conducted by Thomas Veltzke at Center for Environmental Research and Sustainable Technology (UFT), University of Bremen. Detail description of the experimental apparatus is given in Refs. [58].

6.4 Results and discussion

The analytical and numerical simulations are carried out for the tapered channel according to Fig. 6.1. This configuration is slightly different from that used for the measurements which is due to the manufacturing process as described in Chapter 5 of Ref. [58]. From the measurement both inlet and outlet temperatures are identical and therefore the flow can be considered as the isothermal flow and the average temperature value $T_0 = 0.5(T_1 + T_2)$ was taken for the simulations. For a calculation of $\dot{M}$ the velocity slip coefficient σ_p in Eq. (6.8) was set to 1.016 for all three gases. It is to note that this value $\sigma_p \sim 1$ corresponds to the completely diffuse reflection of the molecules from the solid surface. This value increases when the reflection becomes more specular. Some experimental data on the values of the velocity slip for different surfaces and various gases may be found in [57, 183].

6.4.1 Validation of analytical approach

First, expressions (6.18) - (6.22) are used to obtain the analytical solutions in diffusor and nozzle directions. The Variable Hard Sphere model (VHS) [107] is used as the intermolecular potential which leads to the following expression of the k_λ coefficient in Eq. (6.11): $k_\lambda = (7 - 2\omega)(5 - 2\omega)/(15\sqrt{\pi})$. For the viscosity the power law dependence from temperature according to the VHS is adopted

$$\mu = \mu_{ref} \left(\frac{T}{T_{ref}} \right)^{\omega}. \tag{6.29}$$

Here ω is the viscosity index depending on the gas nature. The required parameters ω and μ_{ref} for $T_{ref} = 273.15K$ are stated in Table 6.1.

Table 6.1: Properties of gases used for experiments. The reference viscosities are those for $T_{ref} = 273.15K$. Values are taken from Bird [107].

Gas	$R(\mathrm{J\,kg^{-1}\,K^{-1}})$	$\mu_{ref}(10^{-5}\,\mathrm{Pa\,s})$	ω	k_λ
CO_2	188.96	1.380	0.93	0.607
N_2	296.93	1.656	0.74	0.731
Ar	207.85	2.117	0.81	0.684

Table 6.2: Experimental results obtained in *diffusor* direction on the tapered channel according to Fig. 6.2 with CO_2 as working gas, analytical solution, numerical solution. Measurements were performed in triplicate and arithmetic mean and standard deviation are calculated. The deviation α of the numerical solution to the experimental results is: $|(\dot{M}_{exp}/\dot{M}_{num}) - 1| \cdot 100\%$.

p_1(kPa)	p_2(kPa)	T_0(°C)	$\dot{M}(10^{-9}\ \mathrm{kg\,s^{-1}})$			α(%)
			exp.	anal.	num.	num.
23.0389 ± 0.0963	3.0266 ± 0.0949	20.04	2.411 ± 0.047	2.6041	2.7810	13.3
28.3679 ± 0.0852	3.3626 ± 0.0943	20.03	3.404 ± 0.045	3.5473	3.7466	9.1
33.7133 ± 0.0746	3.7084 ± 0.0721	20.05	4.513 ± 0.047	4.6146	4.8329	6.6
39.0586 ± 0.0887	4.0720 ± 0.0768	20.05	5.733 ± 0.049	5.8039	6.0353	5.0
44.4236 ± 0.0821	4.4461 ± 0.0797	20.05	7.067 ± 0.059	7.1204	7.3634	4.0
55.1305 ± 0.0816	5.1696 ± 0.0639	20.07	10.049 ± 0.074	10.1177	10.3803	3.2
66.1574 ± 0.0712	5.9504 ± 0.0662	20.06	13.653 ± 0.080	13.7189	13.9981	2.5

As shown in Fig. 6.3 the analytical, numerical, and experimental results are in good agreement for the diffusor case. In the nozzle direction, however, the both numerical and analytical approaches systematically overestimate the experimental results, see Tables 6.2 - 6.7. For all gases it can be observed that the mass flow rate in nozzle direction is slightly but significantly higher compared to the diffusor direction. This is a reasonable result since the amount of molecules entering the channel aperture (cross-sectional area) is higher. Nevertheless, the finding is indeed intriguing because it vanishes in the hydrodynamic regime [65, 58] and is postulated to be absent in the free molecular regime [62, 68].

Further, the reasonable agreement of the analytical model to the numerical model and the experiments (see Tables 6.2 - 6.7 and Fig. 6.3) indicates the validity of the presented approach. It is noteworthy that the analytical solutions are obtained here in the Knudsen number range from 0.0471 to 0.2263, where the highest value is really in the limit of the applicability of the approach. However, even for this relatively high Knudsen number the agreement with the measurements is surprisingly good.

Table 6.3: Experimental results obtained in *nozzle* direction on the tapered channel according to Fig. 6.2 with CO_2 as working gas, analytical solution, numerical solution. Measurements were performed in triplicate and arithmetic mean and standard deviation are calculated. The deviation α of the numerical solution to the experimental results is: $|(\dot{M}_{exp}/\dot{M}_{num}) - 1| \cdot 100\%$.

p_1(kPa)	p_2(kPa)	T_0(°C)	$\dot{M}(10^{-9}$ kg s$^{-1})$			α(%)
			exp.	anal.	num.	num.
23.0154 ± 0.0459	3.0140 ± 0.0358	20.10	2.588 ± 0.042	3.1587	3.2192	19.6
28.3679 ± 0.0530	3.3753 ± 0.0374	20.10	3.656 ± 0.052	4.2626	4.3396	15.8
33.7229 ± 0.0596	3.7466 ± 0.0415	20.10	4.847 ± 0.046	5.4891	5.5829	13.2
39.0837 ± 0.0634	4.1230 ± 0.0514	20.07	6.139 ± 0.061	6.8407	6.9516	11.7
44.4620 ± 0.0603	4.5079 ± 0.0442	20.07	7.542 ± 0.053	8.3193	8.4468	10.7
55.1912 ± 0.0522	5.2426 ± 0.0376	20.08	10.662 ± 0.065	11.6449	11.8047	9.7
66.2069 ± 0.0694	6.0228 ± 0.0435	20.05	14.354 ± 0.099	15.5730	15.7628	8.9

Table 6.4: Experimental results obtained in *diffusor* direction on the tapered channel according to Fig. 6.2 with N_2 as working gas, analytical solution, numerical solution. Measurements were performed in triplicate and arithmetic mean and standard deviation are calculated. The deviation α of the numerical solution to the experimental results is: $|(\dot{M}_{exp}/\dot{M}_{num}) - 1| \cdot 100\%$.

p_1(kPa)	p_2(kPa)	T_0(°C)	$\dot{M}(10^{-9}$ kg s$^{-1})$			α(%)
			exp.	anal.	num.	num.
25.5150 ± 0.0955	3.3040 ± 0.0581	20.08	1.722 ± 0.044	2.0490	2.2330	22.9
31.4279 ± 0.0680	3.6811 ± 0.0295	20.08	2.431 ± 0.040	2.7513	2.9595	17.9
37.3339 ± 0.0457	4.0762 ± 0.0531	20.05	3.223 ± 0.011	3.5326	3.7636	14.4
43.2610 ± 0.0577	4.4717 ± 0.0475	20.06	4.095 ± 0.013	4.3972	4.6453	11.8
49.1804 ± 0.0175	4.8795 ± 0.0108	20.07	5.048 ± 0.034	5.3408	5.6053	9.9
61.0077 ± 0.0474	5.6739 ± 0.0210	20.06	7.178 ± 0.043	7.4699	7.7561	7.5
73.2224 ± 0.0176	6.5315 ± 0.0254	20.06	9.751 ± 0.023	10.0061	10.3127	5.4

Table 6.5: Experimental results obtained in *nozzle* direction on the tapered channel according to Fig. 6.2 with N_2 as working gas, analytical solution, numerical solution. Measurements were performed in triplicate and arithmetic mean and standard deviation are calculated. The deviation α of the numerical solution to the experimental results is: $|(\dot{M}_{exp}/\dot{M}_{num}) - 1| \cdot 100\%$.

p_1(kPa)	p_2(kPa)	T_0(°C)	$\dot{M}(10^{-9}$ kg s$^{-1})$			α(%)
			exp.	anal.	num.	num.
25.4982 ± 0.0234	3.3167 ± 0.0131	20.08	1.848 ± 0.027	2.5415	2.5966	28.8
31.4365 ± 0.0376	3.7172 ± 0.0181	20.12	2.611 ± 0.019	3.3859	3.4543	24.4
37.0293 ± 0.0284	4.0850 ± 0.0142	20.10	3.462 ± 0.019	4.2574	4.3394	20.2
42.9162 ± 0.0304	4.4908 ± 0.0212	20.26	4.384 ± 0.034	5.2477	5.3447	18.0
48.8057 ± 0.0230	4.9114 ± 0.0696	20.26	5.387 ± 0.012	6.3192	6.4314	16.2
60.6650 ± 0.0216	5.7264 ± 0.0327	20.31	7.615 ± 0.023	8.7218	8.8644	14.1
72.7721 ± 0.0331	6.5730 ± 0.0234	20.09	10.252 ± 0.020	11.5187	11.6916	12.3

Table 6.6: Experimental results obtained in *diffusor* direction on the tapered channel according to Fig. 6.2 with Ar as working gas, analytical solution, numerical solution. Measurements were performed in triplicate and arithmetic mean and standard deviation are calculated. The deviation α of the numerical solution to the experimental results is: $|(\dot{M}_{exp}/\dot{M}_{num}) - 1| \cdot 100\%$.

p_1(kPa)	p_2(kPa)	T_0(°C)	$\dot{M}(10^{-9}$ kg s$^{-1})$			α(%)
			exp.	anal.	num.	num.
24.1557 ± 0.0517	3.1894 ± 0.0273	20.29	1.855 ± 0.035	2.2111	2.4305	23.7
29.8508 ± 0.0545	3.5046 ± 0.0275	20.30	2.619 ± 0.053	2.9675	3.2207	18.7
35.0942 ± 0.0649	3.8842 ± 0.0242	20.30	3.494 ± 0.049	3.7328	4.0099	12.9
40.4200 ± 0.0402	4.2844 ± 0.0281	20.29	4.440 ± 0.039	4.5815	4.8817	9.0
46.0627 ± 0.0674	4.6966 ± 0.0457	20.30	5.459 ± 0.057	5.5599	5.8788	7.1
57.1809 ± 0.0531	5.4635 ± 0.0570	20.30	7.762 ± 0.072	7.7283	8.0797	3.9
68.6523 ± 0.0605	6.2922 ± 0.0259	20.48	10.537 ± 0.073	10.2871	10.661	1.2

Table 6.7: Experimental results obtained in *nozzle* direction on the tapered channel according to Fig. 6.2 with Ar as working gas, analytical solution, numerical solution. Measurements were performed in triplicate and arithmetic mean and standard deviation are calculated. The deviation α of the numerical solution to the experimental results is: $|(\dot{M}_{exp}/\dot{M}_{num}) - 1| \cdot 100\%$.

p_1(kPa)	p_2(kPa)	T_0(°C)	$\dot{M}(10^{-9}$ kg s$^{-1})$			α(%)
			exp.	anal.	num.	num.
23.9157 ± 0.0294	3.2167 ± 0.0346	20.08	1.998 ± 0.023	2.7266	2.7895	28.4
29.4861 ± 0.0311	3.5476 ± 0.0420	20.06	2.822 ± 0.023	3.6227	3.6999	23.7
34.8385 ± 0.0409	3.9118 ± 0.0374	20.04	3.759 ± 0.032	4.5532	4.6453	19.1
40.3653 ± 0.0440	4.2902 ± 0.0286	20.06	4.762 ± 0.048	5.5904	5.6985	16.4
46.0374 ± 0.0501	4.6987 ± 0.0596	20.31	5.832 ± 0.043	6.7281	6.8533	14.9
57.1578 ± 0.0368	5.4656 ± 0.0331	20.33	8.245 ± 0.045	9.2108	9.3707	12.0
68.6183 ± 0.0449	6.2951 ± 0.0431	20.33	11.092 ± 0.056	12.096	12.2903	9.8

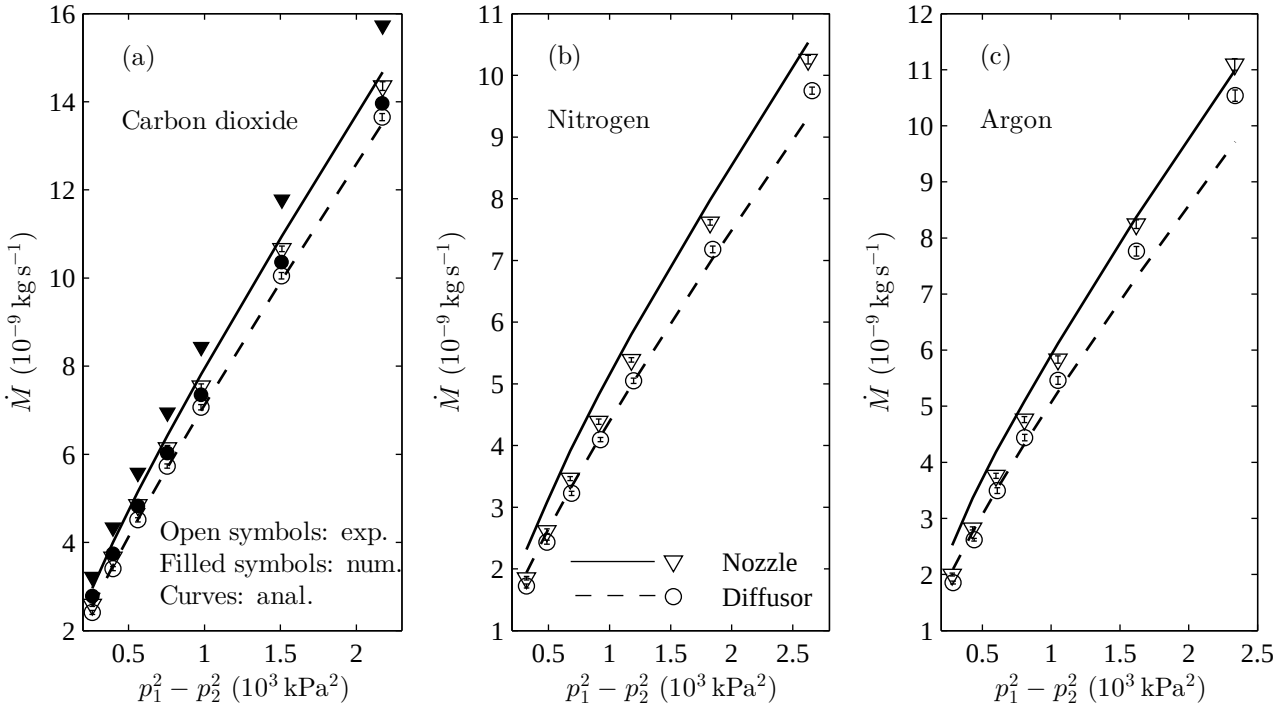

Figure 6.3: Experimental data in comparison to the proposed analytical approach and data obtained numerically using method of Ref. [68]: (a) carbon dioxide; (b) nitrogen; (c) argon. The curves for the analytical solutions in nozzle direction (solid line) and diffusor direction (dashed line) are obtained using expressions (6.18 - 6.22). Measurements were performed in triplicate under isothermal conditions at 20°C. Error bars are throughout smaller than symbols. Data are additionally provided in Tables 6.2 - 6.7

6.4.2 Gas flow diodicity

As shown by means of Fig. 6.3 the measured flow in nozzle direction is throughout higher compared to the flow in diffusor direction. To quantify the disparity of the permeability in both directions, we use the diodicity D given by Eq. (6.23). For the calculation of the experimental diodicity the mean values of three identical measurement series were used. Since Eq. (6.23) contains six measured values, the standard deviation of D is calculated according to the Gaussian error propagation:

$$\xi(D) = \sqrt{\sum_{i=1}^{6} \left(\frac{\partial D}{\partial z_i} \xi(z_i) \right)^2}; \quad z = p_1^{noz}, p_2^{noz}, p_1^{dif}, p_2^{dif}, \dot{M}^{noz}, \dot{M}^{dif}. \tag{6.30}$$

We want to show and discuss the diode effect as a function of the gaseous rarefaction. Therefore we use the Knudsen number according to Eq. (6.11) as abscissa value. To allow for comparison of nozzle and diffusor direction, we define Kn by means of the average pressure values of nozzle and diffusor directions $\bar{p} = 0.25(p_1^{noz} + p_2^{noz} + p_1^{dif} + p_2^{dif})$. Thus, $\bar{Kn}$ is a function of five measured

values having errors and its uncertainty is obtained as

$$\xi(\bar{Kn}) = \sqrt{\sum_{i=1}^{5}\left(\frac{\partial \bar{Kn}}{\partial z_i}\xi(z_i)\right)^2}; \quad z = p_1^{noz}, p_2^{noz}, p_1^{dif}, p_2^{dif}, h_1. \tag{6.31}$$

All values obtained for D (as a function of $\bar{Kn}$) by means of the numerical approach and experiments are provided in Tables 6.8 - 6.10.

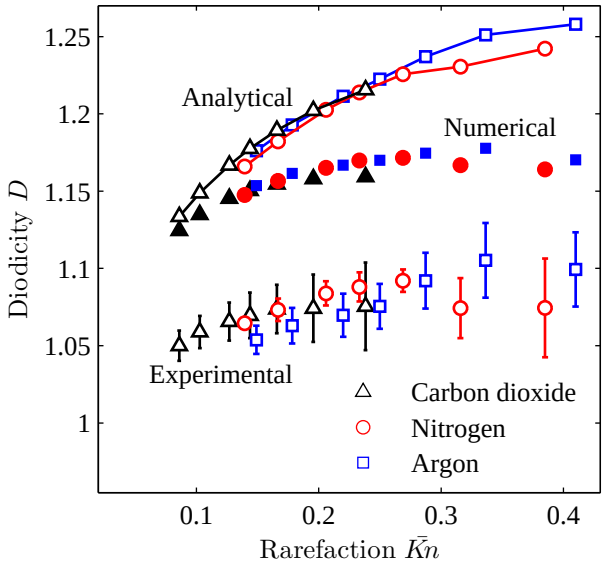

Figure 6.4: Diodicity versus mean Knudsen number. Analytical data (interconnected with lines), numerical data (filled symbols) and experimental data (open symbols) are prepared according to Eqs. (6.11) and (6.23) with values stated in Tables 6.2-6.7. The experimental uncertainty of D is expressed by vertical errorbars that are calculated according to Eqs. (6.30). The horizontal errorbars are not shown but the experimental uncertainty of $\bar{Kn}$ according to Eqs. (6.31) is tabulated. All depicted values are provided in Tables 6.8-6.10.

In Fig. 6.4 the diodicity D is plotted versus the average Knudsen number $\bar{Kn}$ for all three working gases. The analytical solutions obtained by means of Eq. (6.24) are given by solid lines and the numerical results obtained applying model of Ref. [68] are indicated by filled symbols. The experimental results indicated by open symbols and error bars are calculated using Eqs. (6.11) and (6.23). For the three considered gases the analytical and the numerical approach are in qualitative agreement to the experiment since both theoretical approaches show that the diode effect increases with gaseous rarefaction in slip regime.

When comparing first the numerical approach with the experiments we can see that D approaches a constant level at approx. $\bar{Kn} = 0.15$. It is to note that the numerical approach reproduces the experimental behavior very well: the numerical results exhibit an offset of approx. 8, (see Tables 6.8 - 6.10) that is quite constant. The offset is explained by the larger

Table 6.8: Mean Knudsen number and experimental and numerically calculated diodicity of carbon dioxide (CO_2) at 20.07°C. $\bar{Kn}$ and D are calculated according to Eqs. (6.11), (6.23), (6.30) and (6.31) using values stated in Tables 6.1, 6.2 and 6.3. The deviation α of the numerical solution to the experimental results is: $|(D_{\text{exp}}/D_{\text{num}}) - 1| \cdot 100\%$.

$\bar{Kn}$	D		$\alpha(\%)$
	exp.	num.	num.
0.2382 ± 0.0447	1.0755 ± 0.0284	1.1598	7.27
0.1955 ± 0.0367	1.0742 ± 0.0218	1.1584	7.27
0.1657 ± 0.0311	1.0737 ± 0.0157	1.1548	7.02
0.1437 ± 0.0270	1.0696 ± 0.0148	1.1506	7.04
0.1268 ± 0.0238	1.0657 ± 0.0123	1.1455	6.96
0.1028 ± 0.0193	1.0588 ± 0.0105	1.1350	6.71
0.0860 ± 0.0161	1.0500 ± 0.0098	1.1246	6.63

Table 6.9: Mean Knudsen number and experimental and numerically calculated diodicity of nitrogen (N_2) at 20.07°C. $\bar{Kn}$ and D are calculated according to Eqs. (6.11), (6.23), (6.30) and (6.31) using values stated in Tables 6.1, 6.4 and 6.5. The deviation α of the numerical solution to the experimental results is: $|(D_{\text{exp}}/D_{\text{num}}) - 1| \cdot 100\%$.

$\bar{Kn}$	D		$\alpha(\%)$
	exp.	num.	num.
0.3849 ± 0.0722	1.0745 ± 0.0319	1.1646	7.74
0.3157 ± 0.0592	1.0743 ± 0.0194	1.1669	7.93
0.2688 ± 0.0504	1.0920 ± 0.0073	1.1723	6.85
0.2332 ± 0.0437	1.0880 ± 0.0094	1.1694	6.96
0.2059 ± 0.0386	1.0838 ± 0.0078	1.1654	7.00
0.1668 ± 0.0313	1.0732 ± 0.0072	1.1562	7.18
0.1394 ± 0.0261	1.0646 ± 0.0034	1.1480	7.27

Table 6.10: Mean Knudsen number and experimental and numerically calculated diodicity of Argon (Ar) at 20.07°C. $\bar{Kn}$ and D are calculated according to Eqs. (6.11), (6.23), (6.30) and (6.31) using values stated in Tables 6.1, 6.6 and 6.7. The deviation α of the numerical solution to the experimental results is: $|(D_{\text{exp}}/D_{\text{num}}) - 1| \cdot 100\%$.

$\bar{Kn}$	D		$\alpha(\%)$
	exp.	num.	num.
0.4097 ± 0.0768	1.0993 ± 0.0241	1.1716	6.17
0.3362 ± 0.0630	1.1053 ± 0.0241	1.1782	6.19
0.2871 ± 0.0538	1.0921 ± 0.0181	1.1759	7.13
0.2498 ± 0.0468	1.0755 ± 0.0145	1.1706	8.12
0.2200 ± 0.0413	1.0697 ± 0.0140	1.1671	8.34
0.1783 ± 0.0334	1.0630 ± 0.0115	1.1607	8.42
0.1491 ± 0.0280	1.0538 ± 0.0091	1.1540	8.68

systematic overestimation of the nozzle experimental data discussed in the context of Fig. 6.3.

In contrast, the analytical approach can not describe the attenuation of D. In the full slip regime the analytical solution is in reasonable agreement to the experimental results that are slightly overestimated. Although, with increasing $\bar{Kn}$ the overestimation would become very large. This might be due to the limited validity of the analytical approach. As already mentioned in Section 6.4.1, the applicability of the approach concerning rarefaction is at its very limit.

Nevertheless, the theoretical and experimental finding perfectly confirms our hypothesis and verifies the reliability of both approaches for the considered Knudsen number range. From the analysis presented here we are sure that the gas flow diode effect is not an artifact because it is found analytically, numerically, and experimentally. Furthermore, the finding is in agreement with results obtained on tapered silicon-etched microchannels [65, 58].

A complete physic explanation of the diode effect is probably complex. But some comments may be proposed. The diode feature does not exist in the hydrodynamic regime and vanish in the free molecular regime. Thus, this effect appears when a gas slip velocity and a sufficient gas density allow a transfer, more or less important, of macroscopic momentum from the wall to the gas flow. However, it would be more difficult to explain clearly why the nozzle configuration promotes larger mass flow rate than the diffusor one.

6.5 Conclusions

In this work we apply three approaches, an experimental, an analytical and a numerical one, that allow us to confirm, describe and understand the phenomenon of gas flow diodicity. By means of the two theoretical approaches we could predict the mass flow rate through a long channel with variable rectangular cross section for arbitrary pressure gradients. Solutions obtained by means of both models are compared with one another and with experimental data for validation purpose.

The analytical approach based on the solution of the Stokes equation subjected to the velocity slip boundary condition is developed for the slip flow regime. The numerical approach is based on the implementation of the solution of the linearized S-model kinetic equation obtained previously in [106, 68]. For the experiments we used single-gas measurements obtained on a rectangular channel with slightly varying cross section. The test channel was manufactured by micro-milling (raster fly-cutting). It is noteworthy that this is a novel method for production of test channels for research on gaseous microflows.

All the numerical and analytical results are in good agreement to the experimental ones although experimental data are systematically overestimated in the nozzle case.

Moreover, we can show that the mass flow rate is significantly higher when the tapered channel is perfused like a nozzle. It can therefore be stated that under moderately rarefied conditions micro-sized ducts with alongside varying cross section act as a gas flow diode. The theoretically and experimentally analyzed diode effect increases with gaseous rarefaction whereby both presented models can predict that effect qualitatively.

The analyzed diode effect is primarily a physical phenomenon and hence an academic issue. However, it might be applicable in future MEMS if the diodicity can be pushed to pronounced values. Probable applications are devices for dosing and pumping gas streams or actual diodes that only allows the flow in one direction.

Chapter 7

Couette and Fourier flows of binary gaseous mixture

In many practical applications like the vacuum technology, porous media, and chemical industry, the information about the heat/mass transfer of rarefied gas mixtures is indispensable. Benchmark test cases are of great importance since they can help to validate new numerical models developed for the description of gas flows or test the validity of existing approaches under various physical conditions. Here, Couette and Fourier flows between two parallel plates are chosen as benchmark test cases as they are the classical problems of fluid mechanics. Although solutions for the single-species gas can be found in books [69] and [70], only few papers are dedicated to gas mixtures.

The plane Couette flow of binary gas mixture is firstly studied [71, 72, 73, 74, 75] based on the kinetic models of the Boltzmann equation, such as the Hamel model [13] for Maxwellian molecules and the McCormack model for general intermolecular potentials [14]. Notably, based on the McCormack model, the influence of intermolecular interactions on the velocity and shear stress for three mixtures (Ne-Ar, He-Ar, and He-Xe) [74] and the influence of gas-surface interaction on the flow properties of the He-Ar mixture between Molybdenum and Tantalum plates are investigated [75]. Later, the linearized Boltzmann equation (LBE) for hard-sphere (HS) molecules is solved by an analytical version of the discrete-ordinates (ADO) method [76], and the accuracy of the McCormack is assessed for He-Ar mixture: the McCormack model produces accurate ($1 \sim 3$ figures of accuracy) shear stress of each component and velocity of the heavier species [75, 76], however, the velocity of the lighter species and especially the heat flux significantly deviate from the LBE results (well above 100% for some entries).

Very few papers are devoted to the heat transfer through a gas mixture. The plane Fourier flow is firstly simulated by solving the nonlinear Boltzmann equation using an iterative finite-difference technique [77]. Later, the heat transfer between two plane plates with small temperature difference is studied using the McCormack model [78] and LBE [79]. Surprisingly, the normalized heat flux for Ne-Ar and He-Xe mixtures obtained from the linearized equations

are found to agree with results from the full Boltzmann equation, with the maximum relative deviation being about 4%. However, between the McCormack model and LBE, there are large differences in the density and temperature profiles: for density, up to 15% for Ne-Ar mixture and 51% for He-Xe mixture are observed, while for temperature, the maximum differences are 12% and 20% for Ne-Ar and He-Xe mixtures, respectively. The influence of intermolecular potentials on the heat flux between two parallel plates for three binary mixtures of nobles gases (Ne-Ar, He-Ar, He-Xe) is studied based on the McCormack model [80]: the heat flux is sensitive to the intermolecular potential, and the difference between the HS and realistic potentials [81] can reach 15% near the hydrodynamic regime.

To summarize, it is only two papers devoted to the comparison between the McCormack model and the LBE for the mixtures of Ne-Ar and He-Xe [79] and He-Ar [76]. Therefore, new systematic comparisons between the McCormack model and LBE will be useful for the further development of the numerical tools for the simulation of gas mixture flows. In the present study, the Couette and Fourier flows are considered for two types of the binary gas mixture composition.

7.1 Problem statement

(a) Couette flow

(b) Fourier flow

Figure 7.1: Two parallel plate configuration

Consider a binary mixture of monatomic gases, where the mass of a molecule of the first (second) component is m_1 (m_2), and the corresponding number density is n_1 (n_2). Without loss of generality, we assume $m_1 < m_2$. The gas mixture is confined between two parallel plates situated at $y' = \pm H/2$, see Fig. 7.1. In Couette flow, the two plates with temperature T_0 move in opposite directions with the speed $U/2$. In Fourier flow, both plates are stationary, but the plate at $y' = -H/2$ has a temperature of $T_0 - \Delta T/2$, while the other one has a temperature $T_0 + \Delta T/2$. The temperature difference ΔT is much smaller than the equilibrium gas temperature T_0, and the relative speed U is much smaller than the most probable molecular velocity v_0 of the mixture, so the gas mixture deviates only slightly from equilibrium. The most probable molecular velocity of the mixture is defined as:

$$\upsilon_0 = \sqrt{\frac{2kT_0}{m}}, \tag{7.1}$$

where k is the Boltzmann constant, $m = C_0 m_1 + (1 - C_0)\, m_2$ is the mean molecular mass of the mixture, with C_0 being the equilibrium mole fraction (molar concentration):

$$C_0 = \frac{n_{0_1}}{n_{0_1} + n_{0_2}}. \tag{7.2}$$

In Couette flow, we are interested in the profiles of the shear stress P'_{xy} and flow velocity u'_x, which are defined as

$$P'_{xy} = C_0 P'_{xy_1} + (1 - C_0)\, P'_{xy_2}, \qquad u'_x = \frac{m_1 n_{0_1} u'_{x_1} + m_2 n_{0_2} u'_{x_2}}{m_1 n_{0_1} + m_2 n_{0_2}}, 7.3 \tag{7.3}$$

For further derivation it is convenient to introduce the following dimensionless quantities

$$y = \frac{y'}{H}, \qquad \mathbf{c}_\alpha = \sqrt{\frac{m_\alpha}{2kT_0}}\mathbf{v}_\alpha, \qquad u_\alpha = \frac{u'_{\alpha_x}}{U}, \qquad u = \frac{u'_x}{U}, \qquad P = -\frac{\upsilon_0}{2Up_0}P'_{xy}, \tag{7.4}$$

$\mathbf{v}_\alpha$ is molecular velocity of the species α, p_0 is the equilibrium pressure.

In Fourier flow, we are interested in the dimensionless heat flux

$$q_y = \frac{q'_y}{p_0 \upsilon_0}\frac{T_0}{\Delta T}, \tag{7.5}$$

as well as the profiles of the deviated temperature, density, and concentration

$$T(y) = \frac{T'(y) - T_0}{\Delta T}, \quad n(y) = \frac{n'(y) - n_0}{n_0}\frac{T_0}{\Delta T}, \quad C(y) = \frac{C'(y) - C_0}{C_0}\frac{T_0}{\Delta T}, \tag{7.6}$$

where the molar concentration of the mixture

$$C' = \frac{n'_1}{n'_1 + n'_2}. \tag{7.7}$$

and n'_α $(\alpha = 1, 2)$ is the number density of species α.

7.2 Kinetic equation

The Boltzmann kinetic equation is used in the simulation of both problems at arbitrary rarefaction parameter. Since the plate's velocities are small compared to the most probable velocity of the mixture (Couette flow) and only small temperature difference between the plate's surfaces is considered (Fourier flow), the Boltzmann equation can be linearized by classical manner as

$$f_\alpha = f_\alpha^M(\mathbf{c}_\alpha)\left[1 + h_\alpha(y, \mathbf{c}_\alpha)\varepsilon\right], \quad \alpha = 1, 2, \quad \varepsilon \ll 1, \tag{7.8}$$

where $\varepsilon = U/v_0$ for the Couette flow and $\varepsilon = \Delta T/T_0$ for the Fourier flow, f_α^M is the equilibrium Maxwellian distribution function:

$$f_\alpha^M(\mathbf{c}_\alpha) = n_{0_\alpha}\left(\frac{m_\alpha}{2\pi k T_0}\right)^{3/2} \exp\left(-\mathbf{c}_\alpha^2\right), \tag{7.9}$$

and $h_\alpha(y, \mathbf{c}_\alpha)$ is the perturbation function, which obeys the following two coupled linearized Boltzmann equations [70]

$$c_{\alpha y}\frac{\partial h_\alpha}{\partial y} = H\sqrt{\frac{m_\alpha}{2kT_0}}\sum_{\beta=1}^{2}\hat{L}_{\alpha\beta}h, \tag{7.10}$$

where $\hat{L}_{\alpha\beta}h$ is the linearized collision term. Two models are used here for the linearized collision term: the classical expression of the linearized collision term of the Boltzmann equation [70] and its approximation in form of the McCormack model [14].

7.2.1 McCormack model for the collisional term

The McCormack model collisional term $L_{\alpha\beta}$ was obtained by requiring that the first three moments of the model collision operator be the same as the corresponding moment of the full collision operator calculated with the third order approximation to the distribution function. The third-order collision term of the McCormack model has the following form

$$
\begin{aligned}
L_{\alpha\beta} = &-\gamma_{\alpha\beta}h_\alpha+\gamma_{\alpha\beta}n_\alpha \\
&+2\sqrt{\frac{m_\alpha}{m}}\left[\gamma_{\alpha\beta}u_{\alpha i}-\upsilon_{\alpha\beta}^{(1)}\left(u_{\alpha i}-u_{\beta i}\right)-\frac{\upsilon_{\alpha\beta}^{(2)}}{2}\left(q_{\alpha i}-\frac{m_\alpha}{m_\beta}q_{\beta i}\right)\right]c_{\alpha i} \\
&+\left[\gamma_{\alpha\beta}T_\alpha-2\frac{m_{\alpha\beta}}{m_\beta}\left(T_\alpha-T_\beta\right)\upsilon_{\alpha\beta}^{(1)}\right]\left(c_\alpha^2-\frac{3}{2}\right) \\
&+4\left[\left(\gamma_{\alpha\beta}-\upsilon_{\alpha\beta}^{(3)}\right)P_{\alpha xy}+\upsilon_{\alpha\beta}^{(4)}P_{\beta xy}\right]c_{\alpha x}c_{\alpha y} \\
&+2\left[\left(\gamma_{\alpha\beta}-\upsilon_{\alpha\beta}^{(3)}\right)P_{\alpha yy}+\upsilon_{\alpha\beta}^{(4)}P_{\beta yy}\right]\left(c_{\alpha y}^2-\frac{1}{2}c_{\alpha x}^2-\frac{1}{2}c_{\alpha z}^2\right) \\
&+\frac{4}{5}\sqrt{\frac{m_\alpha}{m}}\left[\left(\gamma_{\alpha\beta}-\upsilon_{\alpha\beta}^{(5)}\right)q_{\alpha i}+\upsilon_{\alpha\beta}^{(6)}\sqrt{\frac{m_\beta}{m_\alpha}}q_{\beta i}-\frac{5}{4}\upsilon_{\alpha\beta}^{(2)}\left(u_{\alpha i}-u_{\beta i}\right)\right]c_{\alpha i}\left(c_\alpha^2-\frac{5}{2}\right),
\end{aligned}
\tag{7.11}
$$

where $\alpha,\beta=1,2$ and $i=x,y$ for Couette and Fourier flows, respectively; the quantities $\upsilon_{\alpha\beta}^{(n)}$ are given by Eqs. (A.1).

The parameters $\gamma_{\alpha\beta}$ are proportional to the collision frequency between the species α and β and appear in the collision term (7.11) only in the combinations as $\gamma_1=\gamma_{11}+\gamma_{12}$ and $\gamma_2=\gamma_{21}+\gamma_{22}$, so it is sufficient to define γ_1 and γ_2. The collision frequencies and the viscosity coefficients can be related in the same form as for the S-model kinetic equation [11, 184, 74]:

$$
\gamma_\alpha=\frac{p_{0_\alpha}}{\mu_\alpha},\qquad \alpha=1,2, \tag{7.12}
$$

where $p_{0_\alpha}=n_{0_\alpha}kT_0$ is the equilibrium partial pressure and μ_α is the partial viscosity given as

$$
\mu_\alpha=p_{0_\alpha}\frac{S_\beta+\upsilon_{\alpha\beta}^{(4)}}{S_\alpha S_\beta-\upsilon_{\alpha\beta}^{(4)}\upsilon_{\beta\alpha}^{(4)}},\quad S_\alpha=\upsilon_{\alpha\alpha}^{(3)}-\upsilon_{\alpha\alpha}^{(4)}+\upsilon_{\alpha\beta}^{(3)},\quad \alpha=1,2\quad\text{and}\quad\beta\neq\alpha. \tag{7.13}
$$

The viscosity of the mixture can be found as the sum of the partial viscosities of the species: $\mu=\mu_1+\mu_2$.

When the perturbation functions h_α are known, the macroscopic flow characteristics are calculated as follows

$$
\begin{aligned}
n_\alpha &= \frac{1}{\pi^{3/2}}\sqrt{\frac{m}{m_\alpha}}\int h_\alpha \exp\left(-\boldsymbol{c}_\alpha^2\right) d\boldsymbol{c}_\alpha,\\
u_{\alpha i} &= \frac{1}{\pi^{3/2}}\sqrt{\frac{m}{m_\alpha}}\int h_\alpha c_{\alpha i} \exp\left(-\boldsymbol{c}_\alpha^2\right) d\boldsymbol{c}_\alpha,\\
P_{\alpha xy} &= \frac{1}{\pi^{3/2}}\int h_\alpha c_{\alpha x} c_{\alpha y} \exp\left(-\boldsymbol{c}_\alpha^2\right) d\boldsymbol{c}_\alpha,\\
P_{\alpha yy} &= \frac{1}{\pi^{3/2}}\int h_\alpha \left(c_{y\alpha}^2 - \frac{1}{3}c_\alpha^2\right) \exp\left(-\boldsymbol{c}_\alpha^2\right) d\boldsymbol{c}_\alpha,\\
T_\alpha &= \frac{1}{\pi^{3/2}}\int h_\alpha \left(\frac{2}{3}c_\alpha^2 - 1\right) \exp\left(-\boldsymbol{c}_\alpha^2\right) d\boldsymbol{c}_\alpha,\\
q_{\alpha i} &= \frac{1}{\pi^{3/2}}\sqrt{\frac{m}{m_\alpha}}\int h_\alpha c_{\alpha i} \left(\boldsymbol{c}_\alpha^2 - \frac{5}{2}\right) \exp\left(-\boldsymbol{c}_\alpha^2\right) d\boldsymbol{c}_\alpha.
\end{aligned}
\tag{7.14}
$$

In addition to the shear stress and the velocity of the mixture, Eq. (7.3), the other mixture's quantities are defines as follows

$$
\begin{aligned}
u(y) =& \frac{C_0 m_1 u_1(y) + (1-C_0) m_2 u_2(y)}{m},\\
T(y) =& C_0 T_1(y) + (1-C_0) T_2(y),\\
q(y) =& C_0 q_1(y) + (1-C_0) q_2(y),\\
n(y) =& C_0 n_1(y) + (1-C_0) n_2(y),\\
C(y) =& (1-C_0)(n_1(y) - n_2(y)).
\end{aligned}
\tag{7.15}
$$

7.2.2 Boundary conditions

The Maxwell diffuse-specular boundary condition is used to describe the gas-wall interaction. For Couette flow the boundary conditions have the following forms

$$
\begin{aligned}
h^+_{\alpha(y=1/2)} &= \left(1 - a_\alpha^{y=1/2}\right) h^-_{\alpha(y=1/2)} + a_\alpha^{y=1/2}\sqrt{\frac{m_\alpha}{m}} c_{\alpha x},\\
h^+_{\alpha(y=-1/2)} &= \left(1 - a_\alpha^{y=-1/2}\right) h^-_{\alpha(y=-1/2)} - a_\alpha^{y=-1/2}\sqrt{\frac{m_\alpha}{m}} c_{\alpha x},
\end{aligned}
\tag{7.16}
$$

where $\alpha = 1, 2$, $a_\alpha^{y=\pm 1/2}$ are the accommodation coefficients of species α on the up and down plate, respectively, the superscripts $+$ and $-$ of the perturbation function h_α in (7.16) refer to the outgoing and incoming molecules with respect to the surfaces, respectively.

In the case of Fourier flow the boundary conditions read

$$
\begin{aligned}
h^{+}_{\alpha(y=1/2)} &= \left(1-a_{\alpha}^{y=1/2}\right)\sqrt{\frac{m_\alpha}{m}}h^{-}_{\alpha(y=1/2)} + a_{\alpha}^{y=1/2}\left(n_{\alpha}^{y=1/2} - \frac{3}{4} + \frac{1}{2}c_{\alpha}^{2}\right), \\
h^{+}_{\alpha(y=-1/2)} &= \left(1-a_{\alpha}^{y=-1/2}\right)\sqrt{\frac{m_\alpha}{m}}h^{-}_{\alpha(y=-1/2)} + a_{\alpha}^{y=-1/2}\left(n_{\alpha}^{y=-1/2} + \frac{3}{4} - \frac{1}{2}c_{\alpha}^{2}\right),
\end{aligned}
\tag{7.17}
$$

where $\alpha = 1, 2$, $n_{\alpha}^{y=\pm 1/2}$ the number density on the surfaces, which is calculated from non-penetration conditions.

7.2.3 Numerical techniques

The kinetic equations (7.9) are solved for two expressions of the linearized collision term: the McCormack model collision term, equation (7.11), [14] and classical linearized Boltzmann collision term [70].

The solve the kinetic equations (7.9) with the the linearized collision term: the McCormack model [14] collision term, equation (7.11), the discrete velocity method (DVM) is used [74]. To reduce the computational efforts the projection procedure was implemented for the molecular velocity in z direction. The first order of accuracy numerical scheme is used in the physical space and the equations are solved by the fixed point method. The number of points (uniform grid) in the full physical space (N_y) and in the molecular velocity space (N_{c_x}, N_{c_y}) are $N_y \times N_{c_x} \times N_{c_y} = 400 \times 50 \times 50$. The convergence criterion for Couette flow in the form

$$
\int_{-1/2}^{1/2} u_x^{l+1}/u_x^{l} dy < \varepsilon \tag{7.18}
$$

is used, with $\varepsilon = 10^{-10}$, where l is the iteration index. For Fourier flow, the quantity q_y is used instead of u_x for the same convergence criterion (7.18).

7.3 Results and discussion

Both Couette and Fourier flows are determined by the following rarefaction parameter:

$$
\delta_0 = \frac{H p_0}{\mu \upsilon_0}, \tag{7.19}
$$

where μ, p_0, and υ_0 are the viscosity of the mixture, equilibrium gas pressure, and the most probable molecular velocity (7.1). For comparison purpose we introduce here the Knudsen

number Kn defined as following

$$Kn = \frac{1}{Hn_{av}d_1^2\sqrt{2}\pi}, \tag{7.20}$$

where d_1 is the molecular diameter of the lighter specie, n_{av} is the averaged over the distance between plates the number density of the mixture.

Two kinds of gas mixture, *i.e.* Ne-Ar and He-Xe, are chosen in this comparative study to see the influence of the molecular mass ratio. Three values of the mole fraction $C_0 = 0.1, 0.5, 0.9$ are considered for three values of rarefaction parameter $\delta_0 = 0.1, 1, 10$. The HS model was chosen for comparison as the most simple model of the intermolecular interaction. The equilibrium temperature is taken equal to $T_0 = 300K$.

When use the HS model we need to define the ratio of the molecular diameters and also the molecular masses. For Ne-Ar mixture and He-Xe mixture the ratios $d_2/d_1 = 1.406$ and 2.226 are used, respectively. For Ne-Ar mixture the molecular masses are $m_1 = 20.183$ and $m_2 = 39.948$; for He-Xe mixture $m_1 = 4.0026$ and $m_2 = 131.30$.

7.3.1 Couette flow

We reported the detailed numerical results obtained by the McCormack model. Two mixtures, Ne-Ar and He-Xe, are considered for three values of the molar concentration $C_0 = 0.1$, 0.5 and 0.9 and three values of the rarefaction parameter.

The values of the dimensionless values of the mixture shear stress P_{xy}, eqs.(7.3), (7.4) are summarized in Table 7.1. The shear stress has to be constant between two plates due to the momentum conservation. However the numerical results vary slightly because of numerical error. Therefore, the average value over the distance between the plates is calculated and provided in Table 7.1 together with the maximum variation of the shear stress, presented in the brackets, which is calculated as following

$$\Delta P_{xy} = \max \left\| \frac{P_{xy}(i) - P_{xy}^{av}}{P_{xy}^{av}} \right\|, \tag{7.21}$$

where P_{xy}^{av} is average value of shear stress over the physical space. This maximum variation of the shear stress is provided in percentage in Table 7.1 and it shows a good measure of accuracy.

For the previous study the complete accommodation between gas species and the plate's

Table 7.1: Shear stress of the mixture P_{xy} and their the relative error ΔP_{xy} (given in parentheses) obtain by McCormack model.

δ_0	$C_0 = 0.1$	0.5	0.9
		Ne-Ar	
0.1	0.2601 (0.00%)	0.2576 (0.00%)	0.2594 (0.00%)
1.	0.1689 (0.02%)	0.1675 (0.02%)	0.1685 (0.02%)
10.	0.0415 (0.31%)	0.0414 (0.31%)	0.0415 (0.31%)
		He-Xe	
0.1		0.2163 (0.00%)	
1.		0.1482 (0.01%)	
10.		0.0400 (0.25%)	

Table 7.2: Shear stress P_{xy} of the mixture for mixture He-Ar with $C_0 = 0.3$.

δ_0	$a_{He}^{y=\pm1/2} = 0.4$, $a_{Ar}^{y=\pm1/2} = 0.7$			$a_{He}^{y=\pm1/2} = 1.$, $a_{Ar}^{y=\pm1/2} = 1.$		
	present	McCormack [75]	LBE [76]	present	McCormack [75]	LBE [76]
0.2	−0.1226035	−0.1226026	−0.1220812	−0.2294735	−0.2294745	−0.2285585
1	−0.0986182	−0.0986073	−0.0987467	−0.1615599	−0.1615592	−0.1626466
10	−0.0350417	−0.0350071	−0.0355460	−0.0410181	−0.0410056	−0.0417171

surfaces was assumed. However in practice the non-complete accommodation is often observed. The authors of Ref. [75] underlined their results on the shear stress are greatly affected by the accommodation coefficients used to define combinations of specular and diffuse reflection boundary conditions. Therefore we compare are the results, obtained here by the McCormack model, with those obtained in Refs. [75] and [76] using also McCormack model and linearized Boltzmann equation, respectively. The authors of [75] provided the results for the shear stress of the mixture for the case of the complete accommodation of the gas species on the surfaces and for three sets of the accommodation coefficients different from 1. We taken the two values of the accommodation coefficients: $a_{He}^{y=\pm1/2} = 0.4$ and $a_{Ar}^{y=\pm1/2} = 0.7$ for comparison. In order to compare the both results we found that our rarefaction parameter δ_0 is twice of a parameter in Ref. [75] and we need to divide the shear stress given in Ref. [75] by 2.

Several value of the shear stress reported in Table 3 from Refs. [75, 76] are compared in Table 7.2 with obtained here results. Analyzing the presented in Table 7.2 results we would like first to underline that the obtained here results and the results from Ref. [75], where the McCormack model was also used but with different method of solution (ADO method) , are very close one to the other, which is the good confirmation of the validity of our McCormack results. Then, the results obtained by the linearized Boltzmann equation are also close to the results of McCormack model. For the complete accommodation the difference between the McCormack model results and the results of the linearized BE is less than 0.7% and less than 1.4% for the non-complete accommodation case. The macroscopic profiles of the shear stress are shown in Fig. 7.2. This comparison of shear stress of Couette flow shown the excellent agreement between

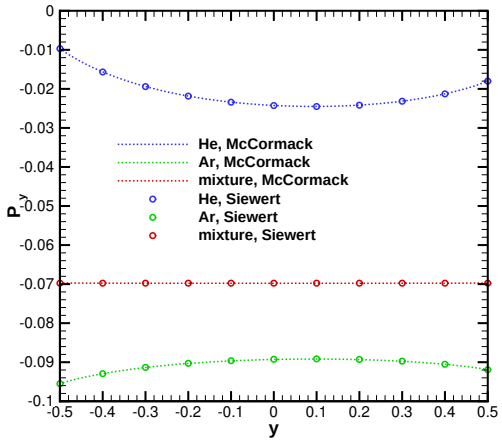

Figure 7.2: Comparison of shear stress profiles obtained by McCormack in the present study and in Ref. [75]. The He-Ar mixture $C_0 = 0.3$ with $\delta_0 = 3.$ and $a_{He}^{y=-1/2} = 0.2$, $a_{He}^{y=1/2} = 0.46$, $a_{Ar}^{y=-1/2} = 0.67$, $a_{Ar}^{y=1/2} = 0.78$.

Table 7.3: Heat flux of the mixture q_y and their the relative error Δq_y (given in parentheses) obtain by McCormack model.

δ	$C_0 = 0.1$	0.5	0.9
		Ne-Ar	
0.1	0.5430 (0.00%)	0.5589 (0.00%)	0.5446 (0.00%)
1.	0.4058 (0.02%)	0.4172 (0.02%)	0.4070 (0.02%)
10.	0.1364 (0.34%)	0.1397 (0.33%)	0.1368 (0.34%)
		He-Xe	
0.1		1.3012 (0.00%)	
1.		0.9839 (0.01%)	
10.		0.3304 (0.33%)	

the McCormack model and linearized Boltzmann equation technique developed in [76].

7.3.2 Fourier flow

Similarly to Couette flow, the same mixtures and its parameters are considered.

The values of the dimensionless heat flux q_y, eq. (7.5), are summarized in Table 7.3. It is to note that for the Fourier problem the heat flux of the mixture is independent of y because of the conservation of mass and that of energy. The numerical results of the heat flux varies slightly with y, as it was observed for the shear stress, because of numerical error. Its averaged values together with its maximum variation, calculated in the similar way as that of the shear stress, eq. (7.21), are provided in Table 7.3.

Table 7.4: Comparison of dimensionless heat flux q_y^{Kosuge} obtained by different methods for mixture of $m_B/m_A = 0.5$ and $d_B/d_A = 1$. The relation between q_y^{Kosuge} and q_y is expressed in eq. (7.22) with $T_0/\Delta T = 3/2$ corresponding to $T_H/T_C = 2$.

n_B/n_A	C_0	Kn	δ_0	present	McCormack [78]	LBE [79]	BE [77]
0.1	0.91	0.1	9.027	0.181	0.181	0.187	0.184
		1	0.903	0.519	0.519	0.529	0.509
		10	0.090	0.683	0.683	0.684	0.656
1	0.50	0.1	9.037	0.205	0.205	0.212	0.209
		1	0.904	0.599	0.599	0.610	0.589
		10	0.090	0.794	0.794	0.795	0.763
10	0.09	0.1	9.038	0.241	0.241	0.249	0.245
		1	0.904	0.689	0.689	0.702	0.677
		10	0.090	0.906	0.906	0.908	0.871

Table 7.5: Comparison of dimensionless heat flux q_y^{Kosuge} obtained by different methods for mixture of $m_B/m_A = 0.25$ and $d_B/d_A = 0.5$. The relation between q_y^{Kosuge} and q_y is expressed in eq. (7.22) with $T_0/\Delta T = 3/2$ corresponding to $T_H/T_C = 2$.

n_B/n_A	C_0	Kn	δ_0	present	McCormack [78]	LBE [79]	BE [77]
0.1	0.91	0.1	8.442	0.202	0.202	0.210	0.207
		1	0.844	0.557	0.557	0.568	0.547
		10	0.084	0.721	0.721	0.723	0.693
1	0.50	0.1	5.708	0.358	0.358	0.376	0.370
		1	0.571	0.830	0.830	0.846	0.814
		10	0.057	1.006	1.006	1.008	0.966
10	0.09	0.1	2.875	0.653	0.653	0.677	0.659
		1	0.288	1.159	1.159	1.170	1.124
		10	0.029	1.298	1.298	1.299	1.244

Similarly to Couette flow, the heat fluxes, in the dimensionless quantities q_y^{Kosuge} defined in Ref. [77], obtained here are compared with data in the literature (see Tables 7.4, 7.5) . The relation between dimensionless heat flux q_y^{Kosuge} and the present dimensionless heat flux q_y is as follows

$$q_y = q_y^{Kosuge} \sqrt{m/m_A} \left(T_0 - \Delta T/2\right)^{3/2} / \left(\Delta T \sqrt{T_0}\right). \tag{7.22}$$

The McCormack solutions obtained by this study and by ADO method [78] are perfectly machted. In Table 7.4, calculated for the mixture of $m_B/m_A = 0.5$ and $d_B/d_A = 1$, the maximum deviation between McCormack solutions and (linearized) BE solution is (3.4%) 4.0%. This maximum deviation increases to (5.0%) 4.2% when the differences between two species rise, *i. e.*, the mixture of $m_B/m_A = 0.25$ and $d_B/d_A = 0.5$ in Table 7.5.

7.4 Conclusions

Couette and Fourier flows between parallel plates are simulated using the McCormack kinetic model of the linearized Boltzmann equation and the linearized Boltzmann equation itself. Two types of gas mixture are considered: one with similar molecular masses (Ne-Ar) and one with very different molecular masses (He-Xe). Three values of concentrations are considered and the simulations are carried out in the near free molecular, transitional and slip flow regimes. For plane Couette and Fourier flows of gaseous mixture, McCormack model gives reliable solutions, which are in good agreement with solutions of linearized Boltzmann equation.

Chapter 8

Oscillatory Couette flow of binary rarefied gas mixture

The stationary Couette flow problem has been studied extensively for the large range of the gas rarefaction by solving the time-independent Boltzmann kinetic equation or the model kinetic equations [82, 83, 84, 85, 86]. More complex, oscillatory Couette flow behaviors have been also simulated by using the Monte Carlo method [87, 88], by solving the kinetic model equations [89, 90, 91, 92] or by applying the Lattice Boltzmann method [93]. In the hydrodynamic flow regime the problem can be easily solved on the basis of the Navier-Stokes equation[94]. Several solutions are proposed for the slip flow regime, using the first [87, 90, 92] and second order [88] slip boundary conditions. In some papers, Refs. [95, 96], the transverse oscillations of one of two parallel infinite plates are considered. However all these simulations have been carried out for a single gas. Only one paper can be found in the open literature, Ref. [97], where the transverse oscillatory flow of the gas mixture was simulated using the linearized BGK type model for the gas mixture. To the best of the author's knowledge, the McCormack model has not been applied to oscillatory flow of a gas mixture. It can capture the time evolution naturally without any additional assumption for the form of the distribution function.

Despite of the lack of the simulations of the oscillating gas mixture flows, the spectrum of their practical applications is broad, including various MEMS devices, like microaccelerometers, and also the inertial sensing, acoustic transduction, optical signal manipulation, resonant filters and the radio frequency components. Devices ranging from nanoscale resonators, switches, and valves have applications in tasks as diverse as information processing, molecular manipulation, and sensing [98, 99, 100, 101].

The aim of this work is to extent the approach, developed in [102, 103] for the transient gas flow simulation, to the case of the oscillatory flow of a gas mixture. The structure of this article is the following. First, the brief description of the McCormack model for the gas mixture is given with the comments on the implemented time-dependent numerical approach. After that the developed approach is tested for two problems: the steady state Couette flow of the gas

mixture and the oscillatory Couette flow of the single gas. The results for these test cases are compared with the results obtained previously by the other authors. Then, the two mixtures, Ne-Ar and He-Xe, are simulated using proposed numerical approach and the dynamic behavior of oscillation Couette flow for the mixtures are studied.

8.1 Statement of the problem

Consider a binary gaseous mixture confined between two infinite parallel plates positioned at $y' = \pm H_0/2$, where H_0 is the distance between the plates. The upper plate ($y' = H_0/2$) is fixed whilst the lower one ($y' = -H_0/2$) starts to oscillate harmonically in the x'-direction with frequency ω_0. Variation of the oscillating plate's velocity in time can be expressed as

$$u'_w\left(t'\right) = U_0 \sin\left(\omega_0 t'\right), \tag{8.1}$$

where t' is the time. The amplitude U_0 of the oscillated plate velocity is assumed to be very small compared to the most probable molecular velocity of the mixture υ_0 ($U_0 \ll \upsilon_0$), defined as

$$\upsilon_0 = \sqrt{2\frac{k}{m}T_0}. \tag{8.2}$$

Here k is the Boltzmann constant, T_0 is the equilibrium temperature, m is the mean molecular mass of the mixture defined as

$$m = \textstyle\sum_\alpha C_{0\alpha} m_\alpha, \quad C_{0\alpha} = n_{0\alpha}/\left(n_{01} + n_{02}\right), \quad \alpha = 1, 2, \tag{8.3}$$

where m_α is the molecular mass of specie α, $C_{0\alpha}$ is the mole fraction in equilibrium, $C_{01} + C_{02} = 1$, and $n_{0\alpha}$ is the equilibrium number density of the gas specie α. In the following the subscript 1 will be used for the lighter specie while the heavier component will be denoted with 2, so $\alpha = 1, 2$.

The macroscopic quantities of the gas, *i.e.* the mixture velocity $\mathbf{u}'$ and the heat flux $\mathbf{q}'$ have only the x' direction component different from zero; for the shear stress the only p'_{xy} component is nonzero. The other macroscopic quantities, *i.e.* the density, temperature, and pressure are constant. It is to note that the heat flux can be present in a flow even if the temperature of the gas is assumed to be uniform [185]. The shear stress p'_{xy}, the hydrodynamic velocity of the mixture u'_x and the x' component of the heat flux vector of the mixture q'_x are defined as

$$p'_{xy} = \sum_{\alpha=1}^{2} C_{0\alpha} p'_{xy_\alpha}, \qquad u'_x = \sum_{\alpha=1}^{2} m_\alpha n_{0_\alpha} u'_{\alpha_x} / \sum_{\alpha=1}^{2} m_\alpha n_{0_\alpha}, \qquad q'_x = \sum_{\alpha=1}^{2} C_{0_\alpha} q'_{x_\alpha}. \tag{8.4}$$

The oscillatory Couette flow is governed by two dimensionless parameters. The first one is the ratio between two characteristic length scales: the distance between two plates H_0 and the equivalent molecular mean free path ℓ:

$$\delta = \frac{H_0}{\ell} = \frac{H_0 p_0}{\mu_0 \upsilon_0}, \tag{8.5}$$

here μ_0 is the viscosity of the mixture at equilibrium temperature T_0 and p_0 is an equilibrium pressure of the mixture. It is to note that the gas rarefaction parameter δ is inversely proportional to the Knudsen number. The second parameter, which was firstly introduced in [186], characterizes the oscillation speed and is defined as the ratio between the mean intermolecular collision frequency γ' (proportional to p_0/μ_0) and the oscillation frequency of the down plate ω_0 as

$$\theta = \frac{p_0/\mu_0}{\omega_0}. \tag{8.6}$$

In some previous works, Refs. [87, 88], the Stokes number was used, which represents the balance between unsteady and viscous effects. However, we prefer to use here the θ parameter which can relate two frequencies of the microscopic and macroscopic scales. The two independent parameters δ and θ fully describe the relation between macroscopic scale, characterized by the distance between the plates and the oscillation frequency of the down plate, and microscopic scale, characterized by the mean free path and the molecular collision frequency.

It is useful to define the dimensionless quantities as follows

$$\begin{aligned} t = \frac{t'}{H_0/\upsilon_0}, y = \frac{y'}{H_0}, \qquad & \boldsymbol{c}_\alpha = \frac{\boldsymbol{\upsilon}_\alpha}{\upsilon_{0\alpha}}, \\ u_\alpha = \frac{u'_{\alpha x}}{U_0}, p_{xy_\alpha} = -\frac{p'_{xy_\alpha}}{2p_0}\frac{\upsilon_0}{U_0}, \quad & q_\alpha = \frac{q'_{x_\alpha}}{2m\upsilon_0^2 U_0}, \end{aligned} \tag{8.7}$$

where $\boldsymbol{\upsilon}_\alpha = (\upsilon_{x\alpha}, \upsilon_{y\alpha}, \upsilon_{z\alpha})$ is the molecular velocity, $\upsilon_{0\alpha} = \sqrt{2kT_0/m_\alpha}$ is the most probable molecular speed of specie α. It is to note that $t_0 = H_0/\upsilon_0$ is the acoustic time scale: the ratio of the gap between the plates to the most probable molecular velocity of the gas molecules.

Under the harmonic excitation of the down plate, given by eq. (8.1), a gas response of the following form is expected

$$\begin{aligned} u_\alpha(t,y) &= U_\alpha(t,y)\sin\left(\delta/\theta t + \varphi_{u_\alpha}(y)\right), \\ p_{xy_\alpha}(t,y) &= P_\alpha(t,y)\sin\left(\delta/\theta t + \varphi_{p_\alpha}(y)\right), \end{aligned} \tag{8.8}$$

where U_α, φ_{u_α}, P_α, φ_{p_α} are the amplitude and the phase of specie velocity and shear stress, respectively. The shear stress and the velocity of the mixture depend on time through the relations

$$p_{xy} = P(t,y)\sin\left(\delta/\theta t + \varphi_P(y)\right), \qquad u = U(t,y)\sin\left(\delta/\theta t + \varphi_U(y)\right), \tag{8.9}$$

where P, φ_P, U, φ_U are the amplitude and phase of the shear stress and of the hydrodynamic velocity of the mixture, respectively. The dimensionless period of oscillation can be calculated as

$$T = 2\pi\theta/\delta. \tag{8.10}$$

Different flow regimes can be observed for the oscillating Couette flow of a single gas, see Table 8.1 and Refs. [90, 92]. When the rarefaction parameter is small ($\delta \to 0$), so the distance H_0 between two plates is so small (or the mean free path is so large) that the molecules move in the gap without intermolecular collisions (free molecular regime). It was found that in this case the oscillation speed parameter θ does not have any influence on the flow behaviors. In the case of the large values of the rarefaction parameter $\delta \to \infty$ the distance between the plate is large enough that the influence of the fixed (upper) plate can be neglected. Two limit cases may also be recognized for the oscillation speed parameter θ, which represents the ratio of the frequencies, molecular collision frequency of the mixture and the excitation frequency of the plate's motion, see eq. (8.6). If $\theta \to \infty$, then the excitation frequency ω_0 is much larger than intermolecular collision frequency, so many intermolecular collisions occur during one cycle of oscillations; this is the low oscillation frequency regime, see Table 8.1. When θ is large and for the large value of the rarefaction parameter δ, the Navier-Stokes equation is applicable and the corresponding regime can be identified as the hydrodynamic regime. In the other limit, when the oscillation speed parameter tends to zero ($\theta \to 0$), very few intermolecular collisions occur during one oscillation cycle. This regime can be called the high oscillation speed regime. In this regime the intermolecular collisions can be neglected and the problem was solved analytically on the level of the velocity distribution function in the case of the single gas flow [90]. In the limit regimes the Navier-Stokes or free molecular approaches can be used to obtain the solutions, but in the intermediate range of the parameters δ and θ the kinetic equation must

Table 8.1: Different regimes of oscillations. The numbers from 1 to 9 represents a number of each simulated case: number 7, for example, corresponds to the pair $\delta = 0.1$ and $\theta = 10$.

<table>
<tr><th>δ</th><th>$\theta \to 0$</th><th>$\theta = 0.1$</th><th>$\theta = 1$</th><th>$\theta = 10$</th><th>$\theta \to \infty$</th></tr>
<tr><td>$\delta \to 0$</td><td></td><td colspan="3">distance H_0 is so small that the molecules move between the plates without collisions</td><td></td></tr>
<tr><td>$\delta = 0.1$</td><td rowspan="3">high oscillation frequency</td><td>1</td><td>4</td><td>7</td><td rowspan="3">low oscillation frequency quasi stationary flow</td></tr>
<tr><td>$\delta = 1$</td><td>2</td><td>5</td><td>8</td></tr>
<tr><td>$\delta = 10$</td><td>3</td><td>6</td><td>9</td></tr>
<tr><td>$\delta \to \infty$</td><td></td><td colspan="3">distance H_0 is so large that it can be considered as infinite</td><td></td></tr>
</table>

be solved to obtain the solution.

8.2 Kinetic equation

8.2.1 McCormack model

As has been assumed above $U_0 \ll v_0$, the distribution function of specie α can be linearized according to

$$f'_\alpha\left(t', y', \boldsymbol{v}_\alpha\right) = f_\alpha^{M'}\left(v_\alpha\right)\left[1 + h_\alpha\left(t', y', \boldsymbol{v}_\alpha\right)\frac{U_0}{v_0}\right], \tag{8.11}$$

where $f_\alpha^{M'}$ is the Maxwellian equilibrium distribution function which corresponds to an equilibrium state

$$f_\alpha^{M'}\left(v_\alpha\right) = n_{0\alpha}\left(\frac{m_\alpha}{2\pi k T_0}\right)^{3/2}\exp\left(-\frac{m_\alpha v_\alpha^2}{2kT_0}\right), \tag{8.12}$$

h_α are the perturbation functions that satisfy the McCormack kinetic model [14]

$$\frac{\partial h_\alpha\left(t', y', \boldsymbol{v}_\alpha\right)}{\partial t'} + v_{y\alpha}\frac{\partial h_\alpha\left(t', y', \boldsymbol{v}_\alpha\right)}{\partial y'} = \sum_{\beta=1}^{2} L_{\alpha\beta}(h_\alpha), \qquad \alpha = 1, 2, \tag{8.13}$$

where $L_{\alpha\beta}(h_\alpha)$ is the model collision term, which is obtained by correlating their expansion coefficients to have the same moments as full collision operator of the linearized Boltzmann equation. Incorporating dimensionless quantities, eq. (8.7), into McCormack kinetic equation, eq. (8.13), the dimensionless form of governing equation is obtained

$$\frac{\partial h_\alpha\left(t,y,\boldsymbol{c}_\alpha\right)}{\partial t}+c_{y\alpha}\frac{\partial h_\alpha\left(t,y,\boldsymbol{c}_\alpha\right)}{\partial y}\sqrt{\frac{m}{m_\alpha}}=K\sum_{\beta=1}^{2}L_{\alpha\beta}(h_\alpha),\qquad \alpha=1,2, \tag{8.14}$$

where the collision term reads

$$\begin{aligned}L_{\alpha\beta}(h_\alpha)=&-\gamma_{\alpha\beta}h_\alpha+2\sqrt{\frac{m_\alpha}{m}}\left[\gamma_{\alpha\beta}u_\alpha-\upsilon_{\alpha\beta}^{(1)}\left(u_\alpha-u_\beta\right)-\frac{\upsilon_{\alpha\beta}^{(2)}}{2}\left(q_\alpha-\frac{m_\alpha}{m_\beta}q_\beta\right)\right]c_{x\alpha}\\&+4\left[\left(\gamma_{\alpha\beta}-\upsilon_{\alpha\beta}^{(3)}\right)p_{xy\alpha}+\upsilon_{\alpha\beta}^{(4)}p_{xy\beta}\right]c_{x\alpha}c_{y\alpha}\\&+\frac{4}{5}\sqrt{\frac{m_\alpha}{m}}\left[\left(\gamma_{\alpha\beta}-\upsilon_{\alpha\beta}^{(5)}\right)q_\alpha+\upsilon_{\alpha\beta}^{(6)}\sqrt{\frac{m_\beta}{m_\alpha}}q_\beta-\frac{5}{4}\upsilon_{\alpha\beta}^{(2)}\left(u_\alpha-u_\beta\right)\right]c_{x\alpha}\left(c_\alpha^2-\frac{5}{2}\right),\\&\alpha,\beta=1,2.\end{aligned} \tag{8.15}$$

The $\upsilon_{\alpha\beta}^{(i)}$ functions and the self and cross-collision frequencies $\gamma_{\alpha\beta}$ in the collision term, eq. (8.15), are provided in A.1. The viscosity of the mixture μ is calculated as

$$\mu=\sum_{\alpha=1}^{2}\mu_\alpha=\sum_{\alpha=1}^{2}p_{0\alpha}/\gamma_\alpha, \tag{8.16}$$

where $p_{0\alpha}=n_{0\alpha}kT_0$ is the equilibrium partial pressure, μ_α is the partial viscosity. Coefficient K in eq. (8.14) is given by

$$K=\delta\sum_{\alpha=1}^{2}\frac{C_{0\alpha}}{\gamma_\alpha}. \tag{8.17}$$

The macroscopic flow parameters are calculated in terms of perturbation function as follows

$$\begin{aligned}u_\alpha&=\frac{1}{\pi^{3/2}}\sqrt{\frac{m}{m_\alpha}}\int h_\alpha c_{x\alpha}\exp\left(-\boldsymbol{c}_\alpha^2\right)d\boldsymbol{c}_\alpha,\\p_{xy\alpha}&=\frac{1}{\pi^{3/2}}\int h_\alpha c_{x\alpha}c_{y\alpha}\exp\left(-\boldsymbol{c}_\alpha^2\right)d\boldsymbol{c}_\alpha,\\q_\alpha&=\frac{1}{\pi^{3/2}}\sqrt{\frac{m}{m_\alpha}}\int h_\alpha c_{x\alpha}\left(\boldsymbol{c}_\alpha^2-\frac{5}{2}\right)\exp\left(-\boldsymbol{c}_\alpha^2\right)d\boldsymbol{c}_\alpha.\end{aligned} \tag{8.18}$$

The shear stress and macroscopic velocity of the mixture can be expressed via the concentration and the specie shear stress and velocity, respectively

$$p_{xy} = -\sum_{\alpha=1}^{2} C_{0\alpha} p_{xy_\alpha}, \qquad u = \sum_{\alpha=1}^{2} C_{0\alpha} u_{x_\alpha}. \tag{8.19}$$

The Maxwell-type diffuse-specular conditions are applied as boundary condition on the plate's surfaces as follows

$$\begin{aligned} h^{+}_{\alpha(y=1/2)} &= \left(1 - a^{y=1/2}\right) \sqrt{\frac{m_\alpha}{m}} h^{-}_{\alpha(y=1/2)}, \\ h^{+}_{\alpha(y=-1/2)} &= \left(1 - a^{y=-1/2}\right) \sqrt{\frac{m_\alpha}{m}} h^{-}_{\alpha(y=-1/2)} + 2a^{y=-1/2} c_{x\alpha} \sin\left(\delta t/\theta\right), \end{aligned} \tag{8.20}$$

where $a^{y=\pm 1/2}$ are the accommodation coefficients of the upper and bottom plates, the superscripts $+$ and $-$ refer to the outgoing and incoming molecules with respect to the walls, respectively.

8.2.2 Projection procedure

Equations (8.14) are one-dimensional in the physical space and three-dimensional in the molecular velocity space. For our one dimensional in physical space case the dependence of distribution function on $c_{z\alpha}$ can be eliminated by means of projection procedure. For this purpose, two reduced distribution functions are introduced

$$\begin{aligned} \Phi_\alpha\left(t, y, c_{x\alpha}, c_{y\alpha}\right) &= \frac{1}{\sqrt{\pi}} \sqrt{\frac{m}{m_\alpha}} \int h_\alpha\left(t, y, c_{x\alpha}, c_{y\alpha}, c_{z\alpha}\right) \exp\left(-c_{z\alpha}^2\right) dc_{z\alpha}, \\ \Psi_\alpha\left(t, y, c_{x\alpha}, c_{y\alpha}\right) &= \frac{1}{\sqrt{\pi}} \sqrt{\frac{m}{m_\alpha}} \int h_\alpha\left(t, y, c_{x\alpha}, c_{y\alpha}, c_{z\alpha}\right) c_{z\alpha}^2 \exp\left(-c_{z\alpha}^2\right) dc_{z\alpha}. \end{aligned} \tag{8.21}$$

Multiplying eqs. (8.14) by $\frac{1}{\sqrt{\pi}} \sqrt{\frac{m}{m_\alpha}} \exp\left(-c_{z\alpha}^2\right)$ and then integrating over $c_{z\alpha}$, after that multiplying eqs. (8.14) by $\frac{1}{\sqrt{\pi}} \sqrt{\frac{m}{m_\alpha}} c_{z\alpha}^2 \exp\left(-c_{z\alpha}^2\right)$ and then integrating over $c_{z\alpha}$, the system of two kinetic equations for each specie is obtained

$$\frac{\partial \Phi_\alpha}{\partial t} + c_{y\alpha} \frac{\partial \Phi_\alpha}{\partial y} \sqrt{\frac{m}{m_\alpha}} = KL_{\alpha\beta}(\Phi_\alpha), \qquad \alpha, \beta = 1, 2, \tag{8.22}$$

$$\frac{\partial \Psi_\alpha}{\partial t} + c_{y\alpha} \frac{\partial \Psi_\alpha}{\partial y} \sqrt{\frac{m}{m_\alpha}} = KL_{\alpha\beta}(\Psi_\alpha), \qquad \alpha, \beta = 1, 2. \tag{8.23}$$

The expressions of the collision terms in eqs. (8.22) and (8.23) are given in eqs. (A.8) and (A.9). The macroscopic flow parameters, given by eqs.(8.18), are calculated in terms of reduced distribution functions as follows

$$
\begin{aligned}
u_\alpha &= \frac{1}{\pi}\int \Phi_\alpha c_{x\alpha} \exp\left(-c_{x\alpha}^2 - c_{y\alpha}^2\right) dc_{x\alpha} dc_{y\alpha},\\
p_{xy_\alpha} &= \frac{1}{\pi}\int \Phi_\alpha c_{x\alpha} c_{y\alpha} \exp\left(-c_{x\alpha}^2 - c_{y\alpha}^2\right) dc_{x\alpha} dc_{y\alpha},\\
q_\alpha &= \frac{1}{\pi}\int \left[\Phi_\alpha\left(c_{x\alpha}^2 + c_{y\alpha}^2 - \frac{5}{2}\right) + \Psi\right] c_{x\alpha} \exp\left(-c_{x\alpha}^2 - c_{y\alpha}^2\right) dc_{x\alpha} dc_{y\alpha}.
\end{aligned}
\tag{8.24}
$$

Boundary conditions on the two plates read

$$
\begin{aligned}
&\Phi^+_{\alpha(y=1/2)} = \left(1 - a^{y=1/2}\right)\Phi^-_{\alpha(y=1/2)}, \quad \Phi^+_{\alpha(y=-1/2)} = \left(1 - a^{y=-1/2}\right)\Phi^-_{\alpha(y=1/2)} + 2a^{y=-1/2} c_{x\alpha} \sin\left(\delta t/\theta\right),\\
&\Psi^+_{\alpha(y=1/2)} = \left(1 - a^{y=1/2}\right)\Psi^-_{\alpha(y=1/2)}, \quad \Psi^+_{\alpha(y=-1/2)} = \left(1 - a^{y=-1/2}\right)\Psi^-_{\alpha(y=1/2)} + a^{y=-1/2} c_{x\alpha} \sin\left(\delta t/\theta\right).
\end{aligned}
\tag{8.25}
$$

In the following only diffuse boundary conditions will be implemented, so $a^{y=\pm 1/2} = 1$.

8.3 Method of solution

8.3.1 Numerical scheme

In several previous studies the oscillatory Couette flow is simulated on the basis of the non-stationary kinetic equation [90, 92], where it was assumed that the oscillation is to be fully established through the gas flow and, consequently, the solution is harmonic with respect to the time. In this case the perturbation function has an oscillatory behavior with respect to the molecular velocity and, as consequence, a great number of nodes in the velocity space is necessary leading to a consequent computational efforts. Contrary to these previous works we do not assume a prior that the oscillations are fully established and that the dependence of the solution on the time is harmonic, the time-dependent kinetic equation is solved here directly.

Firstly, the discrete velocity method (DVM) is used to separate the continuum molecular velocity spaces $c_x = (-\infty, \infty)$, $c_y = (-\infty, \infty)$ in the kinetic equations (8.22), (8.23) into discrete velocity sets c_{x_m} $(m = 1, 2, .., N_{c_x})$, c_{y_n} $(n = 1, 2, .., N_{c_y})$, the same for each specie, which are taken to be the roots of Hermite polynomial of the order N_{c_x} and N_{c_y}, respectively. Next, the set of independent kinetic equations, corresponding to discrete velocity sets c_{x_m}, c_{y_n},

is discretized in time and space by Finite difference method (FDM).

In the physical space, the uniform grid with N_y points is constructed. The spacial derivatives are approximated by the second-order accurate TVD upwind scheme. The time derivative is approximated by the time-explicit Euler method. Various tests are carried out to determine the optimal number of the grid points. It was found that $N_{c_x} = N_{c_y} = 50$ and $N_y = 100$ provide the results with 1% of accuracy.

The simulation time step is chosen according to satisfy three conditions. First, the time step has to be smaller than the time to cross a grid cell, this is the classical numerical stability condition for the transport part of kinetic equations. Second, the time step has to be smaller than the mean collision time of each species so that the intermolecular collisions can be captured properly. Third, the time step has to be significantly smaller than the oscillation period in order to trace correctly the down plate oscillation via gas-wall collisions.

8.3.2 Numerical tests

In order to examine the developed numerical technique two tests are carried out. The first one aims to test the correctness of the numerical scheme for the gas mixture model and the second one explores the capacity of the proposed approach to capture the oscillation phenomena.

8.3.2.1 Steady state Couette flow for the gas mixture

This study aims to compare the results, obtained by the developed numerical approach, with the results of Ref. [74], where the same McCormack model was used to simulate the steady state Couette flow of various mixtures. The authors of Ref. [74] adopted the fixed point technique to obtain the steady solution. The results, obtained by both techniques, are compared below for the steady state Couette flow of the gas mixture.

The system of equations (8.22), (8.23) subjected to the diffuse boundary conditions (8.25) is solved here by the time-explicit Euler method. The collisional terms, the right-hand sides of eqs. (8.22), (8.23) , contain the omega integrals [70], so the intermolecular interaction potential is to be defined. Two intermolecular interaction laws are tested: the Hard Sphere (HS) model [70, 107] and the Realistic Potential (RP) [81, 74]. The results, obtained with these two potentials, are compared with those of Ref. [74]. For the Realistic Potential the omega integrals are calculated from the analytical expressions provided in Ref. [81]. The proposed here approach is tested for the He-Xe and Ne-Ar mixtures with various concentrations and different values of the rarefaction parameter.

Table 8.2: The mixture shear stress p_{xy}, velocity of each specie u_{He}, u_{Xe} and hydrodynamic velocity of the mixture u, near the upper plate $y = 0.5$. The solution, obtained here with the time dependent technique, is compared with the steady solution of Ref. [74] for the He-Xe mixture with $C_0 = 0.1$.

δ	p_{xy}		u_{He}		u_{Xe}		u
	present	[74]	present	[74]	present	[74]	present
	HS		HS	RP	HS	RP	HS
0[a]	0.2722						
0.01	0.2700	0.2701	0.0096	0.0088	0.0161	0.0132	0.0161
0.1	0.2527	0.2527	0.0558	0.0510	0.0716	0.0719	0.0715
1	0.1655	0.1655	0.2171	0.2049	0.2495	0.2499	0.2494
40	0.01181	0.01187	0.4796	0.4793	0.4829	0.4828	0.4829
40[b]	0.01187						0.4749

[a] eq. (8.27)
[b] eq. (8.26)

The results for the dimensionless shear stress p_{xy} of the He-Xe mixture, see eqs. (8.4), (8.7), (8.19), are compared to the results of Ref. [74], see Tables 8.2, 8.3, for the concentration of the lighter specie (Ne), equal to 0.1 and 0.5, respectively, and near to the upper (fixed) plate. Very good agreement is found for HS potential while the slight difference (less than 2%) appears in the case, when the Realistic Potential is used.

The specie velocities, obtained also for both potentials, are shown in Tables 8.2, 8.3 for the concentration 0.1 and 0.5, respectively and at the upper plate ($y = 0.5$). Only the results, obtained by the realistic potential, are available in Ref. [74]. It is clear that the results for the small values of the rarefaction parameter and for the lighter specie are different from the results of [74] for the RP. This difference reduces for the heavier specie. The specie velocities, obtained here with the HS potential, are very close to the results of Ref. [74] for the RP potential in all considered range of the rarefaction parameter.

Analytical expressions for the shear stress and velocity profile were obtained in Ref. [74] for the steady state gas mixture flow in the hydrodynamic ($\delta \to \infty$) and slip flow regimes:

$$u(y) = y\left(1 + \frac{2\sigma_p}{\delta}\right)^{-1}, \qquad p_{xy} = \frac{1}{2\delta + 4\sigma_p}. \tag{8.26}$$

Here σ_p is the velocity slip coefficient. The corresponding values of the mixture velocity and shear stress in the hydrodynamic flow regime can by obtained by setting $\sigma_p = 0$ in the previous expressions. For the gas mixture flows the values of this coefficient for several gas mixture compositions can be found in [187, 188, 189, 143].

The values of the mixture shear stress and velocity in the slip regime ($\delta = 40$) for

Table 8.3: The mixture shear stress p_{xy}, velocity of each specie u_{He}, u_{Xe} and hydrodynamic velocity of the mixture u near the upper plate $y = 0.5$. The solution, obtained here with the time dependent technique, is compared with the steady solution of Ref. [74] for the He-Xe mixture with $C_0 = 0.5$.

δ	p_{xy}				u_{He}			u_{Xe}		
	HS		RP		HS	RP		HS	RP	
	present	[74]	present	[74]	present	present	[74]	present	present	[74]
0[a]	0.2308									
0.01	0.2292	0.2292	0.2290	0.2291	0.0091	0.0064	0.0089	0.0118	0.0131	0.0121
0.1	0.2163	0.2163	0.2154	0.2162	0.0537	0.0408	0.0517	0.0660	0.0715	0.0667
1	0.1482	0.1482	0.1455	0.1480	0.2104	0.1759	0.2050	0.2368	0.2486	0.2382
10	0.03995	0.03999	0.03937	0.03937	0.4227	0.4034	0.4204	0.4326	0.4374	0.4331

[a] eq. (8.27)

He-Xe mixture, calculated using eq. (8.26), are shown in Table 8.2. The velocity slip coefficient for the He-Xe mixtures with Helium concentration $C_{He} = 0.1$ is taken to be equal to 1.057 [143]. Good agreement is found between the values of the mixture shear stress and mixture velocity calculated, from the analytical expressions (8.26), and the numerical results, see Table 8.2.

In the free molecular regime the explicit analytical expression for the stress tensor reads [74]:

$$p_{xy}^{FM} = \frac{1}{2\sqrt{\pi}} \left(\frac{C_0}{\sqrt{C_0 + (1 - C_0)m_2/m_1}} + \frac{1 - C_0}{\sqrt{C_0 m_1/m_2 + (1 - C_0)}} \right). \tag{8.27}$$

The values of the shear stress for the He-Xe mixture with $C_0 = 0.1$ and 0.5 in the free molecular regime ($\delta = 0$) are given in Tables 8.2, 8.3, respectively. The good agreement is found with the present numerical results for $\delta = 0.01$.

From the present comparison we can conclude that the developed here numerical technique for the simulation of the transient gas mixture behavior gives the results, which are very close to the results from Ref. [74] for the steady state Couette flow for the binary gas mixture.

8.3.2.2 Oscillatory Couette flow for the single gas

To test the efficiency of the proposed approach to capture the unsteady flow properties the oscillatory Couette flow of a single gas is simulated using the McCormack model for the same gas species. The obtained results are compared with those of Ref. [90], where the single gas

oscillatory flow is simulated using the linearized BGK kinetic equation. The authors of Ref. [90] assume the oscillation to be fully established so as the dependence of the solution on the time is harmonic. In this case, introducing the complex distribution function of a special form, the time dependence of the linearized BGK equation was eliminated and the amplitude and phase were calculated directly from the solution of the linearized steady state BGK equation.

In the present work the time-dependent McCormack kinetic model equations (for the same specie) are solved directly and the time dependent data for each macroscopic quantity are obtained. The amplitude can be extracted from these data by two ways: either numerically as a half space between a nearest maximum and minimum appearing in the time evolution of the macroscopic quantity; or by using the fast Fourier transformation [190]. In the present study the both approaches are used. The following numerical procedure is adopted for the numerical extraction of the phase and amplitude of a macroscopic quantity. Firstly the last oscillatory period of a macroscopic quantity is analyzed and the maximum of the recorded values is associated to the amplitude of oscillation. The corresponding time, t_a, is used then to determine a phase of oscillation. The down plate is assumed to oscillate harmonically with the initial phase equal to zero, see eq. (8.1). Using eq. (8.1) we can calculate easily the time moment t_p, when the oscillated plate has a maximum velocity during the last period of oscillations. Then the phase of a macroscopic quantity can be calculated by $2\pi\left(t_p - t_a\right)/T$. With this definition a phase is found in 2π range.

The numerical solution of the time dependent kinetic equation allows the simulation of the fully established oscillating flow and also of the "starting time" (delay), *i.e.* a time needed to the full establishment of the harmonic oscillatory flow. For several sets of considered δ and θ parameters it is found that the "starting time" is need and the harmonic oscillations establish only after some delay. In this case the phase of oscillations increases essentially and it can be much larger than 2π. This "starting time" is directly related to the penetration depth of the flow. The both properties for the gas mixture flows will be discussed in Section 8.4.

The numerical results on the amplitude and phase of the shear stress at the down (oscillating) plate and upper (fixed) plate obtained by the proposed approach are compared in Table 8.4 with the results of Ref. [90], where the linearized BGK kinetic equation is solved for a single gas oscillating Couette problem. As it is clear from Table 8.4, the difference between two results does not exceed 1% for the shear stress and 2% for its phase.

It is to note that very large numerical grids in physical ($N_y = 10000$) and molecular velocity ($N_c = 400$) spaces were needed in Ref. [90] while in the present work the number of points is essentially reduced and it is equal to $N_y = 100$ and $N_{c_x} = N_{c_y} = 50$, in the physical and molecular velocity spaces, respectively.

In the hydrodynamic and slip flow regimes the analytical expressions for the velocity and shear stress for a single gas were obtained in Ref. [87, 90] and then in Ref. [90]:

$$u(y) = \frac{\sin\left((1+i)\left(\frac{\delta}{\sqrt{\theta}} - (y+0.5)\sqrt{\theta}\right)\right)}{\sin\left((1+i)\frac{\delta}{\sqrt{\theta}}\right)} \times \frac{1 + (1+i)\frac{\sigma_p}{\sqrt{\theta}}\cot\left((1+i)\left(\frac{\delta}{\sqrt{\theta}} - (y+0.5)\sqrt{\theta}\right)\right)}{1 - 2i\frac{\sigma_p^2}{\theta} + 2(1+i)\frac{\sigma_p}{\sqrt{\theta}}\cot\left((1+i)\frac{\delta}{\sqrt{\theta}}\right)}, \tag{8.28}$$

$$p_{xy}(y) = \frac{1+i}{2\sqrt{\theta}} \times \frac{\cos\left((1+i)\left(\frac{\delta}{\sqrt{\theta}} - (y+0.5)\sqrt{\theta}\right)\right)}{\sin\left((1+i)\frac{\delta}{\sqrt{\theta}}\right)} \times \frac{1 - (1+i)\frac{\sigma_p}{\sqrt{\theta}}\tan\left((1+i)\left(\frac{\delta}{\sqrt{\theta}} - (y+0.5)\sqrt{\theta}\right)\right)}{1 - 2i\frac{\sigma_p^2}{\theta} + 2(1+i)\frac{\sigma_p}{\sqrt{\theta}}\cot\left((1+i)\frac{\delta}{\sqrt{\theta}}\right)}. \tag{8.29}$$

The both previous expressions depend besides on the two rarefaction δ and oscillation speed θ parameters also on the velocity slip coefficient σ_p. This coefficient was calculated for several gas mixtures in Refs. [187, 188, 189, 143]. In Section 8.4 we will compare the values of the mixture velocity and shear stress, obtained numerically by the proposed approach, with the analytical expressions (8.28), (8.29) from Ref. [90], calculated with the velocity slip coefficient for the corresponding mixture.

It was also found in Refs. [87, 90] that in the free molecular flow regime ($\delta = 0$) the stationary solution

$$u = \frac{1}{2}, \qquad p_{xy} = \frac{1}{2\sqrt{\pi}} \tag{8.30}$$

can be used for any value of the oscillation speed parameter θ. In the high oscillation speed limit ($\theta \to 0$) and for arbitrary rarefaction parameter δ the analytical solution for the case of the single gas was also obtained in [90]. For the bottom oscillating plate this analytical solution reduces to the same expression, eq. (8.30).

8.4 Results: Oscillatory Couette flow for the gas mixture

After the series of tests the McCormack model with the Hard Sphere intermolecular potential is applied for simulation of the oscillatory Couette flow. Two mixtures are considered: Ne-Ar mixture for three values of the concentration $C_0 = 0.1, 0.5, 0.9$ and He-Xe mixture for only one value of concentration $C_0 = 0.5$. The numerical simulations are conducted for three values of rarefaction parameter $\delta = 0.1, 1, 10$ and three values of the frequency scale $\theta = 0.1, 1, 10$. The

Table 8.4: The amplitude P and phase φ_P of shear stress near the two plates $y = \pm 0.5$ for oscillatory Couette flow for the oscillatory speed parameter $\theta = 1$. The present solution is compared with the solution obtained in Ref. [90] for a single gas. The results for $\delta = 10$ do not provided in Ref. [90] due too that fact that for this case the penetration depth, see Section 8.4.1 for details, is smaller than the distance between the plates.

δ	P				φ_P			
	present		BGK [90]		present		BGK [90]	
	$y = -0.5$	$y = 0.5$	$y = -0.5$	$y = 0.5$	$y = -0.5$	$y = 0.5$	$y = -0.5$	$y = 0.5$
0.1	0.2634	0.2579	0.2634	0.2580	−0.0221	0.1605	−0.0222	0.1608
1	0.2647	0.1114	0.2665	0.1114	−0.1871	1.2839	−0.1868	1.3051

molecular masses for Ne-Ar and He-Xe mixtures are equal to 20.183 and 39.948; and 4.0026 and 131.3 atomic units, respectively. The molecular diameter ratio is equal to 1.406 and 2.226, respectively, see Refs. [81, 74]. The numbers are associated for each pair of the governed parameters (θ and δ) and they are listed in Table 8.1. All cases are calculated on the same numerical grid provided in the beginning of Section 8.3.

8.4.1 Penetration depth

To analyze the oscillating flow behavior, namely to estimate the intensity of the perturbation's propagation from the down oscillating plate, the penetration depth [87, 90] can be very helpful. The penetration depth, d_p, is a measure of how deep the initial perturbation can penetrate into a media. It is defined as the distance from moving wall at which the velocity amplitude decays to 1% of its excitation value ($U(y = d_p)/U_0 = 0.01$). It will be interesting to calculate the penetration depth for various mixture, but it needs the simulation of the gas behavior near a single oscillating plate (Stokes' second problem) and therefore to change the problem statement considered here. The second possibility to calculate the penetration depth, by using the two parallel plates configuration, is to simulate the case, when the rarefaction parameter tends to infinity.

The penetration depth was calculated in Ref. [89] for the case of the longitudinally oscillated plate in a single gas. The penetration depth is found decreasing with increasing of the oscillation speed parameter θ. We use here the results obtained in [89] to estimate the penetration depth in the oscillatory Couette flow of the gas mixture. Three values of the penetration depth, 7.5355, 3.6010 and 1.3080 are provided by the authors of Ref. [89], which correspond to three values of the oscillation speed θ, 0.1, 1 and 10. Using adopted here dimensionless parameters the dimensionless penetration depth is recalculated from the results of Ref. [89] and it is provided in Table 8.5.

Table 8.5: Some data on the penetration depth d_p for Ne-Ar and He-Xe mixtures with $C_0 = 0.5$. The penetration depth, obtained in Ref. [89] for the case of a oscillating plate in a single gas, is given in the last column. The initial values from Ref. [89] are recalculated by using adopted here dimensionless parameters.

θ	δ	Ne-Ar		He-Xe		Single gas [89]
		Ne	Ar	He	Xe	
0.1	0.1	> 1	> 1	> 1	> 1	7.5355
	1	0.60	0.43	> 1	> 1	0.7536
	10	0.09	0.07	0.25	0.16	0.0754
1	0.1	> 1	> 1	> 1	> 1	36.010
	1	> 1	> 1	> 1	> 1	3.601
	10	0.37	0.36	0.49	0.33	0.3601
10	0.1	> 1	> 1	> 1	> 1	130.8
	1	> 1	> 1	> 1	> 1	13.08
	10	> 1	> 1	> 1	> 1	1.308

In the case when the penetration depth for a single gas is estimated smaller than the dimensionless distance between the plates, equal to 1, the values of the penetration depth for each specie are provided in Table 8.5. The symbol " > 1" in Table 8.5 means that the amplitude of the specie velocity at the upper plate is larger than 1% of its initial value. It is clear that the estimated here penetration depth of each specie is different from the penetration depth of a single gas, especially for the He-Xe mixture. However, we consider these results for the specie penetration depth with precaution, because we calculated these values in the two plate configuration statement and for moderate value of the rarefaction parameter $\delta = 10$, so in this case the second upper plate can impact slightly the results. We would like to underling anew that an additional study to determine the penetration depth for the gas mixture will be interesting.

If we refers on the single gas results for the penetration depth, so for three pairs of δ and θ parameters, $(1, 0.1)$, $(10, 0.1)$, $(10, 1)$, which correspond to the cases 2, 3 and 6, see Table 8.1, the penetration depth (established for a single gas) is smaller than the dimensionless distance between the plates. Therefore, we expect that the amplitude of the macroscopic velocity at the upper plate will be smaller than 1% of that at the oscillated plate.

8.4.2 Transient behaviors

The mixture shear stress time evolution on the down and upper plates ($y = \pm 0.5$) are shown in Figure 8.1a) for $\delta = 1$ and $\theta = 1$ in the He-Xe mixture with $C_0 = 0.5$. The differences in the mixture shear stress amplitude and phase between two plates are clearly seen, Figure 8.1a). The specie velocities at the moving plate follow the plate's displacement, with the smaller

amplitude as the amplitude of the plate's oscillation, see Fig. 8.1b), where the velocities for each specie are shown. Near the moving plate the amplitudes of both species are very close one to the other, the amplitude of the lighter gas is slightly higher, and the both velocities have the same phase. However, the oscillations of the gas at the upper (fixed) plate become different, see Fig. 8.1b): the specie amplitudes decrease and the phases shift compared to the phase of the moving plate. The amplitudes of each specie and their phases become different. Therefore the gas mixture oscillations at the upper plate can be considered as a response of the media on the perturbation cased by the moving bottom plate, so in the following we will analyze the behavior of the gas mixture at the upper (fixed) plate.

Two types of the transient behavior is be observed for the upper (fixed) plate. The first type, see 8.2, is the most common type. The cases $1, 4, 5, 7, 8, 9$, see Table 8.1 for the numbers associated to each set of δ and θ parameters, belong to this first type. Figure 8.2 represents the time evolution of the specie velocities and the specie shear stress and that of the mixture at the upper plate for the case 1 ($\delta = 0.1$ and $\theta = 0.1$) of Ne-Ar mixture with $C_0 = 0.5$. As it is clear from Fig. 8.2, for this type of the transient behavior the gas mixture oscillations on the upper plate start quasi immediately. However, the amplitude of each macroscopic parameter during the first period is slightly higher than its the steady state value. The amplitude of Neon velocity is larger than that of Argon, withal the shear stress amplitude of Argon is higher than that of Neon.

It is also to note that for all simulated cases of this first type, the penetration depth, calculated for a single gas, is larger than the distance between the plates, see Table 8.5. Consequently the starting time is near to zero because the oscillations starts quasi immediately at the upper plate.

In the case of the transient behavior of the second type, cases $2, 3$ and 6, several non-harmonic motions are needed to establish the steady state oscillating flow behaviors. The time evolution of the species velocities, of the species shear stress and that of the mixture for the case 6 ($\delta = 10$ and $\theta = 1$) of Ne-Ar mixture with $C_0 = 0.5$ are shown on Fig.8.3a) and b), respectively. As it is clear from this Figure a relatively long time ("starting time" delay time) is needed to establish the oscillations of the gas mixture at the upper plate. It is also to note, that the amplitudes of the all oscillating parameters are very small, they are smaller than 1% of the excitation amplitude. For all the cases of this second type the penetration depth (estimated with a single gas) is smaller than the distance between the plates, see Table 8.5. We can conclude that this transient behavior appears only for the cases, where the penetration length is smaller compared to the dimensionless distance between the plates. Contrary to the previous case 1, $\delta = 0.1$ and $\theta = 0.1$, see Fig. 8.2, the shear stress amplitude of Neon is larger than that of Argon, see Fig.8.3d) and 8.2b).

Table 8.6: Amplitudes of specie shear stress P_{Ne}, P_{Ar} and velocity U_{Ne}, U_{Ar} versus θ and δ at $y = \pm 0.5$, the concentration is equal to 0.5.

θ	δ	P_{Ne}		P_{Ar}		U_{Ne}		U_{Ar}	
		$y=-0.5$	$y=+0.5$	$y=-0.5$	$y=+0.5$	$y=-0.5$	$y=+0.5$	$y=-0.5$	$y=+0.5$
0.1	0.1	0.2300	0.1676	0.3247	0.2045	0.5017	0.2445	0.5000	0.2000
	1	0.2310	0.0019	0.3250	0.0119	0.5008	0.0165	0.5007	0.0167
	10	0.2278	–	0.3204	–	0.5074	–	0.5069	–
1	0.1	0.2177	0.2141	0.3020	0.2945	0.5533	0.4154	0.5593	0.3976
	1	0.2172	0.0990	0.3079	0.1198	0.5575	0.1465	0.5548	0.1253
	10	0.2188	–	0.3075	–	0.5563	–	0.5563	–
10	0.1	0.2162	0.2162	0.2990	0.2989	0.5661	0.4335	0.5770	0.4224
	1	0.1491	0.1444	0.1953	0.1872	0.7335	0.2569	0.7523	0.2369
	10	0.1377	0.0077	0.1840	0.0097	0.7895	0.0132	0.8027	0.0120

Here, we do not present any detailed discussion on the dynamic system responses for the individual cases, since the behaviors are qualitatively similar to that of the described cases 1 and 6 and they are similar for each gas mixture.

8.4.3 Amplitude and phase

The amplitudes of the specie shear stress and specie velocity for the Ne-Ar mixture with $C_0 = 0.5$ at the down and upper plates are shown in Table 8.6. For several pairs of θ, δ the amplitude of the macroscopic quantities near the fixed plate does not appear in this Table. It is related to the fact that the corresponding penetration depth is small compared to the distance between the plates and so the amplitude of any macroscopic parameter is smaller than 0.1% of the initial amplitude, and thus it is too small to be interesting to be provided.

The data, given in Table 8.6 on the amplitudes of the specie shear stress, are plotted in Fig. 8.4a) and b) at the bottom and upper plates, respectively. These amplitudes have different behaviors. At the bottom plate the amplitudes of the specie shear stress are quasi constant for the oscillation speed parameter θ equal to 0.1 and 1 and for various values of the rarefaction parameter, while for $\theta = 10$ they decrease with δ increasing. In the same time, the upper plate's amplitudes decrease with δ decreasing for all considered values of the oscillation speed parameter. The difference between the amplitudes of the species shear stress is still reduced near the upper plate, see Fig. 8.4b), but the amplitude of heavier specie (Ar) remains larger than that of the lighter one.

The amplitudes of the specie velocities, provided in Table 8.6, are shown in Fig. 8.4c) and d). At the oscillating plate the amplitudes of each specie velocity are very similar, the maximal difference between two amplitudes is found for $\theta = 10$ and it does not exceed 3%,

the heavy specie (Ar) has slightly larger velocity. The amplitudes of specie velocities on the bottom plate depend strongly on the oscillation speed parameter θ: they remain constant for $\theta = 0.1$ and 1, with δ increases, as the amplitude of the shear stress, while for $\theta = 10$ the specie velocity amplitudes increase considerably.

Completely different behavior is observed for the amplitude of the specie velocities on the upper plate. For all considered values of the oscillation speed parameter θ the amplitudes of the specie velocity decrease with δ increasing and the specie velocity vanishes for $\delta = 10$. Conversely to the bottom plate, the lighter specie (Ne) has the slightly larger velocity.

The phases of the species shear stress and that of the specie velocity are shown in Table 8.7 on the bottom and upper plates. Near the oscillating plate the phases of the shear stress for each specie are close one to the other. For each fixed oscillation speed, the phase behaviors non-monotonically with increasing of the rarefaction parameter, see Table 8.7, except for $\theta = 10$, where the phase increases with the rarefaction parameter increases. On the upper fixed plate the phases of the specie shear stress are always negative and increase in absolute value with δ increases. The phases of the specie velocity, see 8.7, are always negative for both plates and they are similar for both species at the bottom plate. For the upper plate the difference between the phase of each specie increases as for the shear stress; the phases increase in absolute value with δ increases.

The amplitudes of the mixture shear stress for the Ne-Ar mixture with $C_0 = 0.5$ via distance between the plates are shown on Fig. 8.5a) for $\theta = 1$ and for three values of the rarefaction parameter. The qualitative behavior of the mixture amplitude is similar to that of the single gas, see Ref. [90]. It can be seen, Fig. 8.5a), that the variation of P is small for $\delta = 0.1$, while for $\delta = 10$ it sharply decays near the moved plate. Figure 8.5b) shows the dependence of the amplitude of the specie velocities on dimensionless distance between the plates. The specie velocity amplitude profiles decay faster with higher δ. This decay behavior is similar to, but steeper than that of shear stress amplitude profiles. Neon velocity amplitude is almost slightly higher than that of Argon at the same position. However, the two specie velocity amplitude profiles cross each other at around $y = -0.25$ only for the case with $\delta = 0.1$.

8.4.4 Influence of the concentration

The influence of the specie concentration is studied for three values of the concentration $C_0 = 0.1$, 0.5 and 0.9. The amplitude of the mixture shear stress P and its phase for all three values of concentration are shown in Tables 8.8 and 8.9, respectively. For the amplitude of the shear stress at the bottom and upper plates the similar trend is observed: the minimal value is obtained for the concentration equal to 0.5. It is to note that the minimum of the concentration was

Table 8.7: Phase of specie shear stress $\varphi_{P_{Ne}}$, $\varphi_{P_{Ar}}$ and specie velocity $\varphi_{U_{Ne}}$, $\varphi_{U_{Ar}}$ versus θ and δ at $y = \pm 0.5$.

θ	δ	$\varphi_{P_{Ne}}$		$\varphi_{P_{Ar}}$		$\varphi_{U_{Ne}}$		$\varphi_{U_{Ar}}$	
		$y=-0.5$	$y=+0.5$	$y=-0.5$	$y=+0.5$	$y=-0.5$	$y=+0.5$	$y=-0.5$	$y=+0.5$
0.1	0.1	0.02338	−1.069	0.02474	−1.418	−0.02900	−1.386	−0.02818	−1.846
	1	0.01822	−11.94	0.01890	−8.952	−0.02433	−15.25	−0.02433	−15.39
	10	0.03256	–	0.03256	–	−0.02180	–	−0.02180	–
1	0.1	0.01825	−0.1350	0.02559	−0.1825	−0.04512	−0.2462	−0.05618	−0.3155
	1	0.1730	−1.135	0.1893	−1.421	−0.1825	−1.470	−0.1920	−1.762
	10	0.1522	–	0.1658	–	−0.1659	–	−0.1740	–
10	0.1	0.0022	−0.0138	0.0031	−0.0188	−0.00593	−0.02653	−0.00767	−0.03452
	1	0.1013	−0.1543	0.1292	−0.1881	−0.05871	−0.2023	−0.06518	−0.2368
	10	0.4796	−2.695	0.5147	−2.802	−0.1700	−2.830	−0.1687	−2.894

Table 8.8: Influence of concentration on amplitude of mixture shear stress P at $y = \pm 0.5$ for Ne-Ar mixture. The results for the single gas oscillating Couette flow from Ref. [90] are provided in the last two columns.

θ	δ	P							
		$C_0 = 0.1$		$C_0 = 0.5$		$C_0 = 0.9$		single gas [90]	
		$y=-0.5$	$y=+0.5$	$y=-0.5$	$y=+0.5$	$y=-0.5$	$y=+0.5$	$y=-0.5$	$y=+0.5$
0.1	0.1	0.2801	0.1887	0.2773	0.1832	0.2793	0.1870	0.2813	0.2813
	1	0.2806	0.0147	0.2780	0.0051	0.2798	0.0137	0.2819	0.0073
	10	0.2769	–	0.2742	–	0.2762	–	–	–
1	0.1	0.2624	0.2569	0.2598	0.2542	0.2617	0.2561	0.2634	0.2580
	1	0.2648	0.1105	0.2625	0.1083	0.2641	0.1099	0.2665	0.1114
	10	0.2188	–	0.3075	–	0.5563	–	–	–
10	0.1	0.2602	0.2601	0.2576	0.2575	0.2594	0.2594	0.2612	0.2611
	1	0.1735	0.1672	0.1722	0.1679	0.1732	0.1668	0.1741	0.1679
	10	0.1615	0.0089	0.1609	0.0087	0.1613	0.0088	0.1627	0.0091

found for $C_0 = 0.85$ in Ref. [74] in the case of the steady-state Couette flow of the gas mixture. The maximal difference in the shear stress amplitude, with the concentration changing, is of the order of 1% for the bottom plate and 2% for the upper plate. The results, obtained in Ref. [90] for the single gas oscillation Couette flow are given in the last two column of Tables 8.8 and 8.9. It is clearly seen that the shear stress amplitude of a single gas is slightly larger than that of the mixture. The impact of the molar concentration on the phase of the shear stress is very small, see Table 8.9.

Table 8.9: Influence of concentration on phase of mixture shear stress φ_P at $y = \pm 0.5$ for Ne-Ar mixture. The results for the single gas oscillating Couette flow from Ref. [90] are provided in the last two columns.

θ	δ	φ_P							
		$C_0 = 0.1$		$C_0 = 0.5$		$C_0 = 0.9$		single gas [90]	
		$y = -0.5$	$y = +0.5$	$y = -0.5$	$y = +0.5$	$y = -0.5$	$y = +0.5$	$y = -0.5$	$y = +0.5$
0.1	0.1	−0.0249	1.2555	−0.0241	1.2585	−0.0246	1.2566	−0.0248	1.2514
	1	−0.0181	13.220	−0.0189	21.530	−0.0181	12.453	−0.0188	6.9678
	10	−0.0210	–	−0.0210	–	−0.0210	–	–	–
1	0.1	−0.0223	0.1613	−0.0225	0.1625	−0.0224	0.1616	−0.0222	0.1608
	1	−0.1855	1.2958	−0.1826	1.2912	−0.1845	1.2916	−0.1868	1.3051
	10	−0.1623	–	−0.1609	–	−0.1623	–	–	–
10	0.1	−0.0027	0.0166	−0.0027	0.0167	−0.0027	0.0166	−0.0026	0.0165
	1	−0.1161	0.1723	−0.1172	0.1734	−0.1164	0.1725	−0.1158	0.1719
	10	−0.5023	2.7606	−0.4997	2.7547	−0.5015	2.7576	−0.5053	2.7873

8.4.5 Comparison between two mixtures (Ne-Ar and He-Xe) and with the single gas case

The shear stress amplitude P and phase φ_P of the Ne-Ar and He-Xe mixtures with concentration $C = 0.5$ on both plates are shown in Tables 8.10 and 8.11, respectively, for various values of the rarefaction δ and oscillation speed θ parameters. In the same Tables the shear stress and phase, obtained in Ref. [90] for the single gas are provided. The values of the shear stress amplitude for $\delta = 0$ and ∞ was obtained analytically in Ref. [90] and are also given in Table 8.10. In the case of the free molecular flow regime ($\delta = 0$) the amplitude of the shear stress of the single gas is found to be independent on the oscillation speed, see eq. (8.30). In the case of the hydrodynamic flow regime ($\delta \to \infty$) the analytical expression, found in Refs. [87], [90], can be used with $\sigma_p = 0$, see eq. (8.29) and Refs. [87, 90]. When $\theta \to \infty$ the results obtained in Ref. [74] for the steady state Couette flow for the Ne-Ar and He-Xe mixtures are provided in the last rows of Table 8.10. The mixture shear stress is constant for the steady state Couette flow, therefore the shear stress results are placed only at the column corresponding to $y = -0.5$.

The results obtained in the present paper for the shear stress amplitude of Ne-Ar mixture differ in the order of 2% from the single gas results, except the case $\theta = 0.1$ and $\delta = 1$ and at the upper plate, where this difference is of the order of 30% for the case $\delta = 1$ and $\theta = 0.1$. This difference can be explained by the low level of the shear stress value in this case and therefore more difficult to capture. The same behavior is observed for the phase of the shear stress, see Table 8.11. Therefore, the characteristics of the oscillated mixture flows can be estimated with good accuracy by the results obtained for a single gas case, when the mass ratio of the mixture species is close to one it is equal to 1.979 for the Ne-Ar mixture case).

When comparing the results for the He-Xe mixture, the significant difference, up to 30%, between the single gas results is obtained. This difference reduces when rarefaction parameter increases. Therefore, the single gas results cannot be used for the estimation of the oscillatory gas mixture flow with the disparate molecular masses, (it is equal to 1.979 for the He-Xe mixture case).

When comparing the results for oscillation speed parameter $\theta = 10$ with those obtained for the steady state flow ($\theta \to \infty$) one can observes that these results are very different, especially for $\delta = 10$, with $\sim 74\%$ of difference for both mixtures. Therefore the steady state results cannot be used for the estimation of the oscillatory characteristics, even if the oscillation speed parameter is relatively high and so the oscillations are slow.

8.4.6 Slip regime

The amplitude and phase profiles of mixture shear stress between the plates are compared with the analytical solutions, eqs. (8.28) and (8.29) obtained in Refs. [87, 90] in the case of hydrodynamic and slip flow regime and for the oscillations of a single gas, see Figs. 8.6. It is clear that very good agreement is found for the case of $\theta = 10$ and $\delta = 10$. However for the smaller value of the oscillation speed $\theta = 1$, also in slip regime ($\delta = 10$) the single gas analytical solution cannot predict the results of the gas mixture.

8.5 Conclusions

The simple approach is implemented for the simulation of the oscillatory Couette flow of the gas mixtures. The proposed approach was firstly tested by comparing with the results, previously obtained by the other authors in the case of the steady-state flow of the gas mixtures and also in the case of oscillatory flow of a single gas. Very good agreement with these previously obtained results was found. Then, the simulation of the Ne-Ar and He-Xe mixtures are carried out for large range of the rarefaction parameter, oscillation speed parameter and for three values of the concentration, only for Ne-Ar mixture. It is found that the characteristics of the mixture, like the amplitudes of the mixture shear stress and mixture velocities, are very close to those found for the oscillatory flow of a single gas and the single gas results can be used for the estimations of the mixture parameters in the case, when the molecular masses of the components are relatively close one to the other. However, in the case of the He-Xe mixture the results are very different (up to 30%) from the single gas results. It was found that similarly to the steady state flows the amplitude of the mixture shear stress is lower than that of the single gas. It was also found that even for the relatively large oscillation speed parameter $\theta = 10$,

Table 8.10: Amplitude of the mixture (Ne-Ar and He-Xe with $C_0 = 0.5$) shear stress P versus θ and δ at $y = \pm 0.5$ compared with single gas results, obtained using the linearized BGK kinetic model in Ref. [90]. For $\theta \to \infty$ the steady-state solution from Ref. [74] is provided. The steady-state solution of the Couette flow for the single gas from Ref. [83] is used.

θ	δ	P					
		$y = -0.5$			$y = +0.5$		
		Ne-Ar	He-Xe	single [90]	Ne-Ar	He-Xe	single [90]
0	all	–	–	0.2821	–	–	–
0.1	0			0.2821			0.2821
	0.1	0.2773	0.2303	0.2813	0.1832	0.1249	0.1819
	1	0.2780	0.2307	0.2819	0.0051	0.0157	0.0073
	10	0.2742	0.2282	–	–	–	–
	∞	0.4137	0.3521	0.4220			
1	0			0.2821			0.2821
	0.1	0.2598	0.2187	0.2634	0.2542	0.2119	0.2580
	1	0.2625	0.2229	0.2665	0.1083	0.0826	0.1114
	10	0.2631	0.2219	–	–	–	–
	∞	0.3088	0.2743	0.3132			
10	0			0.2821			0.2821
	0.1	0.2576	0.2614	0.2612	0.2575	0.2163	0.2611
	1	0.1722	0.1536	0.1741	0.1679	0.1458	0.1658
	10	0.1609	0.1504	0.1627	0.0087	0.0071	0.0091
	∞	0.1633	0.1541	0.1644			
∞	0	0.2781^a	0.2308^a	0.2821^b			
	0.1	0.2576^a	0.2162^a	0.2612^b			
	1	0.1675^a	0.1480^a	0.1695^b			
	10	0.04139^a	0.03994^a	0.0416^b			
	∞	0^a	0^a	–			

[a] Results from Ref. [74] for the steady-state gas mixture
[b] Results from Ref. [83] for the steady-state gas mixture

Table 8.11: Phase of the mixture (Ne-Ar and He-Xe with $C_0 = 0.5$) shear stress φ_P versus θ and δ at $y = \pm 0.5$ compared with single gas results, obtained from the linearized BGK kinetic equation in Ref. [90].

θ	δ	φ_P					
		$y = -0.5$			$y = +0.5$		
		Ne-Ar	He-Xe	single [90]	Ne-Ar	He-Xe	single [90]
0.1	0						
	0.1	−0.0241	−0.0159	−0.0248	1.2585	−4.8972	1.2514
	1	−0.0189	−0.0140	−0.0188	21.530	−4.7309	6.9678
	10	−0.0210	−0.0210	–	–	–	–
	∞	−0.1312	−0.1116	−0.1339			
1	0						
	0.1	−0.0225	−0.0215	−0.0222	0.1625	−6.0899	0.1608
	1	−0.1826	−0.1313	−0.1868	1.2912	−4.8629	1.3051
	10	−0.1609	−0.1174	–	–	–	–
	∞	−0.3139	−0.2778	−0.3186			
10	0						
	0.1	−0.0027	−0.0029	−0.0026	0.0167	−6.2630	0.0165
	1	−0.1172	−0.1220	−0.1158	0.1734	−6.0810	0.1719
	10	−0.4997	−0.4498	−0.5053	2.7547	−3.5240	2.7873
	∞	−0.5428	−0.5089	−0.5469			

slow oscillations, the steady-state results are very different from that obtained here for the oscillatory gas mixture flows.

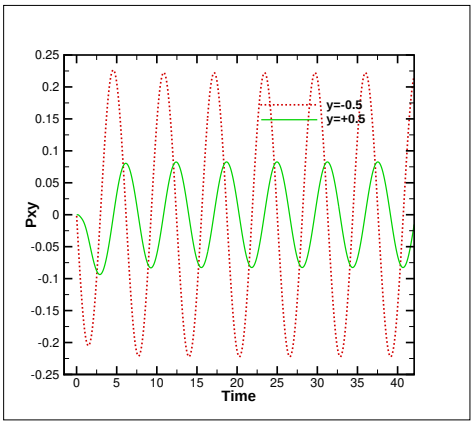

(a) p_{xy}

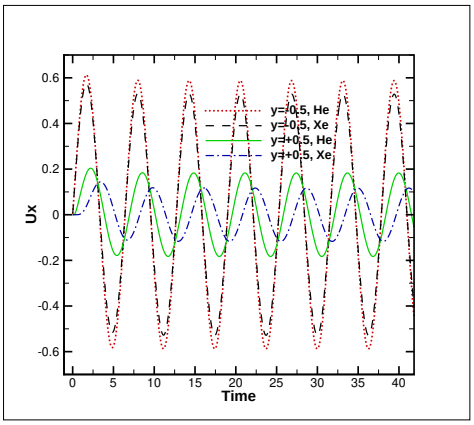

(b) u_x

Figure 8.1: The evolution in time of the mixture shear stress (a) and of the specie velocity (b) on the down and upper plates for He-Xe mixture $C_0 = 0.5$, the case of $\delta = 1$, $\theta = 1$.

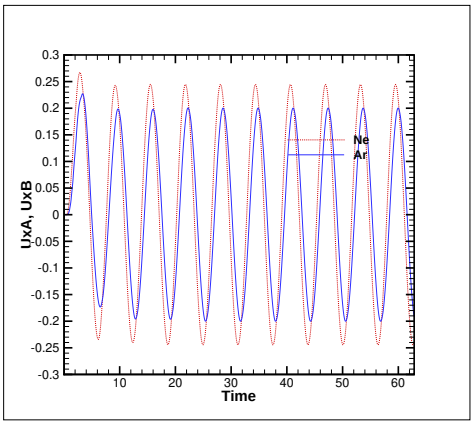

(a) u_x

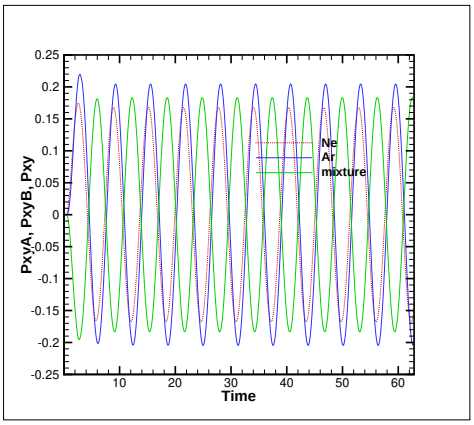

(b) p_{xy}

Figure 8.2: Time evolution of the macroscopic parameters at the upper plate for the case 1, see Table 8.1, $\theta = 0.1$ and $\delta = 0.1$, the Ne-Ar mixture with $C_0 = 0.5$; (a) specie velocity time evolution, (b) specie shear stress and mixture shear stress time evolution.

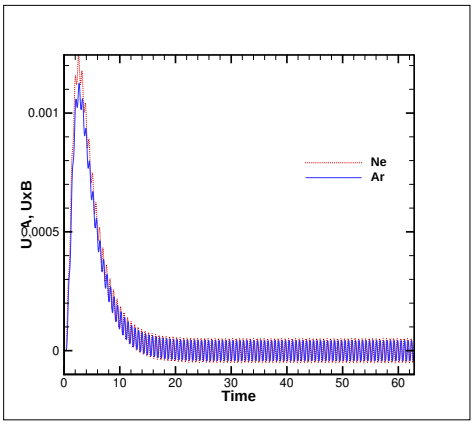

(a) u_x

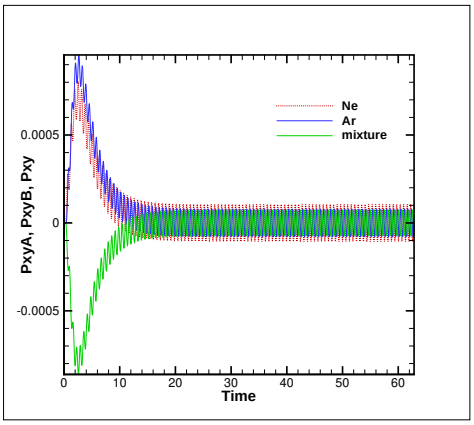

(b) p_{xy}

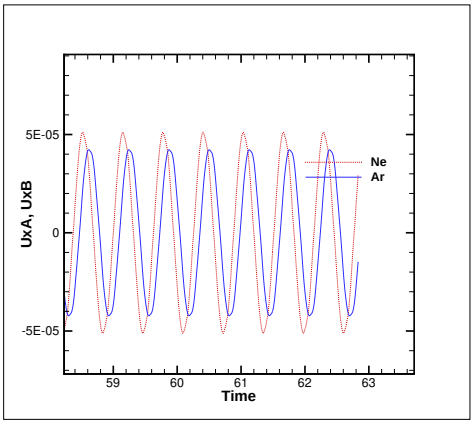

(c) Detail on a few last periods u_x

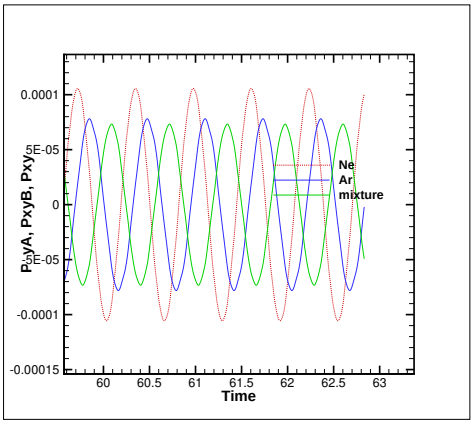

(d) Detail on a few last periods p_{xy}

Figure 8.3: Time evolution of macroscopic parameters at the upper plate for the case 6, $\theta = 1$, $\delta = 10$, Ne-Ar mixture with $C_0 = 0.5$; (a) specie time evolution, (b) specie and mixture shear stresses; (c) specie velocity time evolution, several last periods; (d) specie and mixture shear stress evolution, several last periods.

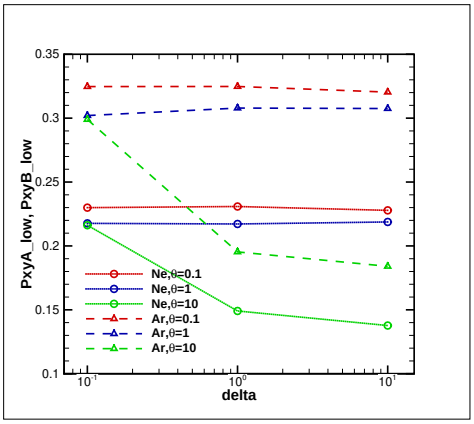

(a) P_{xy} at lower plate $y = -0.5$

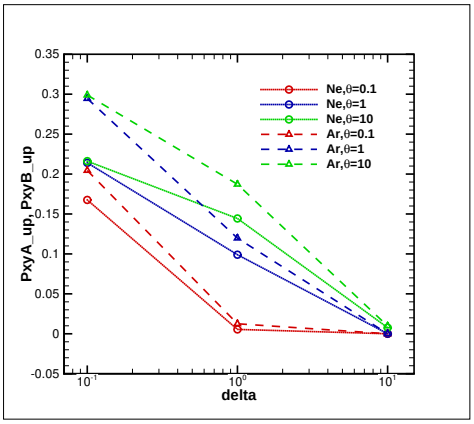

(b) P_{xy} at upper plate $y = +0.5$

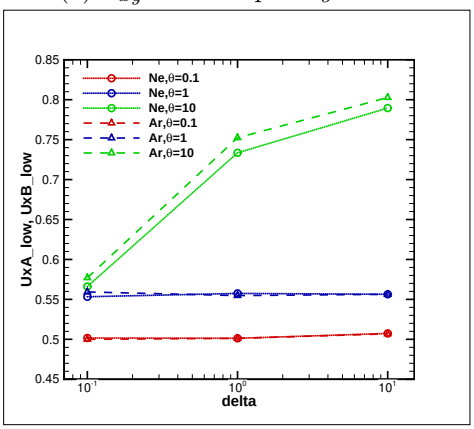

(c) U_x at lower plate $y = -0.5$

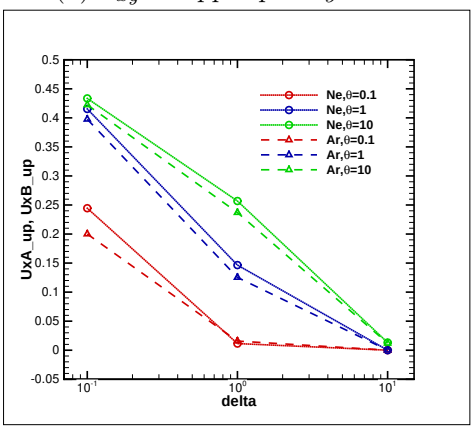

(d) U_x at upper plate $y = +0.5$

Figure 8.4: Amplitude of macroscopic parameters (specie shear stress and velocity) via δ and θ for Ne-Ar mixture with $C_0 = 0.5$.

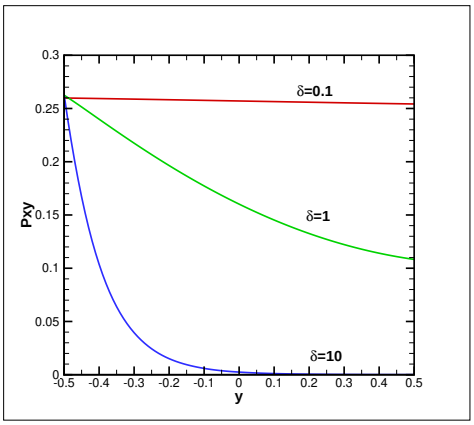

(a) Shear stress amplitude profiles

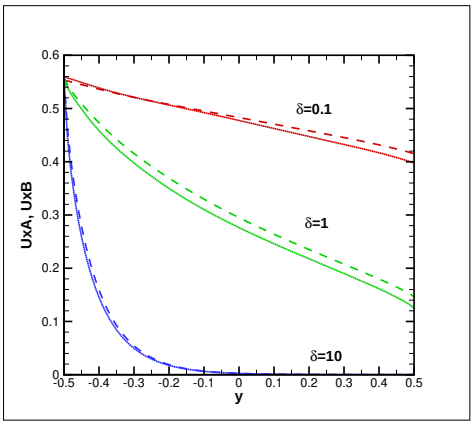

(b) Specie velocity amplitude profiles

Figure 8.5: Ne-Ar mixture with $C_0 = 0.5, \theta = 1$: profiles of (a) the mixture shear stress amplitude, (b) the species velocity amplitude, Ne (dashed line), Ar (dotted line).

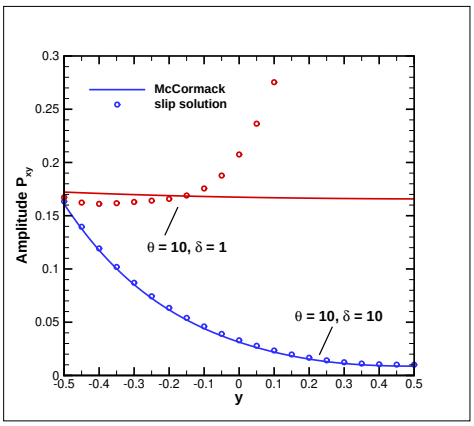

(a) Amplitude P_{xy} profile

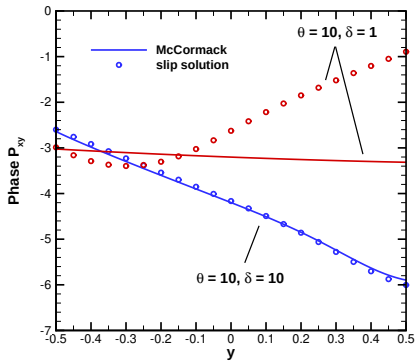

(b) Phase φ_p

Figure 8.6: The amplitude and phase profiles of mixture shear stress are compared with slip analytical solution proposed in Ref. [90] for the cases $8, 9$ and for Ne-Ar mixture with $C_0 = 0.5$.

Chapter 9

Conclusions and Outlook

9.1 Conclusions

This thesis is devoted to the development of various numerical tools for simulation of rarefied gas flows based on kinetic models of the Boltzmann equation. Several iso/non-isothermal internal flow problems of single/binary gas mixture are simulated with steady/unsteady formulations. The obtained numerical results are compared with the open literature and with the available analytical solutions. It is shown that discrete velocity method of kinetic equations is a reliable and efficient compared to numerical methods for full Boltzmann equation (DSMC method and FSM). The main results of this work are summarised as follows:

- Heat transfer between two concentric spheres is simulated using the nonlinear form of the S-model kinetic equation for the large range of the rarefaction parameter. Small, moderate and large temperature and radius ratios are considered. The classical Maxwell diffuse-specular boundary conditions are used at the internal sphere surface and the complete accommodation is assumed on the external sphere. The time-dependent governing equations are discretized based on the discrete velocity method. The upwind approximation is used for the spatial derivatives. The implicit algorithm allows us to reduce considerably the computational time when only steady state solution is needed. Non monotonic behavior of the heat flux as a function of the rarefaction parameter δ_0 is found in the case of the strong temperature ratio between the spheres' surfaces. The essential pressure variation in the radial direction is found for the small and moderate values of the rarefaction parameter. The analytical relations for the temperature and the heat flux in the slip flow regime is obtained for the arbitrary temperature and radius ratio and very good agreement has been found between these analytical expressions and the numerical solution of the S-model equation. The analytical expressions for the number density, temperature and heat flux have been derived for the free molecular regime under assumption

of the complete accommodation for the external sphere and the diffuse-specular reflection on the internal sphere surface. The approximate expression for the heat flux valid for all flow regimes and arbitrary temperature and radius ratio and under an assumption of the diffuse-specular reflection on the internal sphere and diffuse reflection on the external sphere is proposed.

- Unsteady heat transfer between two coaxial cylinders due to the sudden change of the internal cylinder temperature is studied on the basis of the S-model kinetic equation. The simulations have been carried out from the near free molecular to the hydrodynamic flow regimes for one cylinders radius ratio and two cylinders' walls temperature ratios. It is found that for the smallest temperature ratio $\mathcal{T} = 1.3$ the time to reach the steady state value for the averaged heat flux varies approximately from 2.5 to 44 of the characteristic times between the near free molecular and the hydrodynamic flow regimes and it has a minimum in the beginning of the transitional flow regime. Comparing the monoatomic gases behavior in a real geometry it is obtained that at the same working pressure the time needed for Xenon to reach its steady state is 6 times longer than that for Helium. When the temperature ratio increases up to $\mathcal{T} = 2$ the steady state time decreases approximately by 5%. In the slip flow regime the time t_s can also be found from the solution of the energy equation subjected to the temperature jump boundary conditions.

- Transient flow of rarefied gas through an orifice is studied on the basis of nonlinear S-model kinetic equation. The simulations are conducted from the free molecular to hydrodynamic regimes for four values of pressure ratio between reservoirs. The mass flow rate evolution in time is analyzed and it is found that the time to reach the steady state mass flow rate depends essentially on the pressure ratio between the reservoirs and on the gas flow regime in the left reservoir. It needs from 2.35 to 30.37 characteristic times to obtain the steady state mass flow rate, the maximal time to reach the steady state is found in the slip regime for the largest pressure ratio 0.9. The simple fitting formula for the time dependence of the mass flow rate is proposed. It is shown numerically that the flow through the thin orifice never becomes really choked.

- The simple method, proposed previously by other authors, is applied to calculate the gas mass flow rate through the channel of the variable rectangular cross section. The calculations are based on the results of the numerical solution of the linearized S-model kinetic equation obtained by other authors and completed using the same approach in the present paper. The explicit analytical expressions are proposed in the case of the hydrodynamic and free molecular flow regimes. The simple interpolation method is realized to calculate the mass flow rate in the transitional flow regime. The numerical results are compared with analytical solutions and measurements to investigate the phenomenon of

gas flow diodicity. It is shown that the mass flow rate is significantly higher when the tapered channel is perfused like a nozzle (compared to diffusor). It can therefore be stated that under moderately rarefied conditions micro-sized ducts with alongside varying cross section act as a gas flow diode. The theoretically and experimentally analyzed diode effect increases with gaseous rarefaction whereby both presented models can predict that effect qualitatively.

- Couette and Fourier flows between parallel plates are simulated using the McCormack kinetic model of the linearized Boltzmann equation and the linearized Boltzmann equation itself. Two types of gas mixture are considered: one with similar molecular masses (Ne-Ar) and one with very different molecular masses (He-Xe). Three values of concentrations are considered and the simulations are carried out in the near free molecular, transitional and slip flow regimes. For plane Couette and Fourier flows of gaseous mixture, McCormack model gives reliable solutions, which are in good agreement with solutions of linearized Boltzmann equation.

- The simple approach is implemented for the simulation of the oscillatory Couette flow of the gas mixtures. The proposed approach was firstly tested by comparing with the results, previously obtained by the other authors in the case of the steady-state flow of the gas mixtures and also in the case of oscillatory flow of a single gas. Very good agreement with these previously obtained results was found. Then, the simulation of the Ne-Ar and He-Xe mixtures are carried out for large range of the rarefaction parameter, oscillation speed parameter and for three values of the concentration, only for Ne-Ar mixture. It is found that the characteristics of the mixture, like the amplitudes of the mixture shear stress and mixture velocities, are very close to those found for the oscillatory flow of a single gas and the single gas results can be used for the estimations of the mixture parameters in the case, when the molecular masses of the components are relatively close one to the other. However, in the case of the He-Xe mixture the results are very different (up to 30%) from the single gas results. It was found that similarly to the steady state flows the amplitude of the mixture shear stress is lower than that of the single gas. It was also found that even for the relatively large oscillation speed parameter $\theta = 10$, slow oscillations, the steady-state results are very different from that obtained here for the oscillatory gas mixture flows.

9.2 Outlook

Potential developments of this work are given as follows

- Development a hybrid scheme that couple kinetic equation with Navier-Stokes solver to simulate two-phase gas-liquid flow.

- Development of kinetic equation solver in an open source software such as OpenFOAM allows users freedom to customize.

- Development a numerical tool on the basis of kinetic equation to simulate rarefied gas flow through porous media offers many application in petroleum engineering and membrane engineering.

References

[1] S. A. Schaaf and Chambre, *Flow of Rarefied Gases*. Princeton University Press, USA, 1961.

[2] N. G. Hadjiconstantinou, A. L. Garcia, M. Z. Bazant, and G. He, "Statistical error in particle simulations of hydrodynamic phenomena," *J Comput Phys*, vol. 187, no. 1, pp. 274–297, 2003.

[3] J. Fan and C. Shen, "Statistical simulation of low-speed rarefied gas flows," *J. Comput. Phys*, vol. 167, pp. 393–412, 2001.

[4] L. L. Baker and N. G. Hadjiconstantinou, "Variance reduction for Monte Carlo solutions of the Boltzmann equation," *Phys. Fluids, 17 (2005) 051703*.

[5] T. M. M. Homolle and N. G. Hadjiconstantinou, "A low-variance deviational simulation Monte Carlo for the Boltzmann equation," *J. Comput. Phys.*, vol. 226, pp. 2341–2358, 2007.

[6] C. Mouhot and L. Pareschi, "Fast Algorithms for Computing the Boltzmann Collision Operator," *Mathematics of Computation*, vol. 75, no. 256, pp. pp. 1833–1852, 2006.

[7] F. Filbet, "On deterministic approximation of the Boltzmann equation in a bounded domain," *Multiscale Model. Simul. 10 (2012) 792-817.*, vol. 10, pp. 792–817, 2012.

[8] L. Wu, C. White, T. J. Scanlon, J. M. Reese, and Y. Zhang, "Deterministic numerical solutions of the Boltzmann equation using the fast spectral method," *Journal of Computational Physics*, vol. 250, pp. 27–52, Oct. 2013.

[9] L. Wu, J. M. Reese, and Y. Zhang, "Solving the Boltzmann equation deterministically by the fast spectral method: application to gas microflows," *J. Fluid Mech.*, vol. 746, pp. 53–84, 2014.

[10] P. L. Bhatnagar, E. P. Gross, and M. Krook, "A model for collision processes in gases. I. Small Amplitude processes in charged and neutral one-component systems," *Phys. Rev*, vol. 94, no. 3, pp. 511–525, 1954.

[11] E. M. Shakhov, "Generalization of the Krook kinetic relaxation equation," *Fluid Dyn.*, vol. 3, no. 5, pp. 95–96, 1968.

[12] L. H. Holway, "New statistical models in kinetic theory: methods of construction," *Physics of fluids*, vol. 9, no. 9, pp. 1658–1673, 1966.

[13] B. B. Hamel, "Kinetic model for binary gas mixture," *Phys. Fluids*, vol. 8, no. 3, pp. 418–425, 1965.

[14] F. J. McCormack, "Construction of linearized kinetic models for gaseous mixture and molecular gases," *Phys. Fluids*, vol. 16, pp. 2095–2105, 1973.

[15] V. Garzó, A. Santos, and J. J. Brey, "A kinetic model for a multicomponent gas," *Physics of Fluids A*, vol. 1, no. 2, 1989.

[16] P. Andries, K. Aoki, and B. Perthame, "A Consistent BGK-Type Model for Gas Mixtures," *Journal of Statistical Physics*, vol. 106, no. 5-6, pp. 993–1018, 2002.

[17] S. Kosuge, "Model Boltzmann equation for gas mixtures: Construction and numerical comparison," *European Journal of Mechanics - B/Fluids*, vol. 28, no. 1, pp. 170–184, 2009.

[18] S. Brull, V. Pavan, and J. Schneider, "Derivation of a BGK model for mixtures," *European Journal of Mechanics - B/Fluids*, vol. 33, pp. 74–86, May 2012.

[19] J. C. Maxwell, *The Scientific Papers of James Clark Maxwell.* Cambridge University Press, 1890.

[20] L. Lees, "Kinetic theory of description of rarefied gas flow," *Journal of the Society for Industrial and Applied Mathematics*, vol. 13, no. 1, pp. 278–311, 1965.

[21] G. S. Springer and S. F. Wan, "Note on the application of a moment method to heat conduction in rarefied gases between concentric spheres.," *AIAA Journal*, vol. 4, no. 8, pp. 1441–1443, 1966.

[22] Y. Demirel and S. C. Saxena, "Heat transfer in rarefied gas at a gas-solid interface," *Energy*, vol. 21, no. 2, pp. 99–103, 1996.

[23] N. Pazooki and S. K. Loyalka, "Heat transfer in rarefied polyatomic gas - II. Sphere," *International Journal of Heat and Mass Transfer*, vol. 31, no. 5, pp. 977–985, 1988.

[24] V. G. Chernyak and A. Y. E. Margilevskiy, "The kinetic theory of heat and mass transfer from a shperical particle in a rarefied gas," *International Journal of Heat and Mass Transfer*, vol. 32, no. 11, pp. 2127–2134, 1989.

[25] H. Yamaguchi, T. Imai, T. Iwai, A. Kondo, Y. Matsuda, and T. Niimi, "Measurement

of thermal accommodation coefficients using a simplified system in a concentric sphere shells configuration," *Journal of Vac. Sci. Technol. A*, vol. 32, no. 6, p. 61602, 2014.

[26] F. O. Goodman and H. Y. Wachman, *Dynamics of Gas-Surface scattering.* Academic Press, New York, NY, USA, 1976.

[27] D. R. Willis, "Heat Transfer and Shear between Coaxial Cylinders for Large Knudsen Numbers," *Phys. Fluids*, vol. 8, no. 10, pp. 1908–1910, 1965.

[28] C.-L. Su., "Heat Conduction in a Rarefied Gas between Concentric Cylinders," *Phys. Fliuds*, vol. 11, no. 10, p. 2131, 1968.

[29] D. G. M. Anderson, "On the steady Krook kinetic equation: Part 2," *Journal of Plasma Physics*, vol. 1, no. 2, pp. 255–265, 1966.

[30] F. M. Sharipov and G. M. Kremer, "On the frame dependence of constitutive equations. I. Heat transfer through a rarefied gas between two rotating cylinders," *Continuum Mechanics and Thermodynamics*, vol. 7, no. 1, pp. 57–72, 1995.

[31] F. M. Sharipov and G. M. Kremer, "Heat conduction through a rarefied gas between two rotating cylinders at small temperature difference," *ZAMP Zeitschrift fur angewandte Mathematik und Physik*, vol. 46, pp. 680–692, Sept. 1995.

[32] F. Sharipov and G. Bertoldo, "Heat transfer through a rarefied gas confined between two coaxial cylinders with high radius ratio," *Journal of Vacuum Science Technology A: Vacuum, Surfaces, and Films*, vol. 24, pp. 2087–2093, Nov. 2006.

[33] S. Pantazis and D. Valougeorgis, "Heat transfer through rarefied gases between coaxial cylindrical surfaces with arbitrary temperature difference," *European Journal of Mechanics - B/Fluids*, vol. 29, pp. 494–509, Nov. 2010.

[34] F. M. Sharipov and G. M. Kremer, "Non-isothermal couette flow of a rarefied gas between two rotating cylinders," *European Journal of Mechanics - B/Fluids*, vol. 18, no. 1, pp. 121–130, 1999.

[35] W. Jitschin and S. Ludwig, "Dynamical behaviour of the Pirani sensor," *Vacuum*, vol. 75, no. 2, pp. 169–176, 2004.

[36] D. C. Wadsworth, D. A. Erwin, and E. P. Muntz, "Transient motion of a confined rarefied gas due to wall heating or cooling," *Journal of Fluid Mechanics*, vol. 248, no. 1, p. 219, 1993.

[37] A. Alexeenko, D. Fedosov, S. Gimelshein, D. Levin, and R. Collins, "Transient Heat Transfer and Gas Flow in a MEMS-Based Thruster," *Journal of Microelectromechanical Systems*, vol. 15, pp. 181–194, Feb. 2006.

[38] F. Sharipov, "Transient flow of rarefied gas through a short tube," *Vacuum*, vol. 90, pp. 25–30, Apr. 2013.

[39] K. Jousten, S. Pantazis, J. Buthing, R. Model, and M. Wuest, "A standard to test the dynamics of vacuum gauges in the millisecond range," *Vacuum*, vol. 100, pp. 14–17, 2014.

[40] T. C. Lilly, S. F. Gimelshein, A. D. Ketsdever, and G. N. Markelov, "Measurements and computations of mass flow and momentum flux through short tubes in rarefied gases," *Phys. Fluids*, vol. 18, no. 9, pp. 093601.1–11, 2006.

[41] S. Varoutis, D. Valougeorgis, and F. Sharipov, "Simulation of gas flow through tubes of finite length over the whole range of rarefaction for various pressure drop ratios," *J. Vac. Sci. Technol. A.*, vol. 22, no. 6, pp. 1377–1391, 2009.

[42] I. Graur, A. P. Polikarpov, and F. Sharipov, "Numerical modelling of rarefied gas flow through a slit at arbitrary gas pressure ratio based on the kinetic equations," *ZAMP*, vol. 63, no. 3, pp. 503–520, 2012.

[43] S. Misdanitis, S. Pantazis, and D. Valougeorgis, "Pressure driven rarefied gas flow through a slit and an orifice," *Vacuum*, vol. 86, no. 11, pp. 1701–1708, 2012.

[44] V. V. Aristov, A. A. Frolova, S. A. Zabelok, R. R. Arslanbekov, and V. I. Kolobov, "Simulations of pressure-driven flows through channels and pipes with unified flow solver," *Vacuum*, vol. 86 SI, no. 11, pp. 1717–1724, 2012.

[45] V. A. Titarev and E. M. Shakhov, "Computational study of a rarefied gas flow through a long circular pipe into vacuum," *Vacuum*, vol. 86, no. 11, pp. 1709–1716, 2012.

[46] V. A. Titarev, "Rarefied gas flow in a circular pipe of finite length," *Vacuum*, vol. 94, pp. 92–103, 2013.

[47] V. A. Titarev, E. M. Shakhov, and S. V. Utyuzhnikov, "Rarefied gas flow through a diverging conical pipe into vacuum," *Vacuum*, vol. 101, no. 0, pp. 10–17, 2014.

[48] F. Sharipov, "Transient flow of rarefied gas through an orifice," *J. Vac. Sci. Technol. A*, vol. 30, no. 2, pp. 021602.1–5, 2012.

[49] J. Lihnaropoulos and D. Valougeorgis, "Unsteady vacuum gas flow in cylindrical tubes," *Fusion Engineering and Design*, vol. 86, no. 9-11, pp. 2139–2142, 2011.

[50] A. Polikarpov and I. Graur, "Unsteady rarefied gas flow through a slit," *Vacuum*, vol. 101, pp. 79–85, 2014.

[51] F. Sharipov and V. Seleznev, "Data on internal rarefied gas flows," *J. Phys. Chem. Ref. Data*, vol. 27, no. 3, pp. 657–706, 1998.

[52] B. T. Porodnov, P. E. Suetin, S. F. Borisov, and V. D. Akinshin, "Experimental investigation of rarefied gas flow in different channels," *J. Fluid Mech.*, vol. 64, no. 3, pp. 417–437, 1974.

[53] H. Ashkenas and F. S. Sherman, "The structure and utilization of supersonic free jets in low density wind tunnels," in *Proceedings of the 4th International Symposium on RGD*, vol. 2, pp. 84–105, 1964.

[54] C. Aubert and S. Colin, "High-order boundary conditions for gaseous flows in rectangular microducts," *Microscale Thermophys. Eng.*, vol. 5, no. 41, 2001.

[55] S. Colin, P. Lalonde, and R. Caen, "Validation of a second-order slip flow model in a rectangular microchannel," *Heat Transf Eng*, vol. 25, no. 3, pp. 23–30, 2004.

[56] T. Ewart, P. Perrier, I. A. Graur, and J. G. Méolans, "Mass flow rate measurements in microchannel, from hydrodynamic to near free molecular regimes," *Journal of fluid mechanics*, vol. 584, pp. 337–356, 2007.

[57] I. A. Graur, , P. Perrier, W. Ghozlani, and J. G. Méolans, "Measurements of tangential momentum accommodation coefficient for various gases in plane microchannel," *Physic. Fluids*, vol. 21, no. 102004, 2009.

[58] T. Veltzke, *On gaseous microflows under isothermal conditions*. PhD thesis, University of Bremen, 2013.

[59] L. R. de Silva and C. J. Deschamps, "Modeling of gas leakage through compressor valves," in *International compressor engineering conference*, 2012.

[60] N. D. Stevanovic, "A new analytical solution of microchannel gas flow," *J. Micromech MicroEng.*, vol. 17, pp. 1695–1702, 2007.

[61] N. D. Stevanovic and D. Djordjevic V, "The exact analytical solution for the gas lubricated bearing in the slip and continuum flow regime," *Publications de l'Institut Mathématique*, vol. 91, no. 105, pp. 83–93, 2012.

[62] F. Sharipov and G. Bertoldo, "Rarefied gas flow through a long tube of variable radius," *J. Vac. Sci. Technol. A*, vol. 23, no. 3, pp. 531–533, 2005.

[63] V. A. Titarev, S. V. Utyuzhnikov, and E. M. Shakhov, "Rarefied gas flow into vacuum through square pipe with variable cross section," *Comput. Math. and Math. Phys.*, vol. 53, no. 8, pp. 1221–1230, 2013.

[64] C. Aubert, S. Colin, and R. Caen, "Unsteady Gaseous Flows in Tapered Microchannels," in *Thechnical Proceedings of the 1998 International Conference on Modeling and Simulation of Microsystems*, vol. Chapter 11, pp. 486–491, ISBN:0-96661-35-0-3, 1998.

[65] T. Veltzke, M. Baune, and J. Thöming, "The contribution of diffusion to gas microflow: An experimental study," *Phys. Fluids*, vol. 24, p. 82004, 2012.

[66] S. G. A. Stemme E., "Valve-less Diffuser/Nozzle Based Fluid Pump," *Sens. Actuat. A: Phys.*, vol. 39, no. 159-167, 1993.

[67] H. W. Lee and A. H. A, "Neuro-Genetic Optimization of the Diffuser Elements for Applications in a Valveless Diaphragm Micropumps System," *Sensors*, vol. 9, no. 9, pp. 7481–7497, 2009.

[68] I. Graur and M. Ho, "Rarefied gas flow through a long rectangular channel of variable cross section," *Vacuum*, vol. 101, pp. 328–332, Mar. 2014.

[69] C. Cercignani, *Mathematical methods in kinetic theory*. Premium Press, New York, London, 1990.

[70] J. H. Ferziger and H. G. Kaper, *Mathematical Theory of Transport Processes in Gases*. Amsterdam: North-Holland Publishing Company, 1972.

[71] Y. Onishi, "On the behavior of a slightly rarefied gas mixture over plane boundaries," *Z. Angew. Math. Phys. (ZAMP)*, vol. 37, pp. 573–596, 1986.

[72] D. Valougeorgis, "Couette flow of a binary gas mixture," *Phys. Fluids*, vol. 31, no. 3, pp. 521–524, 1988.

[73] C. E. Siewert, "Couette flow for a binary gas mixture," *J. Quant. Spectr. Rad. Tran.*, vol. 70, pp. 321–332, 2001.

[74] F. Sharipov, L. M. G. Cumin, and D. Kalempa, "Plane Couette flow of binary gaseous mixture in the whole range of the Knudsen number," *Eur. J. Mech. B/Fluids*, vol. 23, pp. 899–906, 2004.

[75] R. D. M. Garcia and C. E. Siewert, "The McCormack model for gas mixtures: Plane Couette flow," *Phys. Fluids*, vol. 17, no. 3, pp. 037102.1–6, 2005.

[76] R. D. M. Garcia and C. E. Siewert, "Couette flow of a binary mixture of rigid-sphere gases described by the linearized Boltzmann equation," *Eur. J. Mech. B / Fluds*, vol. 27, pp. 823–836, 2008.

[77] S. Kosuge, K. Aoki, and S. Takata, "Heat transfer in a gas mixture between two parallel plates: finite-difference analysis of the Boltzmann equation," in *Rarefied Gas Dynamics* (T. J. Bartel and M. A. Gallis, eds.), vol. 585, (Melvile), pp. 289–296, 22nd Int. Symp., AIP Conference Proc., 2001.

[78] R. D. M. Garcia and C. E. Siewert, "The McCormack model for gas mixtures: Heat transfer in a plane channel," *Phys. Fluids*, vol. 16, no. 9, pp. 3393–3402, 2004.

[79] R. D. M. Garcia and C. E. Siewert, "Heat transfer between parallel plates: An approach based on the linearized Boltzmann equation for a binary mixture of rigid-sphere gases," *Phys. Fluids*, vol. 19, no. 2, pp. 027102.1–7, 2007.

[80] F. Sharipov, L. M. G. Cumin, and D. Kalempa, "Heat flux through a binary gaseous mixture over the whole range of the Knudsen number," *Physica A*, vol. 378, pp. 183–193, 2007.

[81] J. Kestin, K. Knierim, E. A. Mason, B. Najafi, S. T. Ro, and M. Waldman, "Equilibrium and transport properties of the noble gases and their mixture at low densities," *J. Phys. Chem. Ref. Data*, vol. 13, no. 1, pp. 229–303, 1984.

[82] D. R. Willis, "Comparison of kinetic theory analyses of lineralized Couette flow," *Phys. Fluids*, vol. 5, no. 2, pp. 127–135, 1962.

[83] C. Cercignani and C. D. Pagani, "Variational approach to boundary value problems in kinetic theory," *Phys. Fluids*, vol. 9, no. 6, pp. 1167–1173, 1966.

[84] S. K. Loyalka, N. Petrellis, and T. S. Storvik, "Some exact numerical results for the BGK model: Couette, Poiseuille and thermal creep flow between parallel plates," *Z. Angew. Math. Phys (ZAMP)*, vol. 30, pp. 514–521, 1979.

[85] Y. Sone, S. Takata, and T. Ohwada, "Numerical analysis of the plane Couette flow of a rarefied gas on the basis of the linearized Boltzmann equation for hard-sphere molecules," *Eur. J. Mech. B / Fluids*, vol. 9, no. 3, pp. 273–288, 1990.

[86] C. E. Siewert, "Poiseuille, thermal creep and Couette flow: results based on the CES model for the linearized Boltzmann equation," *Eur. J. Mech. B / Fluids*, vol. 21, pp. 579–597, 2002.

[87] J. H. Park, P. Bahukudumbi, and A. Beskok, "Rarefaction effects on shear driven oscillatory gas flows: A direct simulation Monte Carlo study in the entire Knudsen regime," *Phys. Fluids*, vol. 16, no. 2, pp. 317–330, 2004.

[88] N. G. Hadjiconstantinou, "Oscillatory shear-driven gas flows in the transition and free-molecular flow regimes," *Phys. Fluids*, vol. 17, pp. 1006111.–9, 2005.

[89] F. Sharipov and D. Kalempa, "Gas flow near a plate oscillating longitudinally with an arbitrary frequency," *Phys. Fluids*, vol. 19, no. 1, pp. 017110.1–10, 2007.

[90] F. Sharipov and D. Kalempa, "Oscillatory Couette flow at arbitrary oscillation frequency over the whole range of the Knudsen number," *Microfluidics and Nanofluidics*, vol. 4, no. 5, pp. 363–374, 2008.

[91] T. Doi, "Numerical analysis of oscillatory Couette flow of a rarefied gas on the basis of

the linearized Boltzmann equation," *Vacuum*, vol. 84, pp. 734–737, 2010.

[92] Y. W. Yap and J. E. Sader, "High accuracy numerical solutions of the Boltzmann Bhatnager-Gross-Krook equation for steady and oscillatory Couette flows," *Physics of Fluids*, vol. 24, no. 032004, 2012.

[93] G. H. Tang, X. J. Gu, R. W. Barber, D. R. Emerson, and Y. H. Zhang, "Lattice Boltzmann simulation of nonequilibrium effects in oscillatory gas flow," *Phys. Rev. E*, vol. 78, no. 2, p. 26706, 2008.

[94] L. D. Landau and E. M. Lifshitz, *Fluid Mechanics*. New York: Pergamon, 1989.

[95] T. Veijola, H. Kuisma, and L. J, "The influence of gas-surface interaction on gas-film damping in a silicon accelerometer," *Sensor Actua. A-Phys.*, vol. 66, pp. 83–92, 1998.

[96] L. Desvillettes and S. Lorenzani, "Sound wave resonances in micro-electro-mechanical systems devices vibrating at high frequencies according to the kinetic theory of gases," *Physics of Fluids*, vol. 24, p. 092001, Sept. 2012.

[97] M. Bisi and S. Lorenzani, "Damping forces exerted by rarefied gas mixture in MEMS devices vibrating at high frequencies," in *Proccedings of the HTFFM-V conference*, no. O-120, 2014.

[98] C.-C. Nguyen and R. T. Howe, "An integrated CMOS micromechanical resonator high-Q oscillator," *Solid-State Circuits, IEEE Journal of*, vol. 34, no. 4, pp. 440–455, 1999.

[99] K. L. Ekinci and M. L. Roukes, "Nanoelectromechanical systems," *Review of Scientific Instruments*, vol. 76, no. 6, p. 061101, 2005.

[100] H. Craighead, "Nanoelectromechanical systems," *Science*, vol. 290, no. 5496, p. 1532, 2000.

[101] J. S. Bunch, A. M. van der Zande, S. S. Verbridge, I. W. Frank, D. M. Tanenbaum, J. M. Parpia, H. G. Craighead, and P. L. McEuen, "Electromechanical Resonators from Graphene Sheets," *Science*, vol. 315, no. 5811, pp. 490–493, 2007.

[102] I. Graur, M. T. Ho, and M. Wuest, "Simulation of the transient heat transfer between two coaxial cylinders," *Journal of Vacuum Science & Technology A: Vacuum, Surfaces, and Films*, vol. 31, no. 6, pp. 061603.1–9, 2013.

[103] M. T. Ho and I. Graur, "Numerical study of unsteady rarefied gas flow through an orifice," *Vacuum*, vol. 109, pp. 328–332, 2014.

[104] Y. Wu, "Kinetic theory of thermal molecular flow between coaxial cylinders and concentric spheres," *Journal of Chemical Physics*, vol. 52, no. 3, pp. 1494–1498, 1970.

[105] F. Sharipov, "Numerical simulation of rarefied gas flow through a thin orifice," *Journal of Fluid Mechanics*, vol. 518, pp. 35–60, 2004.

[106] F. Sharipov, "Non-isothermal gas flow through rectangular microchannels," *J. Micromech. Microeng.*, vol. 9, no. 4, pp. 394–401, 1999.

[107] G. A. Bird, *Molecular Gas Dynamics and the Direct Simulation of Gas Flows*. Oxford Science Publications, 1994.

[108] D. Bernoulli, *Hydrodynamica, sive de viribus et motibus fluidorum commentarii*. Argentoria, Strasbourg, 1738.

[109] J. C. M. M.A., "Illustrations of the dynamical theory of gases.Part I. On the motions and collisions of perfectly elastic spheres," *Philosophical Magazine*, vol. 4, no. 19, pp. 19–32, 1860.

[110] J. C. M. M.A., "Illustrations of the dynamical theory of gases.Part II. On the process of difussion of two or more kinds of moving particles among another," *Philosophical Magazine*, vol. 4, no. 20, pp. 21–37, 1860.

[111] L. Boltzmann, "Weitere Studien über das Wärmegleichgewicht unter Gasmolekülen," *Math.-Naturwiss. Cl. Akad. Wiss., Wien*, vol. 66, pp. 275–370, 1872.

[112] S. Chapman and T. G. Cowling, *The mathematical theory of non-uniform gases*. University Press, Cambridge, 1970.

[113] Y. Sone, *Molecular gas dynamics: theory, techniques, and applications*. Birkhäuser, Boston, 2007.

[114] S. Chapman, "On the Law of Distribution of Molecular Velocities, and on the Theory of Viscosity and Thermal Conduction, in a Non-Uniform Simple Monatomic Gas," *Philosophical Transactions of the Royal Society of London A: Mathematical, Physical and Engineering Sciences*, vol. 216, pp. 279–348, Jan. 1916.

[115] S. Chapman, "On the Kinetic Theory of a Gas. Part II: A Composite Monatomic Gas: Diffusion, Viscosity, and Thermal Conduction," *Philosophical Transactions of the Royal Society of London A: Mathematical, Physical and Engineering Sciences*, vol. 217, pp. 115–197, Jan. 1918.

[116] D. Enskog, *The kinetic theory of phenomena in fairly rarefied gases*. Ph.d. thesis, University of Uppsalsa, 1917.

[117] H. Grad, "On the kinetic theory of rarefied gases," *Communications on Pure and Applied Mathematics*, vol. 2, no. 4, pp. 331–407, 1949.

[118] G. A. Bird, "Approach to Translational Equilibrium in a Rigid Sphere Gas," *Physics of*

Fluids, vol. 6, no. 10, 1963.

[119] K. Nanbu, "Direct Simulation Scheme Derived from the Boltzmann Equation. I. Monocomponent Gases," *Journal of the Physical Society of Japan*, vol. 49, no. 5, pp. 2042–2049, 1980.

[120] J. E. Broadwell, "Study of rarefied shear flow by the discrete velocity method," *Journal of Fluid Mechanics*, vol. 19, no. 03, pp. 401–414, 1964.

[121] J. E. Broadwell, "Shock Structure in a Simple Discrete Velocity Gas," *Physics of Fluids (1958-1988)*, vol. 7, no. 8, 1964.

[122] L. Pareschi and B. Perthame, "A Fourier spectral method for homogeneous boltzmann equations," *Transport Theory and Statistical Physics*, vol. 25, no. 3-5, pp. 369–382, 1996.

[123] L. Pareschi and G. Russo, "Numerical Solution of the Boltzmann Equation I: Spectrally Accurate Approximation of the Collision Operator," *SIAM Journal on Numerical Analysis*, vol. 37, no. 4, pp. 1217–1245, 2000.

[124] G. Liu, "A method for constructing a model form for the Boltzmann equation," *Physics of Fluids A: Fluid Dynamics (1989-1993)*, vol. 2, no. 2, pp. 277–280, 1990.

[125] L. Mieussens and H. Struchtrup, "Numerical comparison of Bhatnagar-Gross-Krook models with proper Prandtl number," *Physics of Fluids*, vol. 16, pp. 2797–2813, Aug. 2004.

[126] H. Struchtrup, *Macroscopic Transport Equations for Rarefied Gas Flows: Approximation Methods in Kinetic Theory*. Springer-Verlag Berlin Heidelberg, 1 ed., 2005.

[127] C. Cercignani and F. Sernagiotto, "Cylindrical Couette Flow of a Rarefied Gas," *Physics of Fluids*, vol. 10, no. 6, pp. 1200–1204, 1966.

[128] H. Struchtrup, "The BGK-model with velocity-dependent collision frequency," *Continuum Mechanics and Thermodynamics*, vol. 9, no. 1, pp. 23–31, 1997.

[129] Y. Zheng and H. Struchtrup, "Ellipsoidal statistical Bhatnagar-Gross-Krook model with velocity-dependent collision frequency," *Phys. Fluids*, vol. 17, no. 12, pp. 127103.1–127103.17, 2005.

[130] C. Alekseenko, Alexander and Euler, "A Bhatnagar-Gross-Krook kinetic model with velocity-dependent collision frequency and corrected relaxation of moments," *Continuum Mechanics and Thermodynamics*, vol. xxx, no. xxx, p. xxx, 2015.

[131] P. Jenny, M. Torrilhon, and S. Heinz, "A solution algorithm for the fluid dynamic equations based on a stochastic model for molecular motion," *Journal of Computational Physics*, vol. 229, pp. 1077–1098, Feb. 2010.

[132] M. H. Gorji, M. Torrilhon, and P. Jenny, "Fokker-Planck model for computational studies of monatomic rarefied gas flows," *Journal of Fluid Mechanics*, vol. 680, pp. 574–601, 2011.

[133] J. Mathiaud and L. Mieussens, "A Fokker-Planck model of the Boltzmann equation with correct Prandtl number," *ArXiv e-prints*, 2015.

[134] P. Welander, "On the temperature jump in a rarefied gas," *Ark. Fys.*, vol. 7, no. 5, pp. 507–553, 1954.

[135] T. F. Morse, "Kinetic model equation for gas mixture," *Physic of Fluids*, vol. 7, no. 12, pp. 2012–2013, 1964.

[136] Y. S. Lou and T. K. Shih, "Nonlinear Heat conduction in rarefied gases confined between concentric cylinders and shperes," *Physics of Fluids*, vol. 15, no. 5, pp. 785–788, 1972.

[137] M. N. Kogan, *Rarefied gas dynamics*. Plenum Press New York, 1969.

[138] S. K. Loyalka, "Momentum and temperature-slip coefficients with arbitrary accommodation at the surface," *J. Chem. Phys.*, vol. 48, no. 12, pp. 5432–5436, 1968.

[139] S. K. Loyalka, "Slip in the thermal creep flow," *Phys. Fluids*, vol. 14, no. 11, pp. 21–24, 1971.

[140] S. K. Loyalka, "Temperature jump - rigid-sphere gas with arbitrary gas surface interaction," *Nucl. Sci. Eng*, vol. 108, no. 1, pp. 69–73, 1979.

[141] Y. Sone, T. Ohwada, and K. Aoki, "Temperature jump and Knudsen layer in a rarefied gas over a plane wall: Numerical analysis of the linearized Boltzmann equation for hard-sphere molecules," *Physics of Fluids A*, vol. 1, no. 2, pp. 363–370, 1989.

[142] C. E. Siewert, "Viscous-slip, thermal-slip and temperature-jump coefficients as defined by the linearized Boltzmann equation and the Cercignani-Lampis boundary condition," *Phys. Fluids*, vol. 15, no. 6, pp. 1696–1701, 2003.

[143] F. Sharipov, "Data on the Velocity Slip and Temperature Jump on a Gas-Solid Interface," *J.Phys. Chem. Ref. Data*, vol. 40, no. 2, pp. 23101–23128, 2011.

[144] V. A. Titarev, "Conservative numerical methods for model kinetic equations," *Computers & Fluids*, vol. 36, no. 9, pp. 1446–1459, 2007.

[145] E. M. Shakhov and V. A. Titarev, "Numerical study of the generalized cylindrical Couette flow of rarefied gas," *European Journal of Mechanics - B/Fluids*, vol. 28, no. 1, pp. 152–169, 2009.

[146] I. A. Graur and A. P. Polikarpov, "Comparison of different kinetic models for the heat transfer problem," *Heat and Mass Transfer*, vol. 46, no. 3, pp. 237–244, 2009.

[147] I. Graur, A. P. Polikarpov, and F. Sharipov, "Numerical modelling of rarefied gas flow through a slit into vacuum based on the kinetic equation," *Computers & Fluids*, vol. 49, no. 1, pp. 87–92, 2011.

[148] Y. Wu, "Thermal conductances in a collisionless gas between coaxial cylinders and concentric spheres," *J. Plasma Physics*, vol. 1, no. 2, pp. 209–217, 1967.

[149] Y. A. Koshmarov and Y. A. Ryzhov, *Applied rarefied gas dynamics.* Mashinostroenie, 1977.

[150] L. Lees and C.-Y. Liu, "Kinetic-Theory Description of Conductive Heat Transfer from a Fine Wire," *Physics of Fluids*, vol. 5, p. 1137, Oct. 1962.

[151] F. S. Sherman, "A survey of experimental results and methods for the transitional regime of rarefied gas dynamics," in *Rarefied Gas Dynamic, Proc. 3rd Int. Symp. on Rarefied Gas Dynamics* (J. A. Lauermann, ed.), vol. II, (New York), pp. 228–260, Academic Press, 1963.

[152] G. S. Springer, "Heat transfer in rarefied gases," in *Advanced in heat transfer* (T. F. Irvine and J. P. Harnett, eds.), pp. 163–218, Academic, New York, 1971.

[153] J. Y. Yang and J. C. Huang, "Rarefied flow computations using nonlinear model {B}oltzmann equations," *J. Comput Phys*, vol. 120, no. 2, pp. 323–339, 1995.

[154] V. A. Titarev and E. M. Shakhov, "Numerical study of unsteady evaporation and heat transfer from a spherical surface," *Fluid Dynamics*, vol. 40, no. 1, pp. 159–168, 2005.

[155] P. L. Roe, "Characteristic-based schemes for the Euler equations," *Ann. Rev. Fluid Mech*, 1986.

[156] V. P. Kolgan, "Application of the principle of minimizing the derivative to the construction of finite-difference schemes for computing discontinuous solutions of gas dynamics," *Journal of Computational Physics*, vol. 230, no. 7, pp. 2384–2390, 2011.

[157] C. Tantos, D. Valougeorgis, M. Pannuzzo, A. Frezzotti, and G. L. Morini, "Conductive heat transfer in a rarefied polyatomic gas confined between coaxial cylinders," *International Journal of Heat and Mass Transfer*, vol. 79, pp. 378–389, Dec. 2014.

[158] I. N. Larina and V. A. Rykov, "A numerical method for calculationg axisymmetric rarefied gas flows," *Comput. Math. Math. Phys.*, vol. 38, no. 8, pp. 1335–1346, 1998.

[159] H. Yamaguchi, K. Kanazawa, Y. Matsuda, T. Niimi, A. Polikarpov, and I. Graur, "Investigation on heat transfer between two coaxial cylinders for measurement of thermal accommodation coefficient," *Physics of Fluids*, vol. 24, no. 062002, 2012.

[160] R. Narasimha, "Orifice flow of high Knudsen numbers," *J. Fluid Mech.*, vol. 10, pp. 371–

384, 1961.

[161] D. R. Willis, "Mass flow through a circular orifice and a two-dimensional slit at high Knudsen numbers.," *J. Fluid Mech.*, vol. 21, pp. 21–31, 1965.

[162] B. Van Leer, "A historical oversight: Vladimir P. Kolgan and his high-resolution scheme," *Journal of Computational Physics*, vol. 230, no. 7, pp. 2383–2387, 2011.

[163] L. Mieussens, "Discrete-velocity models and numerical schemes for the Boltzmann-BGK equation in plane and axisymmetric geometries," *J. Comput. Phys.*, vol. 162, no. 2, pp. 429–466, 2000.

[164] R. Courant, K. Friedrichs, and H. Lewy, "On the Partial Difference Equations of MathematicalPhysics," *IBM Journal on Research and development*, vol. 11, no. 2, pp. 215–234, 1967.

[165] M. D. Morse, *Experimental methods in the physical sciences*, vol. 29B, ch. Supersonic, pp. 21–47. Academic Press Inc., 1996.

[166] L. Driskell, *Control-valve selection and sizing*. Research Triangle Park, N.C. : Instrument Society of America, 1983.

[167] R. G. Cunningham, "Orifice meters with supercritical compressible flow," *Transactions of the ASME*, vol. 73, pp. 625–638, 1951.

[168] H. L. Weissberg, "End correction for slow viscous flow through long tubes," *Physics of Fluids*, vol. 5, no. 5, pp. 1033–1036, 1962.

[169] S. Pantazis and D. Valougeorgis, "Rarefied gas flow through a cylindrical tube due to a small pressure difference," *Eur. J. Mech.-B/Fluids*, vol. 38, pp. 114–127, 2013.

[170] A. S. Berman, "Free molecule transmission probabilities," *J. Appl. Phys.*, vol. 36, no. 10, p. 3356, 1965.

[171] C. Cercignani and A. Daneri, "Flow of a rarefied gas between two parallel plates," *Physics of Fluids*, vol. 6, pp. 993–996, 1963.

[172] A. B. Huang, D. P. Giddens, and C. W. Bagual, "Rarefied gas flow between parallel plates based on the discrete ordinate method," *Physics of Fluids*, vol. 10, no. 3, pp. 498–502, 1967.

[173] T. Ohwada, Y. Sone, and K. Aoki, "Numerical analysis of the Poiseuille and thermal transpiration flows between two parallel plates on the basis of the Boltzmann equation for hard sphere molecules," *Physics of Fluids A*, vol. 1, no. 12, pp. 2042–2049, 1989.

[174] J. Stoer and R. Bulirsch, *Introduction to Numerical Analysis*. New York, Springer Verlag,

1980.

[175] V. A. Titarev and E. M. Shakhov, "Kinetic Analysis of the Isothermal Flow in a Long Rectangular Microchannel," *Computational Mathematics and Mathematical Physics*, vol. 50, no. 7, pp. 1221–1237, 2010.

[176] F. Sharipov, "Rarefied gas flow through a long rectangular channel," *J. Vac. Sci. Technol. A*, vol. 17, no. 5, pp. 3062–3066, 1999.

[177] J. G. Méolans, M. H. Nacer, M. Rojas, P. Perrier, and I. Graur, "Effects of two transversal finite dimensions in long microchannel: Analytical approach in slip regime," *Physics of Fluids*, vol. 24, no. 11, 2012.

[178] V. V. Zhvick and O. G. Friedlander, "Poiseuille flow in a capillary at all regimes of rarefied gas flows," in *AIP Conference Proceedings*, vol. 1501, pp. 830–836, American Institute of Physics, Nov. 2012.

[179] S. Albertoni, C. Cercignani, and L. Gotusso, "Numerical evaluation of the slip coefficient," *Physics of Fluids*, vol. 6, no. 993-996, 1963.

[180] C. E. Siewert and F. Sharipov, "Model equations in rarefied gas dynamics: Viscous-slip and thermal-slip coefficients," *Phys. Fluids*, vol. 14, no. 12, pp. 4123–4129, 2002.

[181] W. H. Press, S. A. Teukolsky, W. T. Vetterling, and B. P. Flannery, *Numerical Recipes: The Art of Scientific Computing*. New York, NY, USA: Cambridge University Press, 3 ed., 2007.

[182] T. Ohwada, Y. Sone, and K. Aoki, "Numerical analysis of the shear and thermal creep flows of a rarefied gas over a plane wall on the basis of the linearized Boltzmann equation for hard-sphere molecules," *Physics of Fluids A*, vol. 1, no. 9, pp. 1588–1599, 1989.

[183] P. Perrier, I. A. Graur, T. Ewart, and J. G. Méolans, "Mass flow rate measurements in microtubes: from hydrodynamic to near free molecular regime," *Physic of fluids*, vol. 23, no. 4, 2011.

[184] F. Sharipov and D. Kalempa, "Gaseous mixture flow through a long tube at arbitrary Knudsen number," *J. Vac. Sci. Technol. A*, vol. 20, no. 3, pp. 814–822, 2002.

[185] Y. Sone, *Kinetic Theory and Fluid Mechanics*. Birkhäuser, Boston, 2002.

[186] M. Greenspan, "Propagation of sound in rarefied Helium," *J. Acoust. Soc. Am.*, vol. 22, p. 568, 1950.

[187] I. N. Ivchenko, S. K. Loyalka, and R. V. Tompson, "Slip coefficient for binary gas mixtures," *J. Vac. Sci. Technol. A*, vol. 15, pp. 2375–2381, 1997.

[188] I. N. Ivchenko, S. K. Loyalka, and R. V. Tompson, "Boundary slip phenomena in a binary gas mixture," *Z. Angew. Math. Phys. (ZAMP)*, vol. 53, no. 1, pp. 58–72, 2002.

[189] F. Sharipov and D. Kalempa, "Slip coefficients for gaseous mixtures," in *Rarefied Gas Dynamics* (A. Ketsdever and E. P. Muntz, eds.), vol. 663, (Melville), pp. 164–169, 23rd Int. Symp., Canada, 2002, American Institute of Physics, 2003.

[190] D. F. Elliott and K. R. Rao, *Fast transforms: Algorithms, analyses, applications*. New York: Academic Press, 1982.

APPENDICES

Appendix A

Details on McCormack model

The $\upsilon_{\alpha\beta}^{(i)}$ functions in the collision term of McCormack model (7.11) are defined as following

$$
\begin{aligned}
\upsilon_{\alpha\beta}^{(1)} &= \frac{16}{3}\frac{m_{\alpha\beta}}{m_\alpha} n_\beta \Omega_{\alpha\beta}^{11}, \\
\upsilon_{\alpha\beta}^{(2)} &= \frac{64}{15}\left(\frac{m_{\alpha\beta}}{m_\alpha}\right)^2 n_\beta \left[\Omega_{\alpha\beta}^{12} - \frac{5}{2}\Omega_{\alpha\beta}^{22}\right], \\
\upsilon_{\alpha\beta}^{(3)} &= \frac{16}{5}\frac{m_{\alpha\beta}^2}{m_\alpha m_\beta} n_\beta \left[\frac{10}{3}\Omega_{\alpha\beta}^{11} + \frac{m_\beta}{m_\alpha}\Omega_{\alpha\beta}^{22}\right], \\
\upsilon_{\alpha\beta}^{(4)} &= \frac{16}{5}\frac{m_{\alpha\beta}^2}{m_\alpha m_\beta} n_\beta \left[\frac{10}{3}\Omega_{\alpha\beta}^{11} - \Omega_{\alpha\beta}^{22}\right], \\
\upsilon_{\alpha\beta}^{(5)} &= \frac{64}{15}\left(\frac{m_{\alpha\beta}}{m_\alpha}\right)^3 \frac{m_\alpha}{m_\beta} n_\beta \left[\Omega_{\alpha\beta}^{22} + \left(\frac{15}{4}\frac{m_\alpha}{m_\beta} + \frac{25}{8}\frac{m_\beta}{m_\alpha}\right)\Omega_{\alpha\beta}^{11} - \frac{1}{2}\frac{m_\beta}{m_\alpha}\left(5\Omega_{\alpha\beta}^{12} - \Omega_{\alpha\beta}^{13}\right)\right], \\
\upsilon_{\alpha\beta}^{(6)} &= \frac{64}{15}\left(\frac{m_{\alpha\beta}}{m_\alpha}\right)^3 \left(\frac{m_\alpha}{m_\beta}\right)^{3/2} n_\beta \left[-\Omega_{\alpha\beta}^{22} + \frac{55}{8}\Omega_{\alpha\beta}^{11} - \frac{5}{2}\Omega_{\alpha\beta}^{12} + \frac{1}{2}\Omega_{\alpha\beta}^{13}\right],
\end{aligned}
\tag{A.1}
$$

where

$$
m_{\alpha\beta} = \frac{m_\alpha m_\beta}{m_\alpha + m_\beta} \tag{A.2}
$$

is the reduced mass of the mixture. In expressions (A.1) the $\Omega_{\alpha\beta}^{(ij)}$ functions represent the omega integral [70], which for the case of the HS model are defined as [70]

$$
\Omega_{\alpha\beta}^{(ij)} = \frac{(j+1)!}{8}\left[1 - \frac{1+(-1)^i}{2(i+1)}\right]\left(\frac{\pi kT}{2m_{\alpha\beta}}\right)^{1/2}(d_\alpha + d_\beta)^2, \tag{A.3}
$$

where d_α is the molecular diameter of species α. The numerical simulations are carried out using dimensionless quantities. The dimensionless omega integrals are defined as follows

$$
\Omega_{\alpha\beta}^{*(ij)} = \Omega_{\alpha\beta}^{(ij)}\left[\frac{1}{4}\sqrt{\frac{\pi kT}{2m_{12}}}d_1^2\right]^{-1}. \tag{A.4}
$$

As an example, the dimensional and dimensionless form of $\Omega_{\alpha\beta}^{(1,1)}$ are given below

$$\begin{aligned}\Omega_{\alpha\beta}^{(11)} &= \frac{1}{4}\sqrt{\frac{\pi kT}{2m_{\alpha\beta}}}\left(d_\alpha + d_\beta\right)^2, \\ \Omega_{\alpha\beta}^{*(11)} &= \sqrt{\frac{m_{12}}{m_{\alpha\beta}}}\left(\frac{d_\alpha + d_\beta}{d_1}\right)^2.\end{aligned} \tag{A.5}$$

The dimensionless $\upsilon_{\alpha\beta}^{(n)}$ functions (A.1) are defined as follows

$$\upsilon_{\alpha\beta}^{*(i)} = \upsilon_{\alpha\beta}^{(i)}\left[\frac{1}{4}\sqrt{\frac{\pi kT}{2m_{12}}}d_1^2 n_1\right]^{-1}. \tag{A.6}$$

As an example, the dimensional and dimensionless form of $\upsilon_{\alpha\beta}^{(1)}$ function are

$$\begin{aligned}\upsilon_{\alpha\beta}^{(1)} &= \frac{16}{3}\frac{m_{\alpha\beta}}{m_\alpha}n_\beta\Omega_{\alpha\beta}^{(11)}, \\ \upsilon_{\alpha\beta}^{*(1)} &= \frac{16}{3}\frac{m_{\alpha\beta}}{m_\alpha}\frac{n_\beta}{n_1}\Omega_{\alpha\beta}^{*(11)}.\end{aligned} \tag{A.7}$$

It is noted that γ_α, S_α have the same dimension as $\upsilon_{\alpha\beta}^{(i)}$ so we use the same reference quantity to obtain the dimensionless expressions for these functions.

The expressions for the reduced collision terms in eqs. (8.22) and (8.23)

$$\begin{aligned}L_{\alpha\beta}(\Phi_\alpha) = &-\gamma_\alpha\Phi_\alpha + \\ &+ 2\left[\gamma_\alpha u_\alpha - \upsilon_{\alpha\beta}^{(1)}\left(u_\alpha - u_\beta\right) - \frac{\upsilon_{\alpha\beta}^{(2)}}{2}\left(q_\alpha - \frac{m_\alpha}{m_\beta}q_\beta\right)\right]c_{x\alpha} + \\ &+ 4\sqrt{\frac{m}{m_\alpha}}\left[\left(\gamma_\alpha - \upsilon_{\alpha\beta}^{(3)} - \upsilon_{\alpha\alpha}^{(3)}\right)p_{xy\alpha} + \upsilon_{\alpha\alpha}^{(4)}p_{xy\alpha} + \upsilon_{\alpha\beta}^{(4)}p_{xy\beta}\right]c_{x\alpha}c_{y\alpha} \\ &+ \frac{4}{5}\left[\left(\gamma_\alpha - \upsilon_{\alpha\beta}^{(5)} - \upsilon_{\alpha\alpha}^{(5)}\right)q_\alpha + \upsilon_{\alpha\beta}^{(6)}\sqrt{\frac{m_\beta}{m_\alpha}}q_\beta + \upsilon_{\alpha\alpha}^{(6)}q_\alpha - \frac{5}{4}\upsilon_{\alpha\beta}^{(2)}\left(u_\alpha - u_\beta\right)\right]c_{x\alpha}\left(c_{x\alpha}^2 + c_{y\alpha}^2 - 2\right).\end{aligned} \tag{A.8}$$

$$
\begin{aligned}
L_{\alpha\beta}(\Psi_\alpha) = & -\gamma_\alpha \Psi_\alpha \\
& + \left[\gamma_\alpha u_\alpha - \upsilon_{\alpha\beta}^{(1)} \left(u_\alpha - u_\beta \right) - \frac{\upsilon_{\alpha\beta}^{(2)}}{2} \left(q_\alpha - \frac{m_\alpha}{m_\beta} q_\beta \right) \right] c_{x\alpha} \\
& + 2\sqrt{\frac{m}{m_\alpha}} \left[\left(\gamma_\alpha - \upsilon_{\alpha\beta}^{(3)} - \upsilon_{\alpha\alpha}^{(3)} \right) p_{xy\alpha} + \upsilon_{\alpha\alpha}^{(4)} p_{xy\alpha} + \upsilon_{\alpha\beta}^{(4)} p_{xy\beta} \right] c_{x\alpha} c_{y\alpha} \\
& + \frac{2}{5} \left[\left(\gamma_\alpha - \upsilon_{\alpha\beta}^{(5)} - \upsilon_{\alpha\alpha}^{(5)} \right) q_\alpha + \upsilon_{\alpha\beta}^{(6)} \sqrt{\frac{m_\beta}{m_\alpha}} q_\beta + \upsilon_{\alpha\alpha}^{(6)} q_\alpha - \frac{5}{4} \upsilon_{\alpha\beta}^{(2)} \left(u_\alpha - u_\beta \right) \right] c_{x\alpha} \left(c_{x\alpha}^2 + c_{y\alpha}^2 - 1 \right).
\end{aligned}
\tag{A.9}
$$

Appendix B

Publications

This thesis has contributed to the following publications:

B.1 Peer-review papers

1. M.T. Ho, I. Graur. Heat transfer through rarefied gas confined between two concentric spheres, *International Journal of Heat and Mass Transfer* 90 (2015), 58-71.

2. I. Graur, T. Veltzke, J. G. Méolans, M.T. Ho, J. Thöming. The gas flow diode effect: Theoretical and experimental analysis of moderately rarefied gas flows through a micro channel with varying cross section, *Microfluidics and Nanofluidics* 18 (3) (2015), 391-402.

3. M.T. Ho, I. Graur. Numerical study of unsteady rarefied gas flow through an orifice, *Vacuum* 109 (2014), 253-265.

4. I. Graur and M.T. Ho. Rarefied gas flow through a long rectangular channel of variable cross section, *Vacuum* 101 (2014), 328–332.

5. I. Graur, M.T. Ho, M. Wuest. Simulation of the transient heat transfer between two coaxial cylinders, *Journal of Vacuum Science & Technology A: Vacuum, Surfaces, and Films* 31 (6) (2013) 061603.

B.2 Conferences

1. D. Maharjan*, M. Hadj-Nacer, M. Greiner, MT Ho, I. Graur, S. Stefanov, Simulation of heat transfer across rarefied gas in annular and planar geometries: comparison of Fluent, DSMC and DVM methods results, *ASME 2015 13th International Conference on Nanochannels, Microchannels, and Minichannels*, July 6-9, 2015, San Francisco, CA, USA.

2. Manzo T*, Hadj-Nacer M, Ho MT, Graur I, Greiner M, Phenomena affecting used nuclear

fuel cladding temperatures during vacuum drying operations, *ANS 2015 International High-Level Radioactive Waste Management conference*, April 12-16, 2015, Charleston, SC, USA.

3. M.T. Ho*, J.-D. Parisse, I. Graur, Oscillatory Couette flow of binary rarefied gas mixture, *4th European Conference on Microfluidics*, December 10-12, 2014, Limerick, Ireland.

4. I. Graur, T. Veltzke, J. G. Méolans, M. T. Ho*, J. Thöming, Rarefied Gas Flow Through Divergent- Convergent Micro Channel, *5th International conference on Heat Transfer and Fluid Flow in Microscale*, April 22-25, 2014, Marseille, France.

5. M.T. Ho*, I. Graur, M. Wuest, Time-dependent heat transfer of a gas between two coaxial cylinders, *19th International Vacuum Congress*, September 9-13, 2013, Paris, France.